Precision CCD Photometry of Globular Clusters

Richard Gareth Noble

September 1987

Submitted in accordance with the requirements for the degree of Doctor of Philosophy.

The University of Leeds
Department of Physics

Abstract

The first part of this thesis presents a review of colour-magnitude photometry of Galactic globular clusters. A survey has been made of recently-published colour-magnitude photometry of globular clusters, and a self-consistent distance scale established for these data, using the method of subdwarf matching to the observed main sequences. The distances thus derived have been combined with other published colour-magnitude data to infer cluster ages and horizontal branch magnitudes. The relationship between cluster horizontal branch magnitude and metallicity is dicussed.

In Chapter 2, a review is made of the photometric applications of charge coupled devices, giving particular attention to the aquisition and analysis of crowded field CCD images within globular clusters. Digital photometric techniques are discussed, including analytic profile-fitting to stellar images.

The major experimental part of this thesis concerns observations of the globular cluster ω Centauri. These observations, their subsequent reduction, and photometric analysis, are discussed in Chapter 3. This chapter also contains a discussion of previous work on this cluster, and highlights its extremely unusual nature. The significant discovery of geometrically varying stellar profiles in the programme CCD images, and the techniques for their analysis, are discussed.

The colour-magnitude data from these observations are discussed in Chapter 4. The distance to the cluster is determined, and it is shown that there exists an intrinsic spread in colour upon the cluster main sequence. Theoretical isochrones are employed to show that this spread in colour is consistent with a main sequence metallicity distribution similar to that seen in more highly-evolved stars within the cluster. The age of the cluster is determined as 16 ± 3 Gyr, by comparison with theoretical isochrones. This result is consistent with recent determinations for other clusters, and supports the theory that the Galactic globular cluster system is essentially coeval. The cluster main sequence luminosity function has been constructed, and is compared with recent observations and theory.

In Chapter 5, a preliminary colour-magnitude study of the SMC cluster Lindsay 11 is presented.

Contents

Key to Abbreviations viii
Quotation ix
Acknowledgements x

1 Globular Clusters **1**
1.1 Introduction 1
1.2 The Colour-Magnitude Diagram 2
1.2.1 CM Diagram Morphology 4
1.3 Globular Cluster Distances 11
1.3.1 Main Sequence Fitting 11
1.3.2 RR Lyrae Normalisation 18
1.4 The Ages of Globular Clusters 28
1.5 Some Recent Results 32
1.6 The Globular Cluster Abundance Scale 44
1.6.1 CMD Metallicity Indicators 45
1.6.2 Spectroscopic Observations of Individual Stars 47
1.6.3 Chemical Inhomogeneity Within Clusters 49
1.7 Globular Cluster Luminosity Functions 50

2 CCD Stellar Photometry **53**
2.1 Introduction to Astronomical Photometry 53
2.2 Defining a Photometric System 54
2.2.1 Standard Photometric Systems 57
2.3 The Relationship Between Instrumental and Standard Magnitudes 60
2.3.1 Atmospheric Extinction 60
2.3.2 Colour Transformation 61
2.4 The CCD as a Photometric Detector 61

2.5 The Principles of CCD Operation 63
2.6 Making and Processing CCD exposures 66
2.6.1 Biasing 67
2.6.2 Dark Current 69
2.6.3 Charge Transfer Efficiency 70
2.6.4 Pixel to Pixel Non-Uniformity 70
2.6.5 Discrete Pixel Defects 72
2.6.6 Cosmic Ray Events 73
2.6.7 Fringing 74
2.6.8 Other Image Defects 74
2.6.9 Detector Characteristics 75
2.6.10 A Coherent Strategy for CCD Observations 76
2.7 CCD Photometric Reductions 77
2.7.1 Digital Aperture Photometry 78
2.7.2 Profile Fitting Methods 80

3 ω Centauri **90**
3.1 Introduction 90
3.2 The B and V Observations 95
3.2.1 The SAAO Observations 95
3.2.2 The AAT B and V Observations 97
3.3 Data Reduction 106
3.3.1 The SAAO Data 106
3.3.2 The AAT Data 116
3.4 The WB,WR Observations of ω Centauri 118
3.4.1 The WB,WR Filter System 118
3.4.2 Observations 122
3.4.3 Data Reduction 123

4 Results of the CCD Observations of ω Cen **143**
4.1 The Composite ω Cen CMD 143
4.1.1 The Uncertainties in the CMD 144
4.1.2 The Distance of ω Centauri 148
4.1.3 The Intrinsic Width of the Main Sequence 153

4.1.4 The Age of ω Centauri 167

4.1.5 The Cluster Luminosity Function 172

4.1.6 The Search for Cluster White Dwarfs 178

5 CCD Observations of the SMC Cluster Lindsay 11 **180**

5.1 Introduction 180

5.2 Observations 182

5.2.1 Data Reduction 184

5.3 The CMD of Lindsay 11 189

6 Conclusions **193**

6.1 Observations of ω Centauri 193

6.2 Some Implications of Recent CCD Colour-Magnitude Studies . . . 199

6.3 Observations of Lindsay 11 201

6.4 CCD Photometry 202

References 203

List of Figures

1.1 The main features of the globular cluster CM diagram 3
1.2 The average interstellar extinction curve 13
1.3 Carney's (1979) subdwarf sequence as used in this study 17
1.4 Main sequence isochrone and synthetic ZAHB fits to CM data of the cluster 47 Tuc 33
1.5 Comparison of photographic and CCD photometry of the cluster NGC 6752 34
1.6 Horizontal branch absolute magnitude plotted against metallicity . 37
1.7 The period-shift–metallicity relation as derived by Noble and Dickens (1987) 39
1.8 The correlation of apparent bolometric magnitude with period-shift for RR Lyrae variables in M3 40
1.9 The correlation of apparent bolometric magnitude with period-shift for the RR Lyrae variables in ω Centauri 41
1.10 t_{TO} as a function of cluster metallicity 42
1.11 t_{Δ} as a function of cluster metallicity 43
1.12 The $\Delta V_{1.4}$ and $(B-V)_{o,g}$ metallicity indicators 46

2.1 The colour–temperature relationship for main sequence stars . . . 56
2.2 The Johnson UBV passbands 58
2.3 A schematic diagram of a MOS capacitor 63
2.4 A schematic diagram of a three-phase CCD 66
2.5 Measured aperture flux versus aperture diameter for a single bright star 79
2.6 Typical crowded-field stellar images on a CCD exposure 83
2.7 Hidden line surface drawing of CCD stellar images 84
2.8 Mean radial profile and fitted Lorentzian function 85

2.9 Difference between mean radial ADU count and fitted profile . . . 86
2.10 Stellar image after subtraction of fitted Lorentzian profiles 87

3.1 The location and extent of the ω Centauri observations 96
3.2 The SAAO fields in ω Centauri 99
3.3 The AAT B and V Observations 105
3.4 Residual defect in a cleaned SAAO CCD image 108
3.5 SAAO preflash exposure 109
3.6 The image distortion caused by charge transfer inefficiency 111
3.7 The transformation from instrumental to standard V magnitude for the SAAO data 113
3.8 The transformation from instrumental to standard $(B-V)$ colour for the SAAO data 113
3.9 Comparison of CCD observations with the photoelectric standards of Cannon (1981) 115
3.10 The CMD for the AAT observations made in March 1986 121
3.11 The Transmission of the WB and WR Filter System 122
3.12 Residuals to the derived WB, WR colour equations 125
3.13 The WB,WR instrumental CMD of ω Centauri 127
3.14 Difference between aperture and profile fitting photometry versus CCD x-coordinate for frame 249–5 130
3.15 The variation of profile parameter r_x with CCD x-coordinate for frame No. 5 131
3.16 Schematic diagram showing the postulated misalignment of the AAT CCD chip. 132
3.17 The instrumental CMD for the WB, WR data, as derived by fitting data with a geometrically variant PSF 137
3.18 The composite colour-magnitude diagram of ω Centauri 142

4.1 Determination of the distance modulus of ω Cen by subdwarf sequence fitting 151
4.2 Field star counts in three regions of the ω Cen main sequence colour-magnitude diagram 156
4.3 The mean locus of the ω Cen main sequence 159
4.4 Colour residuals from the main sequence mean locus 160

4.5 The metallicity distribution of evolved stars in ω Cen 162
4.6 The model main sequence metallicity distribution 163
4.7 Overlays of the expected colour-residual distribution derived from the adopted model metallicity distribution 165
4.8 16 Gyr VandenBerg & Bell (1985) isochrones overlaid upon the ω Cen CMD 169
4.9 14, 16, and 18 Gyr VandenBerg & Bell (1985) isochrones of [Fe/H] = -1.27 overlaid upon the ω Cen CMD 170
4.10 The fraction of recovered stars as a function of magnitude 174
4.11 The ω Cen main sequence luminosity function before correction for incompleteness and field star contamination 175
4.12 The ω Cen luminosity function after correction for incompleteness and field star contamination 176
4.13 Comparison of the observed luminosity function of ω Cen with model luminosity functions 177
4.14 The colour-magnitude diagram of ω Cen showing the predicted location of the cluster white dwarf sequence 179

5.1 The SMC cluster L11 183
5.2 Differences between the E-region standard magnitudes and colour indices and those derived from the observations 185
5.3 The Lindsay 11 V, $(B-V)$ colour-magnitude diagram 189
5.4 The Lindsay 11 R, $(V-R)$ colour-magnitude diagram 191
5.5 The R, $(V-R)$ CMD for stars within 40″ of the centre of L11 . . 192

List of Tables

1.1 Lutz-Kelker corrections to observed stellar parallaxes 16
1.2 RR Lyrae absolute magnitudes from main sequence fitting 20
1.3 Colour-magnitude data from recently published CCD photometry . 36

2.1 The Strömgren Filter System 59

3.1 Properties of the RCA 53612 CCD chip in the SAAO/UCL CCD camera 97
3.2 Principal parameters of the SAAO B and V observations 98
3.3 Parameters for the AAT B and V observations 104
3.4 The SAAO colour-magnitude data 117
3.5 The AAT short exposure colour-magnitude data 119
3.6 The AAT WB, WR exposures to field O1 in ω Centauri 123
3.7 Uncertainties in WB,WR photometry 129
3.8 The faint colour-magnitude data from the WB, WR observations . 138

4.1 The observed and calculated internal observational error along the ω Cen main sequence 149
4.2 The predicted number of field stars per magnitude within $\pm 0^m.25$ in $(B-V)$ of the ω Cen principal sequence in the final CMD . . . 155
4.3 Comparison of the predicted and observed field star numbers in the colour-magnitude photometry of field O1 156
4.4 The main sequence intrinsic width in the magnitude range $18 < V < 24$ 161

5.1 The SAAO B, V and R observations of L11 182
5.2 Details of measured stars in Lindsay 11 186

Key to Abbreviations

AAT	Anglo-Australian Telescope
ADU	Analogue to Digital Unit
AGB	Asymptotic Giant Branch
BHB	Blue Horizontal Branch
CCD	Charge Coupled Device
CM	Colour Magnitude
CMD	Colour Magnitude Diagram
CTE	Charge Transfer Efficiency
DAP	Digital Aperture Photometry
DQE	Detective Quantum Efficiency
FWHM	Full-Width Half-Maximum
HB	Horizontal Branch
HST	Hubble Space Telescope
IMF	Initial Mass Function
LED	Light Emitting Diode
LUST	Leeds University Starlink Team
MOS	Metal Oxide Semiconductor
MS	Main Sequence
NASA	National Aeronautical and Space Administration
PSF	Point Spread Function
QE	Quantum Efficiency
RCA	Radio Corporation of America
RGB	Red Giant Branch
RHB	Red Horizontal Branch
SAAO	South African Astronomical Observatory
SGB	Sub-Giant Branch
SMC	Small Magellanic Cloud
ZAHB	Zero-Age Horizontal Branch
ZAMS	Zero-Age Main Sequence

'If you are cheerful, and wish to remain so, leave the study of astronomy alone. Of all the sciences, it alone deserves the character of the terrible...if, on the other hand, you are restless and anxious about the future, study astronomy at once. Your troubles will be reduced amazingly. But your study will reduce them in a singular way, by reducing the importance of everything.'

Thomas Hardy,

Two on a Tower

Acknowledgements

It gives me great pleasure to take this opportunity of expressing my humble gratitude to those people who have advised, aided, cajoled, criticized, tended and tolerated me during the course of my research.

I am indebted to my supervisor, Bill Griffiths, for his guidance and assistance. I am likewise indebted to Phil Marsden for the provision of a postgraduate studentship within the Physics Department. My gratitude to the staff of the Physics Department, academic, technical and administrative and in particular to John Baruch, for his help in meeting this, the final deadline. I would also like to acknowledge the receipt of an SERC award during the course of my research.

My especial thanks to Bob Dickens for his generous and knowledgable advice and inspiration, and to Alan Penny, whose experience and expertise in the field of CCD photometry has been invaluable. My thanks also to Russell Cannon, for his assistance during the early part of my research.

It would be remiss indeed if I did not mention my colleagues and close friends in LUST, both past and present; Nigel Birtwell, Iain Brodie, John Buttress, Nigel Fenney and Steve Marley. Thanks lads! I am also grateful to all of those in the Physics Department who have made my working environment so pleasant; special thanks to Penny & Andy, D.J.T. & Craig.

Affectionate thanks to those friends who have made the last four years so fruitful and enjoyable. In particular, to John & Jill, Mel, Rob, Graeme, Steve, Dave and Stu.

To my family, for their support and understanding, and especially for the love and faith of my mother and father, to whom I respectfully dedicate this thesis.

My love (♡) and eternal gratitude to Imelda, whose contribution has been out of all proportion to her stature.

Chapter 1

Globular Clusters

1.1 Introduction

Conventionally, globular clusters have been considered to be massive, gravitationally bound and dynamically independent systems of up to a million stars (Cannon 1983). The limiting radius of these clusters is normally of the order of 60 pc (Webbink, 1985), and thus they represent a relatively enormous concentration of stars. They have been identified as a "POPULATION II" component of the Galaxy (Baade, 1944) of great antiquity, with ages of the order of 15×10^9 years. Because of their extreme age, globular clusters are seen as valuable probes of the early conditions within the Galaxy (see, for instance, Eggen *et al.* 1962 or Mould, 1982). Classically, globular clusters were considered to have formed from chemically homogeneous and generally low abundance material over a timescale very short compared to their great age.

Two sets of criteria have been employed when deciding if an association of stars should be considered a globular cluster; firstly geometrical properties—the structure and dynamics of a group of stars, and secondly the stellar content, as determined by spectroscopic and photometric observations of both individual stars and integrated samples of stars.

In recent years it has become clear, principally through the study of Magellanic Cloud clusters, that there exist dynamically evolved stellar systems meeting the geometrical criteria above, which photometric and spectroscopic studies show to have ages comparable to our own Galactic open clusters. These are therefore disqualified as being inconsistent with the generally held view of the stellar content of

globular clusters. The approach which has been adopted in recent years, perhaps most notably by Harris and Racine (1979) in their review of globular clusters in galaxies, has been to use photometric data to classify globular clusters by their stellar content.

Developments in globular cluster research over the last decade have questioned many of the above fundamental assumptions about the formation and history of these star systems, however, to quote Cannon (1983) it can still be said that *"Those assumptions are probably still approximately true for most of the clusters most of the time"*.

In the study of stellar content and composition of globular clusters, photometry, the measurement of apparent stellar brightness and colour, is of paramount importance. The most powerful tool available for probing the evolutionary state and properties of a cluster as a whole is undoubtedly the colour-magnitude (CM) diagram.

1.2 The Colour-Magnitude Diagram

The usefulness of the CM diagram stems from the relative ease with which data can be obtained photometrically, assimilated and then, qualitatively at least, compared with the theoretical counterpart, the temperature-luminosity or Hertzsprung-Russell (HR) diagram.

Following the assumption that the formation time of a cluster is small compared with its age, then a cluster's CM diagram should illustrate the different evolutionary positions attained by its constituent stars—all of the same age, but of differing masses.

The outstanding feature of the globular cluster CM diagram, which allowed Baade (1944) to differentiate members of globular clusters from the nearby stars in open clusters, was the presence of a highly luminous red giant branch (RGB). Further studies showed a wealth of morphological features, as shown in Figure 1.1, a schematic diagram of the main features seen in a globular cluster CM diagram. The abbreviated captions of Figure 1.1 are explained in the text.

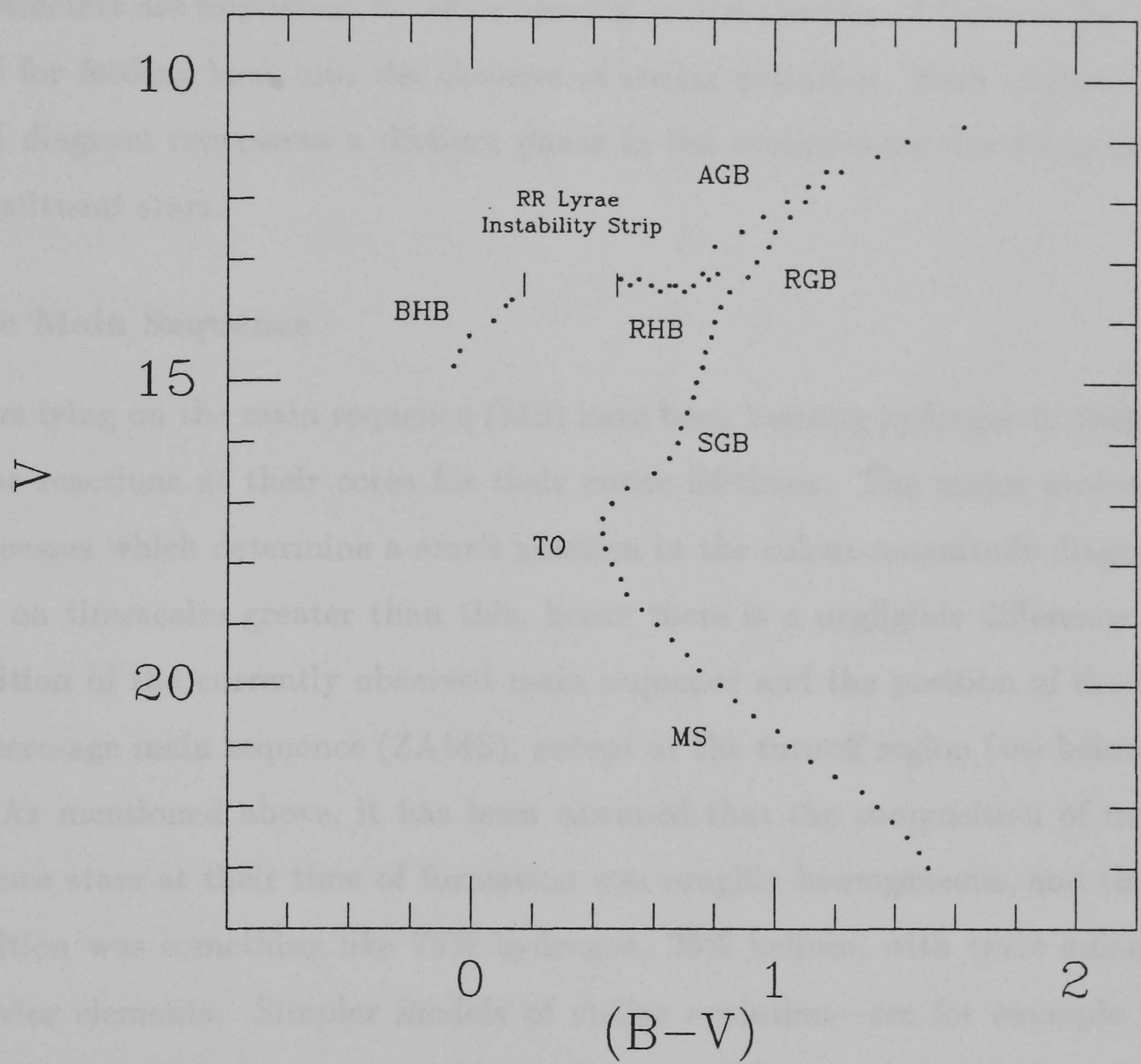

Figure 1.1: The main features of the globular cluster CM Diagram. The abbreviated captions are explained within the text.

1.2.1 CM Diagram Morphology

The globular cluster colour-magnitude diagram gives us an "instant snapshot" of the evolutionary status of the stellar population of that cluster. Not only is it possible to assess the relative differences between clusters, but by appealing to theoretical arguments and calibrating the CM diagram from our knowledge of stellar properties, it is possible to obtain information about the absolute values of certain fundamental parameters pertaining to the cluster—in this way, its age, chemical composition and distance from the observer can be determined. These parameters are important for their bearing on the theories of Galactic formation, and for feeding back into the theories of stellar evolution. Each segment of the CM diagram represents a distinct phase in the evolutionary development of its constituent stars.

The Main Sequence

Stars lying on the main sequence (MS) have been burning hydrogen in thermonuclear reactions at their cores for their entire lifetimes. The major evolutionary processes which determine a star's position in the colour-magnitude diagram occur on timescales greater than this, hence there is a negligible difference in the position of the currently observed main sequence and the position of the initial, or zero-age main sequence (ZAMS), except at the turnoff region (see below).

As mentioned above, it has been assumed that the composition of main sequence stars at their time of formation was roughly homogeneous, and the composition was something like 75% hydrogen, 25% helium, with trace amounts of heavier elements. Simpler models of stellar evolution—see for example Tayler (1970)—consider the star to be spherically symmetrical, hydrostatically supported against gravity, and non-rotating. The great central pressure implies a high central temperature, which is supplied by thermonuclear fusion reactions. The outflow of energy across this thermal gradient heats the outer regions of the star and is the source of the star's luminosity.

The transport of energy from the stellar interior by radiation is dependent on the *opacity* of the material through which it flows. If the radiative process becomes insufficient to transport energy at the rate required to maintain hydrostatic equilibrium, perhaps due to particularly high opacity in some region, then

instabilities will arise in the gas and convection will become an important heat transfer mechanism. Convective zones prove very difficult to model in theory, and a further complication is that, in addition, stellar rotation may cause mixing of materials in the stellar interior.

Stars of mass $M > 1.5M_\odot$ have been shown to have convective cores, whereas those of lower mass ($M \leq M_\odot$) have a considerable fraction of their mass in the form of a convective shell or envelope just below their surface (Iben & Renzini, 1984). The behaviour of the convective envelope in such low mass main sequence stars leads to considerable uncertainty in our understanding of stellar structure.

The main energy sources available within the stellar core are those thermonuclear reactions in which hydrogen is fused to helium. Of the mechanisms available, the most prevalent are the proton-proton (PP) chain, and the carbon-nitrogen (CN) cycle. The PP chain is dominant at temperatures of less than 2×10^7 K, and the CN cycle at temperatures higher than this.

One great difficulty in comparing qualitatively an observed main sequence with theoretical predictions is the conversion of magnitude to total, or bolometric luminosity, and of colour, or spectral index, to the effective temperature, T_e, defined by;

$$L = 4\pi r_s^2 \sigma T_e^4.$$

Where;
L is the total luminosity of the star,
σ is the Stefan-Boltzmann constant,
and r_s is the radius of the star—taken as the radius for which the optical depth, τ, is unity for an observer outside the star.

The position of the main sequence is a function of both the fractional helium abundance, Y, and the fractional abundance of metals, Z, principally because of the effect of the amounts of these elements on the opacity of the stellar material. For instance Castellani (1980) gives $\Delta \log L \approx -1.3\Delta Y$, or for a variation of 0.1 in Y, the ZAMS is shifted by $\approx 0\overset{m}{.}3$.

The Turnoff Region

The lifetime of a main sequence star is principally determined by the availability of hydrogen fuel for conversion to helium in the star's core. The exhaustion of hydrogen in this region causes hydrogen burning to move outward into a shell surrounding the core. The helium-rich, hydrogen-depleted core now contracts and heats up. In response to these central changes the whole structure of the star slowly changes and the star leaves the main sequence toward the right, low temperature side. Because the main sequence lifetime of a star is such a strong function of mass (see for example Iben, 1967) the position of the turnoff from the globular cluster main sequence is the primary indicator of the cluster's age (see below).

The Giant Branch

The development and evolution of a star on the giant branch was first outlined by Hoyle and Schwarzschild (1955), and more recent contributions include Eggleton & Faulkner (1981), and Weiss (1983). The increase in central density caused by gravitational contraction means that low and intermediate mass stars ($M \leq 2.25 M_{\odot}$) develop a degenerate core. In this situation the core pressure depends only on density, and not on temperature as in the classical case. Core temperature therefore rises only slowly as gravitational potential is converted to non-thermal electron kinetic energy. Conduction by electrons and energy loss by neutrino escape stops the degenerate core temperature from rising rapidly. During this time the swelling of the star's convective envelope, powered by hydrogen shell burning, causes the star to move upward in the HR diagram, reaching higher luminosities and lower surface temperatures, approaching the relevant Hayashi track—the path followed in the HR diagram by stars which are convective throughout.

Despite the general details of this stage of stellar evolution being well understood in theory, and matched well by observation, certain observations cannot be explained. Cannon (1983) demonstrated a gap in the sub-giant branch (SGB) of the CM diagram of the cluster NGC 6752, representing a fast stage of stellar evolution which is not predicted by theory, and similar features have been seen by King *et al.* (1985) and McClure *et al.* (1987a).

There is also clearly a dependence of giant branch colour with metallicity, as

shown by Sandage and Smith (1966), but modelling the observations has proved to be problematical because of the strong dependence of the effective surface temperature upon the convective "mixing length" parameter used to describe the heat transfer process from the stellar interior (See, for example VandenBerg, 1983).

Eventually the core temperature is high enough for the ignition of helium. The onset of helium burning is very rapid, and once underway a *thermal runaway* ensues and there is a rapid readjustment of structure, leaving the star with a non-degenerate helium burning core and an envelope which is much less distended than in the red-giant phase of evolution. The sudden spurt of evolutionary activity accompanying the onset of helium burning is known as the *helium flash.* No adequate theory has been developed to describe the behaviour of the star and the processes occurring within it throughout this phase, but it is thought that it is accompanied by considerable mass-loss from the star. The net effect is a sudden increase in effective temperature at the stellar surface and a lowering of the total luminosity, causing rapid migration onto the horizontal branch (HB).

Horizontal Branch Evolution

Stars on the horizontal branch have been conventionally subdivided into three distinguishable components;

The red horizontal branch (RHB) which intersects with the giant branch to the right.

RR Lyrae variable stars, HB stars lying in a region of pulsational instability (see below), generally not plotted on the CM diagram because of this variability.

The blue horizontal branch (BHB), lies to the left of the RR Lyrae group in the CM diagram, with $(B-V) \leq 0.2$, and curves off towards higher temperatures and lower luminosities.

This phase of evolution was first explained theoretically by Faulkner (1966), and Faulkner & Iben (1966), whose work qualitatively predicted the behaviour of stars after the ignition of helium at the giant branch tip, and explained the relative numbers of HB stars from the predicted evolutionary lifetimes of stars at this stage of development. Earlier attempts to model post helium-flash stellar evolution which discounted mixing of the core's contents with the outer envelope of the star

(for instance, Haselgrove & Hoyle, 1958) failed to adequately describe the observed HB morphology. The belief that the horizontal branch phase represents an almost totally mixed star traversing from the helium-rich main sequence position to the giant branch in a fashion analogous to the earlier turn off to the SGB, gained some credence, but Faulkner pointed out several flaws in this argument. There exist clusters in which the HB is seen purely as a clump of stars lying within a small range in colour, eg 47 Tuc (NGC 104), and no stars are seen making the transition in colour from the helium MS. Similarly, no grouping of stars is seen at the helium main sequence position, something which this theory predicts, as such thoroughly mixed stars should spend a considerable fraction of their remaining lifetimes in this region. The concept of selective mixing to produce the requisite number and distribution of stars along the HB is also difficult to invoke, not least because of the suspiciously sharp cutoff in mixing required to explain why there is a range of HB star colour, without large amounts of clumping at the helium main sequence end. Faulkner thus re-examined the hypothesis that stars reached the horizontal branch without mixing. The initial premises which Faulkner worked from were that the model should basically consist of a helium core, surrounded by a hydrogen-rich envelope, the composition being discontinuous at the interface, and that the temperature in the core should be sufficiently high to promote helium burning by the triple-α process. The results of Faulkner's conjectures were that, for the mass range in question, the hydrogen-rich envelope would contain a shell in which hydrogen burning was continuing and it is this shell source which dominates the structure of the star.

The major observational feature of the CM diagram which Faulkner sought to explain with this model was the putative existence of a gap between the low temperature end of the HB and the giant branch, dependent in extent on the metallicity of the cluster. Evidence for such a feature, not to be confused with the allegorical RR Lyrae gap, seemed to come from the photometric observations of horizontal branches which were available at the time. Clusters of high metal abundance seemed to possess short, stubby HBs which coincided at their red ends with the sub-giant branch, whereas those of metal-weak clusters exhibited an HB which extended far into the blue and had a significant gap in colour between its red end and the SGB. Clusters of intermediate metallicities seemed to show HB morphologies in between these extremes.

Faulkner had shown the great sensitivity of the star's position in the HR diagram to relatively small changes in the hydrogen-burning shell at the base of the stellar envelope. He demonstrated too that because the rate of energy generation by the CNO cycle is sensitive to small variations in Z_{CNO}, and hence overall metallicity, the morphology of the HB is in turn a function of metallicity.

This result may, in retrospect, be seen as fortuitous as it was barely a year later that Sandage & Wildey (1967) published the colour-magnitude diagram of NGC 7006, which seemed to disprove the correlation of metallicity and HB morphology. This became the first of a number of similar globular clusters, a group which were dubbed the "second parameter" clusters, because of the seeming inability of the variation of a single parameter, namely the metal abundance, to adequately describe their HB distributions. The classic example cited by Freeman & Norris (1981) is the comparison of the HB morphologies of M13, M3 and NGC 7006. All three clusters have metal abundances of [Fe/H][1]≈ -1.6, but the HB of M13 is predominantly blue, that of M3 is intermediate in colour, and NGC 7006 has a mainly red horizontal branch.

Several attempts were made to classify the HB morphology, and identify any link between the shape of the horizontal branch and any other factor. Such classification schemes included the Dickens (1972a) horizontal branch type, the Mironov (1972) $B/(B+R)$ parameter and the classification scheme due to Castellani *et al.* (1970), which attempted to demonstrate the dependence of HB morphology on both Z and Y. By and large, such schemes only served to illustrate the complexity of the "second parameter" problem.

Iben & Rood (1970) showed that in order to reproduce the observed spread in colour of globular cluster horizontal branch sequences it is necessary to assume some spread in mass along the HB of the order of 0.1–0.2$M_{\odot}$. They also identified the secondary or asymptotic giant branch as consisting of stars which are burning helium in a shell surrounding a carbon-oxygen core. Their calculations, however, predicted a "wedge" shaped blue horizontal branch, something that is not seen observationally.

---

[1][Fe/H] represents the stellar abundance of elements heavier than helium, assuming these elements are present in the same relative ratios as in the sun, and is formally, [Fe/H] = $\log(N_{Fe}/N_H)_* - \log(N_{Fe}/N_H)_{\odot}$. A factor of ten in the relative abundance (*i.e.* a change in [Fe/H] of 1) is referred to as one dex.

Rood (1973) constructed more synthetic HB CM diagrams, and showed that mass dispersion in HB stars gives an acceptable fit to the observational data, but that variations in age of as little as 1×10^9 years, and in He mass fraction by as little as 0.03 could also account for all of the observed morphologies. It was obvious that an adequate theory for mass loss on the giant branch must be sought before any conclusions could be drawn about the likely factors contributing to the HB morphology.

Sweigart and Gross (1976) constructed grids of theoretical horizontal branch evolutionary tracks incorporating semiconvection and variations in Y, Z, and core and total stellar mass. These complicated models highlighted the critical dependence of the HB development on these factors. Freeman and Norris in their 1981 review considered all of the factors which might be relevant, such as Y, Z, Z_{CNO}, core rotation and any mechanism that causes a range of mass-loss on the giant branch and concluded that there must be two types of parameter variation to explain the observed HB morphologies. These are;

star to star variations of a particular parameter within a cluster, required to explain the variation in HB extent between clusters of similar metallicity;

variations of a particular parameter between different clusters, required to explain the difference in HB position between clusters of similar metallicity.

In short there is still no firm preference for any single factor other than metallicity in determining HB extent and shape, but rather, it seems, strong evidence to support the idea that subtle variations of a number of parameters cause the observed differences. In the light of the great sensitivity of HB models to variations in age, Z_{CNO}, Y and mass loss it is hardly surprising that such differences exist. Despite these problems, developing an adequate HB model is still one of the pressing theoretical problems in globular cluster research, and such a model must clearly take into account the wealth of evidence afforded by the observations of varying HB morphologies.

A major obstacle to understanding the processes occurring within a star as it joins the horizontal branch is that the details of the very rapid changes within the star which accompany the helium flash are still not clear. The recent theoretical models by Deupree and Cole (1983) and Deupree (1986), which consider the hydrodynamics of the helium flash, give considerably different results from the

earlier work. It appears there may be considerable mass loss at this stage, and indeed examination of the theoretical models suggest that there must be appreciable mass loss at the helium flash stage in order to form the very blue horizontal branch stars which are seen in some clusters. Observational pointers to mass loss on or immediately after the RGB have been seen recently (Cannon, 1983), but still no adequate theory exists, and the mechanism and even the amount of material involved are still unknown.

Advanced Evolutionary Stages

The theory of post-horizontal branch evolution has been extensively reviewed by Iben and Renzini (1983). This stage of stellar evolution is characterised by the "double-shell" burning of hydrogen and helium around a carbon/oxygen core. The star migrates along the asymptotic giant branch (AGB), a track above the HB, becoming more luminous until it intersects with the locus of the RGB. Some of the more exotic, highly luminous, stars in advanced evolutionary stages which are seen in clusters, such as the CH stars in ω Centauri (Dickens, 1972b) and carbon stars are thought to be at this stage of stellar evolution.

1.3 Globular Cluster Distances

There are two main methods of distance estimation from cluster colour magnitude diagrams;

1. fitting the observed cluster main sequence to a "known" main sequence, whether it is a subdwarf sequence of known trigonometric parallax or a theoretical main sequence locus which has been transformed from the temperature-luminosity plane;

2. adopting some value for the luminosity of the RR Lyrae horizontal branch stars and then using these stars to fix the distance.

1.3.1 Main Sequence Fitting

Given a CM diagram which reaches to faint enough magnitudes, the cluster main sequence may be used to determine the cluster distance. The position of the

ZAMS is a function of the chemical composition (see for instance Sandage, 1986 and references therein). Thus, in order to make an accurate estimate of the distance to the cluster, it is necessary to obtain an estimate of the abundance of metals (and of helium) in the cluster.

As mentioned above there are two distinct approaches to fitting globular cluster main sequences; fitting to observed sequences of subdwarf stars and fitting directly to a theoretical main sequence. Whichever is used, there is a fundamental correction which must be applied to the data, that of the foreground reddening. Despite the physically differing origins of the colour shifts due to reddening and metallicity, it must be noted that the effects are extremely difficult to disentangle in practice and ultimately these factors may contribute significantly to the final error in the distance estimate.

Reddening

The interstellar material between the source and observer is composed of a mixture of hydrogen, helium and heavier elements. The heavy elements, forming about 2% of the interstellar medium, are mainly in the form of grains composed of a mixture of silicates and graphite, their characteristic sizes being in the range of 0.001–0.1 μm. The extinction of light by interstellar dust, at wavelength λ, is denoted by A_λ, and is measured by the number of magnitudes that the source brightness is diminished. There is a strong wavelength dependence of A_λ and because of this the colour of a source is changed by absorption in the the intervening dust, as shown in Figure 1.2. This change in colour is denoted, in the Johnson $(B-V)$ colour index, by $E(B-V)$, called the colour excess or, more simply, the "reddening". The ratio, $R = A_V/E(B-V)$, is called the reddening ratio, and is approximately equal to 3.1 (Savage and Mathis, 1979). In practice, because the chosen wavelength bands are not monochromatic, the actual value of R will depend upon the spectrum of the source and the assumed value of $E(B-V)$. In this thesis the relation used by Sandage and Tammann (1976), and Penny and Dickens (1986) has been adopted, namely $R = A_V/E(B-V) = 3.0$, independent of intrinsic colour. The error introduced by this assumption is likely to be small compared to the uncertainties in $E(B-V)$ and the main sequence photometry.

Webbink (1985), in his survey of globular cluster properties, gives a descrip-

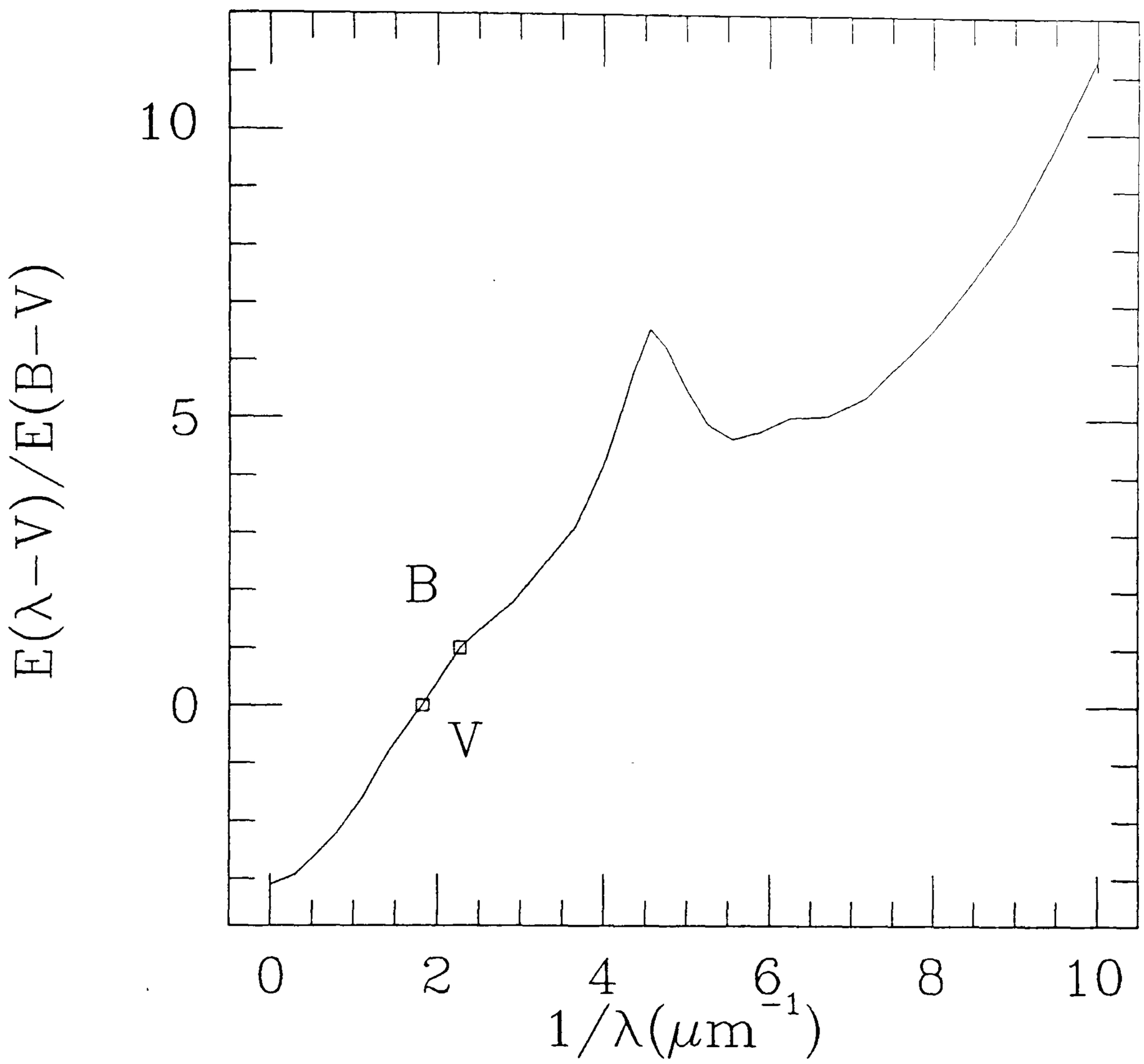

Figure 1.2: The average interstellar extinction curve. The centre of the Johnson V and B passbands are marked. From Savage and Mathis, 1979.

tion of the many techniques employed to make reddening estimates for clusters. Webbink ranks the techniques used for determining $E(B-V)$ in order of their precision. The four methods preferred by Webbink for their superior accuracy are:

1. Comparison of HB photometry with theory. The intrinsic colours of blue horizontal branch stars are nearly independent of metallicity (Mihalas, 1966), and thus the deviation of the photometric observations from the theoretical locus, whether two-colour or colour-magnitude, can be calibrated to give the reddening (see, for example, Sandage, 1969).

2. Photometry of RR Lyrae stars. Depends upon the knowledge of the intrinsic colours of RR Lyrae stars from theory (See, for example Sturch, 1978).

3. Comparison of observed and intrinsic flux distributions of individual giant stars.

4. Asymptotic reddening of foreground field stars.

The three former methods can yield an uncertainty of approximately $0\overset{m}{.}02$ in $E(B-V)$, but methods involving the run of reddening of foreground field stars are generally inferior. Other methods of estimating the reddening, such as the integrated photometric and spectroscopic properties of the cluster (see, for example, Zinn 1980), or applying a reddening correction dependent on Galactic latitude, such as the cosecant law of Sandage (1973), give much larger uncertainties and are thus generally not applicable for the purposes of main sequence fitting. Given an estimate of the foreground reddening, the observed colours and magnitudes can be corrected by subtraction of $E(B-V)$ and A_V respectively.

Distances by Subdwarf Matching

This method relies upon comparing the apparent magnitude of the cluster MS with the absolute magnitude of a standard main sequence composed of nearby metal-poor stars of accurately known parallax. Such stars have been christened "subdwarfs" because they are sub-luminous to the more metal-rich stars of younger stellar populations. The observed CM diagram must be de-reddened, as discussed above; the apparent distance modulus is given by the magnitude difference between the two sequences at constant colour. The true distance modu-

lus is then given by $(m - M)_0 = (m - M)_V - A_V$, where the visual extinction, $A_V = 3.0 \times E(B - V)$. The distance to the cluster, D is then given by $(m - M)_0 = 5 \log D - 5$, where D is in parsecs. Since the subdwarf stars are in the magnitude range $5 < M_V < 8$ it is obviously necessary to have a colour-magnitude diagram which reaches considerably fainter than the main sequence turnoff point, preferably by at least 3 magnitudes. The slope of the main sequence is quite steep, $dM_V/d(B - V) \approx 5$, and so an error of 0.05 in colour translates to an error of approximately 0.2 in $(m - M)_V$. Hence the photometry, its calibration to a standard photometric system, and the determination of the foreground reddening to the cluster must all be of the highest precision in order that this method can be applied. The major source of inaccuracy within this method arises from the poorly known parallaxes of the nearby subdwarf stars which are used to define the standard main sequence. Carney (1979) has published the most complete list of such stars, and Fahlman, Richer and VandenBerg (1985) have used a subset of seven of them, updating them with revised parallaxes and Lutz-Kelker (1973) corrections, a procedure also adopted by Penny and Dickens (1986).

Lutz and Kelker (1973) extended the work of Trumpler and Weaver (1953) who showed that a bias is inherent in the observed value of a stellar parallax, π_o, when stars are selected by applying a lower limit to parallax. If such a boundary is chosen then some stars with true parallaxes greater than this lower limit will be scattered out of the observed sample by observational error, whilst some of those with true parallaxes smaller than the limit will be scattered into the observed sample. However assuming that such stars are distributed uniformly in space there will be more stars scattered into the sample than out of it, simply because the number of stars per unit interval of parallax, $N(\pi)$ varies as $1/\pi^4$. More stars therefore have observed parallaxes, π_o, greater than their true value, π. Lutz and Kelker showed that the value of the lower parallax limit is inconsequential and that the systematic bias exists for all values of π_o and is dependent only upon the ratio σ/π_o, where σ is the standard deviation of π_o. Recently there has been some discussion in the literature on the suitability of these corrections, with some authors choosing to omit the corrections, or apply much smaller values (see for example, Richer & Fahlman, 1987). However, as yet, there have been no quantitative arguments published which suggest these corrections are inappropriate. Table 1.1 shows Lutz and Kelker's tabulation of the corrections to be applied to

Corrections to absolute magnitude	
σ/π_o	ΔM_V
0.000	0.0
0.025	−0.01
0.050	−0.02
0.075	−0.06
0.100	−0.11
0.125	−0.18
0.150	−0.28
0.175	−0.43

Table 1.1: Lutz-Kelker (1973) corrections to observed stellar parallaxes.

observed stellar absolute magnitudes for a range of values of the ratio σ/π_o.

It is also necessary to adjust the observed colours of the individual subdwarf stars for the metallicity difference between the subdwarf and the cluster for which a fit is being sought. This correction, which is non-linear, can be obtained from the main sequence stellar models available in the literature. Fahlman *et al.* (1985) adopt a correction of $\Delta(B-V)/\Delta[\mathrm{Fe/H}] = -0.065$ mag/dex from the main sequence models of VandenBerg and Bell (1985) in the metallicity regime of the cluster in question, M15. The subdwarf stars adopted in the present study are shown in Figure 1.3, corrected to a metallicity of [Fe/H] = −1.5 (subdwarf parallaxes are taken from the 4th Yale Parallax catalogue, to be published by Van Altena; J.E.Hesser, private communication). Omitted from Figure 1.3 is the star HD140283 which has subsequently been classified as a sub-giant star by Magain (1985), and therefore cannot be reliably used in comparison with metal-poor main sequence stars in clusters.

Fitting to Theoretical Sequences

The method involved is similar to fitting the observed MS to a subdwarf sequence as described above, but in this case a theoretical main sequence locus is substituted in the place of the subdwarfs. Such theoretical sequences have been constructed by Simoda and Iben (1968), Ciardullo and Demarque (1979), and VandenBerg (1983).

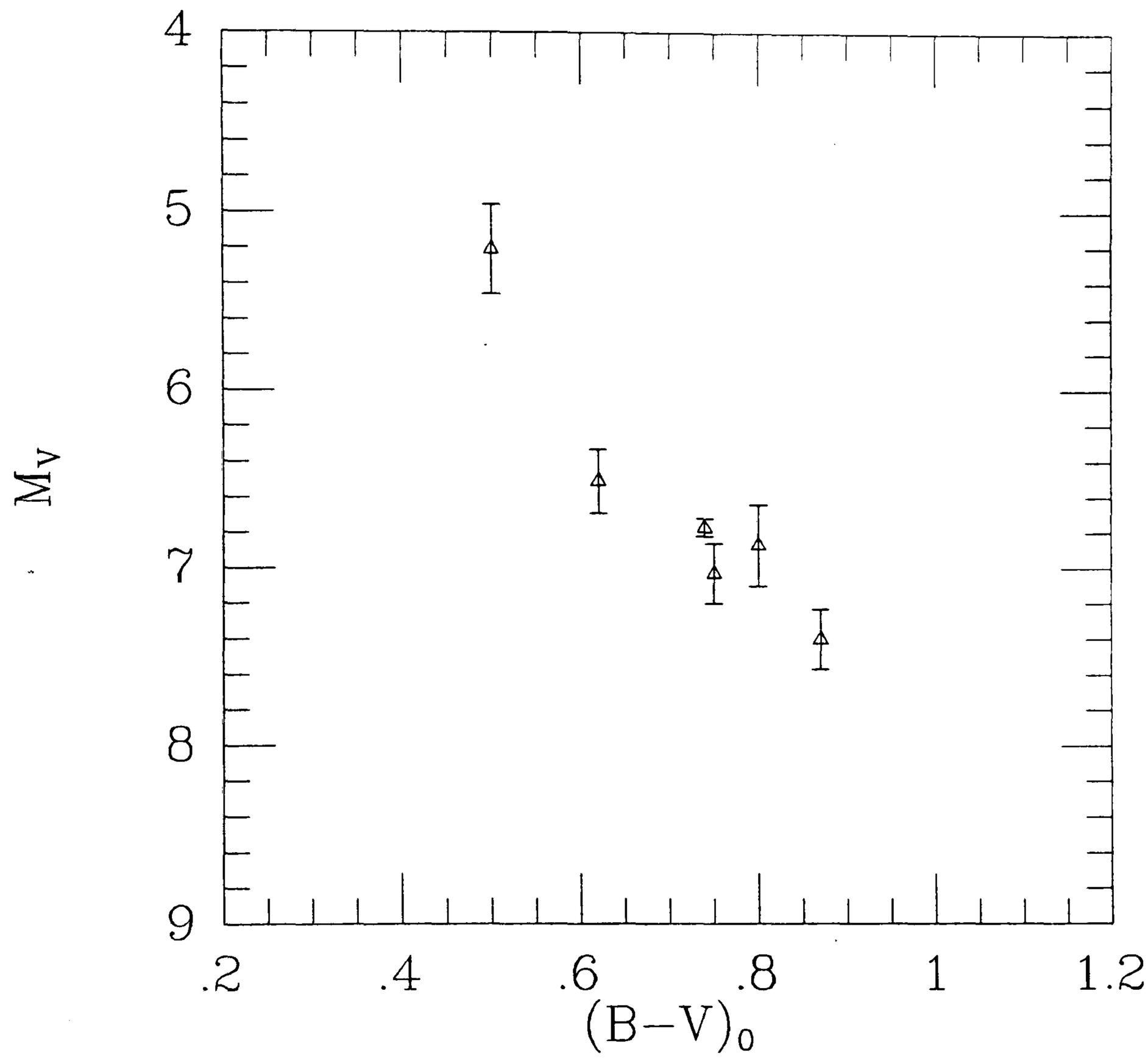

Figure 1.3: Carney's (1979) subdwarf sequence as used in this study. The observed subdwarf colours have been corrected to [Fe/H] = −1.5, and $E(B-V) = 0.11$.

The method relies upon the transformation of theoretical models from the M_{bol}, T_e plane to the observer's M_V, $(B-V)$ coordinate system by applying bolometric corrections and then applying the colour-temperature transform in reverse. The most recently published main sequence isochrones are those of VandenBerg and Bell (1985), who have applied the latest opacity calculations, bolometric corrections and colour-temperature relations. The normalisation of these models to stellar data is achieved by comparison with nearby well studied stars.

In common with the method of subdwarf distance-matching, an accurate estimate of the metallicity and helium mass-fraction of the cluster is required (in order to select an appropriate main sequence model), and once again the foreground reddening must be accurately established. These factors mean that this method is prone to exactly the same kind of observational uncertainties as subdwarf sequence fitting. This method has been favoured in the literature over the past few years because of its apparent convenience for the observer—the comparison of observation with theory is beguilingly simple. It must be noted however that there are still several sources of uncertainty which are not immediately obvious. The colour-temperature transformations are still the subject of some uncertainty, as are the opacities of the model atmospheres used. Fahlman *et al.* (1985) have been forced to apply seemingly arbitrary redward shifts to the VandenBerg and Bell (1985) isochrones in order to achieve a fit to their data of M15. Penny and Dickens (1986) found that the slope of their lower main sequence for NGC 6752 did not agree with the theory, although this may be due in part to slight uncertainties in the transformation they employed from the wide band filter system to the standard Johnson V and B system. Main sequence isochrones are discussed further in Section 1.4.

1.3.2 RR Lyrae Normalisation

The horizontal branch is a feature which is conveniently located for use as a fitting point to find the distance of a cluster. Obviously it is predominantly a horizontal feature in the M_V-$(B-V)$ plane, and unlike those methods dependent upon fitting in colour, is not beset by the disadvantage of requiring a very accurate determination of metallicity and reddening (horizontal branch luminosity is however weakly dependent upon metallicity–see below). The arguments for using the HB

as a distance indicator require knowledge of the intrinsic luminosity of stars on the horizontal branch, and it is this which has proved problematical in the application of this method.

It is the RR Lyrae variable stars, present in many of the Galactic globular cluster horizontal branches, which can provide information about the intrinsic magnitude of horizontal branch stars. The RR Lyrae stars within a particular cluster are known to vary in mean apparent magnitude by only about $\pm 0\overset{m}{.}15$ and so it has long been recognised that they are potentially very effective *"standard candles"* for determining distances to clusters. However one cannot be certain that the absolute magnitude of RR Lyrae stars is constant from one cluster to the next; it is known that the stellar elemental abundance varies between clusters, as may other fundamental properties of the RR Lyrae stars, such as mass or even age.

Whilst relevant theory can predict the effects of such differences, it is a subject of some controversy. Therefore it is necessary to examine carefully the available evidence in order to construct a reliable scheme for determining HB luminosities.

The methods of determining the absolute magnitude of RR Lyrae stars fall basically into four categories.

1. Calibration by cluster main sequence fitting.

2. Comparisons with pulsation theory and stellar modelling.

3. Statistical parallax.

4. Baade-Wesselink methods.

Calibration by Cluster Main Sequence Fitting

In this process, the methods of Section 1.3.1, notably fitting of observed cluster main sequences to an empirically derived, metal-poor main sequence, are used to determine the distance to a cluster, and thus to determine the absolute magnitude of its member RR Lyrae stars. If this is carried out for several clusters with accurate main sequence photometry, an empirical calibration of HB magnitude, and its dependence on metallicity, can be constructed. Sandage (1970) used the ultraviolet excess at $(B - V) = 0.6$, $\delta_{0.6}$, a measure of line-blanketing which correlates with metallicity, of observed metal-poor subdwarfs to calibrate a

Cluster	$[Fe/H]_{CARNEY}$	$M_V^{SANDAGE}$	M_V^{CARNEY}
47TUC	−0.5		0.53
M5	−1.1		0.68
M13	−1.5		0.69
NGC6752	−1.5		0.56
M3	−1.6	0.60	0.80
M15	−2.0	0.98	0.99
M92	−2.1	0.91	1.07

Table 1.2: RR Lyrae absolute magnitudes from main sequence fitting. Data are from Sandage (1970) and Carney (1980).

series of main sequences for differing metallicities. Carney (1980) employed main sequence fitting to theoretical main sequences, which were ultimately calibrated by subdwarf observations, to obtain ages and distances of seven Galactic globular clusters. The results of Sandage (1970) and Carney (1980) are shown in Table 1.2. These results imply that variables in metal-poor clusters are fainter than those in metal-rich clusters, at variance with the results from pulsation theory (as shown below). There is also a large uncertainty associated with these results, perhaps not surprising considering that the data employed in the studies, although of the highest precision available at the time, delineated only a small extent of main sequence and had a large scatter about the main sequence ridge line. In addition, the possibility of systematic errors appearing in the photometry near its faint limit mean that it is unwarranted to place great emphasis upon the trend of RR Lyrae magnitude with metallicity shown in these results.

Although it is feasible to apply this method to any cluster with a significant number of RR Lyrae stars there are in fact few published determinations of RR Lyrae absolute magnitudes by this method because of the previous paucity of accurate main sequence photometry. Recently a number of extremely accurate, faint CCD colour-magnitude diagrams of Galactic globular clusters have been published, and these are discussed in Section 1.5 below.

Comparisons with Pulsation Theory and Stellar Modelling

Much important information on the HB luminosity has come from the application of pulsation theory and stellar evolutionary models to the observed behaviour of cluster RR Lyrae stars. Some models, such as those of Christy (1966), predict a correlation of HB luminosity with metallicity, however other workers adopt a constant value for the absolute magnitude of RR lyrae stars (for example, Harris (1976) adopted a fundamental value of $M_V(RR) = 0\overset{m}{.}6$). With knowledge of the intrinsic relationship between cluster metallicity and horizontal branch luminosity, important constraints can be placed on the current stellar models; modern imaging photometric detectors, such as the CCD, allow the observer to determine, indirectly, the luminosities of RR Lyrae stars within clusters to a level of precision not previously attainable.

Oosterhoff (1939,1944) noted that the mean observed periods of RR Lyrae stars of types a and b exhibit grouping around two distinct values, 0.55 or 0.66 days. Arp (1955) discovered that the two groupings, christened Oosterhoff I and II, are correlated with the metallicity of the parent cluster in the sense that clusters of Oosterhoff group I (shorter period) are of higher metal abundance. The observed properties of RR Lyrae stars in globular clusters have formed the subject of a recent series of papers by Sandage and co-workers (Sandage, Katem & Sandage, 1981, Sandage, 1981, and Sandage, 1982. Henceforth SI, SII, and SIII respectively). Sandage has studied the Oosterhoff period dichotomy in detail and, in SI, presented a study of the phenomenon as displayed by the two RR Lyrae-rich clusters M15 and M3. Sandage found that there is a shift in average period of $\Delta \log P = 0.055$ between the two clusters, in the sense that the average period is longer in M15, the more metal-poor cluster. The interpretation of RR Lyrae properties can be pursued using the period-mean density relation for RR Lyrae pulsation,

$$P\langle\rho\rangle^{1/2} = Q, \tag{1.1}$$

where P is the pulsation period, $\langle\rho\rangle$ the mean density and Q the pulsation constant. Substituting

$$\rho \propto \frac{\mathcal{M}}{R^3}$$

and

$$R \propto \left(\frac{L}{T_e^4}\right)^{1/2}$$

gives

$$\log P = \log Q + 0.75 \log L - 0.5 \log \mathcal{M} - 3 \log T_e, \tag{1.2}$$

or from the more precise models of van Albada & Baker (1971), for fundamental (ab type) pulsators,

$$\log P = 11.497 - 0.681 \log \mathcal{M} + 0.841 \log L - 3.48 \log T_e, \tag{1.3}$$

where $\mathcal{M}$ and L are the stellar mass and luminosity, expressed in solar units. Hence, at constant T_e,

$$\Delta \log P = 0.84 \Delta A, \tag{1.4}$$

where

$$\Delta A = \Delta \log \frac{L}{L_\odot} - 0.81 \Delta \log \frac{\mathcal{M}}{\mathcal{M}_\odot}, \tag{1.5}$$

and A is therefore essentially a mass–luminosity ratio, and must change to accommodate the observed change in period. Here there is a major discrepancy with current horizontal branch models, which fail to predict this variation in the quantity A.

Considering only a change in luminosity in Equation 1.4 leads to

$$\Delta \log P = 0.84 \Delta \log L,$$

or, in the case of Sandage's comparison of M15 and M3, would lead to the result that the RR Lyrae stars in M15 are brighter by an amount $\Delta M_{bol} = 0\overset{m}{.}16$ than those in M3. The models of Sweigart and Gross (1976) show that the dependence of the mass of HB stars upon their metallicity at $\log T_e = 3.85$ (the centre of the instability strip) is

$$\left.\frac{\partial \log \mathcal{M}}{\partial \log Z}\right|_{\log T_e = 3.85} \approx -0.066, \tag{1.6}$$

for $0.2 \leq Y \leq 0.3$ and $-2.3 \leq [\mathrm{Fe/H}] \leq -0.5$. Sandage asserts that this relation implies that RR Lyrae variables of the same T_e should have shorter periods in the more metal-poor clusters, if the stars are at the same luminosity. However the observations presented by Sandage show the opposite to be true. Thus if the relatively metal-poorer variables are of higher mass then (from Equations 1.5 and 1.6) an even greater $\Delta \log L_{HB}$ is required to explain the period shift.

Combining Equations 1.3 and 1.6 gives,

$$\Delta \log P = 0.045 \Delta \log Z + 0.84 \Delta \log L_{HB}. \tag{1.7}$$

Again considering the SI comparison of M15 and M3, where $\Delta \log Z = -0.46$ and $\Delta \log P = 0.055$, Equation 1.7 would give

$$\Delta \log L(M15 - M3) = 0.090,$$

which in a similar fashion as before can be written as,

$$\Delta M_{bol} \approx 4 \Delta \log P.$$

In SII Sandage studied six clusters with many RR lyrae stars and concluded that the data agreed with the relation suggested by SI, that there was a correlation of Oosterhoff period-shift and absolute magnitude of RR Lyrae stars given by the equation

$$\Delta M_{bol} \approx 3 \Delta \log P.$$

In the third paper of the series, SIII, Sandage examined the observed correlation of RR Lyrae period-shift and metallicity, which he determined as

$$\Delta \log P = 0.116[\mathrm{Fe/H}] + 0.173, \tag{1.8}$$

and he studied possible mechanisms for producing this correlation. From the evolutionary models of Sweigart and Gross (1976), and Iben and Rood (1970) Sandage determined that,

$$\Delta M_{bol}^{RR} = -4.20 \Delta Y - 0.126 \Delta \log t + 0.06 \Delta[\mathrm{Fe/H}]. \tag{1.9}$$

Adopting Equation 1.8 and the requirement that $\Delta M_{bol}^{RR} = 3 \Delta \log P$ gives

$$\Delta M_{bol}^{RR} = 0.348 \Delta[\mathrm{Fe/H}]. \tag{1.10}$$

Substituting this into Equation 1.9 and considering all clusters to be coeval leads to the following anticorrelation of helium abundance and metallicity,

$$\Delta Y = -0.069 \Delta[\mathrm{Fe/H}].$$

This is the necessary conclusion within the framework of the canonical horizontal branch models to explain the differing mass to light ratios of RR lyrae stars

within globular clusters, as inferred by the observed metallicity-dependent period-shift between clusters and the assumption that $\Delta M_{bol}^{RR} = 3\Delta \log P$. The discovery by Butler *et al.* (1978) that RR Lyrae stars in ω Centauri show a much weaker correlation between M_V^{RR} and [Fe/H] for a wide range in [Fe/H] is explained, within this scenario, by assuming Y is the same for all the ω Cen variables.

The relation $\Delta M_{bol}^{RR} = 3\Delta \log P$ was used in SIII to fix the relative HB luminosities for eight globular clusters with accurate faint CM diagrams in order to compare the properties of their main sequences and turnoff regions. The absolute values were obtained by adopting $M_V(RR) = +0.8$ for the variables in M3. This value is a mean of the values given by fitting the main sequence photometric data available at the time to empirically derived main sequences composed of both blanketing corrected metal-rich field stars and metal-poor subdwarfs, of known parallaxes, and by the Baade-Wesselink procedure applied to several field RR Lyrae stars.

In a recent review of the properties of field RR Lyrae stars Lub (1987) shows the correlation of period with temperature for field RR Lyrae stars obtained by measurements in the Walraven photometric system (see Lub, 1977 and references therein) and the dependence of this relationship upon metallicity, which leads to the relation,

$$\log\left(\frac{\mathcal{M}^{0.81}}{L}\right) = -1.74 + 0.10[\mathrm{Fe/H}].$$

This is essentially the relation shown by Sandage (1982) for the stars in globular clusters. Combining this relation with the van Albada (1971) pulsation condition, Equation 1.3 gives,

$$M_V = 0\overset{m}{.}37 - 2.03 \log \mathcal{M} + 0.20[\mathrm{Fe/H}]. \tag{1.11}$$

Substituting the most likely ZAHB mass from the canonical HB models of Sweigart and Gross (1976), $\mathcal{M} = 0.63\mathcal{M}_\odot$ gives,

$$M_V = 0\overset{m}{.}78 + 0.20[\mathrm{Fe/H}]. \tag{1.12}$$

Lub (1987) also points out that the masses derived from the double-mode pulsation of RR Lyrae stars (Cox *et al.* 1983) lead to values of masses of $\mathcal{M} = 0.55\mathcal{M}_\odot$ and $\mathcal{M} = 0.65\mathcal{M}_\odot$ for the Oosterhoff group I and II clusters, leading to $M_V = 0\overset{m}{.}65$ and $M_V = 0\overset{m}{.}37$ respectively.

The so-called "Sandage effect" (Equation 1.8) has been examined rigorously in the literature and a number of authors have studied the counter-intuitive and disturbing conclusion that is implicit in the results derived from the observed period-shift versus luminosity relation, namely that the helium abundance of a cluster is anticorrelated with its metallicity. An independent determination of cluster helium abundances by Buzzoni *et al.* (1983) has shown that there is no evidence to support such a spread in cluster helium abundances; indeed their data are consistent with a constant Y for all metallicities (see also Section 1.4).

One principal argument which can be levelled at the evolutionary models used in the above discussion is the implicit assumption that the stellar composition is scaled in the solar ratios. It is perhaps generous to say that this is a somewhat questionable assumption, especially considering that we are comparing stars which were born in the primordial Galaxy with those which are the product of some 10 Gyr of Galactic evolution. In practice it has been an assumption that workers in the field have until recently been forced to adopt because of the difficulty in reliably estimating the abundance of elements, particularly the vitally important light elements. However, in recent years, advances in high resolution spectroscopy and the use of synthetic spectra from model atmosphere calculations have allowed workers to study the abundances of individual elements in cluster stars.

Sneden *et al.* (1979) studied 12 unevolved field stars and found that there was a substantial enhancement of oxygen in metal-poor stars. Clegg *et al.* (1981) examined a sample of 11 metal-poor field subdwarfs and discovered that the ratio of oxygen to iron abundance was anticorrelated such that $[O/Fe] = -0.48(\pm 0.07)[Fe/H]$, in the range $0.0 \geq [Fe/H] \geq -1.0$, tending to flatten out for lower metallicities, with $[O/Fe] \approx 0.6$ at $[Fe/H] = -1.0$.

In a review of cluster compositional trends Pilachowski *et al.* (1983) showed that there is a similar oxygen enhancement in globular cluster stars to that found in field subdwarfs by Clegg *et al.* but to a lesser extent, with the metal-poorest clusters having $[O/Fe] \approx 0.3$. If this difference in oxygen enhancement is real, and was found to apply to globular cluster main sequence stars, it would mean that metal-poor field subdwarf stars are representative of a different stellar population to the main sequence stars in globular clusters. This would of course have important consequences on the use of metal-poor field stars for calibrating the main sequences of globular clusters. Indeed this is suggested by Leep *et al.*

(1986) whose observations of stars in M13 show that oxygen is enhanced in this cluster to [O/Fe] = 0.3. However Leep and Wallerstein (1981) showed that the oxygen enhancement in a sample of 11 field giant stars is only of the order of +0.3 dex, and furthermore they assumed solar carbon to iron ratios when deriving this value. Kraft *et al.* (1982) have determined that [C/Fe] ranges from −0.3 to −1.0 for three of these stars, and correcting the oxygen abundances for this gives a value of [O/Fe] nearer to 0.2, essentially in agreement with that seen in globular clusters by Pilachowski *et al.* (1983) and not in in accord with the suggestion that the low metallicity field stars are representative of a different stellar population to those in globular clusters.

Pilachowski *et al.* (1983) examined the discrepancy between oxygen abundances derived from measurements of giants and those from field subdwarfs. They recognised that it is possible, but unlikely, that this arises from mixing of ON processed material into the surface layers of the evolved (giant) stars. They observed that the most plausible explanation is some systematic error between the analysis of dwarf stars (based upon the 7773 Å oxygen triplet) and that of giant stars (based upon the ground state [OI] line). Although this is obviously an area where some clarification is required, presumably by further high-resolution spectroscopic analysis of globular cluster stars, it is certain that oxygen is present in some globular clusters with abundances substantially above that of the sun.

Rood (1983) briefly discussed the variation of [CNO/H] as a possible explanation of the Sandage effect. However, the synthetic horizontal branches he constructed in this preliminary investigation failed to reproduce the required shift in period. Caputo *et al.* (1983) examined a number of alternative evolutionary scenarios, based upon variations in the [CNO/H] ratio and He-core mass from the canonical values. Citing the double-mode pulsator results of Cox *et al.* (1983), which gave the masses of M15 RR Lyraes as $0\overset{m}{.}65 \pm 0\overset{m}{.}05 M_{\odot}$, Caputo *et al.* infer from their non-canonical models that there is an enhancement of [CNO/H], at least in this one cluster, which provides an explanation of the "Sandage effect".

Sweigart *et al.* (1987) confirmed the finding that an anticorrelation of helium abundance with metallicity, given by

$$\Delta Y = -0.094 \Delta[\mathrm{Fe/H}],$$

is required to explain the period-shift phenomenon within the framework of ex-

isting evolutionary models. They also considered many other factors which may affect the pulsation period of ZAHB stars, finding it unlikely that the period-shift phenomenon could be explained by current inaccuracies in the input physics of the red giant branch, and that a correlation of He-core mass with metallicity some 8 times greater than predicted would be required to explain the observed period–metallicity relation. Renzini (1983) has suggested that, in conventional models, the opacity may be systematically underestimated in the temperature range 0.5×10^6 to 5×10^6 K. It is in this temperature regime that opacity is most sensitive to variations in metal abundance, and is also most difficult to calculate. Prompted by these facts Sweigart *et al.* (1987) produced a set of models with artificially enhanced opacities and found that an increase in opacity by a factor of five over the currently accepted value could produce the required period–metallicity correlation, however they also note that such a large discrepancy is very difficult to understand and for this reason inaccuracies in the opacity tables used to produce current stellar models must be discounted as the sole explanation of their inability to reproduce the observed period shift. They also examined a number of other deviations from the commonly accepted models. Enhancements of oxygen of the scale described above were incorporated into the models, but when all the consequences of such a change in composition were examined they found it too was unable to explain the observed period shift. Similarly the effects of evolution away from the ZAHB positions and of stellar rotation were discounted, effectively leaving no single plausible explanation of the observed period-shift–metallicity relation.

Statistical Parallax

By applying a kinematic model representing the motions of a sample of local stars, such as field RR Lyrae variables, it is possible to estimate the mean absolute magnitude of the sample from their observed proper motions, radial velocities and apparent magnitudes. An early implementation of this technique is that of van Herk (1965), who obtained a mean magnitude of $M_V = 0\overset{m}{.}77$. Recently Strugnell *et al.* (1986) have applied more sophisticated maximum-likelihood analysis to the problem, and have obtained $M_V = 0\overset{m}{.}75 \pm 0.2$. Lub (1987) has indicated a zeropoint error of $0\overset{m}{.}09$ in much of the photometry used to furnish this result, leading to a

revised estimate of $M_V = 0^m.68 \pm 0.10$. The relatively small samples used in these studies and the range of metallicities involved preclude their use in determining decisively if any dependence of RR Lyrae magnitude with metallicity exists.

Baade-Wesselink Methods

Photometric light curves of a pulsating star at two or more wavelengths give both the intensity and colour variation of the star during a cycle. If a relation between colour and surface brightness (or temperature) can be derived, the fractional change in radius, $\Delta R/R$ can be obtained. Combining this information with the radial velocity curve for the star allows the absolute value of the radius to be determined, leading to the absolute magnitude of the star. The technique has been used predominantly upon field RR Lyrae stars, and a review of the absolute magnitude values obtained by different authors has been given by Jameson (1986). The absolute magnitudes of RR Lyrae stars derived via the Baade-Wesselink method infer that metal-poor RR Lyraes are brighter than metal-rich ones and the results are in broad agreement with those derived from other methods (Jameson, 1986). The Baade-Wesselink method has been reviewed in some detail by Gautschy (1986), who is critical of the many assumptions required to obtain an estimate of the star's luminosity and concludes *"THE Baade-Wesselink method does not yet exist. Much more work is required. There are at present only realisations of different degree of accuracy in describing the processes involved"*. Similar opinions have been voiced by Cohen & Gordon (1987) in their concluding remarks upon their Baade-Wesselink studies of RR Lyrae in M5. It appears that although this method has great potential for determining RR Lyrae absolute magnitudes, and hence cluster distances, it is not, as yet, a reliable and practical solution to the problem of ascertaining RR Lyrae luminosities.

1.4 The Ages Of Globular Clusters

Cluster age is a particularly interesting parameter, especially with respect to estimates of the "Hubble time", τ_H. The quantity τ_H is defined as the reciprocal of H_0, the Hubble constant, and can be interpreted as an upper limit to the age of the Universe. The currently accepted theories of the formation of the Galaxy, as reviewed by Mould (1982), propose that the globular clusters were formed over

a relatively short time span during the initial rapid collapse of the protogalaxy from a larger volume. Current estimates of H_0 are in the approximate range 50Kms^{-1}Mpc^{-1} (Sandage and Tammann, 1976) to 100Kms^{-1}Mpc^{-1} (Aaronson *et al.* 1980). A recent review of the subject by Rowan-Robinson (1985) outlines the methods used by the various protagonists in this discussion, which continues to be one of the most important and lively debates in astronomy today. Hodge (1981) states that it is neither possible to make an impartial choice of a "best value" for H_0 within this range, nor to ascribe a meaningful uncertainty. Clearly it is somewhat embarrassing for theorists of stellar evolution if their estimates of cluster ages are in excess of "the age of the Universe", and the currently accepted ages of the Galactic globular clusters—of the order of 15 Gyr—are inconsistent with some derived values of the Hubble time. Whilst due attention must be paid to the evidence afforded by these studies, the obviously large uncertainty in the true value of H_0 and hence the Hubble time suggest that these higher values of H_0 do not present insurmountable evidence against the ages determined by evolutionary theory. Of course, those workers in the field of cluster research have inverted the problem, and used the derived cluster ages to infer new estimates of the Hubble time, and hence the age of the Universe.

The methods used to determine globular cluster ages are all based upon the location of the main sequence turnoff. It is important to obtain accurately the position in the CM diagram of the main sequence turnoff, and so the vast improvement in sensitivity and precision afforded by the imaging CCD has allowed improvements to be made in this area. The majority of methods involve fitting the observed cluster loci at turnoff to model isochrones representing stars of the required chemical composition. Demarque (1980) has estimated the age of eight clusters, determining their distances by assuming a constant (*i.e.* metallicity independent) RR Lyrae absolute magnitude of ($M_V^{RR} = +0\overset{m}{.}6$), and then fitting the Yale set of isochrones (Ciardullo and Demarque, 1979) to the observations. This yielded a metallicity dependent age distribution, with an average age of some 13 Gyr, and with the clusters poorest in metals appearing some 5 Gyr older than the richest. Carney (1980) used the turnoff temperature, derived from the Yale isochrones, to estimate cluster age. This method too gave an average age of 13 Gyr, but with a much larger metallicity dependent age spread, again in the same sense as the results of Demarque (1980), but ranging from 6 to 19 Gyr. Subsequently

Carney (1981) has used the distances obtained by subdwarf fits to cluster main sequences to deduce the cluster age from turnoff luminosity, and finds that this method gives an average age of some 17 Gyr, with no dependence upon metallicity. Vandenberg (1983) uses his model isochrones to estimate the ages of 12 globular clusters with published main sequence colour-magnitude diagrams, and determines that the clusters studied are approximately coeval, with ages of 16 ± 2 Gyr, and there is no apparent correlation with metallicity. The most recently published comprehensive set of isochrones are those of VandenBerg and Bell (1985), which incorporate many revisions from the earlier VandenBerg work. Again these show the age of the cluster system to be 16 ± 3 Gyr.

The helium mass-fraction of population II stars has long been a subject of some debate, being impossible to measure directly and difficult to model in theory. This limitation has lead many stellar model-builders to consider a range of helium abundances, the usual convention being to model compositions with $Y = 0.2$ and $Y = 0.3$, these being considered as sensible minimum and maximum likely values, and consistent with the estimate of $Y = 0.23$ given by Big-Bang cosmology (Wagoner, 1973). This situation was not really satisfactory because of the relatively strong dependence of ZAMS position on Y, and several studies have have been undertaken to resolve the problem. Buzzoni *et al.* (1983) have employed the "R-method", first suggested by Iben (1968), which relies upon the comparison of the ratio of theoretical stellar lifetimes on the horizontal and red-giant branches to the observed ratio of HB to RGB stars. This ratio, christened R is strongly dependent upon Y, and Buzzoni *et al.* find a value of $Y = 0.23 \pm 0.02$. Kunth & Sargent (1983) have used an accurate spectrophotometric method to determine the primordial helium abundance, which they give as 0.245 ± 0.003, a value in agreement with that favoured by Yang *et al.* (1984).

Penny and Dickens (1986) have shown that with well planned observations and careful analysis it is now possible to use the observed shape of the cluster main sequence, turnoff, and sub-giant branch regions to simultaneously determine the metallicity and age of a cluster. This was anticipated by Flannery and Johnson (1982) who used an elaborate statistical method of isochrone fitting in an attempt to obtain simultaneously the age, distance, metallicity and helium abundance. In practice they found it impossible to adequately determine all four parameters simultaneously and thus assumed values of Y and [Fe/H], and fitted for distance

modulus and age, these two parameters being the major influences on the main sequence and turnoff positions respectively. The results they obtained seemed to show a large spread in age for the cluster system, but the authors themselves were quick to point out that there existed uncertainties in their results far larger than the formal fitting errors which were quoted. It must be said, however, that the colour-magnitude data and the interpolated Yale isochrones which formed the basis of these studies are rudimentary compared to those available now. The fitting of isochrones to CM data in the literature has always been, at best, subjective, and such techniques as those employed by Flannery and Allen should be re-examined in the light of better observation and theory.

As noted above, recent evidence has pointed towards non-solar CNO ratios in globular cluster stars. The evidence for this has been examined by Rood and Crocker (1985), and VandenBerg (1985) who have constructed isochrones which simulate the the effects of enhanced CNO ratios. These authors find the most significant effect of these modifications is on the relation between isochrone turnoff luminosity and age. Increasing [O/Fe] to 0.5 results in a reduced age by some 15% at the same turnoff luminosity when compared with isochrones of scaled solar abundances.

Iben and Renzini (1984) point out that fitting to isochrones, and methods involving simply the turnoff luminosity, are prone to several disadvantages. Such techniques are biased by the convection theory used in the models—there is no physical reason to prefer any particular value of α, the ratio of pressure scale-height to convective mixing length, and its choice can drastically alter the shape of the derived isochrone. VandenBerg (1983) effectively used the turnoff shape of the oldest open clusters to fix a value of α. Fitting methods are susceptible to uncertainties in the cluster reddening, metallicity, helium abundance, the colour–temperature transformation employed, and the bolometric corrections applied. Add to this the uncertainties, possibly systematic, incurred by independently determining the distance modulus, from any of the methods outlined in Section 1.3, and it can be seen that unless great caution is exercised, the process can be quite precarious. These facts also explain the relatively high uncertainties which must be attached to ages determined in this way. The method which Iben and Renzini recommend is to use the theoretical relation between the luminosities of the horizontal branch and the main sequence turnoff. They use the ZAHB models

of Sweigart and Gross (1976), allied with an interpolation formula for turnoff luminosity derived from the Yale isochrones to provide the relation,

$$\log t_9 \approx -0.352 - 1.88(Y - 0.3) - 1.44(Y_{HB} - Y) - 0.088(3 + \log Z) + 0.41 \Delta M_{TO}^{RR}(bol.)$$

The advantages presented by this method are that it is not affected by the choice of mixing length parameter (L_{TO} is independent of α), it is not dependent on any assumed reddening or distance modulus, it is not as sensitive to the choice of bolometric correction or colour–temperature translation as isochrone fitting, and the derived age is not as sensitive to the cluster metallicity as in the previous method. However, in light of the unresolved problems associated with the Sandage period-shift effect, where the conventional models of the HB fail to produce the observed correlation of RR Lyrae period with metallicity, overwhelming faith cannot be placed in this method. Because of this uncertainty it should be noted that an error of $0^m.1$ in the HB level leads to an error of some 1.5 Gyr in the age of the cluster.

In order to circumvent some of the problems outlined above Fahlman *et al.* (1985), McClure *et al.* (1987a), and Hesser *et al.* (1987) have combined main sequence isochrones with self consistent ZAHB models to obtain fits to their CM data. The latter in particular represents the "state of the art" with respect to cluster age dating and the CMD and fitted isochrones from this study can be seen in Figure 1.4, showing just how accurately observations can now be modelled in theory.

1.5 Some Recent Results

The sheer quality of the latest generation of cluster CM diagrams compel one to reappraise the ages and distances within the cluster system implied by these data. In Figure 1.5 a recent photographic CMD of the cluster NGC 6752 is compared with a CCD colour magnitude study of the same cluster. The improvement in accuracy can be seen from the relative scatter about the principal sequences in each CMD, and it can be seen that, in the CCD diagram, the main sequence is delineated with great precision to some four magnitudes fainter than in the photographic study.

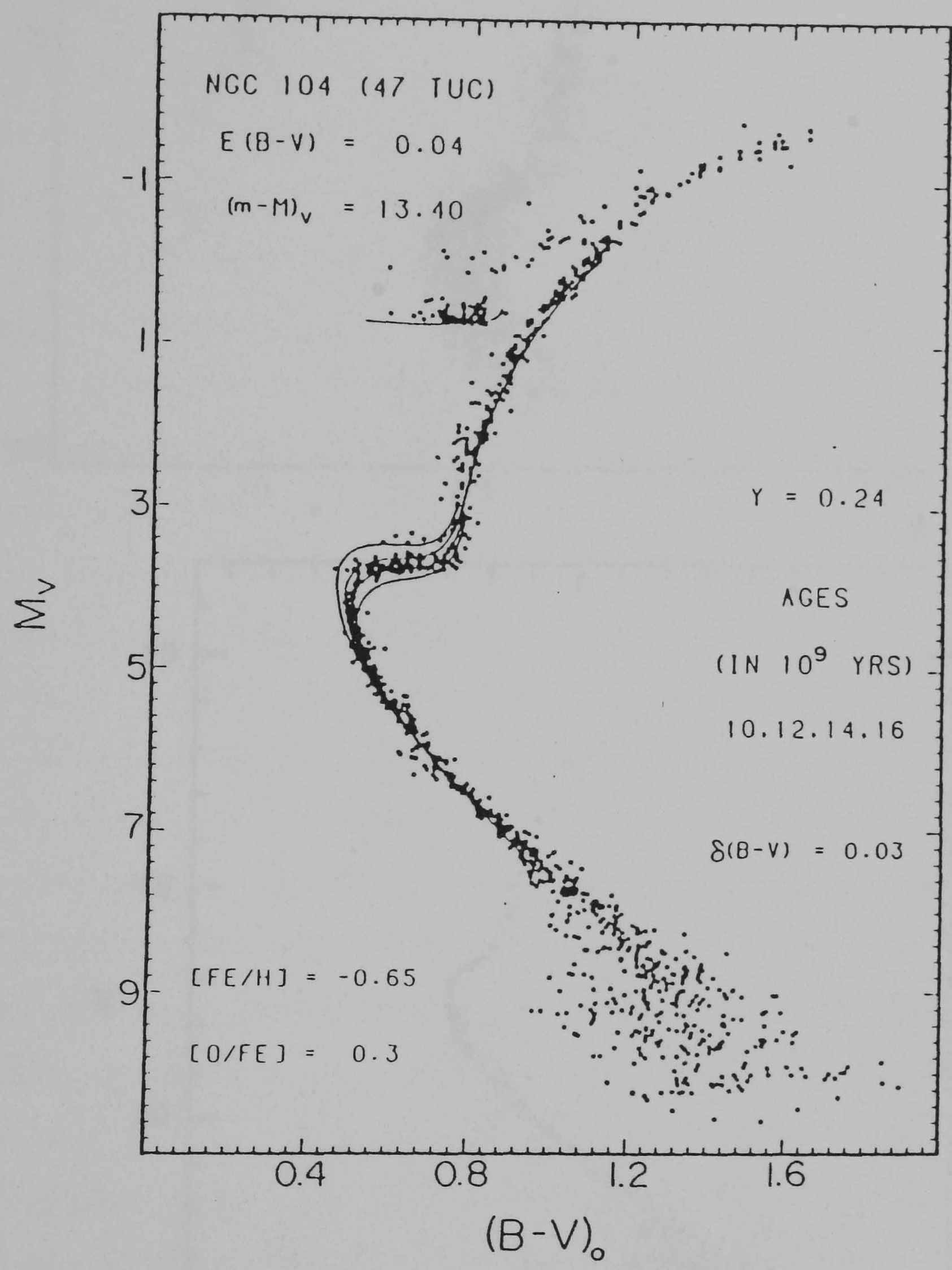

Figure 1.4: Main sequence isochrone and synthetic ZAHB fits to CM data of the cluster 47 Tuc. From Hesser *et al.* (1987).

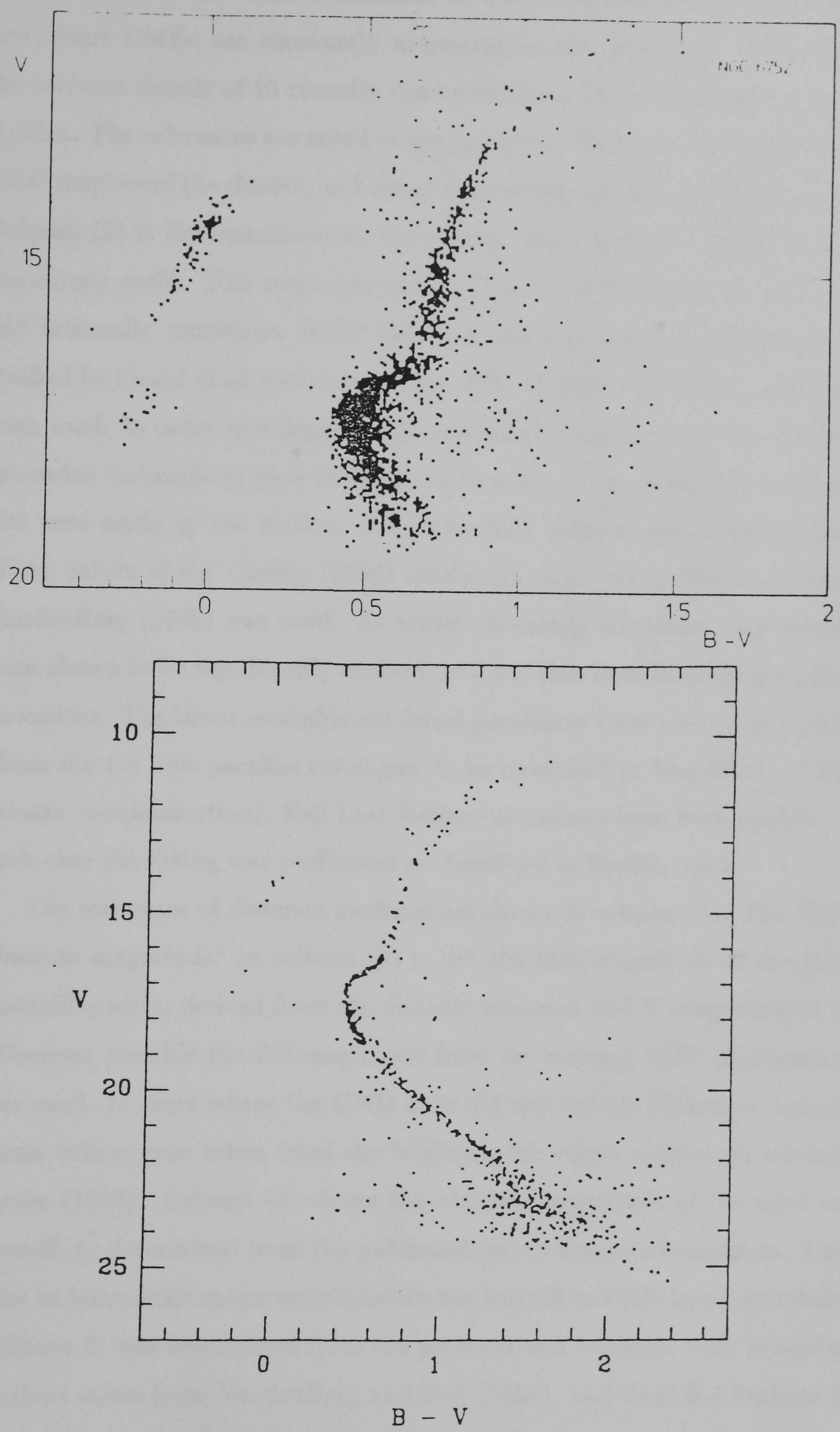

Figure 1.5: Comparison of photographic and CCD photometry of the cluster NGC 6752. Top: Photographic data from Cannon (1983). Bottom: The CCD study of Penny and Dickens (1986).

Never before has such a database of CMD information been available, and new, faint CMDs are constantly appearing in the literature. Table 1.5 shows the relevant details of 10 recently conducted faint CCD cluster colour-magnitude studies. The references are noted in the caption to Table 1.5. Column (1) gives the NGC number of the cluster, and where appropriate the Messier catalogue number. Column (2) is the metallicity of the cluster, taken from the Frogel *et al.* (1983) metallicity scale. This scale was chosen as it is considered to be well calibrated and internally consistent. NGC 7492 was not included in the sample of clusters studied by Frogel *et al.* and so the value of [Fe/H] from Buonanno *et al.* (1987) has been used. In order to independently determine consistent and theoretically well-grounded distances to each of these clusters, fits to the published main sequence loci were made by the Author. An empirically defined main sequence consisting of the subset of the Carney (1979) subdwarfs employed by Fahlman, Richer and VandenBerg (1985) was used. As noted previously HD140283 has subsequently been shown to be significantly evolved, and has thus been omitted from the fitting procedure. The latest available subdwarf parallaxes have been used in this study (from the 4th Yale parallax catalogue, to be published by Van Altena; J.E.Hesser, private communication). Full Lutz-Kelker corrections have been applied. In each such case the fitting was performed as described in Section 1.3.1.

The estimates of distance modulus are shown in column (3). The "RR Lyrae absolute magnitude" in column (4) is the absolute magnitude of the HB at the instability strip, derived from the distance modulus and V magnitude of the HB. Wherever possible the HB magnitude from the relevant CCD photometry paper was used. In cases where the CMD data did not include horizontal branch stars, mean values were taken from the bibliographic colour-magnitude survey of Peterson (1986). Column (5) shows the absolute magnitude of the main sequence turnoff, as determined from the published colour-magnitude diagram. The difference in bolometric magnitude between the turnoff and RR Lyrae instability strip (column 6) was determined from the previous two columns, with bolometric corrections taken from VandenBerg and Bell (1985), and from R.J.Dickens (private communication). Columns (7) and (8) contain, respectively, the cluster ages in Gyr as determined from interpolation in the isochrones of VandenBerg and Bell (1985) and as determined from the $\Delta M_{TO}^{RR}(bol)$ vs. age relation given in equation 9 of Iben and Renzini (1984). It should be noted that the relation due to

Cluster	[Fe/H]	$(m-M)_V$	M_V^{RR}	M_V^{TO}	$\Delta M_{TO}^{RR}(bol)$	t_{TO}	t_Δ
7078 (M15)[1]	-2.21	15.53	0.47	3.76	3.22	15.0	14.2
6341 (M92)[2]	-2.01	14.60	0.49	3.99	3.43	17.0	16.5
4590 (M68)[3]	-1.96	15.35	0.36	3.74	3.30	14.5	14.5
6397[4]	-1.84	12.70	0.39	3.99	3.60	16.5	18.5
6205 (M13)[5]	-1.47	14.50	0.38	3.99	3.51	15.5	16.0
362[6]	-1.39	14.92	0.60	3.97	3.34	14.5	13.4
6752[7]	-1.35	13.29	0.48	4.10	3.52	16.5	15.8
7492[8]	-1.34	17.15	0.57	4.18	3.51	17.5	15.6
6121 (M4)[9]	-0.72	12.90	0.51	3.99	3.40	11.0	12.4
104 (47 TUC)[10]	-0.59	13.51	0.69	4.15	3.46	13.0	12.90

Table 1.3: Colour-magnitude data from recently published CCD photometry

References to Table 1.5

1 Fahlman, Richer and VandenBerg, 1985
2 Heasley and Christian, 1986
3 McClure *et al.* 1987a
4 Anthony-Twarog, 1987
5 Richer and Fahlman, 1986
6 Bolte, 1987
7 Penny and Dickens, 1986
8 Buonanno *et al.* 1987
9 Richer and Fahlman, 1984
10 Hesser *et al.* 1987

Iben and Renzini is derived from interpolation in the Yale isochrones (Ciardullo & Demarque, 1979), and that these models are not entirely consistent with the recent, more sophisticated models of VandenBerg & Bell (1985). The results of both methods are included here to aid comparison with earlier work (for example, Demarque, 1980, Carney, 1980, and VandenBerg & Bell, 1985). It will be interesting and worthwhile to reassess these data when more extensive tabulations of the recent isochrones calculated by VandenBerg and co-workers (McClure *et al.* 1987a, Hesser *et al.* 1987), become available. These incorporate self-consistent main sequence, giant branch, and horizontal branch models, and employ non-solar abundance ratios (see above).

Figure 1.6 shows the derived HB magnitude–metallicity relation. An unweighted least-squares fit to the data in Figure 1.6 gives,

$$\Delta M_V^{RR} = 0.12(\pm 0.05)\Delta[\mathrm{Fe/H}].$$

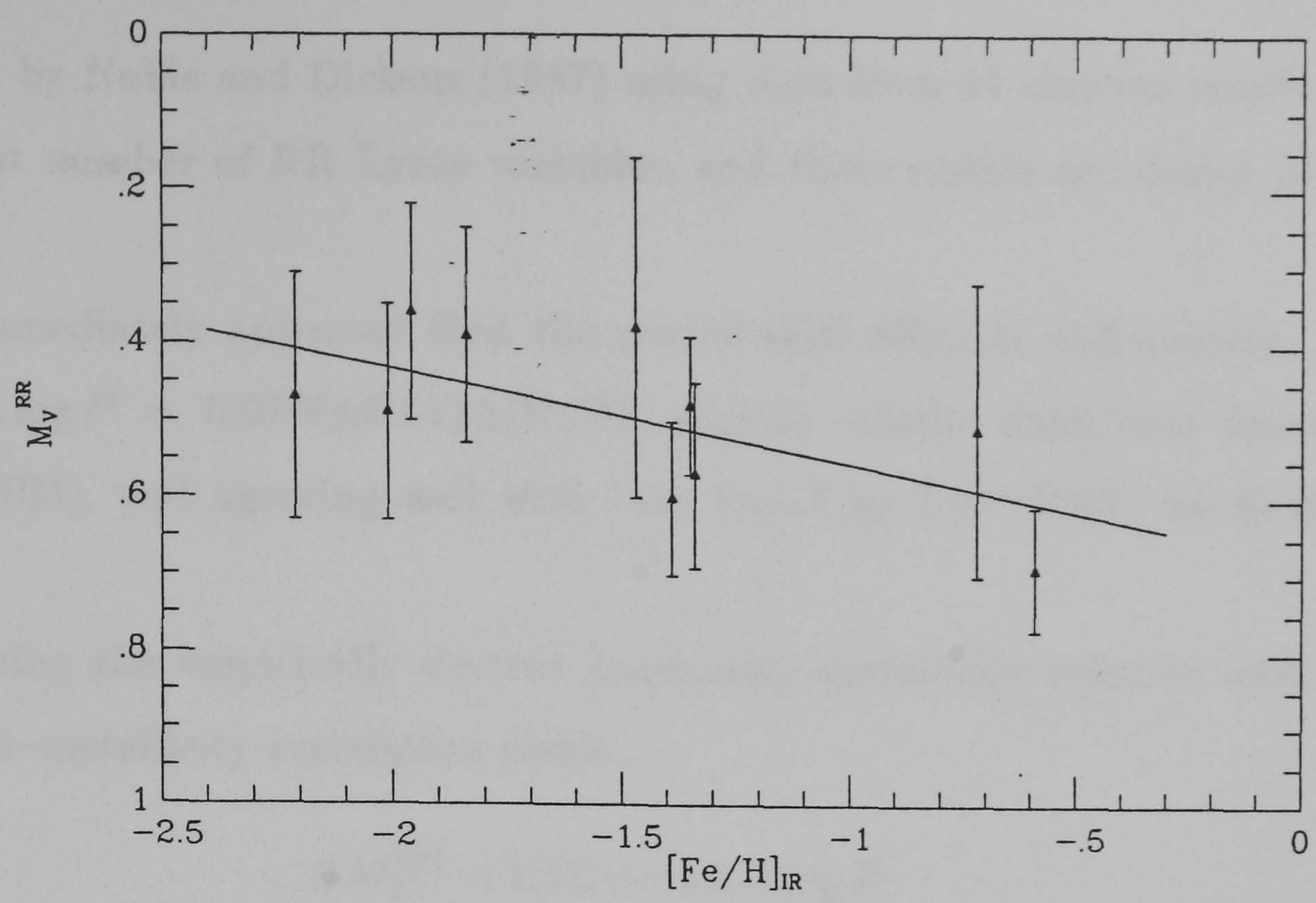

Figure 1.6: Horizontal branch absolute magnitude plotted against metallicity. Derived from Table 1.5. The line show an unweighted least-squares fit to the data, and gives the relation $\Delta M_V^{RR} = 0.12(\pm 0.05)\Delta[\mathrm{Fe/H}]$.

This is significantly smaller than the slope of ~ 0.35 predicted by Sandage (SIII) using the requirement that $\Delta M_{bol}^{RR} = 3\Delta \log P$. However, the derived slope is entirely consistent with the dependence of HB luminosity upon metallicity as predicted by canonical HB models (for example, see Equation 1.9 above). This does not offer an explanation of the period-shift effect, the orthodox HB models still do not explain why there should be a correlation of A in Equation 1.5 with metallicity amongst clusters, but negates the argument that any anticorrelation of Y with [Fe/H] is required to reproduce the M_{bol}^{RR} versus [Fe/H] relation.

An examination of the uncertainties in the fitting procedure and horizontal branch apparent magnitude leads to an estimate of the uncertainty (standard deviation) in each individual value of M_V^{RR} of approximately 0.15. Because of the relatively small number of subdwarf stars used to fix the cluster distances there may well be a systematic effect at this level too, shifting the whole data set slightly in magnitude. This may explain the fact that the derived RR Lyrae luminosities are somewhat brighter than the average of other determinations (see Section 1.3.1 above), but it must be stressed that the precision of the main sequence CMD data makes this the most internally consistent study of the absolute magnitudes of cluster RR Lyrae stars yet published.

An independent reappraisal of the period-shift–metallicity relation has been

UNIVERSITY LIBRARY LEEDS

carried out by Noble and Dickens (1987) using data from 11 clusters which have a significant number of RR Lyrae variables, and these results are shown in Figure 1.7.

It is immediately apparent that the period-shift effect is still present, with a slope, $\Delta \log P = 0.079(\pm 0.01)\Delta[\mathrm{Fe/H}]$, slightly smaller than that found by Sandage (SIII), and agreeing well with that found by Lub (1987) for field RR Lyraes.

Combining the empirically derived luminosity–metallicity relation with this period-shift–metallicity correlation yields,

$$\Delta M_V^{RR} = 1.52(\pm 0.44)\Delta \log P.$$

This is not compatible with the Sandage hypothesis that there is a change in absolute magnitude given by the relation $\Delta M_V^{RR} = 3\Delta \log P$. To further test the plausibility of these findings the data of SII were re-examined to see if the correlation of magnitude with period-shift found above was consistent with the results given by individual RR Lyrae stars in globular clusters. In Figure 1.8 the SII data for variables in M3 are shown. The least-squares fit to these data is shown, the relation is $\Delta m_{bol} = -1.41(\pm 0.25)\Delta \log P$, the minus sign is a result of the different sign convention adopted by Sandage in defining the period shift. This is absolutely in agreement with the result found above from main sequence fitting to field subdwarfs. The SII Omega Centauri data were plotted in a similar manner, and the best fit line to the data gave $\Delta m_{bol} = -2.07(\pm 0.24)\Delta \log P$, once again consistent with the results derived empirically above from the sample of 10 Galactic globular clusters. This result is shown in Figure 1.9. It should be noted that this is in any case an approximation as the values of Δm_{bol} above take no account of the fact that Δm_{bol} should be measured as the difference between the magnitude of an RR Lyrae star and the mean HB magnitude *at the same effective temperature*, whereas Δm_{bol} derived from the SII data above is effectively the difference in magnitude of an individual star from the mean of all the measured stars. This makes very little difference to the expected relationship in the case of M3, where the horizontal branch is almost level, but in the case of ω Cen the horizontal branch has a slight positive slope in the V, $(B-V)$ plane. The effect of this is to reduce slightly the slope of the Δm_{bol} versus $\Delta \log P$ relationship derived from the data of SII.

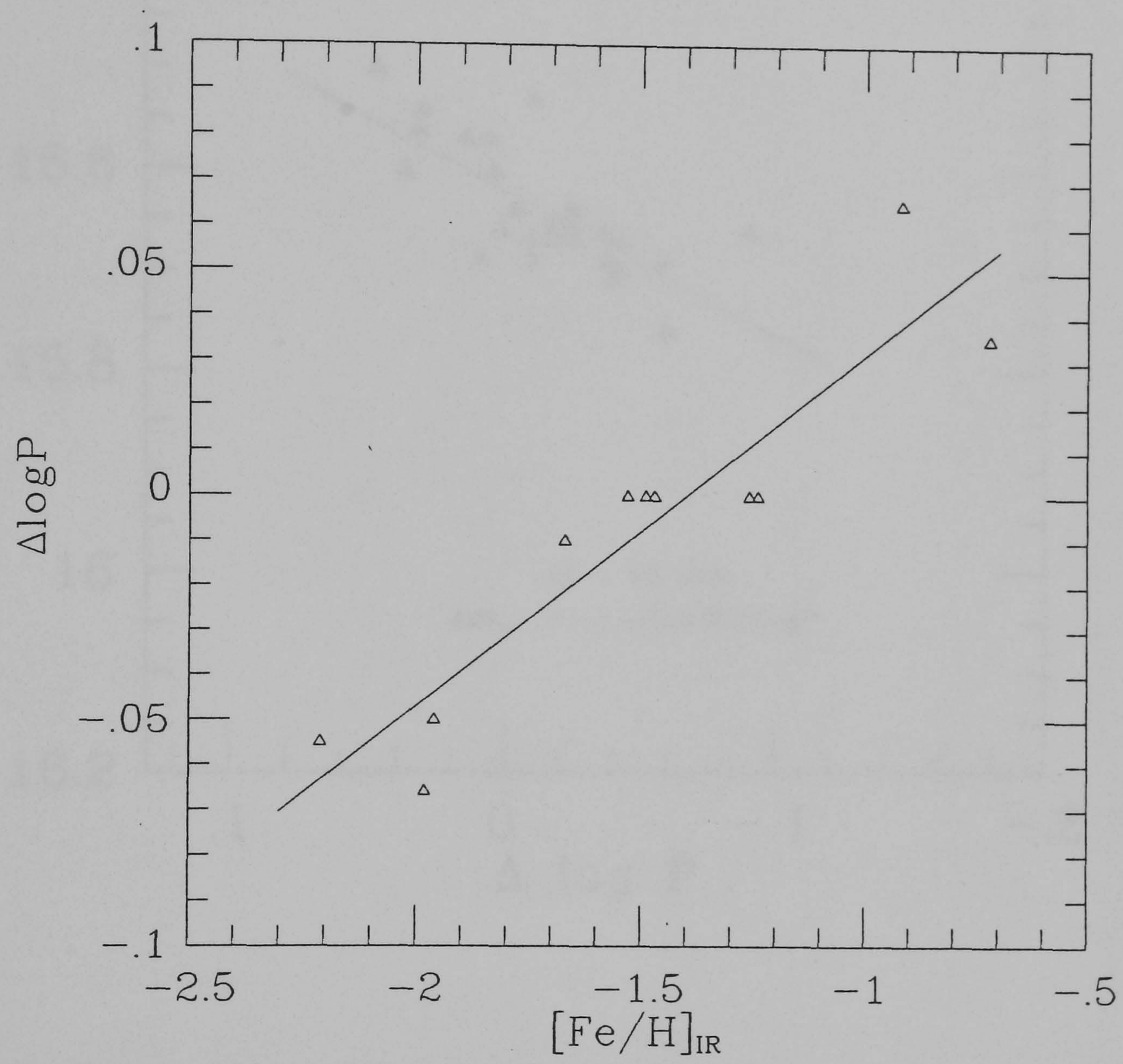

Figure 1.7: The period-shift–metallicity relation as derived by Noble and Dickens (1987). The metallicity scale is that of Frogel *et al.* (1983). The line is a least-squares fit to the data and satisfies the equation $\Delta \log P = 0.11(\pm 0.02) + 0.079(\pm 0.01)[\mathrm{Fe/H}]$

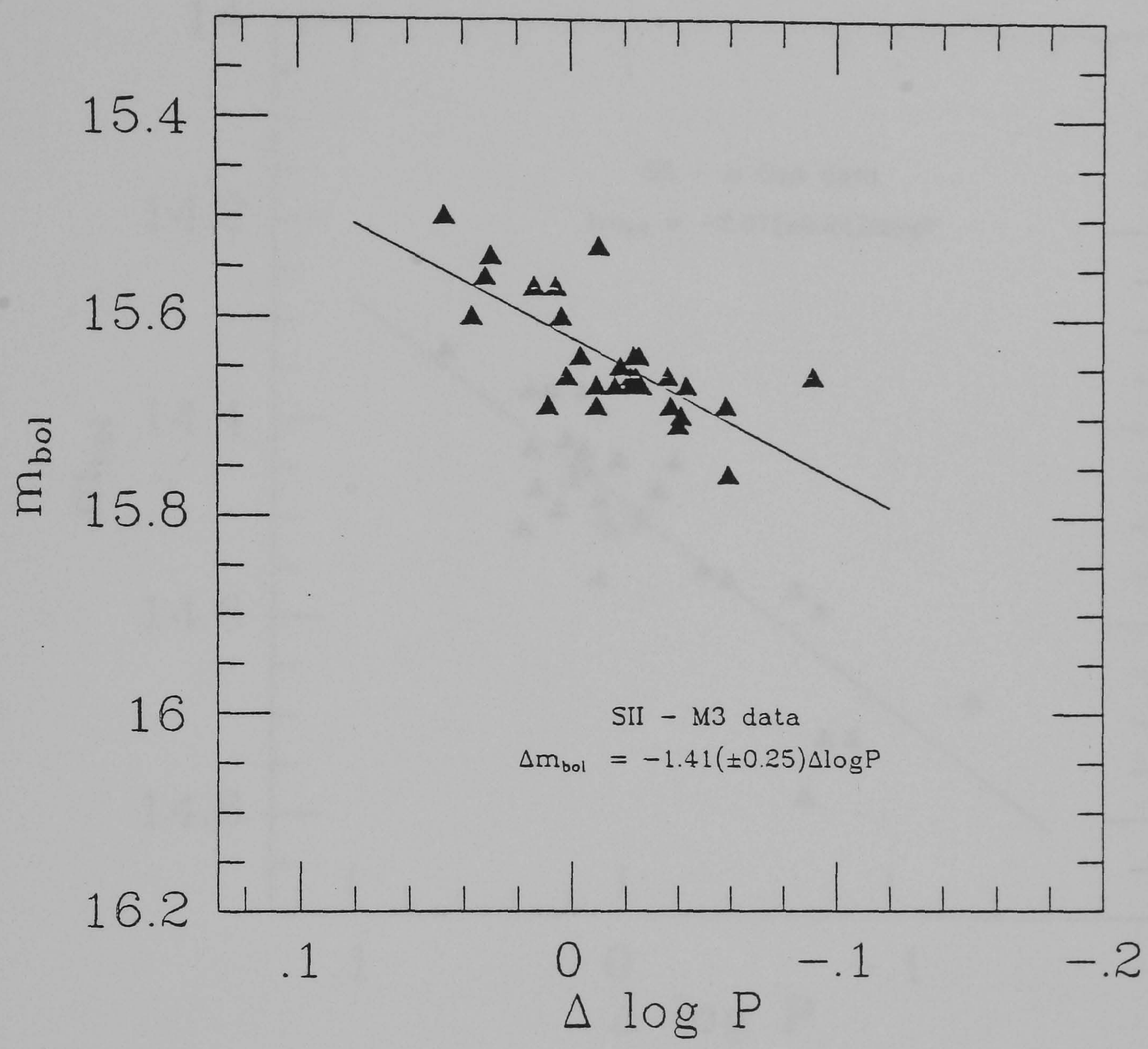

Figure 1.8: The correlation of apparent bolometric magnitude with period-shift for RR Lyrae variables in M3, from the data of Sandage (SII).

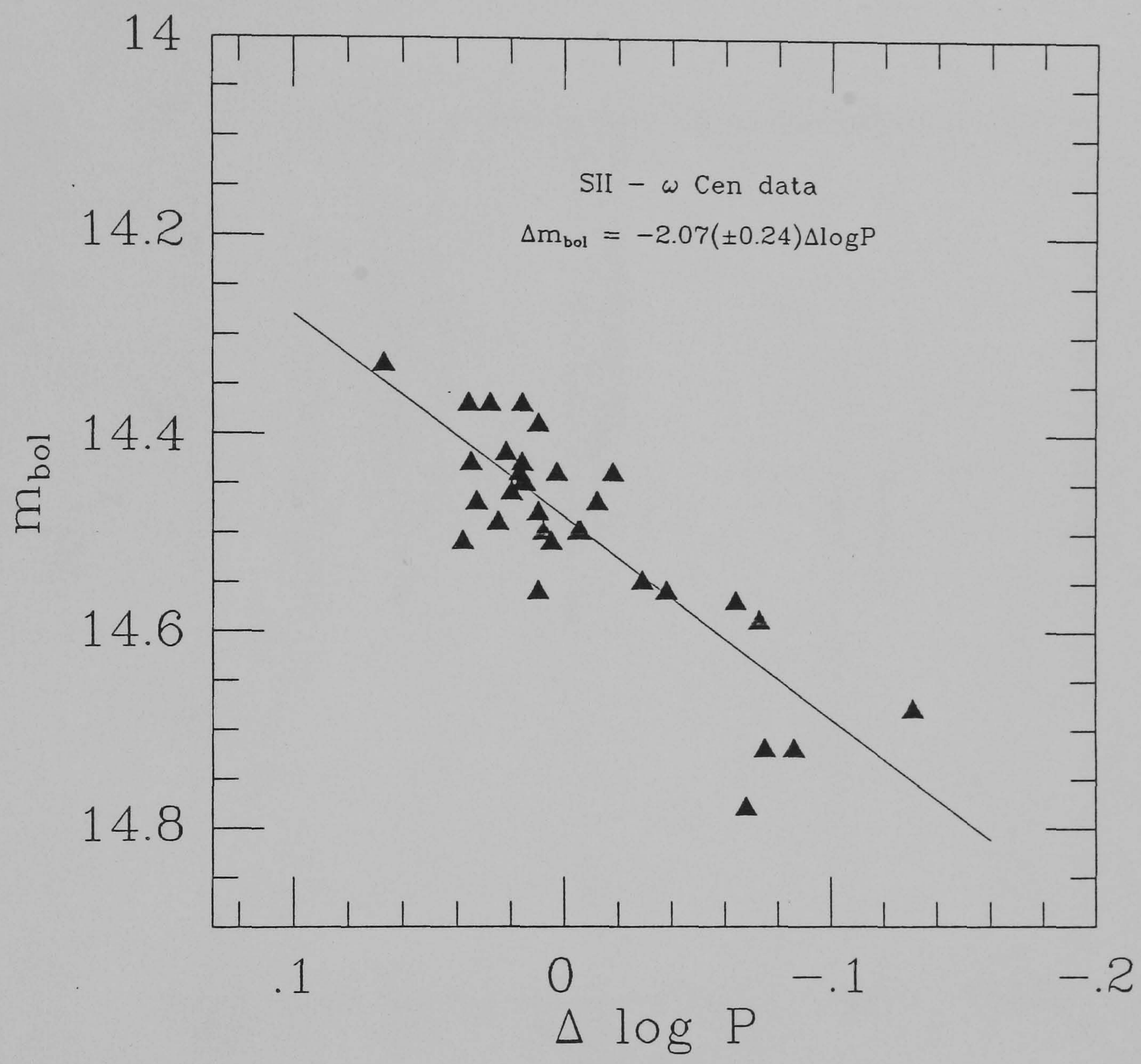

Figure 1.9: The correlation of apparent bolometric magnitude with period-shift for the RR Lyrae variables in ω Centauri, from the data of Sandage (SII).

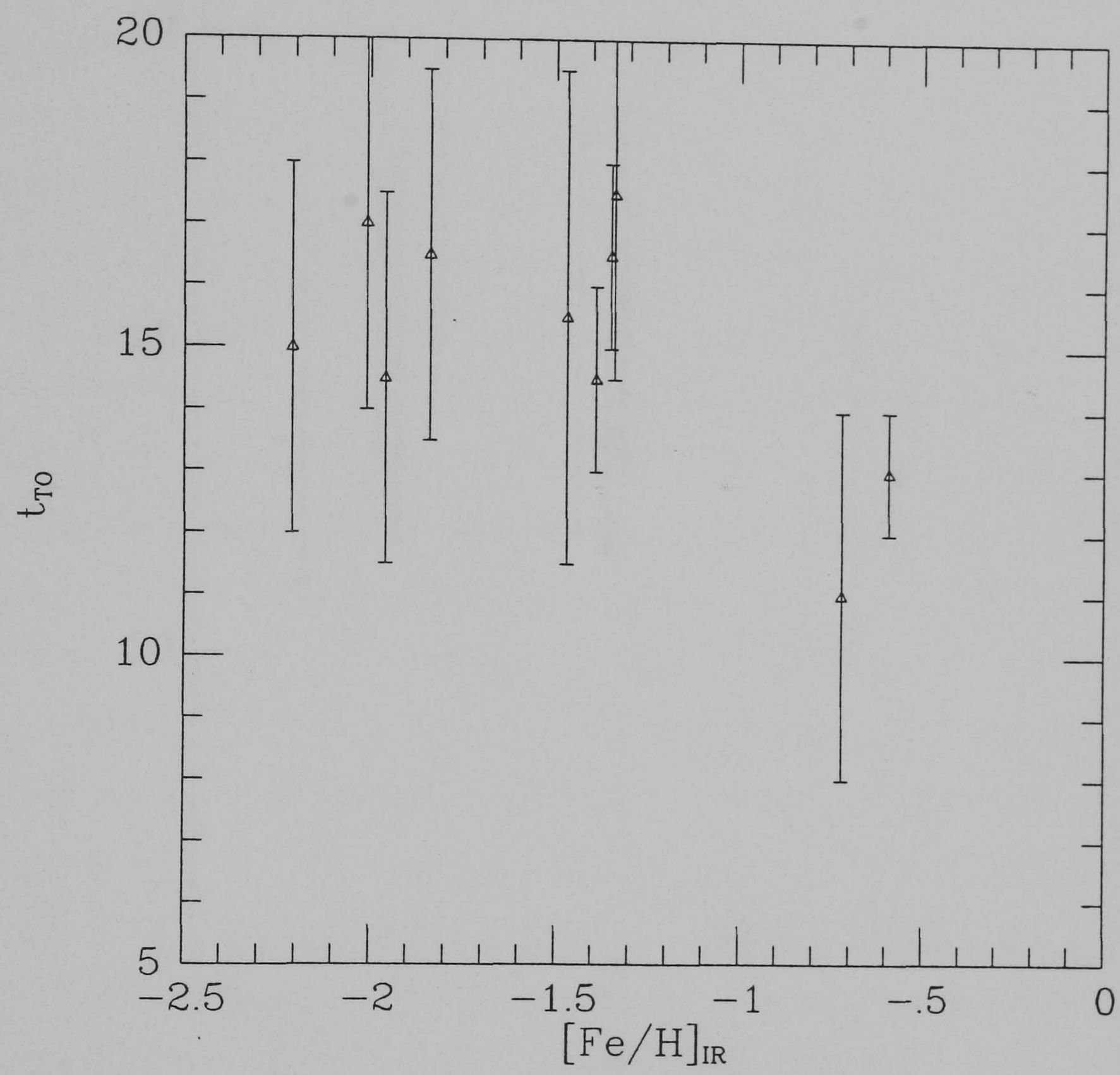

Figure 1.10: Cluster age, as derived from the absolute luminosity of the turnoff, as a function of cluster metallicity. From Table 1.5

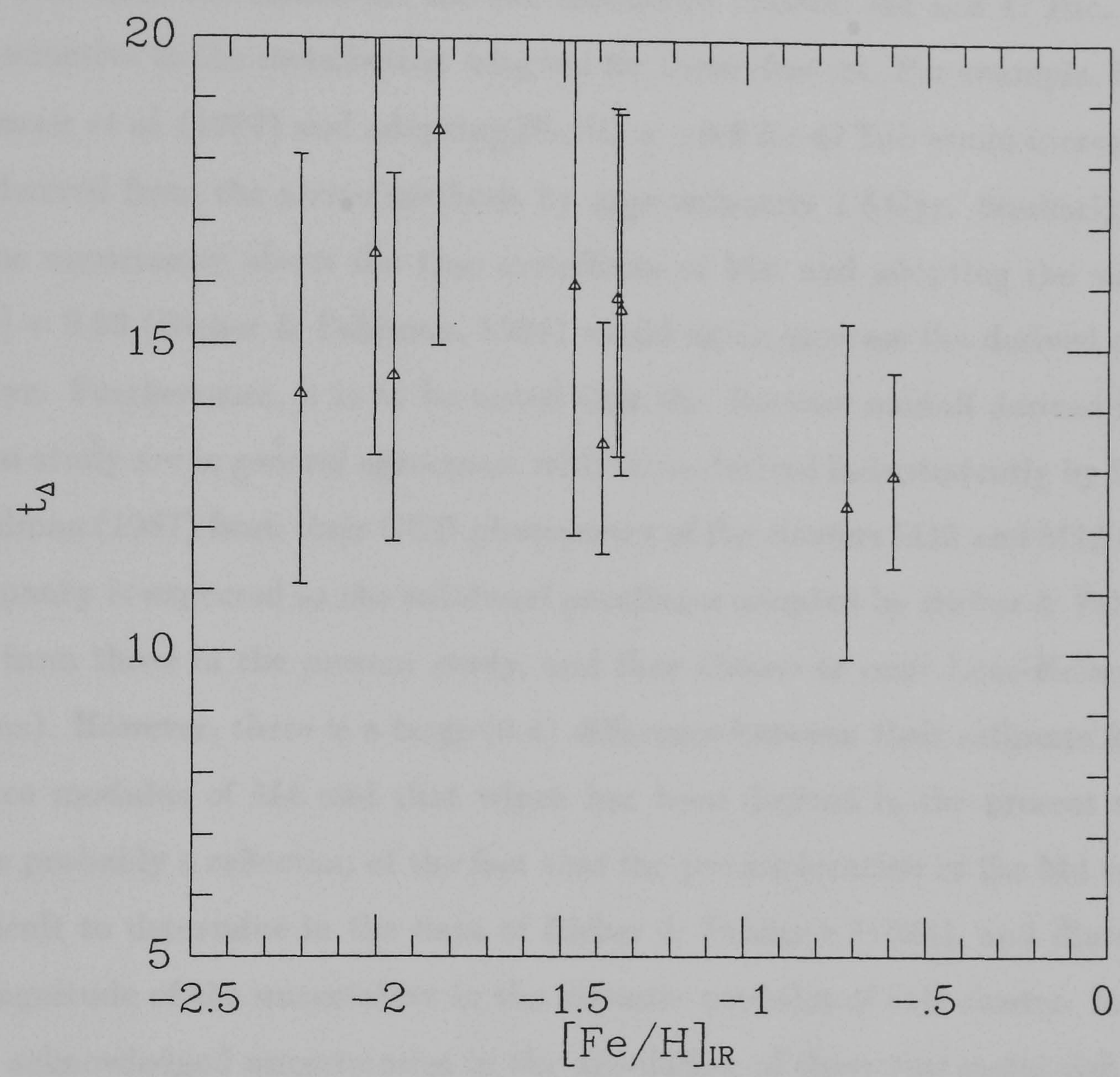

Figure 1.11: Cluster age, as derived from the difference in bolometric magnitude between the turnoff and horizontal branch, as a function of cluster metallicity. From Table 1.5

The age estimates derived in columns (7) and (8) of Table 1.5 are shown as a function of metallicity in Figures 1.10 and 1.11 respectively. The average ages determined from the two methods are $\langle t_{TO} \rangle = 15.1(\pm 1.9)$ Gyr and $\langle t_{\Delta} \rangle = 15.0(\pm 1.8)$ Gyr. There is some suggestion in the plots that there may be a correlation of age with metallicity, in the sense that the most metal-rich clusters appear to be some 2–3 Gyr younger than the most metal-poor. This trend is dependent upon the results for the two metal-rich clusters M4 and 47 Tuc, and is quite sensitive to the metallicities adopted for these clusters. For example, following Hesser *et al.* (1987) and adopting [Fe/H] = −0.8 for 47 Tuc would increase the ages derived from the above methods by approximately 1.5 Gyr. Similarly there is some uncertainty about the true metallicity of M4, and adopting the value of [Fe/H] = 0.93 (Richer & Fahlman, 1984) would again increase the derived age by $\sim$ 2 Gyr. Furthermore, it is to be noted that the distance moduli derived in the present study are in general agreement with those derived independently by Richer & Fahlman (1987) from their CCD photometry of the clusters M15 and M13 (some discrepancy is expected as the subdwarf parallaxes adopted by Richer & Fahlman differ from those in the present study, and they choose to omit Lutz-Kelker corrections). However, there is a large (0.4) difference between their estimate for the distance modulus of M4 and that which has been derived in the present study. This is probably a reflection of the fact that the precise location of the M4 turnoff is difficult to determine in the data of Richer & Fahlman (1984), and illustrates the magnitude of the uncertainty in the distance modulus of this cluster. In light of the acknowledged uncertainties in the age-dating of these two metal-rich clusters, and the evidence afforded by isochrone-fitting, which suggests the cluster system is coeval (see Section 1.4 above), it seems likely that Figures 1.10 and 1.11 do not reflect a real correlation of cluster age and metallicity. It would however be interesting and worthwhile to obtain estimates of $(m - M)_V$ for more clusters, particularly metal-rich ones, and pursue further the points raised in this section.

1.6 The Globular Cluster Abundance Scale

Because of their great age, the Galactic globular clusters are of great worth as probes of the evolutionary history of the Galaxy—both in terms of chemistry and dynamics. The metallicity of clusters can be determined by many techniques, all

based upon variations of photometric and spectroscopic methods. These methods can be categorized into three broad divisions.

- CMD morphology.
- Photometry and spectroscopy of individual stars.
- Photometry and spectroscopy of integrated light from many cluster stars.

Furthermore, the methods can be conceptually divided into those which provide absolute values of metallicity, and those which allow the cluster to be ranked in metallicity relative to other clusters. The single most important example of the former being high-dispersion spectroscopy of individual stars. Photometric methods are dominated by the effects of metallic line blocking on sensitive colour indices, and low resolution spectroscopy upon the relative strengths of metallic lines, most notably in the Ca lines of RR Lyrae stars. In this section the features of the colour–magnitude diagram which have been used to determine the relative overall metallicity are discussed, together with photometric and spectroscopic techniques, and some current results are examined. Some of the anomalous chemical properties of clusters are also discussed.

The composition of cluster stars has been widely reviewed in the literature, and a more complete treatment than space affords can be found in the recent review articles of Kraft (1979), Freeman and Norris (1981), and Bell (1987).

1.6.1 CMD Metallicity Indicators

Because the observed temperature and luminosity of a star are dependent upon its chemical composition, the location of any of the features in the colour–magnitude diagram is, to a greater or lesser extent, dependent upon the cluster chemical composition too. Although many morphological features have been correlated with metallicity, there are two principal metal–dependent parameters which have been widely used in the literature.

$(B-V)_{o,g}$ Defined by Sandage and Smith (1966) to be the intrinsic colour at the intersection of the mean loci of cluster giant branch and horizontal branch. The quantity has been observed to correlate well with metallicity (see, for example, Peterson, 1986), but in common with all "reddening–dependent" fits can be severely affected by any error in the reddening determination.

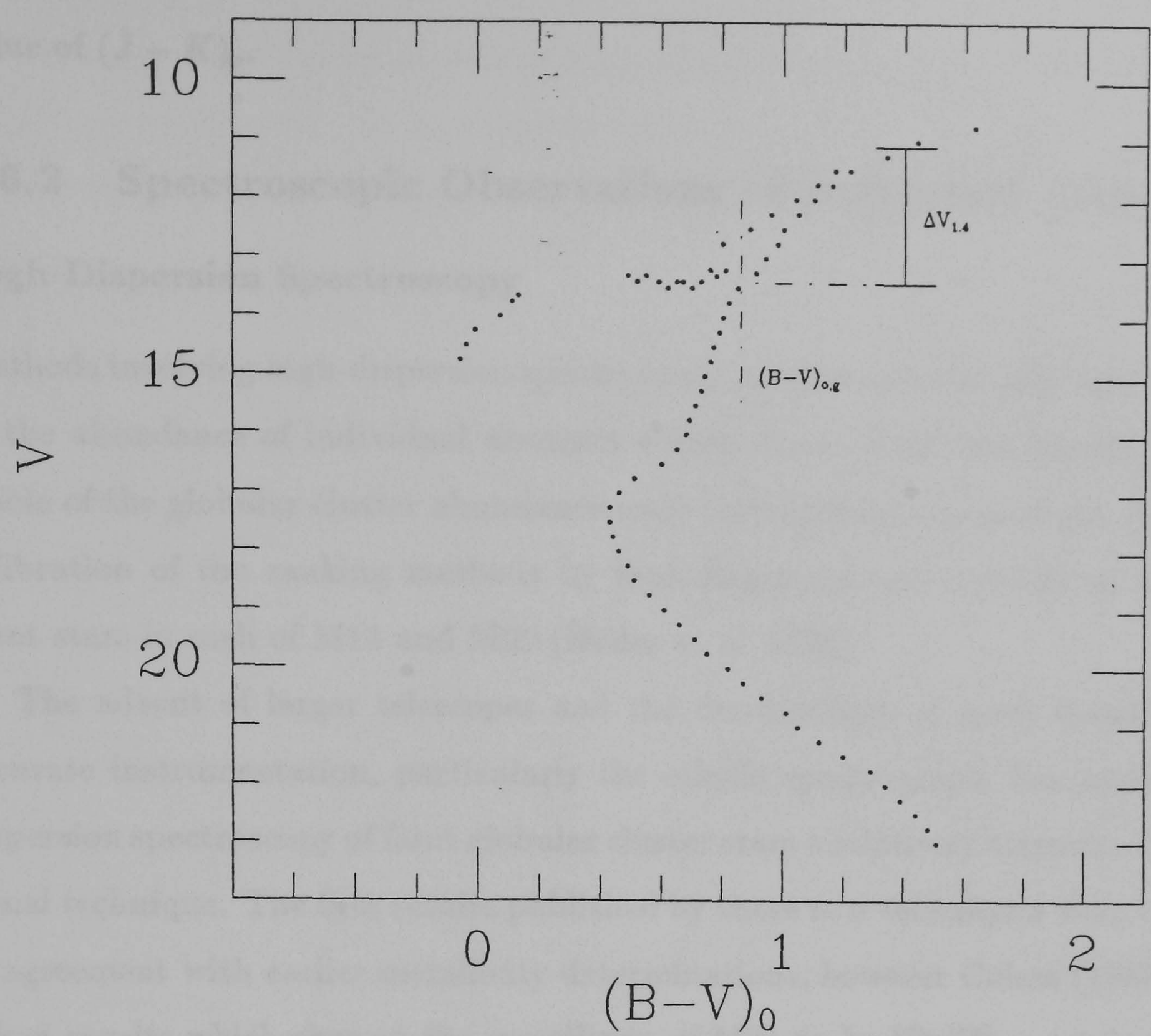

Figure 1.12: The $\Delta V_{1.4}$ and $(B-V)_{o,g}$ metallicity indicators.

$\Delta V_{1.4}$ Defined by Sandage and Wallerstein (1960) as the height of the giant branch above the level of the HB at a colour $(B-V)_o = 1.4$. Again this is dependent upon the choice of reddening adopted.

Both the $(B-V)_{o,g}$ and the $\Delta V_{1.4}$ parameters are illustrated in Figure 1.12. All such methods of determining cluster metallicity from the CM diagram are useful only in ranking the clusters, not as absolute calibrators of metallicity. In order to derive absolute values another method, such as high-dispersion spectroscopy, must be used to calibrate the measurements. These methods are probably now obsolete as "first rank" metallicity indicators for globular clusters, however they do provide a useful check upon the consistency of values derived from other methods.

One extension of the CMD techniques for deriving cluster metallicity is measurement of the $(J-K)_o$ parameter (Frogel *et al.* 1983), which is defined as the infra-red $(J-K)$ colour of the giant branch at $M(K_o) = -5.5$. This is somewhat analogous to $(B-V)_{o,g}$, but in this case the cluster distance must be known in order to obtain $M(K_o)$. This method is also only applicable to the most luminous stars in a cluster, and there may be a paucity of such stars upon which to base a

value of $(J-K)_o$.

1.6.2 Spectroscopic Observations of Individual Stars

High-Dispersion Spectroscopy

Methods involving high-dispersion spectroscopic analysis are the only direct probe of the abundance of individual elements within stars. Until the late 1970's the whole of the globular cluster abundance scale rested rather precariously upon the calibration of the ranking methods by high-dispersion spectroscopy of two red giant stars in each of M13 and M92 (Helfer *et al.* 1959).

The advent of larger telescopes and the development of more sensitive and accurate instrumentation, particularly the echelle spectrograph, has made high-dispersion spectroscopy of faint globular cluster stars a relatively common observational technique. The first results published by these new techniques were broadly in agreement with earlier metallicity determinations, however Cohen (1980) published results which showed the metallicity of M71 to be [Fe/H] = −1.3, a value some 0.8 dex poorer than given by other methods. Similarly Pilachowski *et al.* (1980) determined a value of [Fe/H] = −1.2 for 47 Tuc, compared with the values of around 0.6 derived from other sources. Thus, at the metal-rich end at least, the abundance scale derived from high-dispersion spectroscopy appeared to differ significantly from the values given by earlier work. Pilachowski (1984) has given the results of high-dispersion analyses for some 24 clusters, and whilst re-analysis of some of the earlier work has reduced the magnitude of the discrepancy, it still exists at a significant level. The review of Bell (1987) has recently focussed attention upon the possible reasons for this discrepancy and has examined the likely causes. Bell (1987) noted that Geisler (1986) has examined some of the stars used by Pilachowski *et al.* (1980), and has discovered the presence of TiO bands in the spectra. Because these spectral lines were not allowed for in the analysis of the data, it is likely that the position of the spectral continuum would be drawn wrongly, and thus the derived metallic line strength would be systematically too small. Bell and Gustafsson (1982) also noted that it is much more difficult to place the continuum correctly with high dispersion echelle spectra than it is with other spectroscopic techniques, and that this may cause problems when dealing with the more metal rich stars. Cohen (1983) has critically examined her ear-

lier high-dispersion work, as well as that of others, and found that there were indeed systematic errors in much of the earlier high-dispersion studies of stars in metal-rich clusters due to misplacement of the continuum level.

Low-Dispersion Spectroscopy

The most widely used low-dispersion spectroscopic technique is the ΔS method (Smith, 1984a). The basis of the ΔS method is the difference in spectral type of a cluster RR Lyrae star between that determined from its hydrogen lines, and that determined from the strengths of its calcium H and K lines. The relative difference in these line strengths is used to create the index ΔS which is calibrated by observations of field RR Lyrae stars. Unfortunately this method is not really suitable for the classical metal-rich clusters because of the paucity, or often complete absence, of RR Lyrae variables within them. Similarly it is not applicable to those clusters (such as NGC 6752) with predominantly blue horizontal branches which possess no RR Lyrae stars.

Photometry of Individual Stars

Any photometric colour index which is sensitive to the variation of metallic line strength with metal abundance can be used as a metallicity indicator, providing that an adequate means of calibrating the observations is available.

The Johnson UBV filter system has, in the past been employed with some success (see, for example, Sandage, 1970 and Carney, 1979). The quantity $\delta(U-B)$, the ultraviolet excess, is defined as the deviation in the UBV two-colour diagram from the fiducial $(U-B)$, $(B-V)$ line (usually the Hyades main sequence) of a sample of stars from a particular cluster. This excess is caused by the decreased line blanketing present in metal-poor cluster stars. The method is probably outdated for accurate determinations of cluster metallicity, and there are now other well calibrated photometric systems available which offer greater precision and utility. The most commonly used of these are catalogued by Bell (1987), and include the Washington, DDO, and Strömgren systems (for further references to these systems and their use as metallicity indicators see Davis Philip, 1979). Also of note is the comprehensive system of Searle and Zinn (1978) which characterizes the stellar flux in 18 passbands between 5000Åand 7620Å.

Integrated Light Measurements

Zinn (1980) has carried out integrated light photometry of nearly 80 Galactic globular clusters using an elaborate filter system, and on the basis of these measurements has constructed a reddening-free, and metallicity-dependent index Q_{39}. Zinn and West (1984) have subsequently measured other integrated light spectral features, and correlated their observations with the Q_{39} abundances. One problem with these techniques which has proved difficult to overcome satisfactorily is the dependence of the results upon the relative numbers of stars in different parts of the colour-magnitude diagram. For instance, if a cluster possesses a relatively large number of very hot BHB stars, the shorter wavelengths may well be dominated by the flux from these stars. Because of the variation of HB morphology at intermediate metallicities—the so-called second parameter problem—these methods can give results which are inconsistent with those given by other procedures. Smith (1984b) has developed a correction to the Q_{39} abundances based upon the relative numbers of RHB and BHB stars. It is not clear if it is valid for all abundances, but it lessens the disparity between ΔS and Q_{39} determinations.

The Sandage Period-Shift Effect

It is worth mentioning here that the period-shift–abundance relation (as mentioned in Sections 1.3.2 and 1.5) could be used as a method of ranking the clusters in metallicity. Similarly the horizontal branch luminosity at the RR Lyrae strip, M_V^{RR}, as determined in Section 1.5 could be used, if the cluster distance were known, as a reliable check upon the metallicity.

1.6.3 Chemical Inhomogeneity Within Clusters

One of the fundamental assumptions that had long been adopted in globular cluster studies was that all the stars within a given cluster have identical chemical compositions. Intermediate and high-resolution spectroscopy of individual globular cluster stars have shown this assumption to be invalid. Since this became apparent there have been many contributions in the field, and a number of comprehensive reviews have been published chronicling the developments (see, for example, Kraft, 1979, Freeman & Norris, 1981 and Smith, 1987). Abundance variations involving carbon and nitrogen in cluster stars appear to be common,

and are also exhibited in several ways. Early indications of these peculiarities included the observation of CH stars (stars with the observed carbon abundance exceeding that of oxygen at their surfaces), CN enhanced giants (stars exhibiting greatly increased λ4215 Å CN band strength) and "weak-G-band" stars (showing only faint absorption in the CH G-band feature). More recently it has become apparent that clusters of intermediate and high metallicity tend to exhibit bimodal distributions of CN band strength. Metal-poor clusters do not seem show significant bimodality, however CNO variations do seem to be present amongst their constituent stars. All of these phenomena are comprehensively described in the review of Smith (1987), where references to the original work may be found.

The cluster ω Centauri exhibits a whole range of CNO inhomogeneities, however its most remarkable feature is that it displays marked variations in heavy element abundances amongst its member stars. Further discussion of the abundance inhomogeneities observed within ω Cen is deferred until Chapter 3.

1.7 Globular Cluster Luminosity Functions

The luminosity function of a cluster is the number distribution of member stars as a function of magnitude. Early attempts to construct faint photographic luminosity functions were made by Sandage (M3–1957) and Hartwick (M92–1970). These studies showed the form of the luminosity function for giant branch stars, but the effects of crowding and background fluctuations in these photographic studies seriously hampered the investigation of the main sequence luminosity function. Nevertheless, interesting features, such as the distinctive giant branch "bump" were identified (Simoda, 1972). A recent paper by Ratcliff (1987) has discussed the observed characteristics of cluster luminosity functions on the upper main sequence subgiant and giant branches. Ratcliff (1987) has also constructed theoretical luminosity functions and has used these to demonstrate the possibilities for determining fundamental cluster parameters such as age and chemical composition.

The vast improvement in cluster colour-magnitude diagrams which has been precipitated by the use of CCDs, has allowed the construction of new faint, precise cluster luminosity functions. With profile-fitting photometric techniques (see Chapter 2) it is possible not only to measure stars in crowding conditions which

would make photographic photometry impracticable, but also, by performing simple checks upon the data, to reliably estimate corrections for incompleteness at the faint limit of the photometry. Corrections can also be made to minimise the effects of field star contamination in the cluster luminosity function.

Salpeter (1955) proposed that the form of the cluster mass function (the number distribution of cluster stars as a function of mass) could be described by a power law, $\phi(m)dm = m^{-(1+x)}dm$, where $\phi(m)dm$ is the number of stars in the mass range m to $m+dm$, and x is the power-law mass function index. Theoretical luminosity functions of the form $\Phi = \phi(m)(dm/dM_V)$, where Φ is the number of stars per unit magnitude, can be constructed from theoretical mass-luminosity models (*e.g.* VandenBerg & Bell, 1985). The initial results of the new CCD luminosity function studies were summarized by McClure *et al.* (1986) who showed that in the seven Galactic globular clusters in their sample, there is a strong correlation of the luminosity function slope and the cluster metallicity. McClure *et al.* (1987b) have published faint luminosity functions for a further three clusters, again showing this same correlation. Fits of theoretical luminosity functions to the data show that the correlation of luminosity function slope with metallicity implies a relationship between x, the power-law index of the present-day mass function, with metallicity. The observations imply values of x around 2.5, for the most metal-poor clusters ([Fe/H] $= -2.3$), ranging to $x \simeq 0.0$ for the most metal-rich ([Fe/H] $= -0.5$). The processes of stellar evolution are not expected to have significantly modified the shape of the cluster luminosity function, and hence the mass function of main sequence stars, from their original forms. Dynamical relaxation within clusters (Pryor *et al.* 1986) is expected to have populated the outer regions of clusters (all the present CCD studies have been made in such regions) with an excess of low-mass stars compared to the initial mass function. The correlation remains even after taking into account the effects of such dynamical processes (Smith & McClure, 1987) and thus it seems these results show there to be some fundamental connection between cluster metallicity and protocluster mass function. Smith & McClure (1987) have discussed the possible nature of this relationship, in particular the hypothesis that cluster metallicity has been determined by the influence of the cluster initial mass function on the number of massive stars produced which were able to enrich the cluster by supernovae and stellar winds in the early stages of cluster development. The simple models used

by Smith & McClure (1987) suggest that there is a link between the initial mass function power-law index and the number of such stars produced, and reproduce the general form of the relationship between x and [Fe/H]. However, for low values of x, their models predict metal enhancements far greater than those actually seen in the most-metal rich clusters. Smith & McClure suggest that there may be modifications of the cluster mass function at the highest masses, or alternatively mechanisms for loss of processed stellar ejecta from the cluster, which explain this discrepancy. Whilst this scenario, namely that cluster metallicity is influenced by the initial mass function, seems entirely plausible, it is just as feasible that it is the cluster mass function which has been influenced in some way by the protocluster metallicity. An equally viable alternative is that the observed mass function and cluster metallicity have both been influenced by another factor; for example it could be the case that conditions prevalent in a metal-rich protocluster cloud are suitable for producing stars distributed according to a mass function with a low value of x. It is clear that further observational and theoretical studies are required in order to shed light upon this intriguing phenomenon.

Chapter 2

CCD Stellar Photometry

2.1 Introduction to Astronomical Photometry

Astronomical photometry is, in essence, the determination of the intensity of radiation from extraterrestrial sources. In particular the term is most often applied to the measurement of apparent stellar brightness through a variety of filters in the ultraviolet, optical and near infra-red regimes. Photometry is of unparalleled importance for measuring the energy output of stars in different wavelength bands and providing observational evidence to set constraints upon models of stellar evolution and structure. The colour-magnitude diagram, discussed in Chapter 1, provides the key to understanding the evolution of stars, and is constructed from the photometric observations of stellar associations.

Over 2000 years ago, the Greek astronomer Hipparchus classified over one thousand naked eye stars into six brightness classes, ranked in "magnitudes" from one to six in order of decreasing brightness. In 1856, N.R.Pogson reaffirmed William Herschel's earlier discovery that the light flux from a first magnitude star is approximately one hundred times greater than the flux from a sixth magnitude star. The magnitude scale was based upon the non-linear physiological response of the eye to light stimulus—the eye's response is such that equal magnitude differences correspond to equal flux ratios of detected light. Pogson redefined the magnitude scale, such that a difference of five magnitudes was exactly equal to a factor of one hundred in the detected light intensity. Considering two stars with fluxes F_1 and F_2, the corresponding magnitude relation is,

$$F_1/F_2 = (10^{2/5})^{m_2-m_1}$$

where m_1 and m_2 are the magnitudes of the stars. This can be rewritten as,

$$m_1 - m_2 = -2.5\log(F_1/F_2). \tag{2.1}$$

The scale was made to coincide approximately with the historical magnitude scale by defining the magnitude of the stars Altair and Aldebaran to be 1.0.

2.2 Defining a Photometric System

Unfortunately the situation for the observer is considerably more complicated than Equation 2.1 implies. Equation 2.1 refers to the observed stellar fluxes. Because of absorption in interstellar space, extinction by the atmosphere, and the characteristics of the telescope, detector, and any filter system used, the relation between the emitted stellar flux, and that which is observed, is complicated. At this stage the absorption of light in the interstellar medium is usually neglected as it is a constant factor at a particular wavelength for a particular star. Atmospheric extinction, as well as being wavelength dependent varies with both the zenith distance of the star, and with the observing conditions, and must be explicitly compensated for. Equation 2.1 can thus be rewritten as,

$$m_1 - m_2 = -2.5\log\left(\frac{\int_0^\infty \Phi_A(\lambda,d_1)\Phi_T(\lambda)\Phi_F(\lambda)\Phi_D(\lambda)F_2(\lambda)d\lambda}{\int_0^\infty \Phi_A(\lambda,d_2)\Phi_T(\lambda)\Phi_F(\lambda)\Phi_D(\lambda)F_2(\lambda)d\lambda}\right) \tag{2.2}$$

Where;

$\Phi_A(\lambda, d_1)$ is the fractional transmission of the atmosphere in the direction of star 1 at wavelength λ;

$\Phi_A(\lambda, d_2)$ is the same for star 2;

$\Phi_T(\lambda)$ is the fractional transmission of the telescope at wavelength λ;

$\Phi_F(\lambda)$ is the fractional transmission of the filter combination at wavelength λ;

$\Phi_D(\lambda)$ is the fractional efficiency of the detector at wavelength λ;

$F_1(\lambda)$ is the actual monochromatic flux outside of the earth's atmosphere for star 1 at wavelength λ;

$F_2(\lambda)$ is the same for star 2.

In practice, photometric observations are made with many combinations of detector, telescope, and filters. Obviously, such measurements must be put onto a common scale so that observers can compare results, and so that the body of

observations as a whole may be compared with the predictions of theory. The factors in Equation 2.2 are extremely difficult to determine, and it would be impossible to design a practical photometric system which relied upon the absolute calibration in terms of received flux.

The strength of the magnitude system is that it is not important to know these factors; it is merely necessary that certain stars have precisely *defined* magnitudes. The magnitudes of "unknown"stars can then be determined by comparing their observed fluxes with those of the "known", or standard stars. This is the reason why the seemingly archaic magnitude system is still preferred by optical astronomers. The primary requirement of a stellar photometric detector is that the output signal is related to the input light flux in a simple, reproducible, preferably linear fashion. In the case of DC photoelectric photometry, the quantity measured is the amplified output current, or in pulse counting photometry the number of counts per second from the detector.

The output from an imaging CCD detector is in the form of a digitized image which represents, in ADU (Analogue to Digital Units), the electric charge produced by incident light in each pixel (see Section 2.4). In this case it is the ADU count associated with a stellar image which is proportional to the irradiation from that star. For a CCD system, the "instrumental" magnitude of a star which produces a signal of N_{ADU} counts during an exposure of t seconds can be defined as,

$$m = -2.5\log(N_{ADU}/t).$$

The instrumental magnitude system is intrinsic to the telescope, filter and detector used, and represents the "natural" response of these components to input light stimulus.

In many cases, such as the study of colour magnitude diagrams, the observer wishes to obtain "colour" information about the source. The colour index of a source is defined as the difference in magnitude between observations of this source through two different wavelength passbands. The instrumental colour index of a source, for two passbands centred on wavelengths λ_1 and λ_2 (where by convention $\lambda_1 < \lambda_2$) is,

$$m_{\lambda_1} - m_{\lambda_2} = -2.5\log\left(\frac{N_{\lambda_1}/t_1}{N_{\lambda_2}/t_1}\right).$$

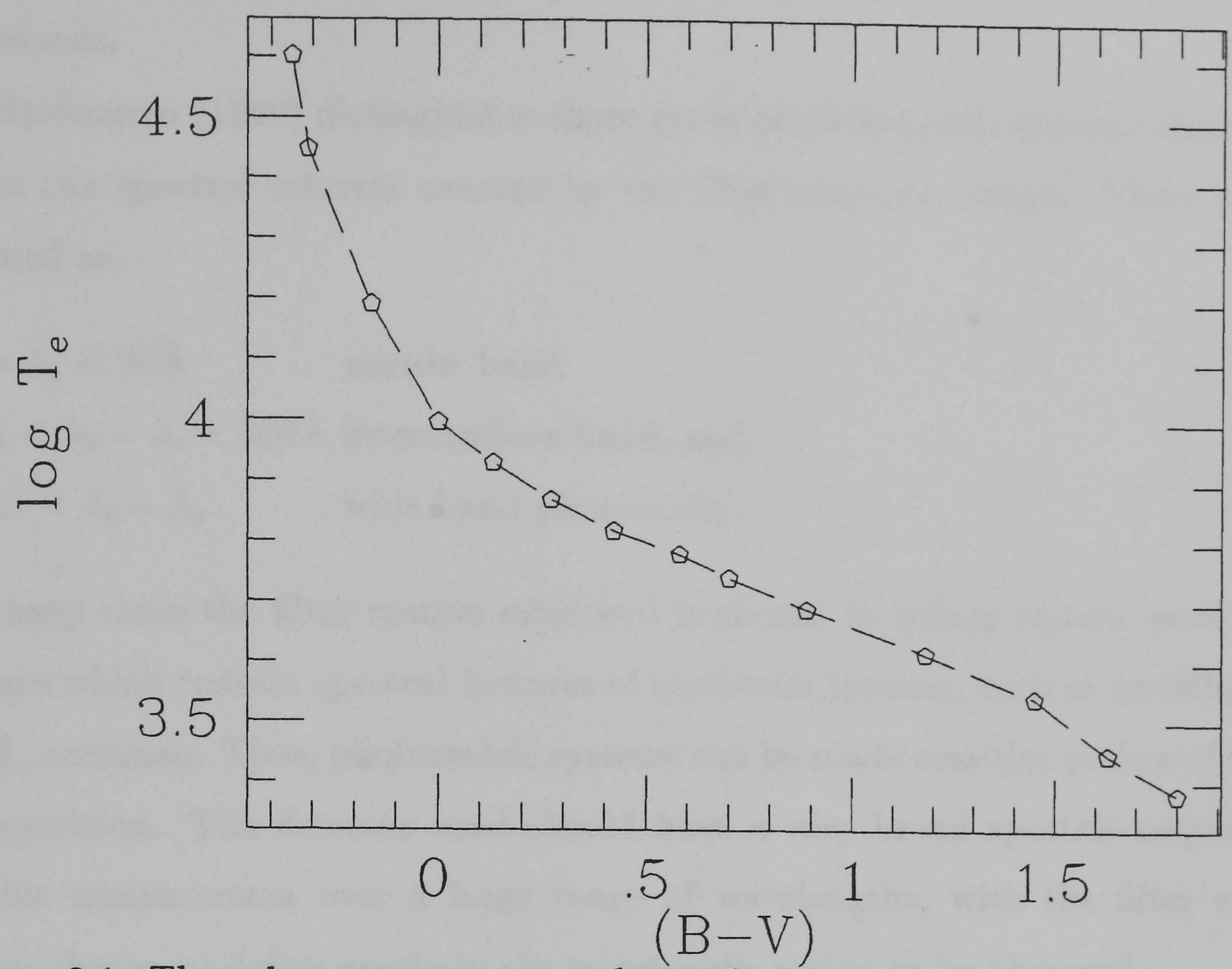

Figure 2.1: The colour–temperature relationship for main sequence stars. Taken from Allen (1973).

The ratio of monochromatic fluxes at different wavelengths is, for a black body emitter, a single valued function of the temperature of the source (see, for instance, Golay, 1974). Because photometric passbands are of finite width, and the stellar spectrum is, at best, only an approximation to a black body spectrum, the colour–temperature relation is a complicated function. Figure 2.1 shows the colour–temperature relationship for main sequence stars (from Allen, 1973). It can be seen that there is a strong correlation of the $(B-V)$ colour index with temperature for main sequence stars.

As noted above, the basis of any photometric system is a sequence of defined, or standard stars. Initially, a small number of stars, with a wide range of colour index in the chosen photometric system, are measured upon an internally consistent scale. The absolute calibration, or "zeropoint", of the magnitude scale is then defined in an essentially arbitrary fashion. These stars form the "primary standards" for this photometric system, and allow observers to transform their own, instrumental, magnitude values to the standard system. As discussed in

Section 2.3.1 below, it is desirable to establish a network of standard stars, spread over the sky; to this end large numbers of stars are measured repeatedly to determine accurately their magnitudes upon the standard system. These are secondary standards.

Strömgren (1966) distinguishes three types of photometric systems depending upon the spectral interval covered by the filter response curves. These can be defined as,

$\lambda_b - \lambda_a < 90$Å narrow band

90Å $< \lambda_b - \lambda_a < 300$Å intermediate band, and

300Å $< \lambda_b - \lambda_a$ wide band photometry.

In many cases the filter system employed is chosen to isolate certain wavelength ranges which contain spectral features of particular interest, such as metallic lines or H_α emission. Thus, photometric systems can be made sensitive probes of stellar composition. The detector used should have a very broad spectral response to enable measurement over a large range of wavelengths, with the filter system being chosen to define precisely the wavelength region to be observed.

2.2.1 Standard Photometric Systems

There are many established photometric systems, each designed for specific purposes. In this thesis the system employed is based upon the Johnson UBV system. The Johnson UBV system is a wide band photometric system, and the basic specifications of the detector, instrument, and filter combination are described by Johnson (1953,1963). The Johnson UBV passbands are shown in Figure 2.2, the maximum transmission in each band is normalised to unity. The filters which define the Johnson B and V passbands were chosen largely to reproduce the older blue and photovisual photographic passbands. The U filter was chosen to add information in the short wavelength region, and to allow comparisons of stellar colour indices to be made. The choice of this filter system for CMD work is largely convention, and recently many alternative system have been suggested because of the additional astrophysical information they can present. The Strömgren (1966) system can provide more precise information on stellar composition than the UBV system, as well as reliable reddening data. The Strömgren system is a narrow band

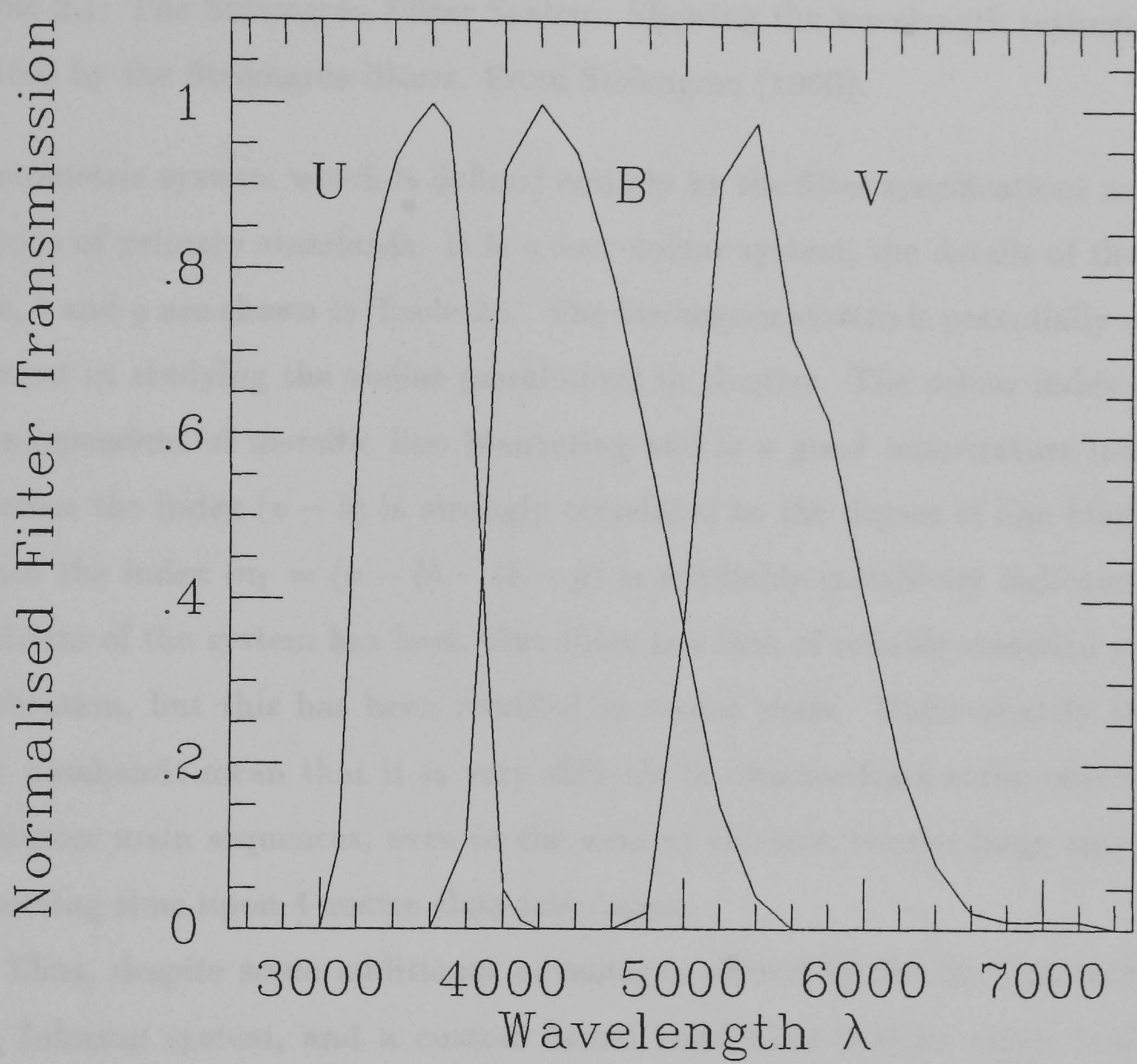

Figure 2.2: The Johnson UBV passbands. In each case the filter response is normalised to unity at maximum transmission.

Filter	$\lambda_{central}$ (Å)	Full Width Half Maximum Transmission (Å)
y	5500	200
b	4700	100
v	4100	200
u	3500	400

Table 2.1: The Strömgren Filter System. Showing the wavelength regimes transmitted by the Strömgren filters. From Strömgren (1966).

photometric system, which is defined entirely by the filter specifications and a sequence of primary standards. It is a four-colour system, the details of the filters u, v, b and y are shown in Table 2.1. The Strömgren system is potentially of great interest in studying the stellar populations in clusters. The colour index $(b-y)$ is independent of metallic line blanketing and is a good temperature indicator, whereas the index $(v-b)$ is strongly correlated to the degree of line blanketing; hence the index $m_1 = (v-b)-(b-y)$ is a reliable metallicity indicator. One criticism of the system has been that there is a lack of reliable standard stars for calibration, but this has been rectified in recent years. Unfortunately the narrow passbands mean that it is very difficult to observe faint stars; observations of cluster main sequences, even in the nearest clusters, require large amounts of observing time upon 4–metre class telescopes.

Thus, despite some additional advantages offered by the Strömgren system, the Johnson system, and a custom broad band filter system which transforms well to the Johnson system, were chosen for the observations presented in this thesis. Additionally, there is a large body of published literature pertaining to cluster photometry in the Johnson system, both in observation and theory; cluster observations made in this system can readily be compared with a large number of similar observations of other clusters.

In order to exploit the information present at longer wavelengths than the Johnson UBV filters a number of extensions, such as the Kron-Cousins $UBVRI$ system (Bessell, 1976), have been developed.

2.3 The Relationship Between Instrumental and Standard Magnitudes

The task of reducing the derived instrumental magnitudes to the standard system can be divided into two logically separate processes; correcting for atmospheric extinction, and correcting for the instrumental response.

2.3.1 Atmospheric Extinction

The observed magnitude of a stellar source through a passband centred on a wavelength λ, m_λ, is related to $m_{\lambda 0}$, the magnitude value which would be measured outside of the Earth's atmosphere by the following expression,

$$m_{\lambda 0} = m_\lambda - (k'_\lambda + k''_\lambda c)X,$$

where k'_λ is the principal, or primary extinction coefficient. The second order extinction coefficient, k''_λ is a term which must be included to correct for the wavelength dependence of atmospheric extinction and thus, c is the colour index of the star. The "airmass", X, is a quantity representing the atmospheric path length of the starlight, and is normalised to a value of 1.0 at the zenith. The airmass can be well represented by the following expression (from Young, 1974),

$$X = \sec z(1 - 0.0012 \tan^2 z),$$

where z is the zenith distance of the star, given by

$$\sec z = (\sin\phi \sin\delta + \cos\phi \cos\delta \cos h)^{-1},$$

where δ and h are the star's declination and hour angle respectively, and ϕ is the latitude of the observer. However, at reasonably small zenith distances ($z \leq 30°$), $X = \sec z$ is a good approximation. It is desirable to observe a star at the minimum possible zenith distance in order to minimise the uncertainties caused by fluctuations in atmospheric conditions, and thus, in the majority of cases this approximation is sufficiently accurate. Although the average values of the extinction coefficients are well determined, there can be substantial variations on a night to night basis, and so the extinction coefficients should be determined each night. Considering the transformation of instrumental magnitudes, and colour indices,

to the Johnson B, V system, we obtain,

$$\begin{aligned} v_0 &= v - (k'_v + k''_v(B-V))X, \\ (b-v)_0 &= (b-v)(1-k''_{bv}X) - k'_{bv}X. \end{aligned}$$

The value of k''_v is generally extremely small if the V filter is well matched to the standard Johnson specification, and is usually neglected in the analysis.

2.3.2 Colour Transformation

The differing spectral responses of different photometers mean that it is necessary to transform the extinction corrected magnitudes and colours to the standard system. The general form of the transformation from the extinction corrected magnitude, $m_{\lambda 0}$, to the standard magnitude, M_λ, is given by,

$$M_\lambda = m_{\lambda 0} + \alpha_1 C + \alpha_2 C^2 + \cdots + \alpha_n C^n + \gamma_\lambda,$$

where $\alpha_1, \ldots, \alpha_n$ are the colour coefficients and γ_λ is the zeropoint constant. The standard colour index, C, is likewise given by

$$C = \beta_1 c_0 + \cdots + \beta_n c_0^n + \gamma_c$$

where c_0 is the observed, extinction corrected, colour index. Again $\beta_1, \ldots, \beta_n$ are colour coefficients, and γ_c is the zeropoint constant for this relationship.

In practice, the transformations are not markedly non-linear if the filters and detector used conform well to the specifications for the particular photometric system in use; generally only the α_1 and β_1 terms are of importance.

2.4 The CCD as a Photometric Detector

There are a number of criteria which should be achieved by a practical two-dimensional, photometric, low-level light detector. Briefly, such properties of the detector can be listed as:

- High quantum efficiency.
- Accuracy, in the sense that the input photon signal would be precisely calculable from the output signal.

- Large dynamic range.
- Extreme linearity.
- Low noise level.
- Wide wavelength coverage.
- Ability to integrate signal over any desired timescale.
- Large detecting area.
- Good spatial resolution, uniformity and stability.
- Reliability in operation.
- Ease of use.
- Flexibility of operation.
- Durability.

The Charge Coupled Device (CCD) is a solid state, two-dimensional photoelectric imaging detector which possesses many of these desirable attributes. Principally a CCD exhibits high quantum efficiency, and extreme linearity over a large dynamic range of input signals, and indeed may be considered to be the nearest pragmatic solution to the problem of constructing an ideal photometric detector. CCDs also offer the obvious practical advantages of greatly reduced size, weight, and power consumption when compared with their predecessors such as the electronographic camera (Penny, 1976) and the SIT vidicon camera (McMullan & Morgan, 1978).

Although the CCD conforms so well to the "ideal" detector, as described above, there are disadvantages, for example the many flaws inherent in the manufactured chip, which are echoed as defects in the recorded image, and the complex stages of data reduction necessary to furnish the final results from raw CCD images. To a certain extent, the problems caused by faults in CCD detectors can be overcome by a prudent choice of the actual device used. Even CCDs of the highest grade suffer from manufacturing defects to some degree; subsequently, processing of the recorded images by digital computer is necessary to minimise the effect of these defects upon the data.

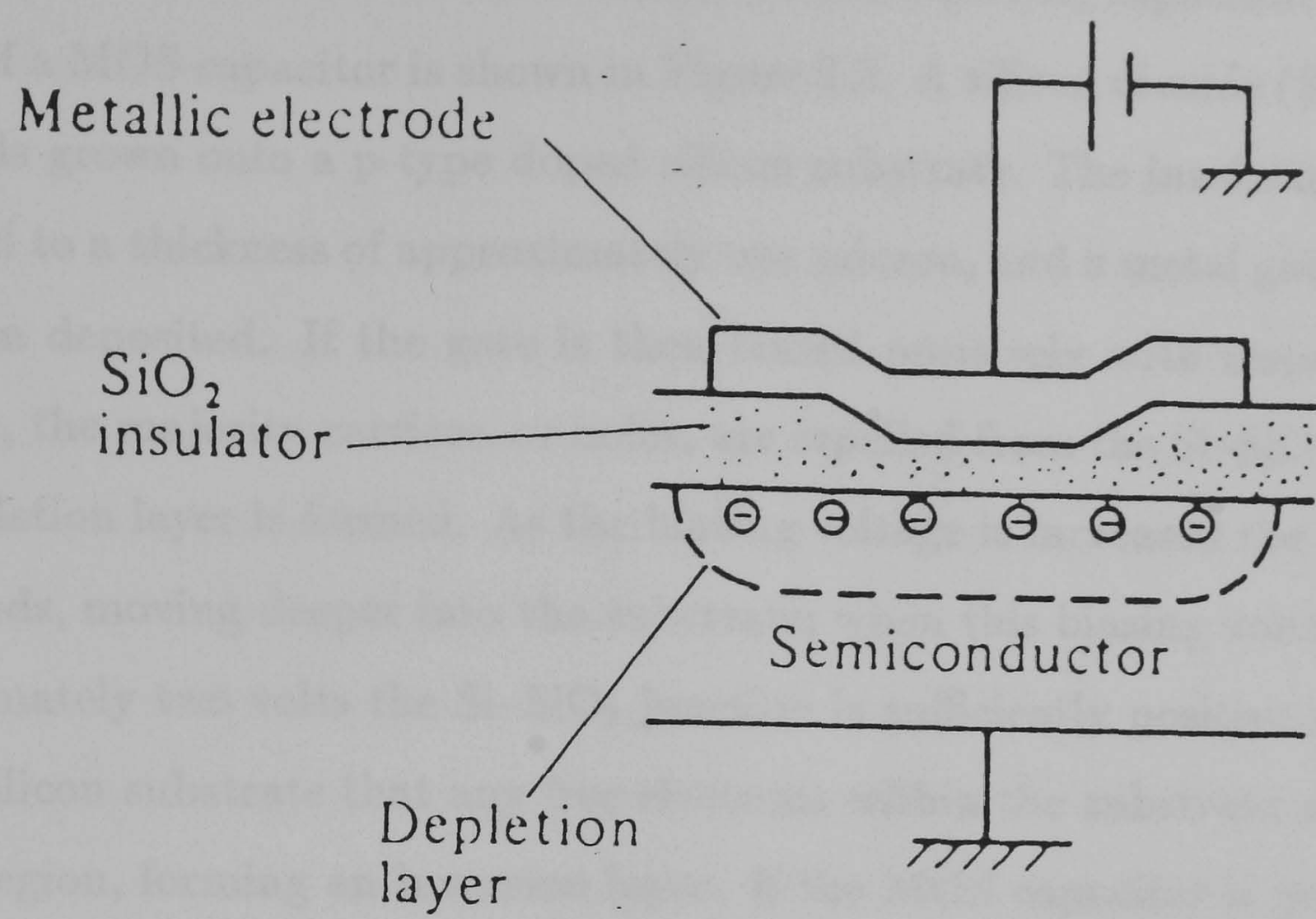

Figure 2.3: A schematic diagram of a MOS capacitor. MOS capacitors form the electrodes which store the electrons created by photon bombardment of the CCD surface.

The extreme sensitivity, and the linear response of imaging CCDs have made their use in astronomical applications commonplace. CCDs have a number of advantages over conventional photometric detectors.They combine the area detecting, and high dynamic range properties of a photographic plate, with the linearity and sensitivity of photoelectric photometers. CCDs also have two great advantages over other, earlier electronic imaging detectors, such as the silicon vidicon camera; namely their much lower readout noise, and the stability of the CCD pixel array with respect to the operating parameters of the device.

2.5 The Principles of CCD Operation

The basic principles of operation of CCDs, and their application to astronomical photometry are outlined below; further information may be found in Eccles, Sim & Tritton (1983) and MacKay(1986).

Photons absorbed in silicon create hole–electron pairs. In native silicon these quickly recombine, however in a CCD an electrode structure upon the silicon surface creates potential wells in the silicon which collect these electrons. The CCD

can be considered as a rectilinear array of picture elements, or "pixels", each of which is in effect a Metal Oxide Semiconductor (MOS) capacitor. The construction of a MOS capacitor is shown in Figure 2.3. A silicon dioxide (SiO_2) insulating layer is grown onto a p-type doped silicon substrate. The insulating layer is then etched to a thickness of approximately one micron, and a metal gate, or electrode, is then deposited. If the gate is then biased positively with respect to the substrate, the majority carriers, or holes, are repelled from the Si–SiO_2 junction, and a depletion layer is formed. As the biasing voltage is increased the depletion layer expands, moving deeper into the substrate; when this biasing voltage exceeds approximately two volts the Si–SiO_2 junction is sufficiently positive with respect to the Silicon substrate that any free electrons within the substrate are attracted to this region, forming an inversion layer. If the MOS capacitor is not cooled, thermally produced electrons will rapidly flow into the junction. However, in a cooled device, the number of thermally produced electrons will generally be negligible, and an inversion layer will not form unless free electrons are generated by photon bombardment. The depletion layer can thus be thought of as a potential well, in which charge, formed by the photoelectric emission of electrons, can be stored and later retrieved. To enable the stored charge to be thus retrieved, it is necessary in a practical device to transfer charge from pixel to pixel, and eventually to an output stage, where the charge is amplified and then recorded on some suitable medium.

The commonest mechanism for the movement of stored charge in CCDs is three-phase charge transfer. In this system, each imaging pixel is actually comprised of three electrodes, the centre electrode being held at a higher potential than the outer two, thus collecting any free electrons created in that region of the substrate. This stored charge may be transferred to a neighbouring electrode if the potential applied to this electrode is raised, whilst simultaneously lowering that applied to the first. This may be repeated to transfer the stored "charge packets" over many pixels. This is essentially a parallel process, each row of imaging pixels being moved concurrently one pixel in the chosen direction. In the CCD readout procedure the contents of each row of imaging pixels are repeatedly transferred, until they reach the output stage at the edge of the chip's frame storage area. Each row of pixel values is transferred to the output register, which is in essence a one dimensional CCD structure with a charge-sensing output amplifier at one

end. Each row of pixel values is read out by charge transfer, in an exactly similar fashion to transfer in the 2–D frame store. This now comprises a serial data stream which, after on-chip amplification, is passed to an analogue to digital converter and via a controller to digital storage medium, such as computer tape or disk.

The charge sensing amplifiers at the output stages of buried channel CCDs (see below) are extremely sensitive and linear devices with very good noise characteristics. Unfortunately though, the amplification process is a major contributor to the uncertainties in the strength of the photon-generated signal at low light levels. The extent of signal degradation due to the readout process is referred to as the readout noise of the instrument, and may be expressed as an equivalent root mean square electron signal. Readout noise is caused by the effects inherent in any electronic system, such as Johnson and shot noise in the sensing and amplification circuitry.

In any real device the architecture is complex, and many additional refinements are necessary if a device is to be used for astronomical low light level imaging and photometry. The simple device, described above, is termed a surface channel CCD, because the charge storage and transfer processes occur in close contact with the Si–SiO_2 interface. This architecture can severely limit the efficiency of the charge transfer process. Because of irregularities in the pixel lattice, the charge transfer efficiency (CTE) may be degraded to such an extent that image "smearing" effectively renders the device useless for quantitative imaging applications. The output signal of such devices is further degraded by the injection of spurious charge into the "signal packets" by surface defects. These problems can be virtually eliminated by adopting a different device configuration, in which the charge is stored and transferred within the silicon substrate; such devices are called buried channel CCDs.

Buried channel devices are made by growing an n-doped layer of silicon onto the p-doped substrate, prior to application of the insulating layer and polysilicon electrodes. The potential profile created, upon application of voltage to the electrode structure, is such that the stored charge is attracted to the interface between the p and n-type silicon; it is within this region of the chip that storage and transfer of charge occurs. Because of the greatly increased charge transfer efficiently of this configuration, buried-channel devices are preferred in low light-level imaging applications.

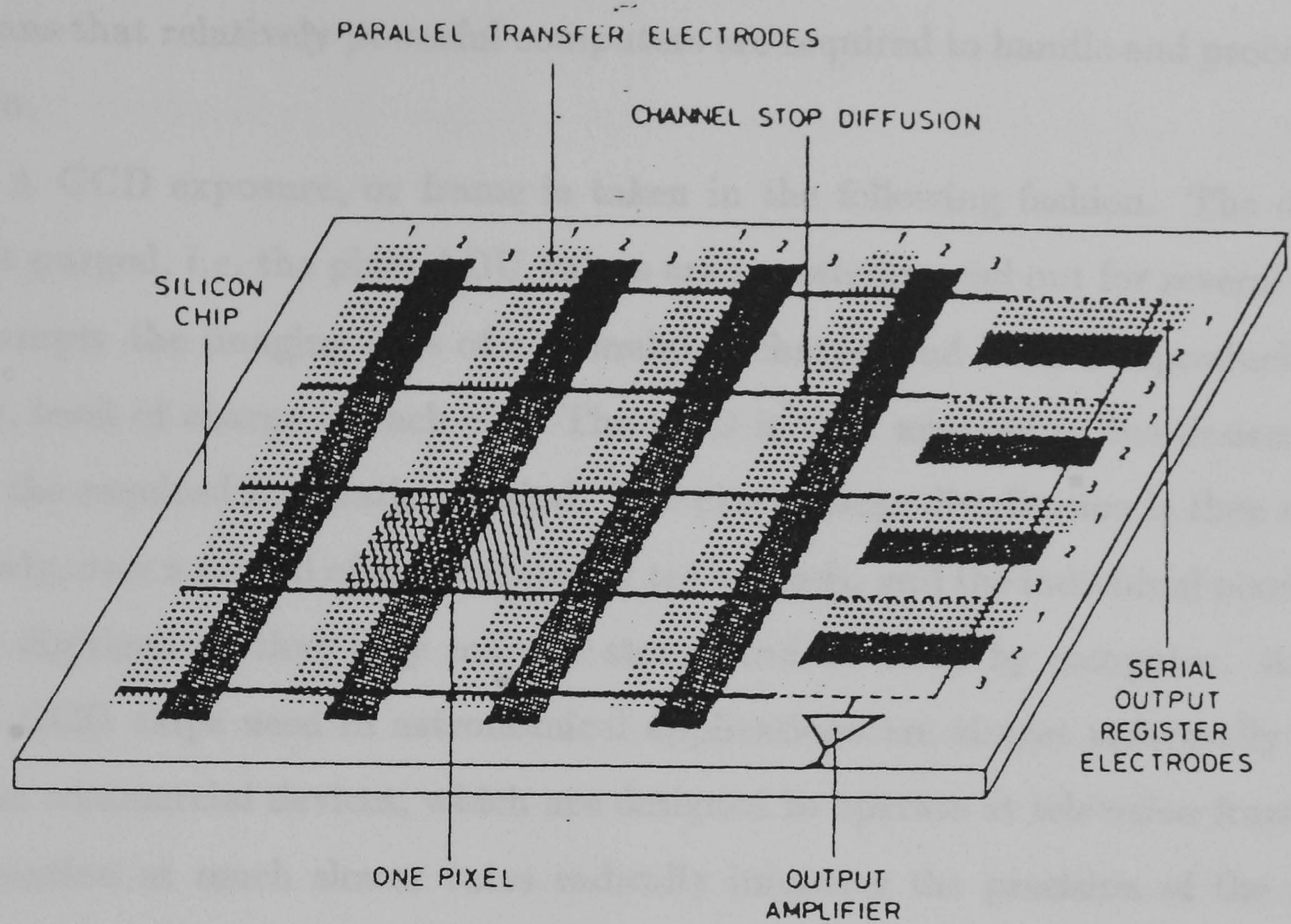

Figure 2.4: A schematic diagram of a three-phase CCD. The sequence 1, 2, 3 on each set of electrodes illustrates the normal direction of charge transfer. Taken from Mackay (1986).

Many other refinements are incorporated into practical CCD detectors, geared towards such ends as improving inter-pixel charge transfer efficiency, increasing the quantum efficiency of the instrument, and reducing the readout noise of the system. Figure 2.4 shows a schematic diagram of the architecture of CCD chip, and illustrates some of the terms used in the text (taken from Mackay, 1986).

2.6 Making and processing CCD exposures

Whilst sharing the virtues of extreme sensitivity and linearity with the more conventional technique of photoelectric photometry, the aquisition, reduction, and analysis of CCD data is almost immeasurably more laborious. Though the technical innovation of the CCD is in itself admirable, it must be noted that it is only complementary advances, in the power and versatility of digital computers, which permit the pragmatic application of the CCD to astronomical photometry. The

size of pixel arrays in the current generation of CCDs (up to about 10^5 elements) means that relatively powerful computers are required to handle and process these data.

A CCD exposure, or frame is taken in the following fashion. The device is first purged, *i.e.* the pixel ADU values are repeatedly read out for several seconds to empty the imaging cells of accumulated charge, and leave a reproducible, but low, level of charge in each cell. The CCD is then exposed to the desired object for the required integration period. The pixel charge distribution is then read out slowly, over a period of approximately ten seconds, and the individual pixel signals are digitized so that they may be stored and accessed by computer. Although the CCD chips used in astronomical applications are almost universally derived from commercial devices, which are designed to operate at television frame rates, operation at much slower rates radically improves the precision of the readout process, and substantially reduces the readout noise levels.

Generally, CCD controllers are versatile enough to allow the data to be read out in a number of image formats. Certain areas of the chip may be selected for readout, with the consequent increase in speed over the readout of the whole imaging area. This is useful in applications where repeated observations of a single object, over short timescales, is required. Alternatively, during the readout process adjacent rows, and/or columns of pixel values may be co-added, a process known as "binning". Rows of data are added together by reading multiple rows into the serial output register in between every complete readout cycle of the register. Similarly, columns are added by reading multiple charge packets from the serial output register into the readout amplifier. Thus the image size may be reduced, and the signal to noise ratio (if this is limited by photon counting statistics) increased, albeit at the expense of device resolution. This technique is often of use where the seeing is of such poor quality that the debasement of the image's spatial information content is not significant.

2.6.1 Biasing

The on-chip charge-sensing amplifier effectively measures the voltage across a capacitor at the output stage, given by $V = Q/C$, where Q is the charge stored in the capacitor, and C the capacitance of the device. In between each transfer

from the output register a constant voltage is applied to the capacitor, this is, in effect, a constant reset to ensure calibration of the readout process. Thus, the voltage measured at this stage is subject to a constant offset, or bias. To obtain an estimate of this bias level it is necessary to examine the ADU count output when a zero signal level is read out. This can be done in two ways; reading out the CCD immediately after purging the chip of all stored charge, or clocking out the serial output register with a larger number of transfer pulses than there are constituent pixels in the register (and hence, larger than the number of pixels per row in the CCD frame). The former results in a "bias frame", which may be subtracted from CCD image frames to remove the bias signal. The latter process, known as "overscanning", will produce a CCD image with a strip of "zero signal area" at the side. The readout procedure is normally configured such that the overscan strip is some 40–60 pixels wide, giving a large number of pixels from which to determine the average bias ADU count. This charge level can subsequently be subtracted from the image. Overscanning is also a simple way of fully clearing charge from the output register, and indeed the frame cleansing between exposures is achieved by substantial numbers of vertical overscan cycles. These, however, are purely a cleansing operation, and are not recorded.

In practice, it is sometimes advisable to employ elements of both techniques if the highest accuracy is to be obtained. Due to deficiencies in the hardware configuration, the bias voltage may not be exactly constant for every readout transfer cycle; bias frames may be used to determine whether this is the case, and to correct the image data if necessary. In most devices this is not a significant problem, but should be examined nonetheless. The bias voltage is also susceptible to changes in the operating parameters of the device, most notably the temperature, and so overscan regions can be used to monitor, and compensate for, any overall change in bias voltage during the observing session. Both techniques provide an estimate of another very important quantity, the readout noise of the chip. Assuming the bias to be constant over the chip, the rms deviation of ADU count in a bias frame is a good estimate of the readout noise of the device.

2.6.2 Dark Current

For all but the very shortest exposures, thermally generated electrons would saturate the imaging cells of a CCD operated at room temperature; this temperature dependent effect is referred to as dark current. Many astronomical applications require observations of extremely faint objects to be made. To attain satisfactory signal to noise ratios, such observations may necessitate integration periods of several hours; therefore it is necessary to to cool the CCD to eliminate the build-up of thermally generated electrons. The seriousness of the problem is critically dependent upon the construction of the chip; in carefully configured buried-channel devices the problematical generation of charge at the Si–SiO_2 interface can be effectively eliminated. Dark current generation within the bulk substrate cannot be eliminated in this way, and follows the relation (Mackay, 1986), $I = A\exp(-B/kT)$, where A and B are constants, k is Boltzmann's constant, and T is the operating temperature of the device. Because of this exponential dependence with operating temperature, cooling the device will result in a critical reduction of dark current; this very fact also means that the operating temperature must be stabilised—at typical CCD operating temperatures ($\sim 150\,\mathrm{K}$), the dark current approximately doubles for every $10\,\mathrm{K}$ rise in temperature.

Even though alleviated by cooling, dark current would significantly affect the photometric quality of the CCD image, if it was not possible to reliably subtract the dark current contribution. This is achieved by making "dark exposures", *i.e.* allowing the thermally generated charge to accumulate in the CCD, over a measured period, and reading out the resulting image to determine the rate of deposition of charge in each pixel. During this process, no light is allowed to fall upon the chip. The accumulation of dark current varies from pixel to pixel in a distinctly non-uniform fashion, and "hot" pixels can accumulate charge at such a high rate that they form large noise spikes in the output image. Providing that the dark current charge-deposition in a particular pixel does not saturate its charge storage capacity, the contribution to total output signal may still be effectively removed by subtraction of a suitably scaled dark frame.

In order to differentiate between thermal noise spikes, and those caused by cosmic ray secondary particles, another mechanism for the unwanted deposition of charge, which is discussed more fully below, it is necessary to repeat dark current

exposures. To provide a statistically meaningful estimate of the dark current such exposures should be of several hours duration, and wherever possible, should be carried out during daylight hours, in order that they do not detract from the observing program.

2.6.3 Charge Transfer Efficiency

As is to be expected, the process of transferring charge from one pixel to another, although extremely efficient, is not 100% effective. A typical CCD may have a charge transfer efficiency of up to 99.998% for each inter-pixel transfer. Hence, in the worst case, where of the order of 1000 such transfers have been applied to a single charge packet, some two percent of the pixel's ADU count may be effectively smeared into adjacent pixels. Generally, in astronomical applications, the effect is only noticeable for very bright images. Low charge transfer efficiency can, however, be a significant problem in some devices, particularly in the sense that certain columns transfer charge much less reliably than others; careful choice of device is important in this respect. Certain devices have a charge threshold, below which the charge transfer from cell to cell is inefficient; in such cases it is necessary to ensure that each imaging cell has accumulated a charge greater than this threshold before the exposure commences. This is particularly crucial for shorter exposures, where the accumulation of charge from the sky background may be small. Devices which suffer from this problem, such as the RCA SID 53612, must be "preflashed", that is, exposed to a uniform, low level of illumination prior to each exposure, ensuring that this charge threshold is surpassed. The charge level deposited by the preflash is sometimes referred to as a "fat zero". Preflashing is normally carried out by illumination for a fixed period by Light Emitting Diodes (LEDs). This process must be readily reproducible, consistently producing a similar charge distribution so that its effect can be reliably subtracted from the output image.

2.6.4 Pixel to Pixel Non-Uniformity

The correction for variation in pixel sensitivity is known as flat fielding, and is ostensibly an easy correction to apply to the raw CCD data. Unfortunately it is a process which involves hidden subtleties, and should be undertaken fastidiously, to

ensure that the precision potentially attainable from CCD photometry is actually achieved.

The CCD is exposed to a diffuse, uniform source of illumination, such as the twilight sky, or a plain, evenly illuminated surface. This exposure is then read out in the same way as a data exposure, and in effect forms a map of the variations in pixel sensitivity. Several of these flat field exposures are averaged, and then normalised to a value of unity, *i.e.* this summed frame is divided by the average pixel value of the data. Data frames can now be divided, pixel by pixel, by the flat field frame to compensate for the pixel sensitivity variations. It must be noted that this not only takes into account the variations due to inhomogeneity in chip response, but also corrects for variations in illumination across the CCD due to the optical performance of the telescope. In photometric applications, it is necessary to take exposures of stars through different filter combinations, such as the Johnson UBV passbands. Each filter combination represents a different optical configuration of the instrument, requiring a different flat field frame. This type of frame arithmetic technique works particularly well for the CCD because of its excellent linearity and pixel stability.

In general, the non-uniform response of the device, on a pixel to pixel level, is caused by defects inherent in the structure of the chip. These fall broadly into two categories; those defects which cause simple, linear modulation of the device sensitivity, and those which exhibit a non-linear response. The former defect can be corrected for by calibrating the CCD response as described above, the latter, discussed in Section 2.6.5, is practically impossible to compensate for, but can be reliably identified by comparing the ratios of flat field exposures taken at different signal levels. Linear non-uniformities in response are generally the result of the differing charge collection area of the device's constituent pixels, although front-illuminated chips may exhibit a modulation of response caused by irregularities within the electrode structure.

In practice, problems arise in trying to obtain flat field images suitable for the calibration of CCD data. The principal problem is that the variations in pixel response are significantly dependent upon the spectral distribution of illumination from the source. It is often possible, with narrow band filter systems, to ensure that the colour of the calibration source adequately matches that of the night sky and observed sources—although in this case the problem of signal modulation due

to optical interference effects may become significant (see below).

In the case of broadband imaging, it is difficult to contrive a truly representative flat-field exposure. The observed source emission is essentially due to the shape of the stellar continuum, and the night-sky emission. Night sky emission is itself composed of scattered starlight, and monochromatic molecular emission lines. At very faint signal levels, the sky component will dominate, and a flat field exposure of the night sky, uncontaminated with stellar images, will suffice. If however the light from astronomical objects dominates the spectral composition of the measured flux then such flat fields are obviously inapplicable. Furthermore, the colours of objects measured upon a single CCD frame may vary considerably, compounding even further the problem of matching the colour of the flat field exposure to the observations. In practice, a compromise is attempted, and it is usual to expose the chip to some evenly illuminated source, such as the twilight sky or the dome interior illuminated by a tungsten lamp.

For high grade astronomical CCDs, the variation in response between pixels is normally in the range 1–5%, and with careful flat fielding it is possible to reduce this to the order of 0.2% (Walker, 1984). At this level, the uncertainty due to residual flat fielding errors represents a significant limiting factor in the ultimate photometric precision attainable with current CCD detectors. As Mackay (1986) notes, it is important not to confuse the repeatability of CCD observations of a single object, which may be at the level of a millimagnitude, with the true uncertainty in any derived magnitude which may be dependent more upon residual flat fielding errors than any other identifiable cause.

2.6.5 Discrete Pixel Defects

These defects are often much more difficult to correct, and often the correction to the data is merely cosmetic, to enhance the appearance of the final image. Certain pixels are found to accumulate thermal charge at a high rate despite device cooling. If this accumulation is not too great, the effect can be corrected for by subtracting a suitably scaled "dark current" frame (see above). For those pixels which accumulate thermal electrons very rapidly indeed, and which soon saturate *i.e.* overfill the pixel's potential well with charge, the only recourse is to remove that particular pixel data value, and replace it with the value interpolated

from its nearest neighbours. Rather more difficult to deal with are pixels with greatly reduced detection and transfer efficiencies. If the transfer efficiency of a pixel is low, it will, during the readout process, severely degrade the charge packets passing through it, with the result that a spurious line will show up on the image along the column in which the "bad" pixel was located. Once again, interpolation from columns of pixels on either side of the spurious line can be employed, but this type of defect generally invalidates photometric data from surrounding areas of the chip.

2.6.6 Cosmic Ray Events

On CCD exposures of greater than a few minutes duration, random single, or few-pixel, events appear, similar to the thermal noise spikes seen in some devices. These are caused by cosmic ray secondary particles, and by low level natural radioactivity. In general all such events tend to be categorised as "cosmic ray events".

On casual inspection these cosmic ray events may be mistaken for stellar images, but isolated events can be relatively easily distinguished as their profiles differ radically from those of genuine stars. When a cosmic ray event coincides with a stellar image on a CCD frame, it is extremely difficult to identify, and in long exposures, the large numbers of such events can cause serious problems.

The rate at which these events occur can be reduced by physically thinning the chip, which has several other advantages. Principally, this allows the chip to be back illuminated, reducing the problem of spatial interference from the CCD electrode structure inherent in front illuminated chips, and improving the blue wavelength response of the chip. These significant advantages are gained at the expense of drastically reducing the mechanical rigidity of the device, which means that the utmost care is required throughout the manufacture, and operation of the CCD.

The CCDs in both the SAAO/UCL and AAT/RGO cameras, from which data for this thesis were obtained, are thinned, back illuminated RCA 53612 devices. The cosmic ray event rate in the CCD frames from these cameras is small, of the order of 1–3 events/minute, over the whole chip, causing only minor problems in the case of even the longest exposures used.

2.6.7 Fringing

Some CCD exposures exhibit alternate light and dark fringes across the whole of the frame, arising from optical interference within the layered polysilicon structure of the chip. If the interference fringes are caused by emission from the night sky, such as the particularly strong 5577 Å oxygen line (Driscoll and Vaughan, 1978), or are due to observing through a narrow band filter system, such as the Strömgren system, it is relatively easy to determine the spatial distribution of the fringes. This can be done by making an exposure of an area of night sky which contains very few stars, down to the detection limit of the CCD. Any stellar images on this "fringe frame" are removed by interpolation over the affected areas, and it can now be suitably scaled and subtracted from the image frame to remove the image degradation caused by the fringes. If, however, the fringing is caused by astrophysical line emission from an object in the CCD frame, such techniques cannot be employed. As this was not the case in any of the CCD exposures used in this thesis, it was relatively straightforward to remove the fringing contribution by simple frame subtraction techniques.

2.6.8 Other Image Defects

Isolated defects, such as pixels which, because of manufacturing faults, have very high charge transfer thresholds or low transfer efficiency, may appear in the final image as spurious light or dark pixels, groups of pixels, or even whole columns of pixels. Such problems are difficult to overcome, and may be remedied only in a cosmetic sense by interpolating from the values of adjacent pixels.

The charge capacity of each pixel is finite, and exceptionally bright stars will "saturate" regions of the detector—the maximum signal which can be stored in a single pixel varies from device to device, but is generally of the order of a few hundred thousand electrons. Where a bright star has saturated the detector, there is a tendency for further charge to "spill" over the inter-pixel channel-stops, and run along the column containing the saturated pixel. Under such circumstances, the linear regime of detector performance will have been long surpassed, and data from the bright star already invalidated. Furthermore, long trails of charge "leakage" from such sites can invalidate data from large areas of the chip. Most CCD systems will require many complete readout cycles to return the pixel bias

level to normal after the device has become saturated. Prior to saturation, the build-up of large numbers of electrons in a single pixel can radically effect the local potential distribution, which in turn can effect the efficiency of the pixel charge-capture process; the strictly linear relationship between incident light flux and stored charge is not preserved under these conditions, and the data from the pixels concerned are not suitable for photometric purposes.

CCDs are notoriously prone to the problems of electrical noise pickup, and are often temperamental with respect to their operating conditions—effects which can seriously degrade the quality of CCD images, and for which the observer should be vigilant.

2.6.9 Detector Characteristics

When quantifying the characteristics of a CCD as an astronomical detector, there are essentially four important factors; pixel size, quantum efficiency, pixel saturation signal and readout noise. To these can be added the cosmic ray event rate, which may place an upper limit on exposure times. The quantum efficiency (QE) of a CCD detector is strongly wavelength dependent, and can be as high as 70% in the case of some thinned, back illuminated devices. A more useful measure of the efficiency of an astronomical detector is the detective quantum efficiency (DQE) given by,

$$\mathrm{DQE} = \frac{(S/N)^2_{out}}{(S/N)^2_{in}},$$

where $(S/N)_{in}$ and $(S/N)_{out}$ are the signal to noise ratios of the input signal and the output from the detector respectively. Thus, DQE describes the degradation of signal to noise, caused by passage through the detector. For low light level operation, such as the photometry of faint stars, the device readout noise is a critical factor, considerably reducing the DQE. For example, in the case of the RCA detectors used in the observations in this thesis, which have readout noise levels of up to $70e^-$/pixel, the DQE for a star which deposits some 10 000 electrons over an area of 8 pixels is as low as 10%, mainly because of the effects of readout noise. Additionally the uncertainties are increased if a preflash is necessary to overcome charge transfer inefficiency. As mentioned above, long exposures can be severely degraded by cosmic ray events, and a compromise must be reached between exposure time, and the number of such events. Whilst impairment of

the performance of CCD systems caused by readout noise is an important factor, often the limiting accuracy for broad-band observations of brighter stars is set by residual flat fielding errors. Thus flat field exposures, at good signal to noise levels, should be repeated regularly during an observing run in order to obtain reliable calibration frames. Similar care should be exercised in the choice of irradiance for flat field exposures, although matching to both the stellar spectra and the night-sky is an intractable problem.

2.6.10 A Coherent Strategy for CCD Observations

The imaging area of CCD detectors is relatively small (of the order of 10 square arcminutes, compared with a photographic plate which may be many hundreds of square arcminutes). Because of this, and the form of cluster luminosity functions, it is necessary to take exposures at small radial distances from the cluster core, in order to populate the brighter regions of the colour-magnitude diagram. In order to delineate the SGB and RGB regions of their colour-magnitude diagram of 47 Tuc, Hesser *et al.* (1987) have even obtained observations at a distance of less than $5r_c$ from the cluster centre, where r_c is the King (1966) core radius, although stellar crowding, and poor seeing caused some loss of accuracy in this study. However, exposures at much greater radial distances, where the crowding is much less severe, are required in order to provide deep main-sequence photometry. In order that the zeropoints of the adopted magnitude scales can be transferred reliably from the outer field to the inner field, it is common practice to make a "strip" of overlapping exposures between the inner and outer fields. Magnitude estimate of stars in the overlap region of adjacent frames can then be compared, and the magnitude scales adjusted, such that a consistent scale is established along the strip. Each "transfer" from one frame to another incurs a small uncertainty, of the order of $0\overset{m}{.}005$, and therefore must be undertaken with care. This process allows the crowded inner fields, where aperture photometry is not feasible, to be tied to the magnitude system defined by the standard star observations; aperture photometry zeropoint-transfers are made to the outer, less crowded fields, and comparison of overlapping areas used to extend the transfer inward. Aperture photometry is not suitable for use in crowded regions, nor are profile-fitting techniques applicable to making zeropoint transfers (these points are discussed

in more detail in Section 2.7.2 below). This procedure has been adopted for the observations of ω Centauri presented in this thesis. Although intensive in terms of observing time, it is also desirable to make as many repeated measurements of each chosen field as possible. It is also beneficial to average the results from many such exposures, to discriminate against the effects of cosmic-ray events, and reduce uncertainties due to readout and photon shot noise. The linearity of CCD detectors also allows multiple exposures of fields to be added together, in order to extend the photometric limits to fainter magnitudes, and improve the signal to noise ratio in stellar images.

If there are not a substantial number (> 5) of reliable secondary standards, for example those set up by earlier photoelectric photometry, in the observed fields, it is necessary to transfer the magnitude scale zeropoints to the programme observations from observations of standard stars in different parts of the sky. In any case, standard star observations should be made in order to determine the nightly extinction coefficients. If it is necessary to fully determine the colour transformation equations of the system, standard star observations should be made of stars with a broad range in colour. In general, the procedures and practices adhered to when making standard star observations using CCD detectors are much the same as those adopted for photoelectric photometry (see, for example, Harris *et al.* 1981). Standard star observations should be interspersed with the program observations, in order that the photometric conditions can be monitored throughout the night. In those fields used primarily for faint (long exposure) observations, it may also be necessary to make observations with short exposure times, in order to ensure that the bright stars (with the highest signal to noise ratios) within the frame are not saturated, and can be used in the transfer of photometric zeropoints.

2.7 CCD Photometric Reductions

The purpose of the analysis of photometric data is to extract, as accurately as possible, the "signal", or stellar image, from the "background" of sky counts, unresolved stars, CCD readout noise, and other spurious sources of noise such as cosmic ray events. There are two basic strategies available to the astronomer.

- Digital aperture photometry.

- Profile-fitting photometry.

2.7.1 Digital Aperture Photometry

This is a direct analogue of conventional aperture photometry, as employed with photoelectric detectors. In this method, the "star flux"—*i.e.* the ADU count—is summed within a chosen radius of the star's centre, and a "sky level", or background ADU count, is obtained from a nearby region of the CCD frame which contains no obvious stellar images. The background level is simply subtracted from the star's ADU count to provide the best estimate of the signal due to the star. However, this method is considerably more versatile than conventional "on telescope" star-sky aperture photometry techniques. Because the image can be digitally processed, and manipulated interactively, it is possible to choose carefully the background region used, and thus minimise the chance of pollution by faint stars. The size, and position, of the apertures used can be varied to optimize the signal to noise ratio. Furthermore, many stars can be measured on one CCD frame, and thus the internal precision of these photometric measurements is extremely high—all stars on one frame are recorded under essentially identical observing conditions.

Ultimately, the limitations involved are, in most cases, the same as those encountered using conventional photoelectric photometry—scintillation variations, changes of sky transparency, photon shot noise, and faint star pollution of star or sky signal. In addition, there are the effects peculiar to the CCD, such as residual flat fielding problems, device readout noise, and cosmic ray events. These factors form a practical limit to the repeatability of observations upon a single star, on a single night, and can be set at a few thousandths of a magnitude (Walker, 1984). It must be stressed that this kind of internal accuracy is only possible if the flat field response of the CCD has been determined precisely, and if the utmost care has been taken when choosing the sky areas for comparison. In order to minimise the photon shot noise contribution to the overall uncertainty, it is desirable to have as large a signal as possible, however, the charge accumulated in each pixel must not reach the level at which the device characteristics become non-linear.

One of the critical factors involved when making aperture magnitude estimates is the choice of aperture size. Figure 2.5 shows the increase of measured flux, ex-

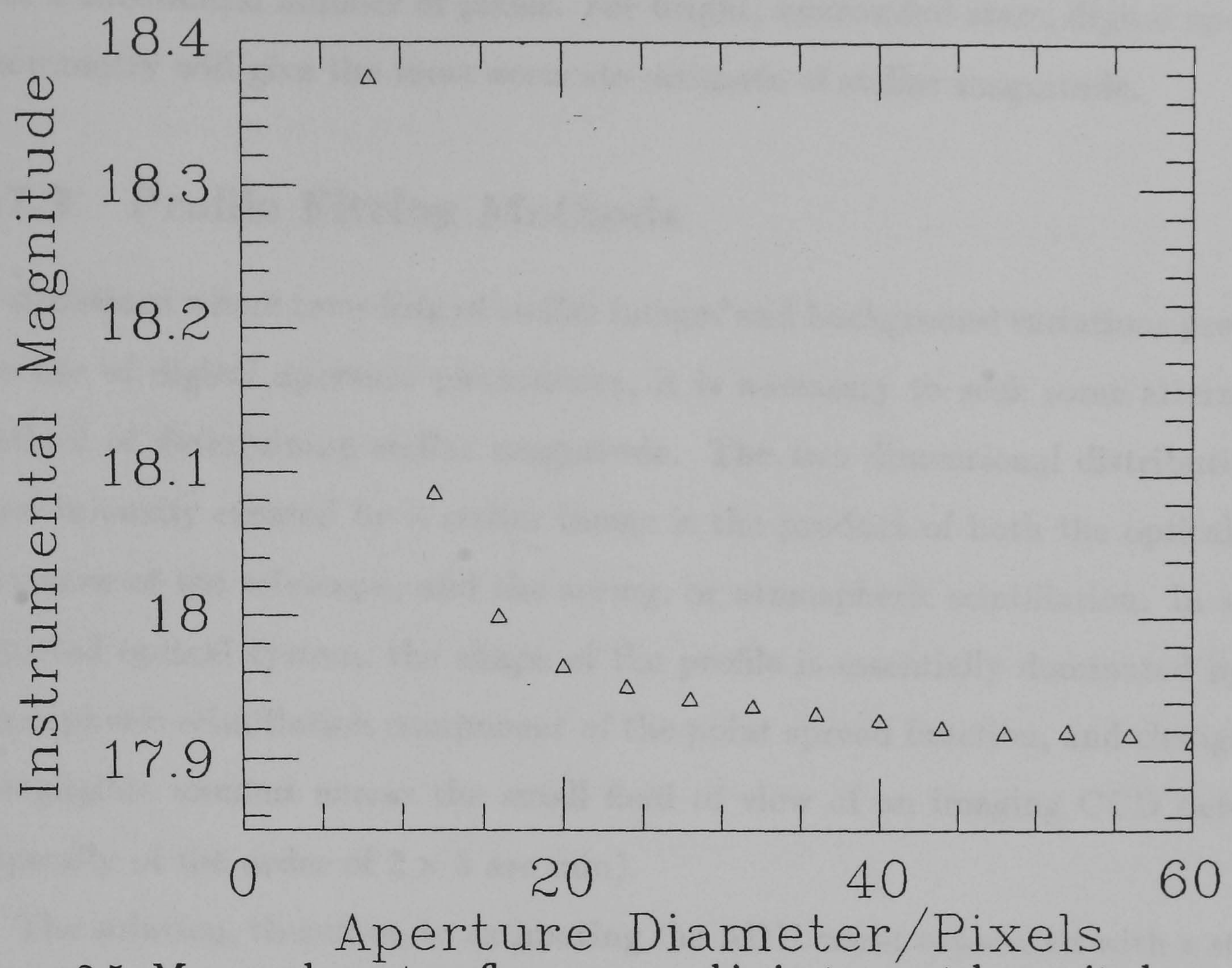

Figure 2.5: Measured aperture flux, expressed in instrumental magnitude, against aperture diameter, in pixels, for a single bright star E666.

pressed in instrumental magnitude, against aperture diameter, expressed in pixels, for a single bright E-region standard star. It can be seen that there is still considerable signal from the star at distances which are large in comparison to the seeing "width" of the stellar profile—some 4 pixels FWHM in this case. It is undesirable to use too large an aperture because of the increased readout noise contribution, the greater chances of contamination from faint stars, and because of the stress this places upon the large scale uniformity of the flat fielding process. Thus, in cases where aperture photometry was used to determine stellar magnitudes, an aperture diameter of approximately 10 seconds of arc was chosen, where other considerations, such as crowding, allowed. The aperture size was held constant for transfers within a particular data set, in order that a consistent instrumental magnitude scale could be established. As mentioned above, the ADU count in each pixel must not be allowed to reach the level at which the device characteristics become non-linear, *i.e.* such that the strict proportionality between ADU count and incident light intensity is no longer preserved. When making observa-

tions of bright stars, such as the many bright standard stars used in this study, it is often necessary to defocus the telescope, so that the stellar image is spread over a substantial number of pixels. For bright, uncrowded stars, digital aperture photometry will give the most accurate estimate of stellar magnitude.

2.7.2 Profile Fitting Methods

In situations where crowding of stellar images and background variations preclude the use of digital aperture photometry, it is necessary to seek some alternative method of determining stellar magnitude. The two dimensional distribution of pixel intensity created by a stellar image is the product of both the optical performance of the telescope, and the seeing, or atmospheric scintillation. In a well adjusted optical system, the shape of the profile is essentially dominated by the atmospheric scintillation component of the point spread function, and changes by a negligible amount across the small field of view of an imaging CCD detector (typically of the order of 2×3 arc min).

The solution, therefore, to estimating the ADU count associated with a stellar image is, to use a two dimensional function, analytic or numerical, which describes the stellar profile, to obtain the "best fit" to the data. The signal is determined from the "volume integral" under the data values representing the stellar image. With an adequate description of the stellar profile, the sky background can be determined simultaneously by the profile fitting procedure.

Initial experiments, using this technique on digitized electronographic data, made by Penny (1976) employed a simple two dimensional Gaussian function to model the profile, and used linear least-square fitting to the observed data to estimate stellar magnitudes. Work by Franz (1973) highlighted the systematic differences between such Gaussian functions and real stellar profiles—notably that the central peak and wide "wings", or periphery, of the Gaussian distribution are too intense in comparison to the observed stellar profile, when fitted according to the least squares criterion. Franz formulated an alternative distribution function in one dimension, which he showed to give a vastly improved fit to the profiles of visual double stars. Franz's analytic function can be generalised to two dimensions as,

$$H = \frac{1}{1 + d_1^{P_1(1+d_2)}} \tag{2.3}$$

Where,

$d_1 = ((x_1/r_{x_1})^2 + (y_1/r_{y_1})^2)^{1/2}$,

$d_2 = ((x_1/r_{x_2})^2 + (y_1/r_{y_2})^2)^{1/2}$,

$x_1 = (x - x_0)\cos\theta + (y - y_0)\sin\theta$ and

$y_1 = -(x - x_0)\sin\theta + (y - y_0)\cos\theta$.

Here the profile maximum height, $H(x_0, y_0)$ is normalised to unity. The parameters x_1, y_1, r_{x_1}, r_{y_1}, P and θ thus completely describe this profile. This profile shape, which is a Lorentzian function, was successfully used by Penny (1979) to fit profiles of double stars.

The major part of the crowded field photometric analysis in this thesis was performed using the LORENTZ software package, written by A.J.Penny (Penny and Dickens, 1986). This analysis software uses a slightly more sophisticated profile, modified to cater for the occasional presence of a (seeing dependent) wide "halo" in the observed stellar profiles, in a particular CCD frame. Evidence of this can be seen from the distribution of signal with radius as shown in Figure 2.5. Thus the full profile used in LORENTZ is given by,

$$H = \frac{1}{1 + d_1^{P_1(1+d_2)}} + Qe^{-d_3^{P_2}}. \tag{2.4}$$

Where d_1 and d_2 are as before,

$d_3 = \frac{[(x-x_0)^2+(y-y_0)^2]^{1/2}}{r_3}$.

Q is small, of the order ≈ 0.01, and

r_3 is large when compared to r_{x_1} and r_{y_1}.

Thus three additional parameters, not included in Equation 2.3, are required to describe the profile; P_2, r_3 and Q. This profile is then fitted to groups of up to eight stars simultaneously with a sloping linear background, such that the ADU count in a pixel of coordinates (x, y) is given by,

$$I(x, y) = \sum_{i=1}^{N} A_i H(x, y, x_{0_i}, y_{0_i}) + Bx + Cy + D.$$

where N is between 1 and 8, and A_i, x_{o_i}, y_{0_i} are respectively the heights and positions of the stars. Neighbouring stars are fitted simultaneously, if they are within a pre-specified radius of each other. This radius is again a function of the seeing width of the image profile, but can in most cases be set to about 7–10 arc seconds—in the case of most imaging CCD detectors, this would correspond to twenty or so pixels.

Because the size of a CCD pixel (typically $\sim 0.4''$) is comparable to the scale size of the stellar images, the problem of undersampling of the data becomes significant. The image data is composed of a grid of discrete pixel values, but the profile is a continuous analytic function. The non-linear nature of the profile, and the rapidly changing intensity from pixel to pixel, mean that a pixel ADU count is not representative of the "best fit" profile intensity at its centre. This problem is dealt with in LORENTZ by interpolating the fitting profile in a fine grid within each pixel, and requiring that the total "intensity", given by the values within this grid, is equal to the pixel ADU count. Although not a perfect solution to the problem of fitting a continuous function to such discrete data points, this process reduces the problem to negligible proportions compared to other sources of error, such as photon or readout noise.

The first step in the analysis of CCD data using LORENTZ is to determine the profile parameters for each individual CCD exposure. Initially, a number of bright, isolated stars are chosen interactively, at an image display, and all the parameters which describe the distribution are allowed to vary until a satisfactory fit is obtained. In crowded fields, it is often impossible to find isolated stars, with good signal to noise ratios, to estimate the profile parameters. Therefore, the program permits the user to mark a bright star, and its nearby companions, and fits them simultaneously. Similarly, where there are regions around the chosen stars which the user does not wish to be included in the profile fit, for instance if there were a significant cosmic ray event, a defect in the CCD chip, or some non-stellar feature, there is the option to ignore that area in the subsequent fit.

The process of determining the profile is iterative, in the sense that the residuals of the fit minus the profile are shown as both a two dimensional image, and as a one dimensional graph of mean image minus profile; thus if evidence of contamination by a faint companion star is shown by these displays, the area in question can be marked, and the process repeated until such problems are eliminated.

Figure 2.6 shows a typical small group of stars from a CCD exposure of a crowded globular cluster field. All preprocessing has been carried out as described above. It can be seen that the three central stars are sufficiently close to one another to make aperture photometry impossible. To illustrate the nature of the ADU count distribution in the CCD image, a hidden-line surface drawing of the central region of Figure 2.6 is shown in Figure 2.7. To measure the magni-

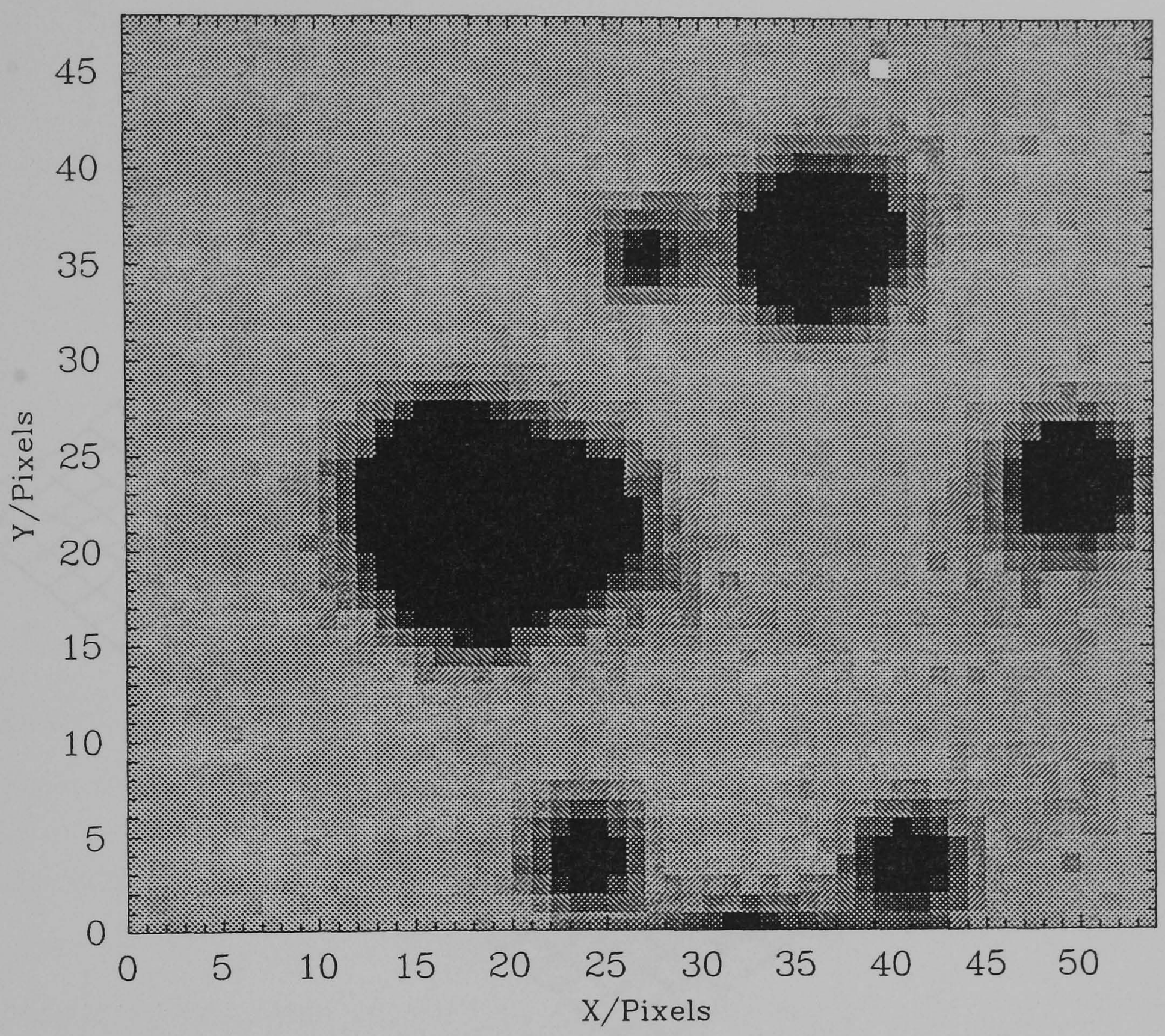

Figure 2.6: Typical crowded-field stellar images on a CCD exposure. A 64×64 area of a CCD exposure of a crowded field in the cluster ω Centauri. The central group consists of 3 bright, blended stars.

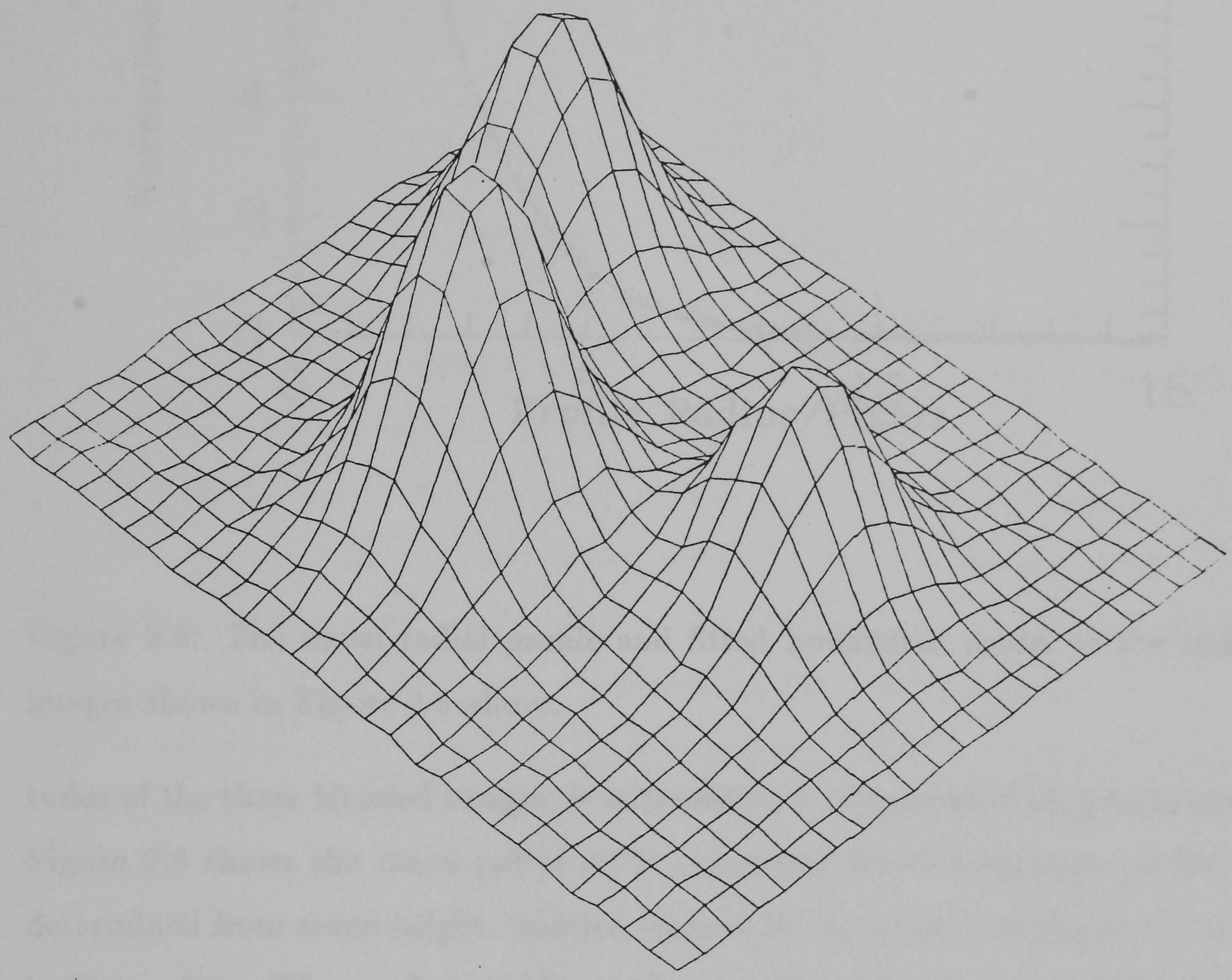

Figure 2.7: Hidden line surface drawing of CCD stellar images. The central part of the CCD data shown in Figure 2.6 is displayed as a hidden line drawing to illustrate the nature of the stellar images and the interference of neighbouring stellar images in crowded fields.

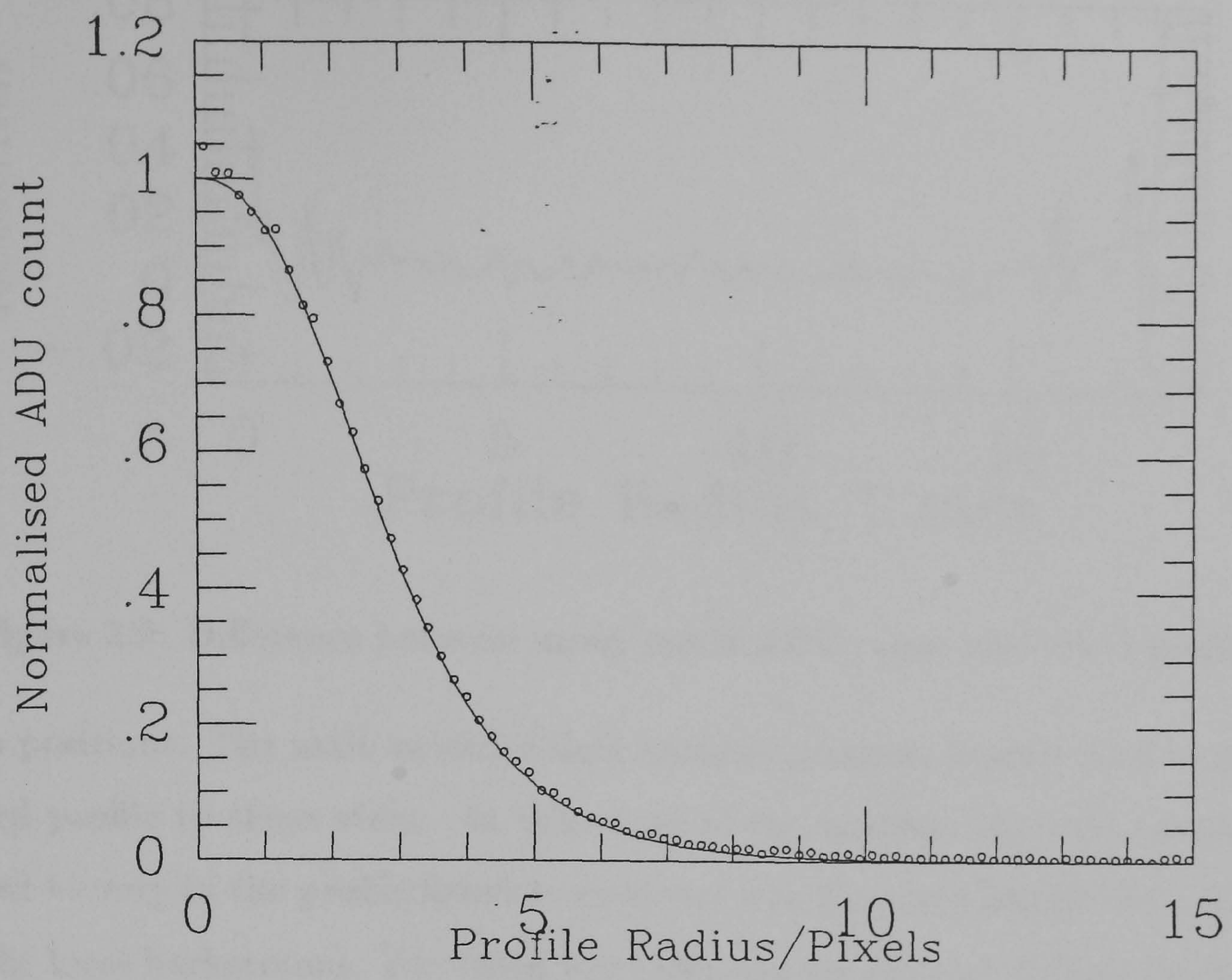

Figure 2.8: The mean radial profile and fitted Lorentzian model to the stellar images shown in Figure 2.6 above.

tudes of the three blended images, it is necessary to use profile-fitting techniques. Figure 2.8 shows the mean radial ADU count and fitted Lorentzian profile, as determined from seven bright, isolated stars in the same CCD frame as the stars in Figure 2.6. The goodness of fit can be seen from Figure 2.9 which shows the difference between the mean radial ADU count and fitted profile against radius. The profile shown graphically in Figure 2.8 has been used to simultaneously determine the "best fit" magnitudes of the central group of three stars shown in Figure 2.6. In order to check the accuracy of the chosen fits, and to ensure that there are no significant companion stars which were previously undetected, the fitted stellar profiles can be subtracted from the original data, and the resulting "cleaned" image examined. Figure 2.10 shows the same area of the CCD frame, after subtraction of the Lorentzian profiles which were fitted to the central three blended stars.

Thus the procedure followed when measuring the stars on a CCD frame is to identify by eye as many target stars as can be seen on the image, and record their

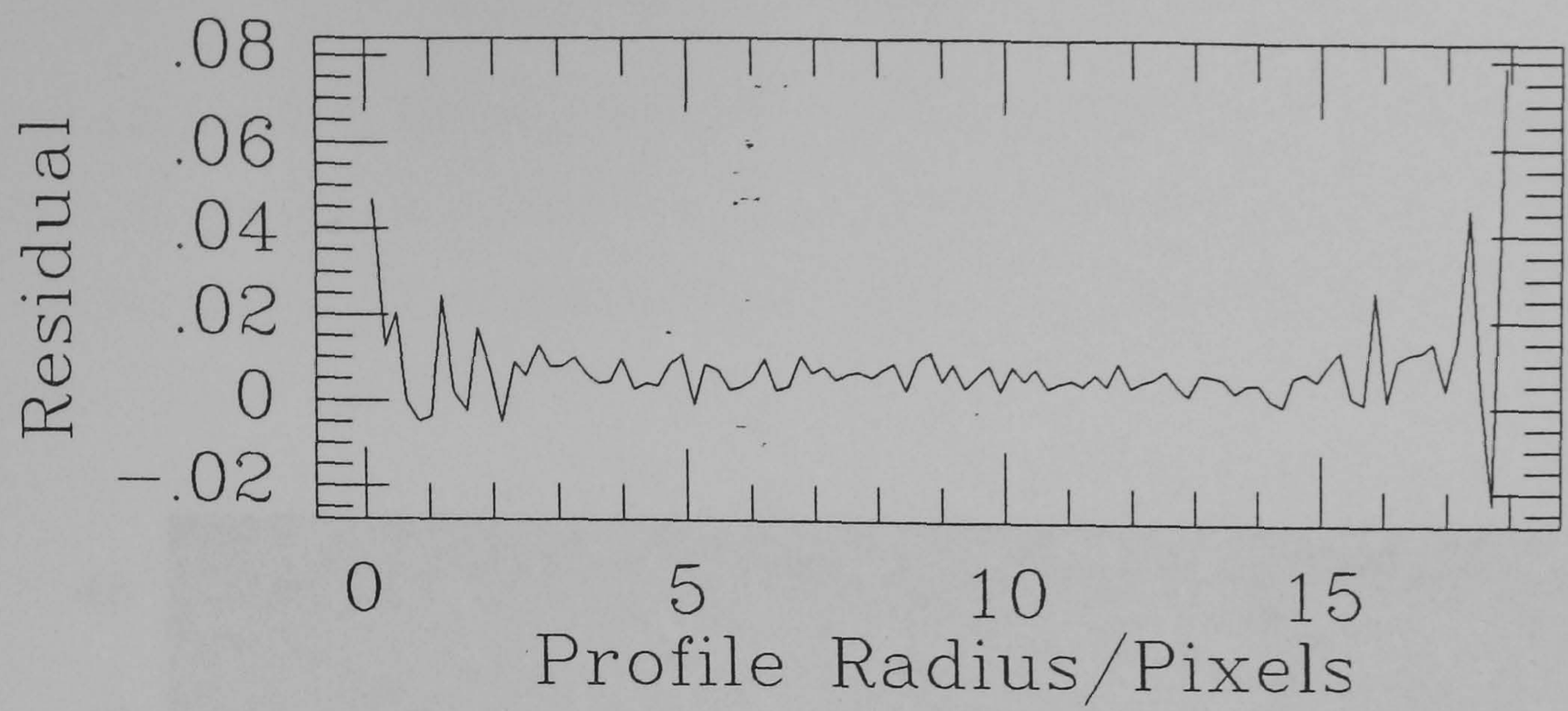

Figure 2.9: Difference between mean radial ADU count and fitted profile

rough positions. The main crowded-field analysis program is then used to fit the derived profile to these stars. At this stage of the analysis the only parameters allowed to vary in the profile fitted to each star are the star's height and position, and the local background. The fitted stars can now be subtracted from the image, as in Figure 2.10, and the resulting image can be inspected to find faint and crowded stars that were missed during the first run. The analysis program can then be run again on the original image, with the option to analyse only the new stars and those from the first run which would be affected by their inclusion. This whole cycle can be repeated until the cleaned image is devoid of measurable stars.

Despite the sophistication of the software available to determine the profile, it is difficult to attain analytic profile fits to the observed stellar profiles within tolerances $\sim 1\%$ of the peak intensity of the stellar profile. Thus, the magnitude scale derived from profile-fitting photometry for a particular frame may differ systematically from the mean instrumental magnitude scale of the particular CCD. This effect can cause a systematic difference between profile-fitting magnitude measurements of the same stars, on different CCD exposures, taken through the same filter combination. This is of no consequence if there are stars of known magnitude and colour within the CCD frame—secondary standard stars. In such a case a transformation can simply be made with reference to these stars. However, when the magnitude scale zeropoint must be transferred to a CCD frame, from observations made of standard stars outside of the CCD frame, random frame to frame errors can be incurred if the profile-fitted magnitude estimates are used. This problem has been discussed by Penny & Dickens (1986) and by McClure *et al.* (1986). A partial solution to the problem is to transfer the zeropoints using digital

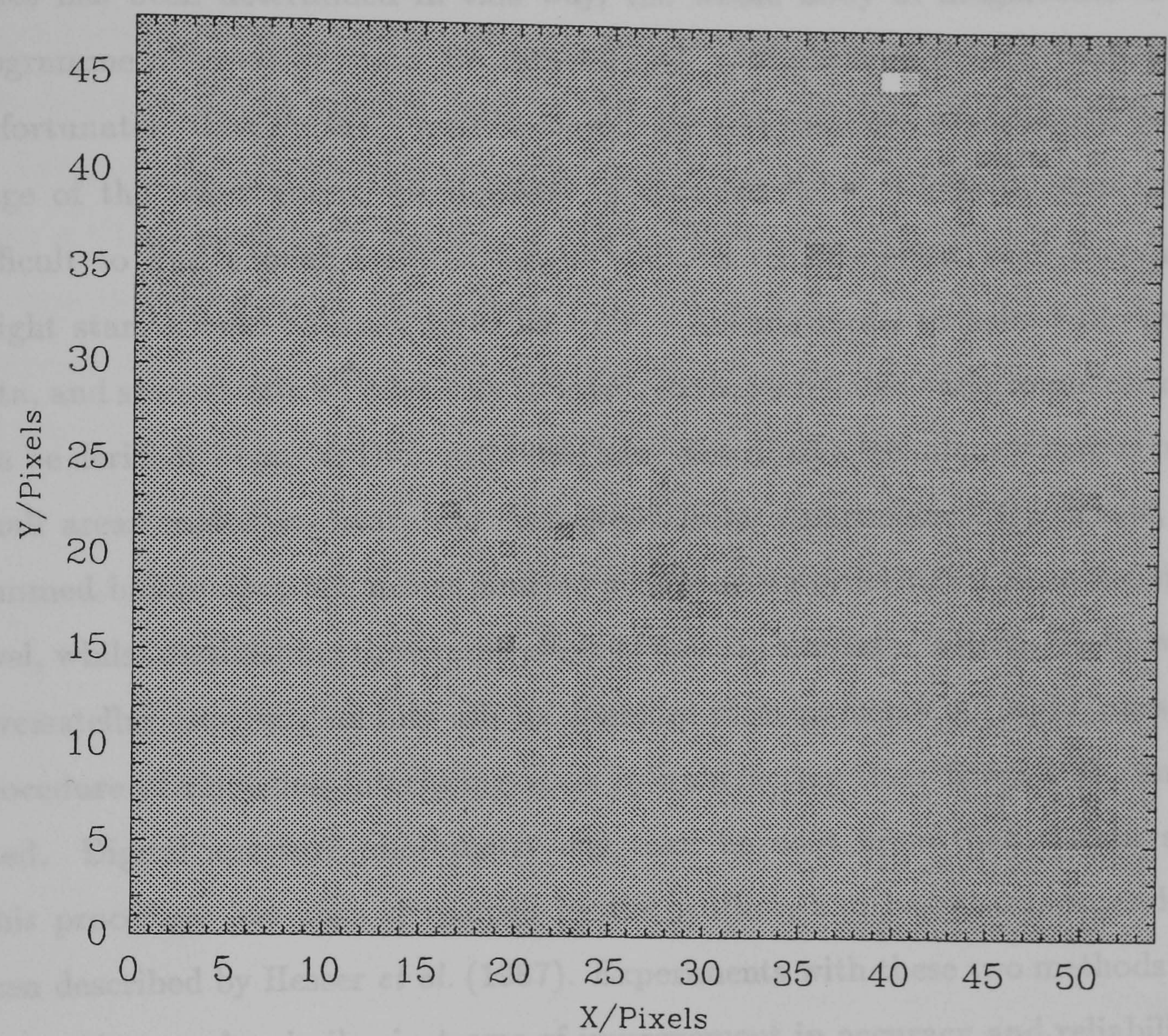

Figure 2.10: The sample CCD data shown in Figure 2.6, after subtraction of Lorentzian/Gaussian profile fits to the visible stars.

aperture photometry. The magnitude scale derived by profile-fitting photometry of standard stars may be transferred to the programme observations by making DAP measurements of bright, uncrowded stars which also have profile-fitted magnitude estimates. Once the difference between the DAP and profile-fitted magnitude scales has been determined in this way, the whole body of magnitudes in the programme observations may be transformed to the standard magnitude scale. Unfortunately though, there may be significant zeropoint error introduced at this stage of the observations, particularly in crowded fields, where it often proves difficult to find enough isolated bright stars to reliably effect such a transfer. Bright stars should be used, in order to increase the signal to noise ratio in the data, and stars should be relatively isolated, so that a reliable background estimate can be derived. Penny & Dickens (1986) have described a technique whereby many small areas containing stars are "removed" from a particular CCD frame, and summed before aperture measurements are made, in order to increase the signal level, whilst diminishing the overall effect of noise in the data. Alternatively, where severe stellar crowding unduly affects aperture measurements of bright stars, the procedure of removing interfering stars by subtracting their fitted PSF may be used. Digital aperture photometry can then be used upon these bright stars. This procedure has been developed by the Author, and has also independently been described by Hesser *et al.* (1987). Experiments with these two methods have shown them to be similar in terms of improvement in accuracy and reliability of measurement, the latter is, however, considerably less time consuming, and has been adopted in this study.

An alternative to fitting profiles which follow the form of a mathematical function, is to use an non-analytic point spread function (PSF) to model the observed distribution of ADU count. In this method, the profile used for fitting is an empirical model of the image distribution function, determined from bright isolated stars in the CCD image. Such methods have been employed by Hesser *et al.* (1987) and McClure *et al.*(1985, 1987a) who have used the DAOPHOT code (Stetson, 1987) with great success in the photometry of globular cluster stars.

One advantage which this method displays over analytic profile fits is that it can deal with significantly distorted stellar profiles, as may, for instance, be caused by poor guiding or focussing, or by the imperfect optical performance of the telescope. A substantial disadvantage, however, is the susceptibility of the derived

PSF to noise, faint companion stars, and other extraneous signal sources. Because there is no formal specification of the profile parameters, such components may be introduced into the PSF, with the result that it is not an adequate description of the true stellar profile. Whilst this is also true of the Lorentzian profile, the constraint of the analytic form of the function will tend to minimise the effect of these factors. Profile fitting methods relying upon a totally empirical PSF can also face problems due to the difficulty of interpolating reliably when the profile is changing rapidly with respect to the scale size of the pixel grid (Stetson, 1987). Such a situation can occur in very good seeing conditions, and it is therefore to be expected that this may present problems in the analysis of data from space observatories. For the majority of ground-based applications the problem is not significant.

Chapter 3

ω Centauri

3.1 Introduction

The major experimental part of this thesis concerns photometric observations of the enigmatic globular cluster Omega Centauri (NGC 5139 = C1323-472). It is both the largest, and intrinsically the most luminous, with $M_V = -10.3$, of the 103 galactic globular clusters in the list of Harris & Racine (1979), who accredit the cluster with a true distance modulus of 13.6. This figure, corresponding to a distance of some 5.7 Kpc, ranks ω Centauri as one of the nearest galactic globular clusters. The cluster lies approximately 7 Kpc from the galactic centre, and 1.5 Kpc above the plane of the galaxy. The low galactic latitude of the cluster means that it has a relatively high line of sight extinction, $E(B-V) = 0.11$ (Burstein & McDonald, 1975). The mass of the cluster has been estimated by Poveda & Allen (1975) to be some $3 \times 10^6 M_\odot$; Seitzer (1983) has determined a similar value, $2.81 \times 10^6 M_\odot$.

Dynamically and structurally ω Centauri is somewhat unusual, but not unique; Peterson (1976) found it to have a large velocity dispersion, escape velocity, and central relaxation time. The King (1966) core and tidal radii are 4 and 90 pc respectively (Peterson & King, 1975), and notably the cluster has a low central concentration (the ratio of core to tidal radius) when compared to other clusters for which measurements are available (McClure & Norris, 1977 and Smith & Norris, 1982).

The cluster appears elliptical in outline, the ratio of the axes being approximately 0.8 at minimum (Dickens & Woolley, 1967), and Harding (1965) has shown

that the cluster is rotating. Again these are not unique findings amongst galactic globulars, both M19 and M22 are elliptical, and M13 is known to rotate (Suntzeff, 1981), but they are sufficiently unusual to provoke comment. As well as these features, Omega Centauri exhibits a number of other notable traits; it has a very large number of RR Lyrae variable stars (Butler, Dickens & Epps, 1978), and is one of only two globular clusters with a confirmed "blue straggler" population (Da Costa, Norris & Villumsen, 1986).

The single most remarkable feature of this cluster is, however, the wide range in chemical composition among its evolved stars. This feature contrasts strongly with the view, held for many years, that the chemical compositions of individual stars within a globular cluster are identical, and depend upon the relative abundances of the various elements within the cluster during the, relatively brief, epoch of star formation. The first indication that ω Centauri is in any way chemically peculiar was the discovery, by Harding (1962), of a CH star in the cluster; others have subsequently been reported (*e.g.* Dickens, 1972b, and Bond, 1975). That there is a large spread in colour of the giant branch stars in the colour-magnitude diagram (CMD), was first demonstrated by Dickens and Woolley (1967) using data from an extensive programme of photoelectric photometry by Woolley *et al.* (1966). They showed that the width of the giant branch of the Omega Centauri CMD was not only much larger than could be expected from the errors inherent in their photometry, but that it was also significantly greater than the widths of the corresponding distributions seen in other globular clusters. Their findings were subsequently confirmed in full by Cannon and Stobie (1973) and Hesser *et al.* (1977). Geyer (1967) showed that there was a correlation of $(B-V)$ colour index with $\delta(U-B)$ (a metallicity indicator) for stars on the RGB. Similar ranges were observed in other photometric colour indices, such as $(V-I)$ (Lloyd Evans, 1977a) and the temperature-sensitive index $(V-K)$ (Persson *et al.* 1980).

Iben (1974) was one of the first to point out that this width could be accounted for by a range of metal abundances within the cluster, a possibility considered in more detail by Dickens and Bell (1976). These developments caused great interest, coming as they did at a time of renewed interest in the properties of globular clusters. Since these early results, there has been considerable interest in these phenomena, and the stellar population of Omega Centauri has been subjected to many different forms of photometric and spectroscopic investigation.

Bessell & Norris (1976) and Norris & Bessell (1975,1977) employed photoelectric photometry in $UBVRI$ and the DDO systems to study some of the stars which were measured by Woolley *et al.* (1966), and also supported the assertion that there was a spread in colour. To further investigate the possible cause of this they took low dispersion spectra of stars on both the blue and red sides of the giant branch. Their primary findings were that the spread in the colours of giant branch stars can not be explained in terms of differential reddening, which they determined to be of the order of $E(B-V) \leq 0.04$, and that the observed spread in colour is due to a range of surface compositions in the giant stars of Omega Centauri. They showed that stars in ω Cen exhibited CN band strength variations, and that some exhibited the weak G-band effect (Smith, 1987). They also calibrated a $(B-V)_{o,g}$ metallicity scale from the available information on $(B-V)_{o,g}$ values for clusters; this was used to deduce that the spread in the observed $(B-V)$ colour at the level of the horizontal branch was insufficient to explain the Δ[Fe/H] $\simeq 1.0$ result given by their metallicity calibration of the DDO and $UBVRI$ photometry. This lead them to suggest that a possible cause was that the the metal abundance was more or less constant throughout the cluster, and that observed variations in colour at a given luminosity are caused by CN enhancements in some Omega Centauri stars. Indeed their low-dispersion spectra of several Omega Centauri members on both the high and low temperature sides of the colour distribution suggested that the redder stars contained enhanced quantities of CN, compared to the bluer stars, whilst the overall metal abundances were similar in all stars.

Freeman & Rodgers (1975) showed spectroscopically that there are calcium abundance variations amongst the RR Lyrae stars in ω Cen, a result that was confirmed by Butler, Dickens & Epps (1978). Spectroscopic studies of giant stars revealed significant variations of Ca, Fe, Sr and Ba (Lloyd Evans, 1977b, Mallia, 1976 and Dickens & Bell, 1976). Manduca & Bell (1978) applied model atmosphere analyses to the spectra of Butler *et al.* (1978), and determined the range of calcium abundance to be $-1.9 \leq$ [Ca/H] ≤ -1.0. Similarly, Bell & Gustafsson (1983) applied synthetic spectrum fitting to the data of Rodgers *et al.* (1979), and determined the range of metallicity within the cluster to be $-1.9 \leq$ [M/H] ≤ -1.2. High dispersion spectra of red giants on the blue and red sides of the RGB have been obtained and analyzed using synthetic spectrum fitting by Caldwell

(1983). Caldwell has deduced that the stellar heavy element abundances lie in the range $-1.8 \leq$ [Fe/H] ≤ -0.8, and that the range in calcium abundance is $-0.3 \leq$ [Ca/H] $\leq +0.4$. Furthermore, Caldwell has shown that carbon and nitrogen abundances are anticorrelated, supporting the theory that processed materials from the stellar interior have been brought to the surface of the star by rotationally-driven meridional circulation currents (Sweigart & Mengel, 1979). Caldwell's synthetic spectrum fits also indicated that the range in metallicity within ω Cen is insufficient to explain the great width of the cluster giant branch, with stars on the red side of the giant branch appearing too cool for their metallicity. To explain this, Caldwell tentatively proposed that the convective mixing length varies across the giant branch, possibly as a result of differential rates of stellar rotation, with the faster (red) rotators mixing larger amounts of processed material into their atmospheres. Hesser *et al.* (1985), from 3–4Å resolution spectroscopy of ω Cen subgiant stars, estimate that there is a fairly uniform distribution in metallicity in the range $-2.0 \leq$ [M/H] ≤ -1.0, with some stars as metal-rich as [M/H] $= -0.7$. An additional important result of this study was the discovery that, at a radial distance of $\sim$ 20 arcmin from the cluster centre, nearly half the stars in the magnitude range $16 < V < 18$ are radial-velocity non-members of the cluster.

In light of the acknowledged inhomogeneities amongst the brighter cluster stars, considerable effort has been expended in trying to obtain reliable, faint colour-magnitude photometry of ω Cen, in order to investigate the nature of the cluster main sequence. The pioneering CMD of Belserene (1959) showed the cluster turnoff and main sequence, reaching as faint as $V \approx 19$, but the faint photoelectric standards used for calibration were rather unreliable, and the internal errors large by current standards. Further photographic photometry by Harding *et al.* (1971), which used an objective grating to extend the calibration from bright standards, reached the main sequence, but again the turnoff location was uncertain, and the internal errors did not permit the structure of the main sequence to be investigated. Cannon & Kontizas (1974) carried out photoelectric and photographic photometry to below $V \approx 19$, and showed the turnoff to be at $V \approx 18.3$. The more accurate photometry of Cannon & Stewart (1981) also indicated that the main-sequence turnoff is at $V \approx 18.3$, and suggested that, after a rudimentary correction for field star contamination, there is an intrinsic

spread in colour of stars on the upper main sequence. Photometry with electronic imaging detectors by Rodgers *et al.* (1980), and Rodgers & Harding (1983), of the subgiant branch and turnoff region confirmed the turnoff location, but once again was unable to provide quantitative information about the morphology of the main sequence. Rodgers and Harding (1983) claimed that their observations were of sufficient precision to show that there is an intrinsic width in colour in the turnoff region; however, they neglected the effects of field star contamination in their analysis, and thus it seems likely that a substantial proportion of their sample of stars are cluster non-members. Da Costa & Villumsen (1981) have presented photometry of several hundred stars around the turnoff region; their study suggests there is a spread in metallicity of the order of Δ[Fe/H] $\geq$ 0.6 dex; once again, this study may be adversely affected by field star contamination.

The colour-magnitude studies described above delineated the subgiant branch of the cluster CMD, and hinted at the structure of the main sequence proper. The aim of the present study was, therefore, to extend the cluster colour magnitude diagram to fainter limits, in order to study the structure of the main sequence—a particularly important goal in view of the noted peculiarities of the cluster giant branch morphology.

The much vaunted chemical inhomogeneity of ω Centauri is manifest in the extreme width of the cluster giant branch sequence. Although composition variations exist of many kinds, it is clear that this spread in colour is at least partly caused by a variation in the abundances of the heavier "iron peak" elements, which are not known to be synthesised within the cluster stars themselves, and which strongly influence the atmospheric opacity in cluster giant stars (Renzini, 1977). Thus, by implication, these inhomogeneities should also be present in cluster main sequence stars. Adopting a metallicity spread of the order of $-2.0 \leq$ [Fe/H] ≤ -1.0 as suggested by spectroscopic studies of giant stars in ω Cen (see for instance Bell & Gustafsson, 1983) then one would expect (from the models of VandenBerg & Bell, 1985) a range in $(B-V)$ colour index on the main sequence of $\sim 0\overset{m}{.}08$, which should be observable with the techniques of CCD photometry.

As well as establishing the intrinsic width in colour of the main sequence, and making comparisons with theory, other aims of this project were to use the properties of the main sequence and turnoff regions to derive estimates of fundamental cluster parameters such as age and distance.

The CCD observations of ω Centauri presented in this thesis fall broadly into two categories, distinguished by the filter systems employed for the observations. Broadband B and V filters, conforming well to the Kron-Cousins $UBVRI$ system were used to obtain exposures to fields in the cluster, with both the Anglo-Australian Telescope (AAT), and the South African Astronomical Observatory (SAAO) 1.0 m. In addition, a customized filter set, with two extremely broad passbands in the blue and red regions of the visible spectrum, was employed to obtain AAT exposures to the same fields observed in B and V. The blue and red passbands of this filter system will hereafter be referred to as WB and WR respectively. This filter system was chosen in order to take advantage of the immense light-gathering power of the 3.9 m AAT to extend the observations as faint as possible. The WB, WR set has been used by Penny and Dickens (1986) in their superlative colour-magnitude study of the cluster NGC 6752, which showed that these filters produce magnitude scales which transform well to the $UBVRI$ system.

The enormous power of the AAT was exploited to obtain deep exposures, delineating the cluster main sequence to fainter levels than any previous study. These observations were made in fields remote from the cluster centre, where crowding presents fewer problems. The observations made at the SAAO were of a larger number of fields, and were used to "fill in" the brighter parts of the colour magnitude diagram, such as the sub-giant and horizontal branches. The region studied lies approximately 20 arcminutes to the west of the cluster core, overlapping substantially the field studied by Cannon & Stewart (1981) and is shown in Figure 3.1.

The observational data described in this chapter were kindly provided by A.J.Penny and R.J.Dickens, to whom I must once again express my gratitude.

3.2 The B and V Observations

3.2.1 The SAAO Observations

The observations were made using the 1.0 m telescope at the South African Astronomical Observatory, Sutherland, Cape Province, South Africa, on the night of $16^{th}/17^{th}$ June 1985. The exposures were made using the UCL CCD camera

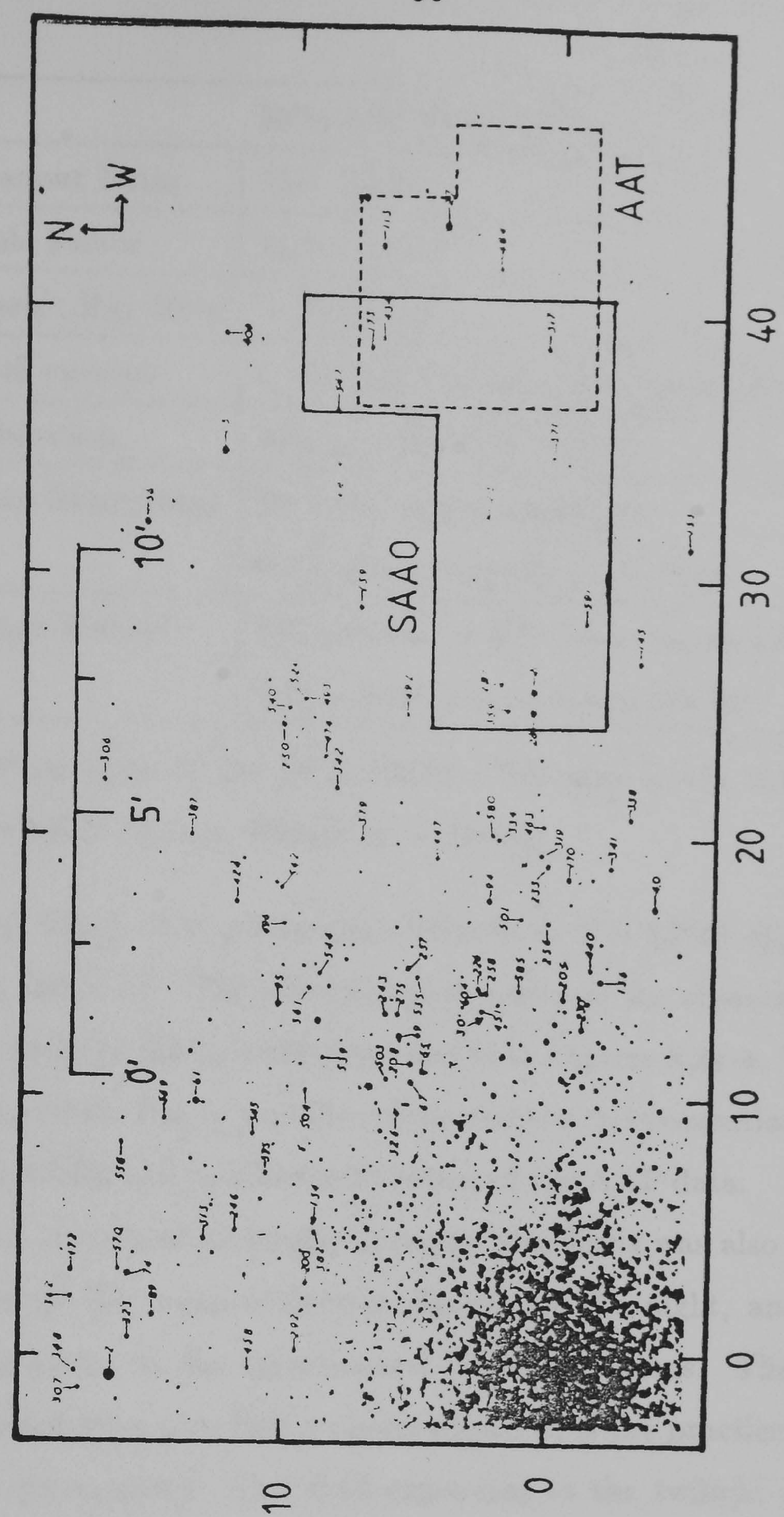

Figure 3.1: The northwest quadrant of ω Centauri showing the location and extent of the B and V observations. The SAAO fields are shown bounded by a solid line, whilst the AAT fields are bounded by a broken line. The star identifiers are ROA numbers from Woolley *et al.* (1966), as is the coordinates system, corresponding to millimetres on the original plate scale.

RCA SID 53612 CCD	
Readout Noise	$73e^-$ RMS
Scale Factor	$11.5e^-$/ADU
Cosmic Ray Rate	~ 200/hour
Dark current	$\sim 4e^-$/pixel/minute average at 160 K
Saturation	Above $\sim 250\,000e^-$/pixel
Pixel Dimensions	$30 \times 30\mu$ corresponding to 0.4×0.4 arcseconds on the sky
Image Format	320 columns $\times$ 512 rows corresponding to 2.12×3.40 arcminutes on the sky

Table 3.1: Properties of the RCA 53612 CCD chip in the SAAO/UCL CCD camera, June 1985. Source: Walker *et al.* (1983).

(Walker *et al.* 1984). The properties of the RCA SID 53612 chip in the camera are shown in Table 3.1. The principal parameters of the observations are shown in Table 3.2, and the fields studied are shown in Figures 3.2a–e. The specific aim of these observations was to provide colour magnitude information in the brighter regions of the CMD and to allow calibration of the AAT data.

A series of exposures to nearby E-region standards was also made to enable determination of the mean extinction figures for the night, and calibration of the zeropoint terms in the instrumental colour equations. These observations were interspersed with the cluster observations, as is the practice in conventional photoelectric photometry. Flat field exposures to the twilight sky were taken, and calibration frames were made to establish the dark current, bias, and preflash characteristics of the camera.

3.2.2 The AAT B and V Observations

These observations were made on the night of $4^{th}/5^{th}$ March 1986 during an observing run by R.J.Dickens and J.R.Lucey at the Anglo-Australian Observatory, Siding Spring, New South Wales, Australia. The exposures were taken using the RGO CCD camera (Jorden, Thorne and Van Breda, 1982), at the prime focus of the 3.9 m AAT. This camera also employed an RCA SID 53612 CCD chip with 30μ square pixels, corresponding to 0.5 arcseconds square upon the sky. Thus

$16^{th}/17^{th}$ June 1985 RCA Cassegrain focus			
Field	Run No.	Exposure	Filter
F5	6053	100	B
F5	6054	500	B
F5	6055	500	V
F5	6056	100	V
F6	6047	100	V
F6	6048	500	V
F6	6049	500	B
F6	6050	100	B
F7	6035	100	B
F7	6036	500	B
F7	6037	100	V
F7	6038	500	V
F8	6039	100	V
F8	6040	500	V
F8	6041	500	B
F8	6042	100	B
F9	6043	100	B
F9	6044	500	B
F9	6045	500	V
F9	6046	100	V

Table 3.2: Principal parameters of the SAAO B and V observations.The field identification is given in column 1, column 3 contains the exposure time in seconds.

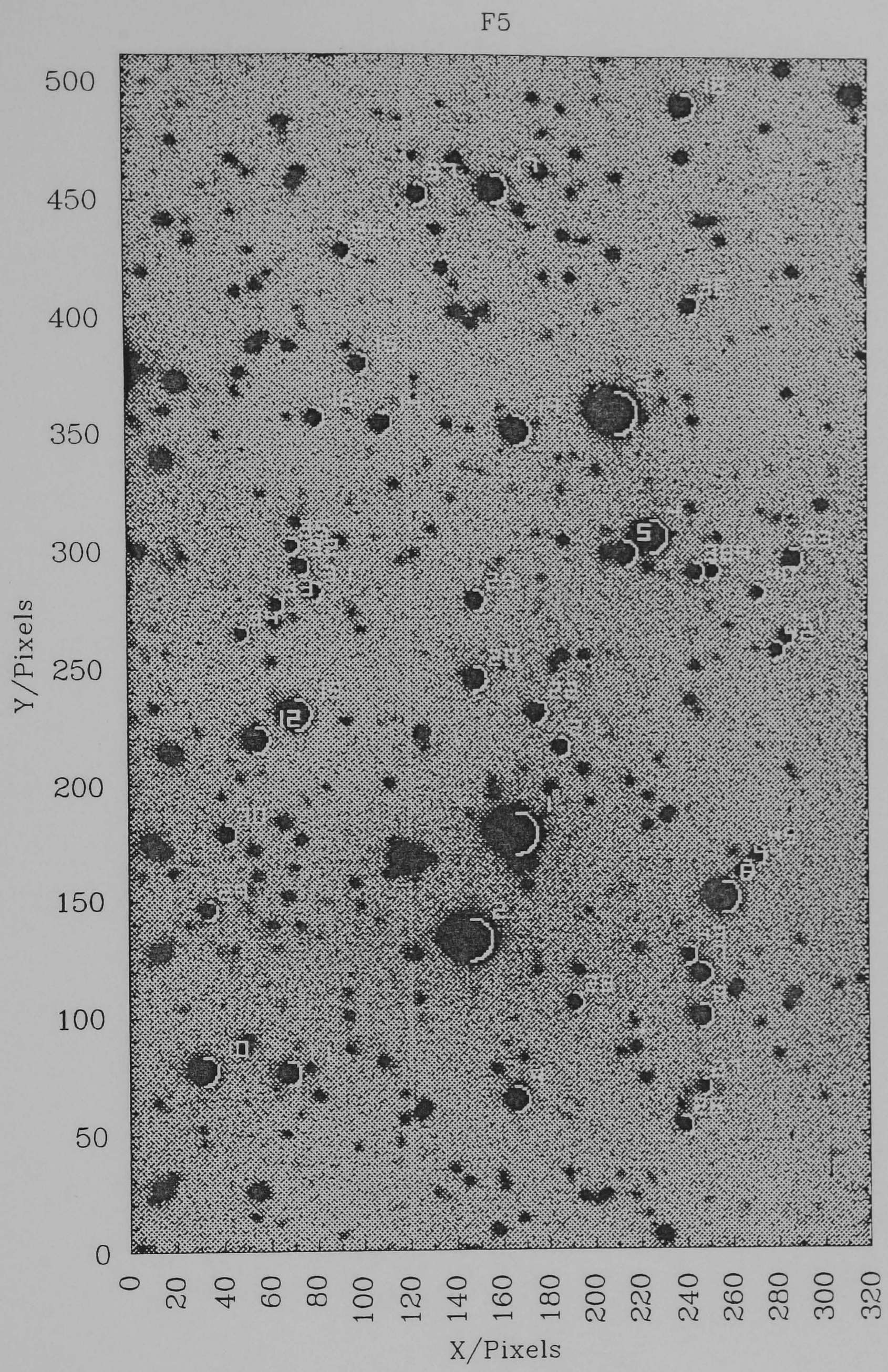

Figure 3.2: The SAAO fields in ω Centauri. The star numbers are from the photometric analysis of Section 3.3.1. In the diagrams, north is up and west is to the right. a) Field F5

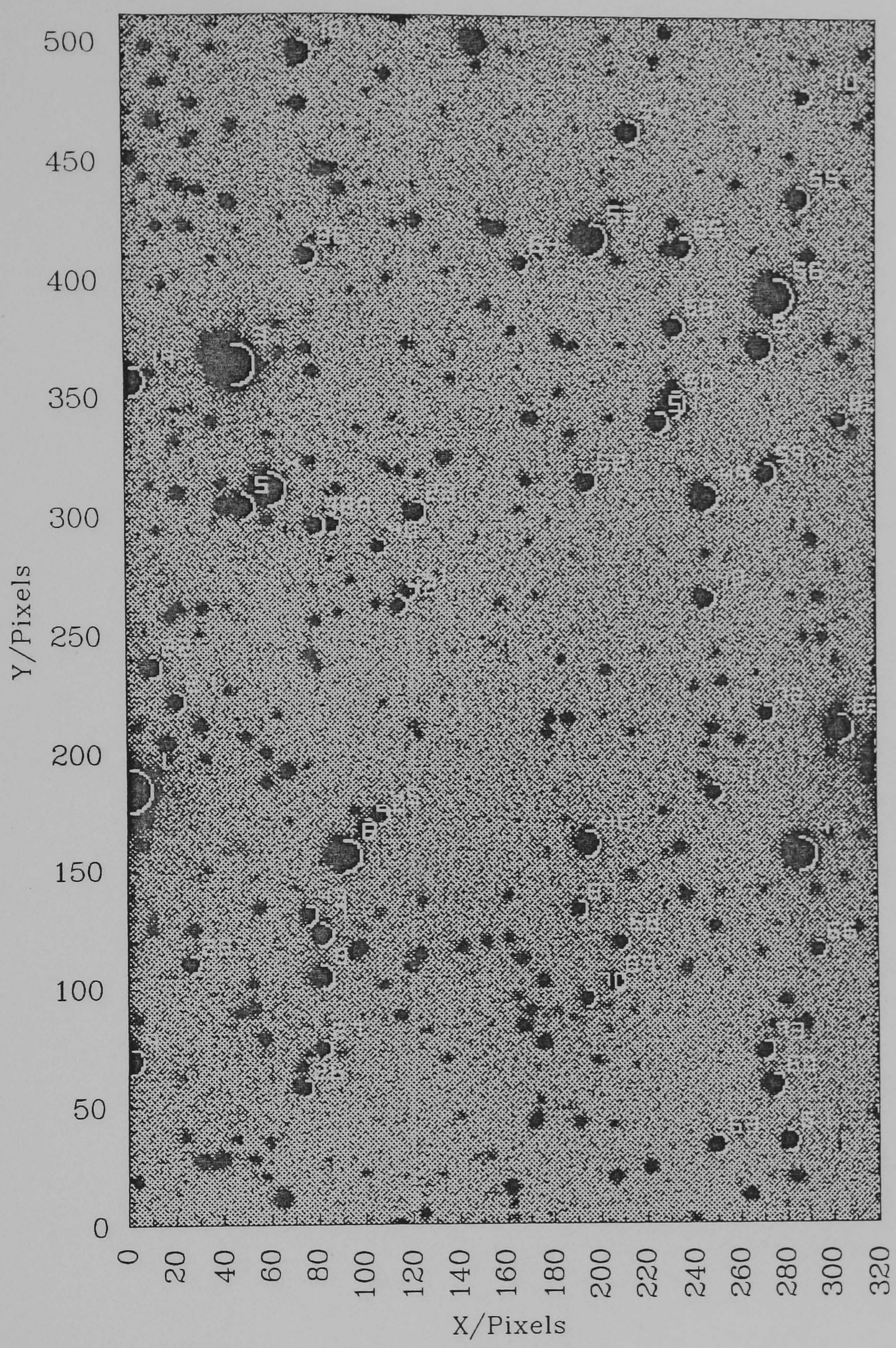
F6
500
450
400
350
300
250
200
150
100
50
0
Y/Pixels
0
20
40
60
80
100
120
140
160
180
200
220
240
260
280
300
320
X/Pixels

b) Field F6

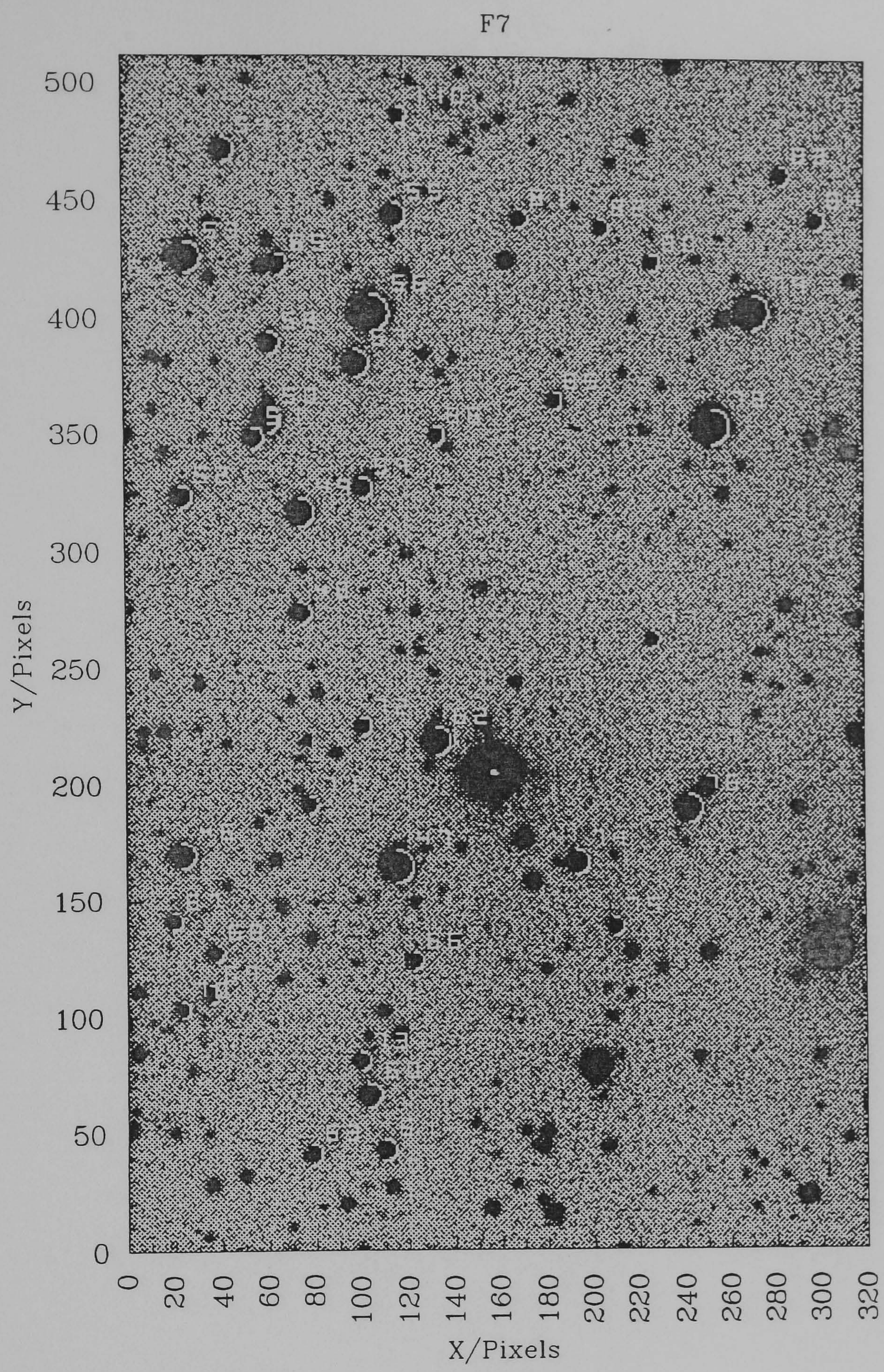
F7
Y/Pixels
X/Pixels
0
50
100
150
200
250
300
350
400
450
500
0
20
40
60
80
100
120
140
160
180
200
220
240
260
280
300
320

c) Field F7

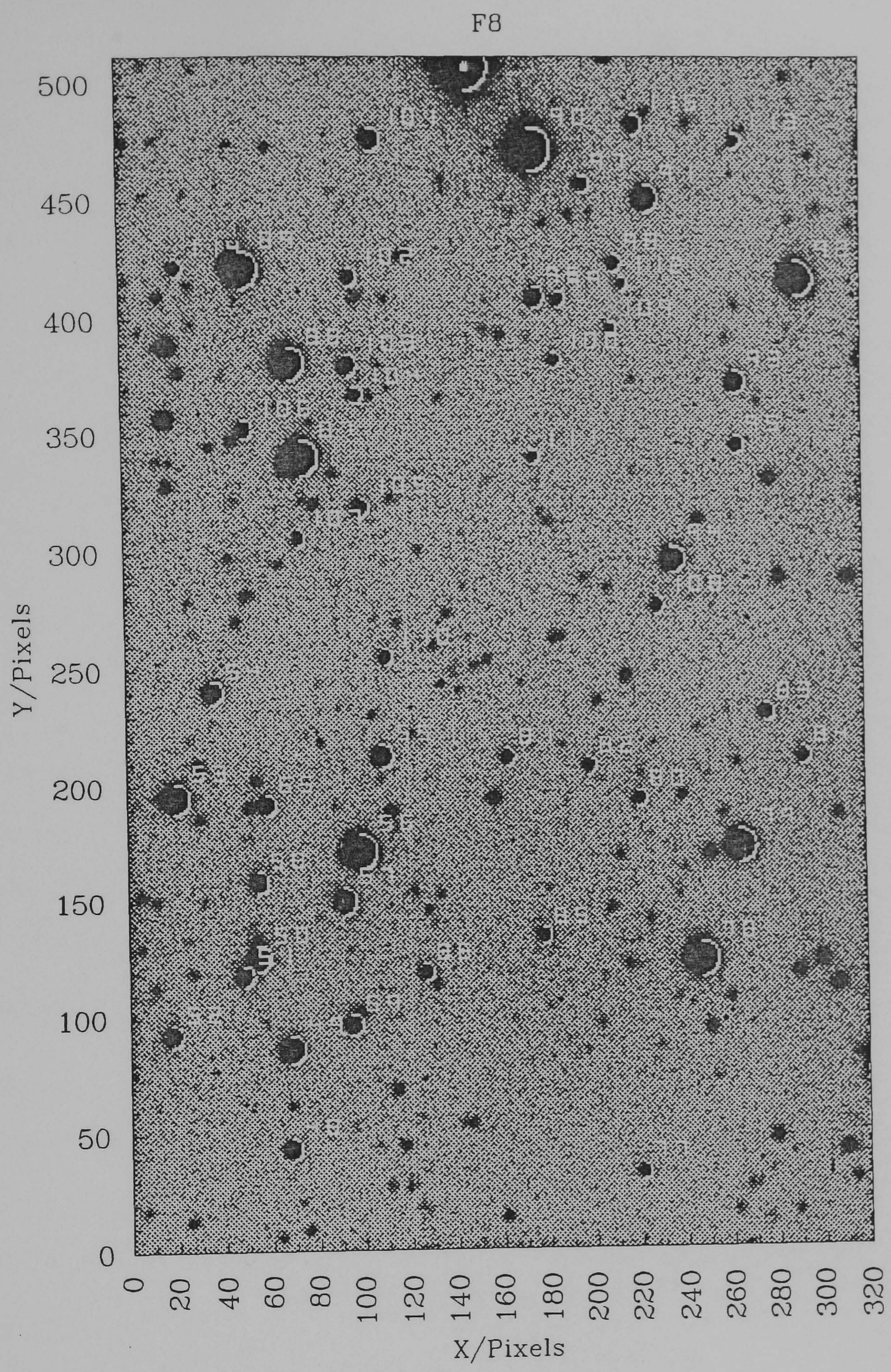
F8
Y/Pixels
X/Pixels
0
50
100
150
200
250
300
350
400
450
500
0
20
40
60
80
100
120
140
160
180
200
220
240
260
280
300
320

d) Field F8

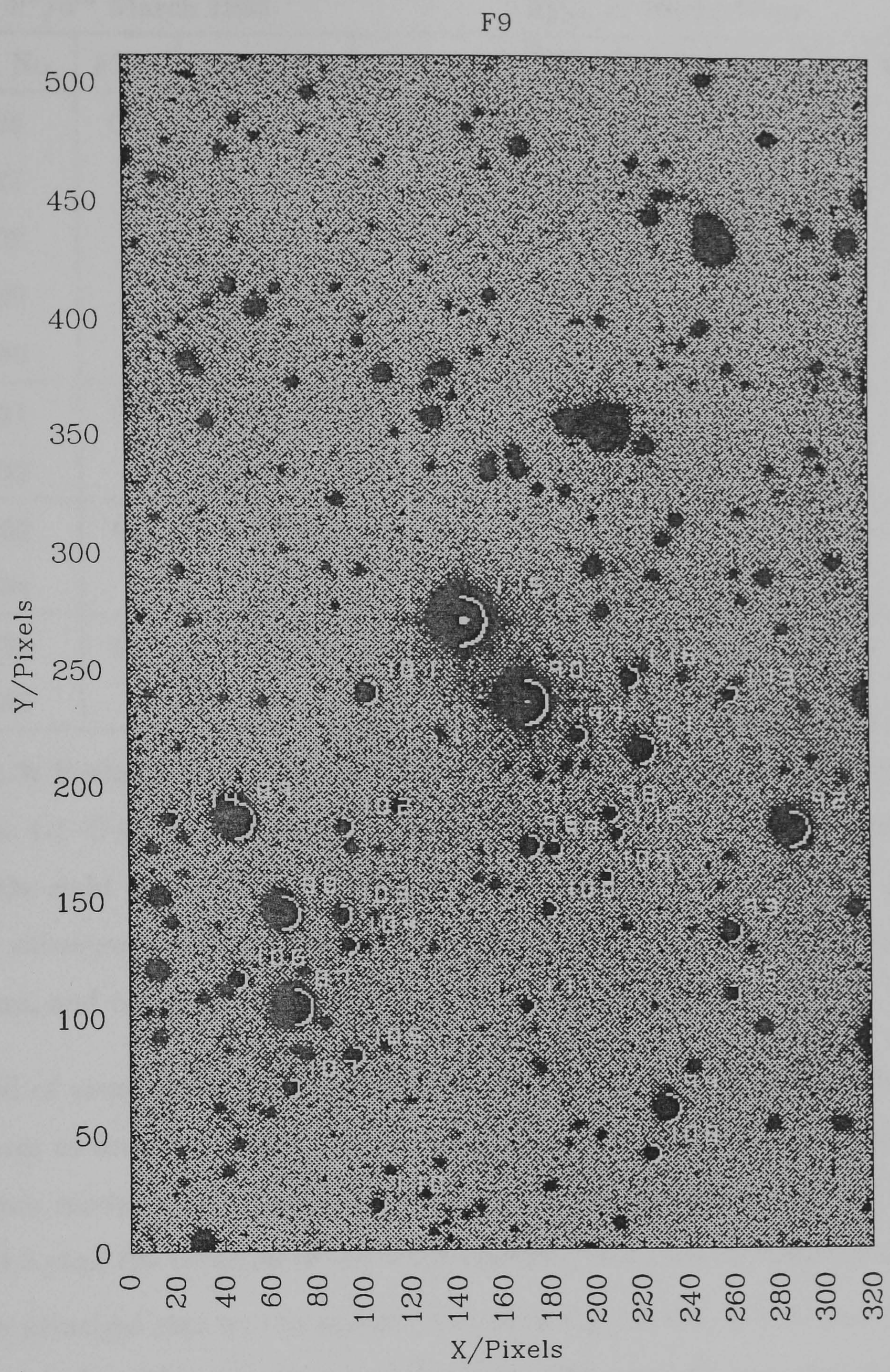
F9
500
450
400
350
300
250
200
150
100
50
0
Y/Pixels
0
20
40
60
80
100
120
140
160
180
200
220
240
260
280
300
320
X/Pixels

e) Field F9

$4^{th}/5^{th}$ March 1986			RCA at Prime focus			
Run No.	Field	$\alpha_{1986.2}$	$\delta_{1986.2}$	UT(Start)	Exposure	Filter
326	O1	$13^h21^m36^s$	$-47°11'38''$	16:56	500	V
327	-	-	-	17:07	500	B
328	-	-	-	17:17	500	V
329	-	-	-	17:27	500	B
330	-	-	-	17:35	500	V
331	O2	$+120''E$	-	17:45	30	V
332	-	-	-	17:46	30	B
333	O3	$+120''E$	$+60''N$	17:47	30	B
334	-	-	-	17:48	30	V
335	O4	$+120''E$	$+120''N$	17:49	30	V
336	-	-	-	17:51	30	B

Table 3.3: Parameters for the AAT B and V observations. A total of 11 exposures to fields O1–O4 were obtained, including 3 deep V and 2 deep B. Column (3) shows the right ascension and declination of field O1, and the offsets in arcseconds for the subsequent fields. Column (4) is Universal Time at the beginning of each exposure, and column (5) is the exposure time in seconds.

the field of view of the 320×512 pixel CCD is some 2.66×4.25 arcmin. Eleven exposures to four overlapping fields, some twenty arcminutes west of the cluster core were made. The principal parameters of these observations are shown in Table 3.3, and the location of the fields observed is shown in Figure 3.3.

The principal aim was to provide deep coverage of the cluster main sequence; this was achieved by concentrating five deep (500 second) exposures to one field (O1), the remaining shorter exposures were for tying the magnitude system of these observations to the brighter stars observed at the SAAO. The observations were made as a secondary programme in an observing run primarily devoted to galaxy observations and as such the standard star observations were inadequate for photometric purposes. Thus it was essential to rely upon the overlapping SAAO fields for calibration of the AAT B and V data.

Flat field observations of the dome interior were made, and dark and bias exposures were taken.

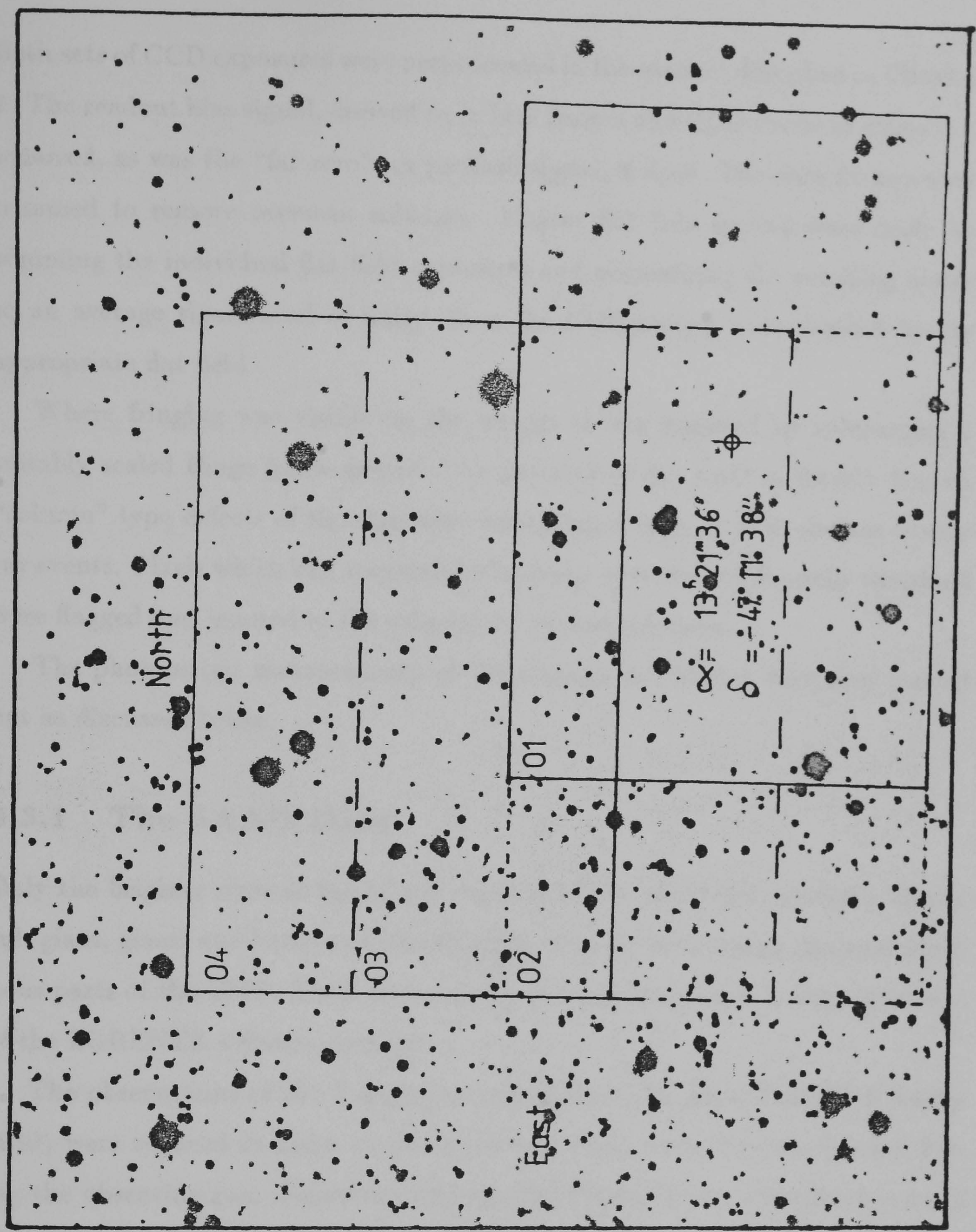

Figure 3.3: The AAT B and V fields O1–O4. The region shown has dimensions of approximately 7.5×5.5 arcminutes and lies some twenty arcminutes to the west of the cluster core.

3.3 Data Reduction

Both sets of CCD exposures were preprocessed in the manner described in Chapter 2. The readout bias signal, derived from bias frames and CCD overscan strips was removed, as was the "fat zero", or preflash signal, if used. The data frames were trimmed to remove overscan columns. Master flat field frames were made by summing the individual flat field exposures and normalising the resulting image to an average signal level of unity; then the CCD images were divided by the appropriate flat field.

Where fringing was visible on the images it was removed by subtracting a suitably scaled fringe frame provided by the staff of the AAO or SAAO. Known "column" type defects of the chip were interpolated over, as were obvious cosmic ray events. Pixels which had accumulated a charge over the non-linearity threshold were flagged and ignored in the subsequent processing chain.

The photometric measurements of the stars in the frames were then carried out as discussed below.

3.3.1 The SAAO Data

Only the brighter stars in the SAAO exposures were measured, generally cluster sub-giant, giant, and horizontal branch stars, in order to delineate the more luminous parts of the CMD. These were measured using the profile-fitting algorithms of the LORENTZ software package.

The observations of the E-region standard stars (Menzies, Banfield & Laing, 1980) were reduced in order to determine the mean extinction coefficients during the observing run. Exposures had therefore been made of standard stars of differing colours, and at airmasses bracketing the cluster observations. These exposures were "cleaned", as described above, prior to measuring the stars by digital aperture photometry as described in Chapter 2.

The Charge Transfer Efficiency Problem

At this preparatory stage of the reductions, a disturbing effect became apparent. Single, dark diagonal bands were visible upon some of the SAAO CCD images. The effect was visible as a low level modulation of the background across the im-

age, of amplitude ~5–10 ADU. An example of a frame suffering from this defect is shown in Figure 3.4. Though the effect is slight in magnitude, it is significant because of its influence upon the determination of background sky flux, when carrying out aperture photometry upon the E-region standards. The uncertainty introduced to the derived aperture magnitudes by the variation in background intensity was investigated, and found to be of the order of a few hundredths of a magnitude. This could, however, be reduced by carefully sampling the background sky level at several points around the star and making a weighted average according to the star's position.

The effect was noticeable on some of the shorter B and V exposures, though varying in amplitude upon these frames. Careful examination of the bias exposures made during the run showed that none of them suffered from the problem and thus, in essence, it must have been due to some effect only operating when actually making exposures, such as scattering of unwanted light onto the chip, preflashing problems or some element of optical vignetting, which had changed in some way since the flat fielding exposures were made. The latter possibility was rejected; flat field exposures were made both before and after the relevant frames were taken, and showed no noticeable variation over this period.

The chip in the UCL CCD camera exhibits poor charge transfer efficiency at very low signal levels, and consequently is preflashed before each exposure, to bring the charge level in each pixel above the CTE threshold. Thus, one possible cause of the residual image defect might be an element of non-linearity, or non-repeatability in the preflashing process. Therefore, the long preflash exposures made during the run were examined critically, to see if there was any evidence of variation between frames. No significant deviation was noted between different preflash exposures, but, it was noted, the intensity level of the preflash exposures showed structure reminiscent of the diagonal bands seen on some of the short CCD images. This is illustrated in Figure 3.5. Furthermore, in parts, the intensity of the preflash signal was significantly lower than suggested by the CCD camera operating manual (below $450e^-$/pixel compared to the quoted charge transfer efficiency threshold of $500e^-$/pixel). It was also noted that the preflash exposures were non-uniform at the twenty percent level, whereas the manual specifies the charge deposited by preflashing should be constant to a few percent. It therefore seems likely that the problem is due to poor CTE in those regions of the CCD where insufficient charge

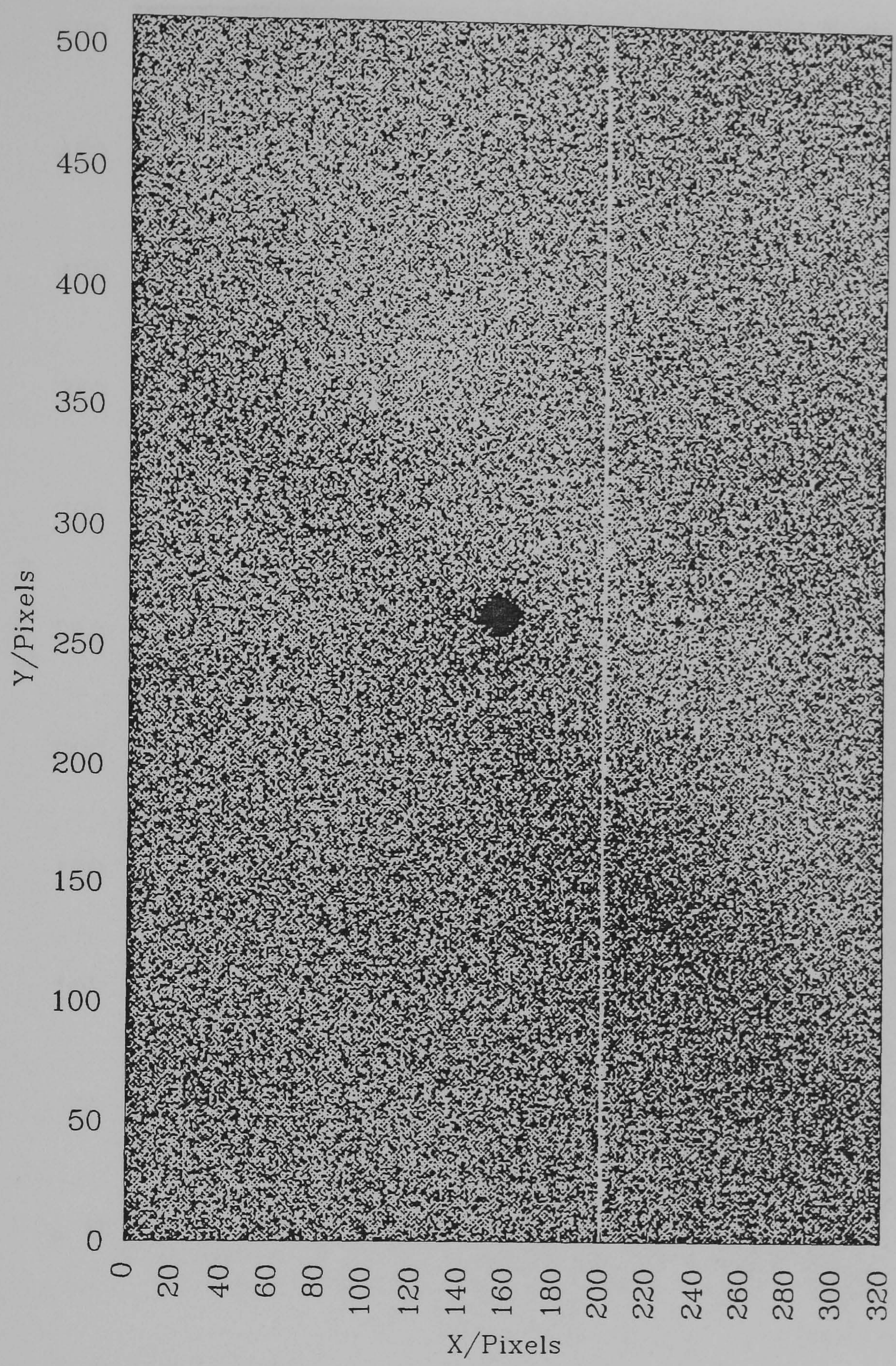

Figure 3.4: Residual Defect in a cleaned SAAO CCD image. The frame is a one second exposure to the E-region standard star E666, a dark band can be seen running from bottom right to top left of the image.

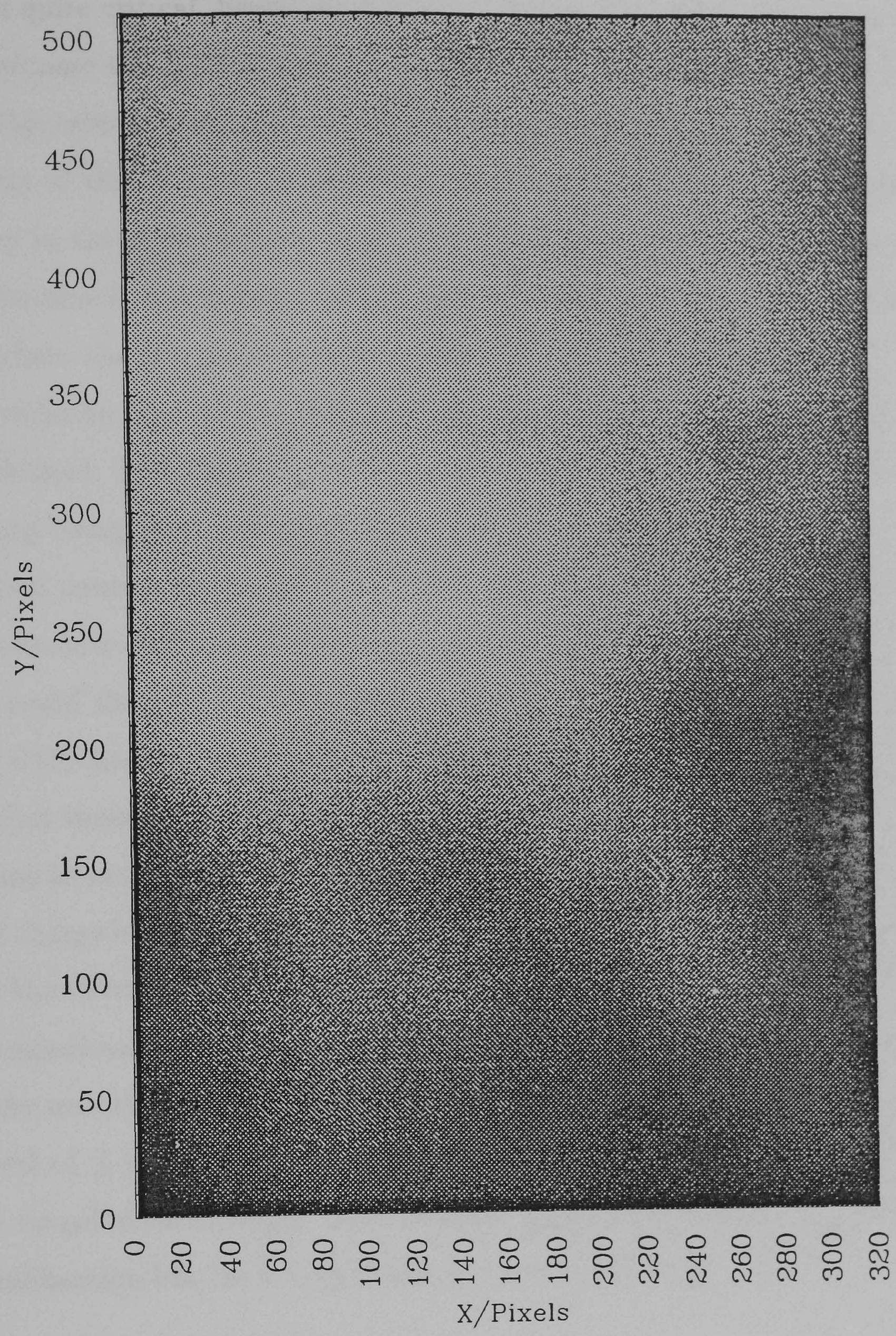

Figure 3.5: SAAO preflash exposure. A diagonal band structure similar to that observed in some of the cleaned SAAO CCD images can be seen running top left to bottom right.

has been deposited by the preflashing process. The background intensity value appears quite critical, hence, on exposures longer than a few seconds, the sky flux will overcome the CTE threshold, and the chip will behave as normal. However, below this critical value significant distortions of the background are evident. The net effect of this is degradation of the photometric accuracy, not because of non-linearity in the stellar image, where the signal intensity substantially exceeds the CTE threshold, but because of the non-uniformity produced in the background level, where the charge distribution falls below the CTE threshold.

In order to combat this problem, the frames exhibiting the diagonal striping were cleaned, had their stellar images removed by interpolation from the surrounding background area, and were summed to produce a "model" of the signal distortion caused by the CTE problem. This image was then smoothed by "top hat" convolution to produce the image shown in Figure 3.6 The resulting "pattern" frame could then be scaled to match the amplitude of the pattern seen in individual CCD images, in the same manner as fringe exposures, and then subtracted from that image. This process ensures background uniformity at approximately the same level as the flat fielding process, but may still not cater for the distribution of charge in the wings of the stellar point spread function. It is very difficult to model the effect of such low level charge transfer efficiency upon the stellar profile, but comparisons of observations of the same star at close intervals in time suggest that the uncertainty in stellar magnitude caused by this problem is probably at the level of $\leq 0\overset{m}{.}01$. This is a significant contribution to the overall uncertainty in the magnitudes of bright isolated stars, and undoubtedly the accuracy of the final calibration has been compromised to some extent by this effect.

Instrumental Transformations

The colour equations of the combination of SAAO 1.0 m telescope and UCL CCD camera are extremely stable with time and have been determined very accurately (A.R.Walker, private communication) as,

$$V = 1.000 v_0 + \gamma_V,$$

$$(B - V) = 1.078(b - v)_0 + \gamma_{(B-V)},$$

where,

$$v_0 = v + (k'_V + k''_V(B - V))X$$

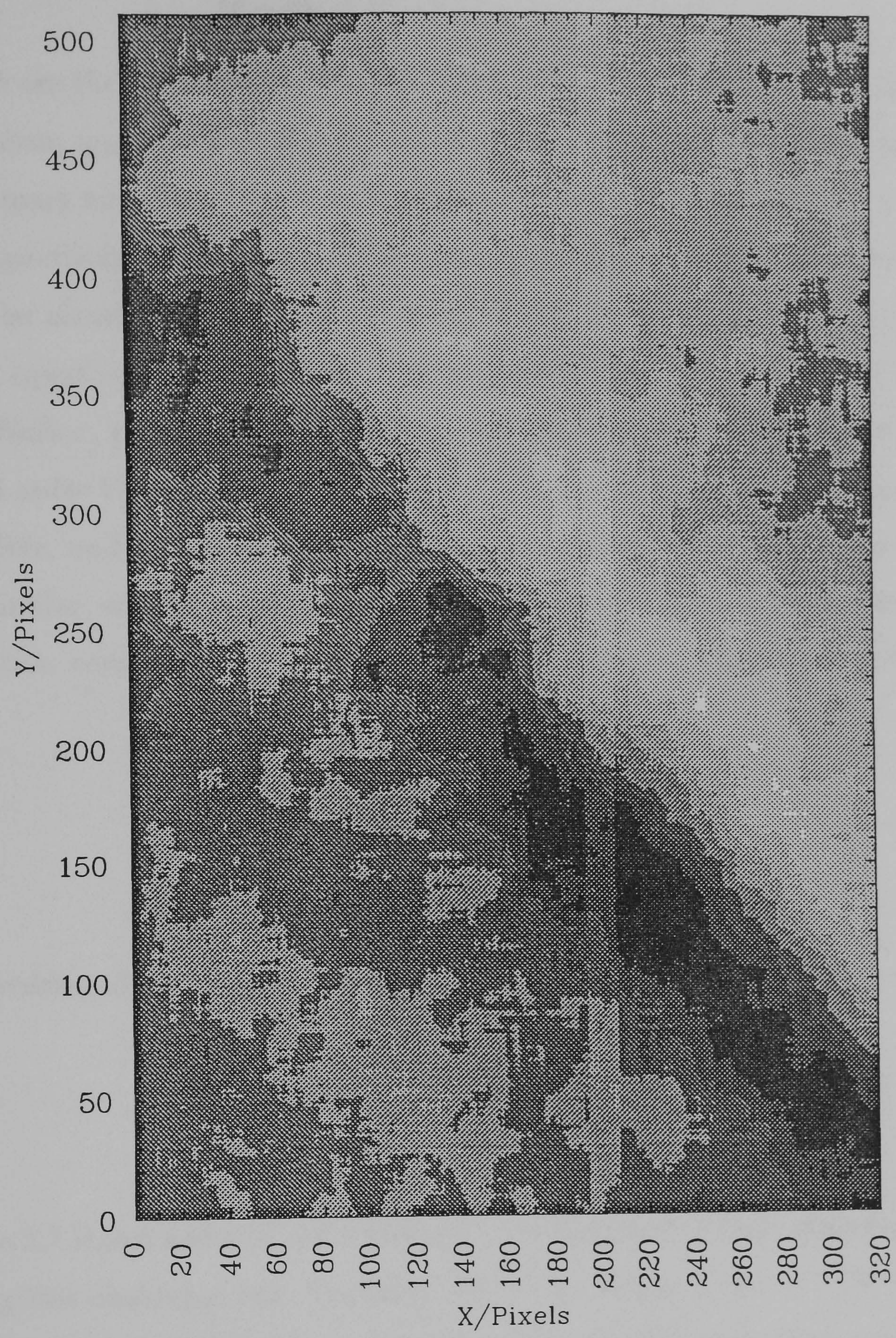

Figure 3.6: The image distortion caused by low level charge transfer inefficiency. This model of the image distortion was produced by summing and then smoothing the CCD exposures exhibiting the problem, first removing areas containing stellar images by interpolation.

and

$$(b-v)_0 = (b-v)(1-k''_{bv}X) - k'_{bv}X.$$

v and b are the instrumental V and B magnitudes respectively, γ_V is the V zero-point term, $\gamma_{(B-V)}$ is the $(B-V)$ zeropoint term, and k'_V and k''_V are respectively the primary and secondary V extinction coefficients. Similarly, $k'_{(B-V)}$ and $k''_{(B-V)}$ are respectively the primary and secondary $(B-V)$ extinction coefficients, and X is the airmass, $\sec z$. There is a small non-linear colour term in the SAAO colour equations, but it is poorly known, and is in any case less than $\pm 0^m.005$ (A.R.Walker, private communication), and has therefore not been applied. The second order V extinction term is, as is to be expected for a well matched system, negligible, and as the standard star and programme observations were made at very similar, small, zenith distances, the magnitude of the second order $(B-V)$ extinction correction was negligible ($\ll 0^m.01$). Hence, the above equations become,

$$V = v + \gamma_V + k'_V X$$

and

$$(B-V) = 1.078(b-v) - 1.078k'_{(B-V)}X + \gamma_{(B-V)},$$

or, rewriting $\Delta V = V - v$, and $\phi(B-V) = (B-V) - 1.078(b-v)$,

$$\Delta V = \gamma_V + k'_V X,$$

$$\phi(B-V) = -1.078k'_{(B-V)}X + \gamma_{(B-V)}.$$

Figure 3.7 shows a plot of ΔV versus $\sec z$ for the standard star observations made during this observing run. Similarly, Figure 3.8 shows a plot of $\phi(B-V)$ versus $\sec z$ for the same E-region standards. The transformation equations for the SAAO data are thus,

$$V = v - 9.417 - 0.110X,$$

and

$$(B-V) = 1.078(b-v) + 0.240 - 0.184X.$$

The root mean square deviation from these relationships is in each case $\sim 0^m.015$, slightly larger than would normally be expected for such short observations of relatively bright stars, but consistent with the predictions of the effects of the preflashing problems described above.

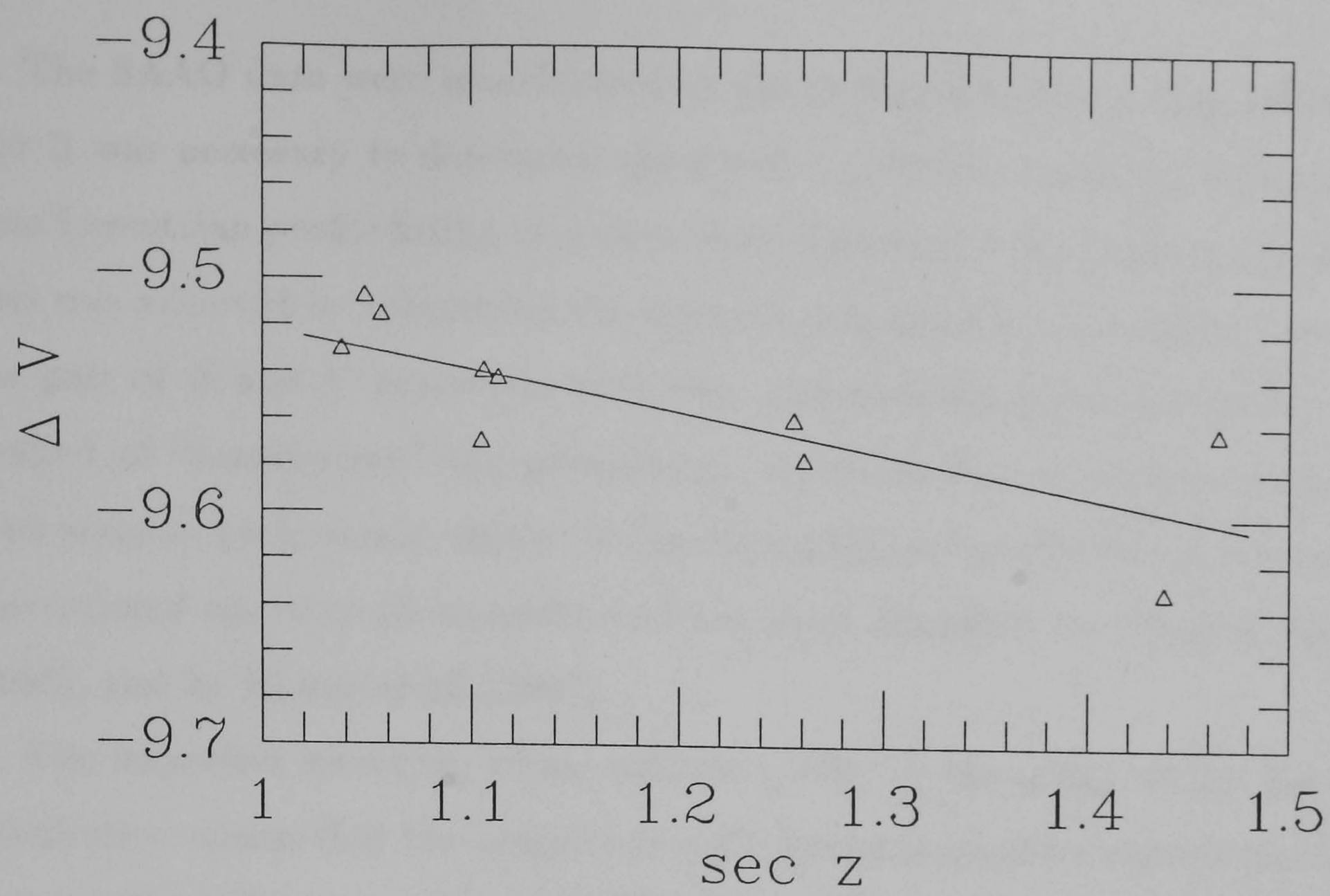

Figure 3.7: The transformation from instrumental to standard V magnitudes for the SAAO data, as derived from observations of E-region standards. The line is a linear least-squares solution to determine the first order extinction and zeropoint terms for V.

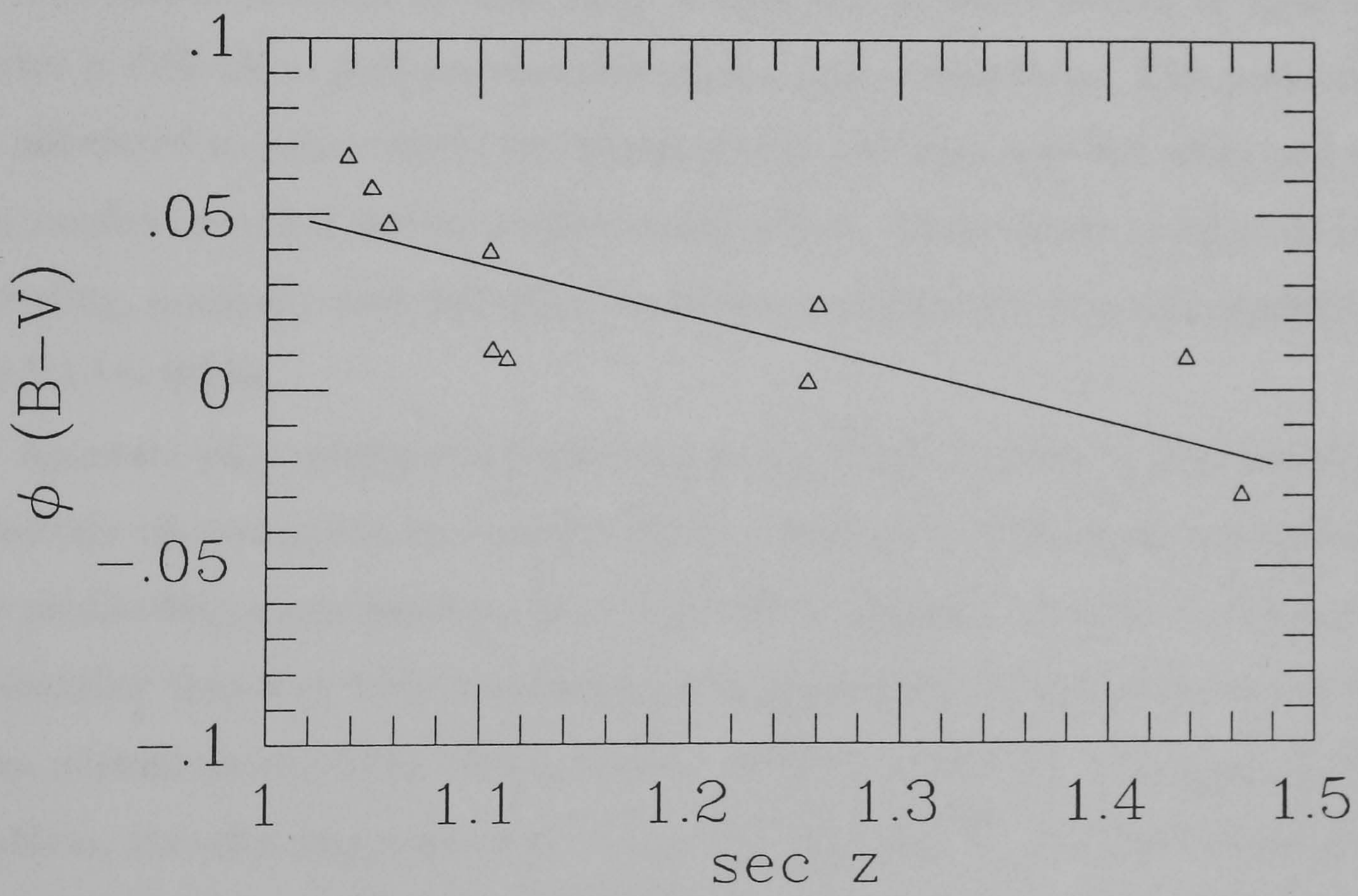

Figure 3.8: The transformation from instrumental to standard $(B-V)$ colour for the SAAO data, as derived from observations of E-region standards. The line is a linear least-squares solution to determine the first order extinction and zeropoint terms for $(B-V)$.

The SAAO data were transformed by the application of these equations, but first it was necessary to determine the relation between the magnitudes derived from Lorentzian profile fitting and those from digital aperture photometry (DAP). This was achieved by comparing the aperture magnitudes of a sample of stars on one pair of B and V exposures with the corresponding profile estimates. This method of "transferring" the photometric zeropoint from observations of standard stars to programme objects is exactly analogous to the techniques used in conventional aperture photometry and has been described by Penny & Dickens (1986), and by Hesser *et al.* (1987).

The imperfect matching of an analytic profile to the actual stellar intensity distribution means that the magnitude scale, as determined for a particular frame from profile fitting, can systematically differ from that established by aperture methods. This systematic mismatch, which can amount to several hundredths of a magnitude, and has been discussed in Chapter 2, means that it is necessary to use DAP when determining transfers from standard stars which are not within the CCD frame.

The major problem at this stage is that the crowded nature of these fields makes it difficult to perform aperture photometry within them. This problem can be alleviated to some extent by choosing only the least crowded areas and using the smallest possible apertures that seeing allows. However the problem of stellar crowding, normally contamination by fainter companions, was still significant in the SAAO fields.

Aperture photometry was performed on the brightest 15 or so stars which were relatively uncrowded in the chosen frames. Only stars with small residuals from the profile-fitting process were chosen for this procedure, in order to minimise the probability that they were contaminated by faint, close companions, undetectable from normal examination of the frames. Where crowding by companions was a problem, the offending stars were "removed" from the frame by subtracting their fitted Lorentzian profiles, allowing digital aperture photometry to be performed upon the chosen star.

The scatter in the differences between the profile fitting, and the aperture photometry measurements indicated an uncertainty (standard deviation), in the transfer of zeropoints from the E-region standards, of some $0\overset{m}{.}006$ in V, and $0\overset{m}{.}009$ in $(B-V)$. Some of the photoelectric standards of Cannon (1981) were within the

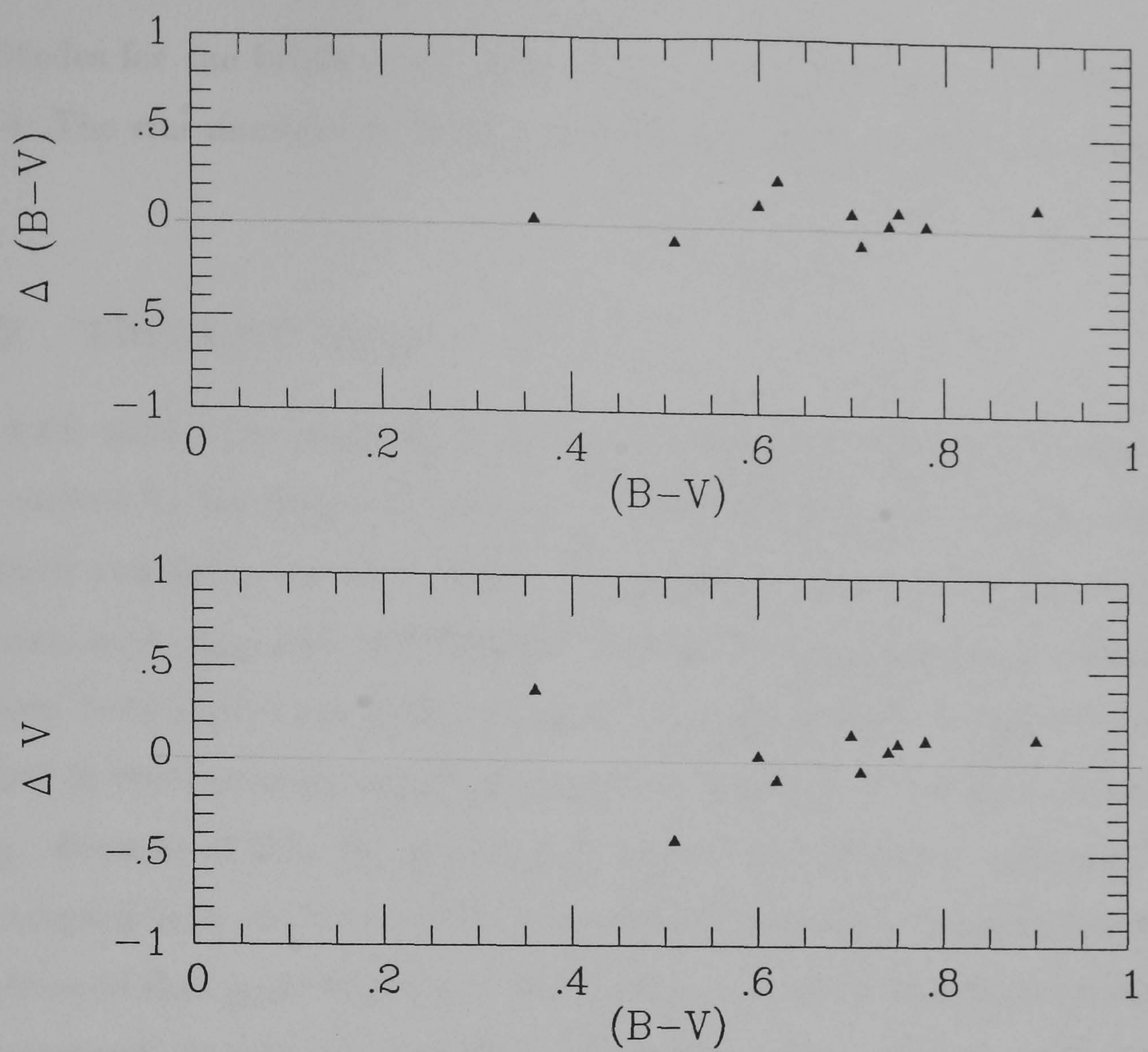

Figure 3.9: A plot showing the difference between CCD measures from this study and the photoelectric measures of Cannon (1981).

fields studied, and comparisons of Cannon's magnitudes and colours with those derived herein show that the CCD system agrees with the earlier photoelectric observations to within $0\overset{m}{.}05$ in both magnitude and colour. This comparison is shown in Figure 3.9. The scatter in the magnitude differences is large ($\sim 0\overset{m}{.}1$), but the uncertainty in the photoelectric values must be nearly $0\overset{m}{.}1$, as can be seen from the scatter in figure 1 of Cannon (1981) where the photoelectric magnitudes of these stars are compared with their smoothed photographic measurements, taken from very deep AAT plates.

Although painstaking care was taken by Cannon (1981) in these observations, and their subsequent reduction, they were made at the faint limit of the 1.0 m telescope and two channel photometer combination used by Cannon. Furthermore, the crowded nature of this field makes conventional aperture photometry difficult, for precisely the same reasons that were discussed above, for the case of digital aperture photometry. Additionally, these stars are some of the faintest measured on the SAAO frames, and thus they have comparatively large photometric uncertainties associated with them (of the order of $0\overset{m}{.}03$ at $V = 17.5$). The derived

magnitudes for the bright stars measured in the SAAO fields are shown in Table 3.4. The star numbers in Table 3.4 correspond to the identifiers in Figure 3.2.

3.3.2 The AAT Data

The AAT data were originally intended as additional exposures to the region (O1) covered by the deep exposures in the WB and WR filter system, which are described and discussed below. The seeing during the V and B exposures was mediocre, averaging some 1.8″ FWHM, and the limiting magnitudes attained in the deep 500 s exposures of the region O1 are significantly brighter than those attained in the extremely broad passbands of the WB, WR system, in excellent seeing. Because of this, the positions of stars in the B and V exposures to O1 were adopted from the the previously measured WB and WR frames (see below). This ensured that many faint stars, which might otherwise have been missed, were still measured, and allowed even the most crowded of stellar groups to be resolved into their component members.

The exposures to the regions O2–O4 were shorter, and provided substantial overlap with both O1 and the SAAO fields, in order that the SAAO magnitude system could be transferred to the AAT observations. This strategy also allowed more bright stars to be measured in the regions O2–O4, expressly for the purpose of "filling in" the brighter regions of the CMD.

In order to aid the comparison of stellar magnitudes and colours from this set of observations with those made through the WB, WR filter set, it was decided to keep the "deep" AAT V, $(B-V)$ exposures in region O1 distinct from the other "short" exposures in regions O2–O4. These observations were all placed upon the same intrinsic magnitude scale by transferring the profile-fitted magnitudes from frame to frame using the substantial overlap between each. The uncertainty in this process is difficult to determine, but scatter in the magnitude differences from frame to frame indicated that it was of the order of $0\overset{m}{.}006$ for each transfer. As all the AAT frames overlap with each other to some extent, it is to be expected that the contribution to the zeropoint error from the transfer procedure would be no more than $0\overset{m}{.}009$, and considerably less for most of the measured stars.

N	V	(B-V)	N	V	(B-V)	N	V	(B-V)
1	13.15	1.06	2	13.19	1.19	3	13.27	0.59
4	15.28	0.80	5	16.93	0.70	6	15.24	0.78
7	17.37	0.85	8	17.01	0.98	9	16.68	0.72
10	15.90	1.08	11	16.87	0.73	12	16.24	0.64
13	15.62	0.75	14	17.14	0.68	15	17.69	0.91
16	17.57	0.67	17	15.92	0.72	18	16.49	0.74
19	15.80	0.90	20	16.77	0.75	21	17.86	0.53
22	17.26	0.92	23	17.32	0.68	24	17.92	0.52
25	17.49	0.92	26	18.21	0.62	27	18.34	0.70
28	18.18	0.54	29	17.86	1.24	30	17.67	0.71
31	18.16	0.51	32	18.02	0.57	33	18.37	0.55
34	18.51	0.49	35	18.56	1.04	36	17.66	0.76
37	17.19	0.83	38	17.87	0.91	39	18.44	0.78
40	18.52	0.60	41	18.20	0.64	42	18.26	0.63
43	18.16	0.47	44	17.93	0.80	45	18.08	0.75
46	16.50	0.77	47	15.15	0.87	48	17.53	0.70
49	16.21	0.63	50	16.55	0.89	51	17.58	0.60
52	17.35	0.74	53	15.54	0.92	54	17.01	0.78
55	16.88	0.69	56	14.48	0.67	57	16.46	0.73
58	17.39	0.62	59	17.47	0.71	60	16.94	0.80
61	17.59	0.56	62	16.07	0.80	63	18.02	0.58
64	18.20	0.71	65	17.55	1.03	66	18.37	0.55
67	18.36	0.56	68	18.41	0.52	69	18.25	0.56
70	18.74	0.56	71	18.24	0.53	72	18.21	0.85
73	17.91	0.53	74	17.06	0.75	75	18.09	1.11
76	16.16	0.90	77	18.51	0.61	78	14.54	0.92
79	15.00	0.15	80	18.30	0.52	81	18.25	0.55
82	18.35	0.78	83	18.13	0.59	84	18.34	0.50
85	18.56	0.36	86	18.41	0.44	87	14.59	0.94
88	14.88	0.20	89	14.33	0.66	90	12.84	1.16
91	16.19	1.31	92	14.65	0.80	93	17.21	0.70
94	16.21	0.71	95	18.24	0.71	96	17.39	0.79
97	18.22	0.55	98	18.35	0.54	99	18.54	0.82
100	18.61	0.49	101	17.01	0.71	102	18.31	0.72
103	17.51	0.65	104	18.38	0.53	105	17.84	0.66
106	18.01	0.58	107	18.48	0.47	108	18.30	0.64
109	18.83	1.03	110	18.51	0.42	111	18.79	0.74
112	19.02	0.34	113	18.69	0.44	114	18.45	0.61
115	12.11	0.74	116	17.74	0.15			

Table 3.4: The SAAO colour-magnitude data. The star numbers correspond to those in Figure 3.2.

Instrumental Transformations

The AAT data were transformed to the same magnitude system as the reduced SAAO observations by comparing the measures of overlapping bright stars. This method—effectively using these stars as local secondary standards—meant that it was unnecessary to apply first order extinction corrections to the AAT data. The second order extinction coefficients were also negligible over the range of airmass involved (R.J.Dickens, private communication). The transforms were determined, using a linear least squares fit, to be,

$$V = v - 3.402(\pm 0.004) + 0.032(\pm 0.008)(b - v)$$

and

$$(B - V) = 1.092(\pm 0.008)(b - v) + 0.029(\pm 0.006).$$

The data from the AAT short exposures is shown in Table 3.5. The positions are given for each AAT CCD field in which a star appears, and are in pixel x and y coordinates. Where applicable, SAAO identifiers are also given (the numbering system is that of Figure 3.2). The colour magnitude diagram for the AAT exposures made in March 1986 is shown in Figure 3.10. The quality of the AAT faint MS colour-magnitude data is inferior to that of the WB, WR observations (see below); because of this (and additional reasons, outlined in Section 3.4.3) the faint AAT B, V data is not tabulated.

3.4 The WB,WR Observations of ω Centauri

In order to delineate the cluster main sequence to fainter limits, the same broad band, WB and WR filter set of Penny and Dickens (1986) was used to make deep observations of field O1. Once again the exposures were made using the 3.9 m AAT and prime focus CCD.

3.4.1 The WB,WR Filter System

The WB and WR system was specifically designed to provide high transmission over large wavelength ranges, taking advantage of the full wavelength range of the CCD's response, and giving an increased light flux at the CCD. The WB passband is defined by the transmission of a 2 mm 80% $CuSO_4$ filter, whilst the

NAME	02 X	02 Y	03 X	03 Y	04 X	04 Y	V	(B-V)	SAAO NAME
1	59	430	-	-	-	-	16.51	0.79	S46
2	177	395	55	393	-	-	16.20	0.63	S49
3	208	407	86	405	-	-	16.55	0.95	S50
4	202	412	80	410	-	-	17.55	0.64	S51
5	181	436	59	434	-	-	17.37	0.75	S52
6	168	493	46	491	-	-	17.34	0.78	S23
7	261	437	139	435	17	433	15.54	0.93	-
8	234	408	112	406	-	-	17.39	0.60	S58
9	228	379	106	377	-	-	16.46	0.75	S57
10	245	374	123	372	2	370	14.47	0.68	S56
11	278	368	156	366	34	363	16.90	0.72	S55
12	260	406	139	404	16	402	17.50	1.03	S65
13	298	426	176	424	53	421	17.00	0.77	S54
14	252	244	130	242	8	239	15.02	0.16	S79
15	213	256	91	254	-	-	14.55	0.92	S78
16	206	208	84	207	-	-	17.86	1.16	-
17	220	184	98	182	-	-	17.44	0.88	-
18	178	191	56	189	-	-	14.73	0.95	-
19	110	201	-	-	-	-	17.17	0.70	-
20	83	259	-	-	-	-	16.23	0.88	S76
21	91	253	-	-	-	-	17.75	0.62	-
22	21	132	101	130	-	-	15.76	0.82	-
23	132	128	10	126	-	-	17.12	0.81	-
24	143	131	21	129	-	-	17.58	0.68	-
25	142	170	20	167	-	-	17.70	0.58	-
26	211	138	89	136	-	-	15.73	0.82	-
27	254	103	132	102	10	99	17.05	0.94	-
28	257	54	135	52	13	50	14.84	1.15	-
29	264	59	142	57	19	54	17.93	0.60	-
30	210	56	89	54	-	-	17.46	0.76	-
31	304	148	182	146	59	143	14.89	0.24	-
32	295	163	174	161	51	158	14.82	0.94	-
33	92	327	-	-	-	-	12.64	1.18	-

Table 3.5: The AAT short exposure colour magnitude data. The positions are shown as X and Y in pixel coordinates for each AAT field. Where the star has also been measured in the SAAO exposures, its identifying number is given in the far right hand column.

NAME	O2 X	O2 Y	O3 X	O3 Y	O4 X	O4 Y	V	(B-V)	SAAO NAME
34	70	315	-	-	-	-	17.70	0.58	-
35	63	297	-	-	-	-	17.11	0.73	S74
36	59	358	-	-	-	-	15.18	0.86	S47
37	143	394	21	392	-	-	17.55	0.72	S48
38	-	-	227	268	104	266	16.22	0.69	S94
39	-	-	202	477	80	475	16.61	0.76	-
40	-	-	210	502	88	499	17.83	0.55	-
41	-	-	267	442	144	440	17.06	0.73	-
42	-	-	292	443	169	440	17.08	0.34	-
43	-	-	265	416	142	412	17.98	0.60	S106
44	-	-	288	401	165	399	14.86	0.18	S88
45	-	-	288	381	166	379	17.50	0.66	S103
46	-	-	256	396	134	393	14.59	0.92	S87
47	-	-	240	376	118	373	17.87	0.55	S105
48	-	-	314	319	192	316	17.45	0.70	S96
49	-	-	288	249	166	246	17.19	0.68	S93
50	-	-	252	196	130	194	14.97	0.80	-
51	-	-	285	148	163	145	17.37	0.78	-
52	-	-	318	418	196	416	14.31	0.65	S89
53	-	-	-	-	224	463	16.85	0.87	-
54	-	-	-	-	298	486	17.88	0.75	-
55	-	-	-	-	242	373	17.03	0.75	S101
56	-	-	-	-	240	319	12.82	1.14	S90
57	-	-	-	-	267	342	12.07	0.57	S115
58	-	-	-	-	226	279	16.18	1.32	S91
59	-	-	-	-	251	284	17.65	0.20	S116
60	-	-	-	-	288	298	17.42	0.67	-
61	-	-	-	-	247	202	16.56	0.83	-
62	-	-	319	229	201	226	14.64	0.79	S92
63	-	-	-	-	227	185	16.21	0.90	-
64	-	-	-	-	257	147	17.87	0.88	-
65	-	-	319	156	197	154	17.03	0.77	-
66	-	-	-	-	233	52	17.56	0.69	-

Table 3.5 (continued).

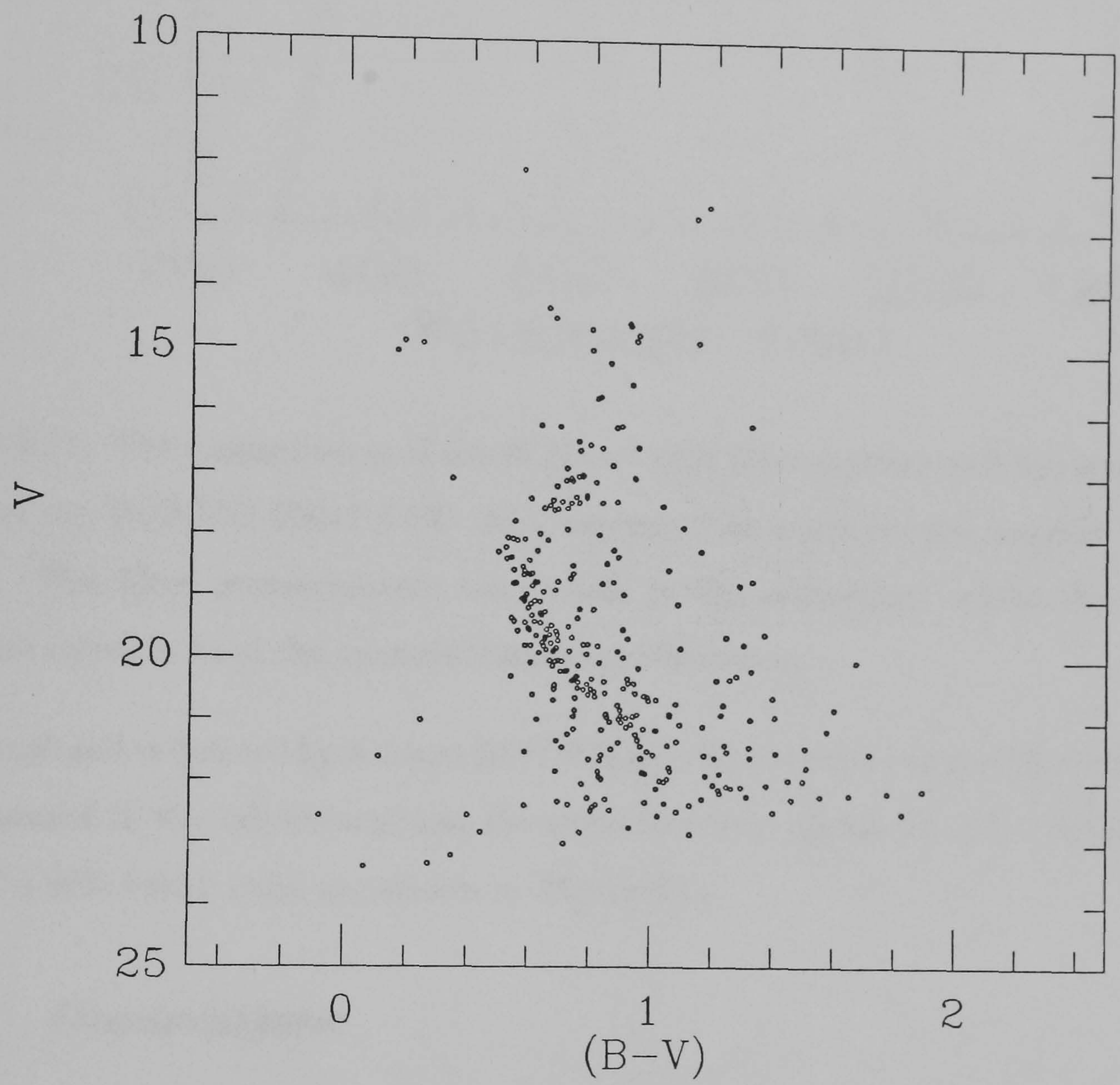

Figure 3.10: The CMD for the AAT observations made in March 1986.

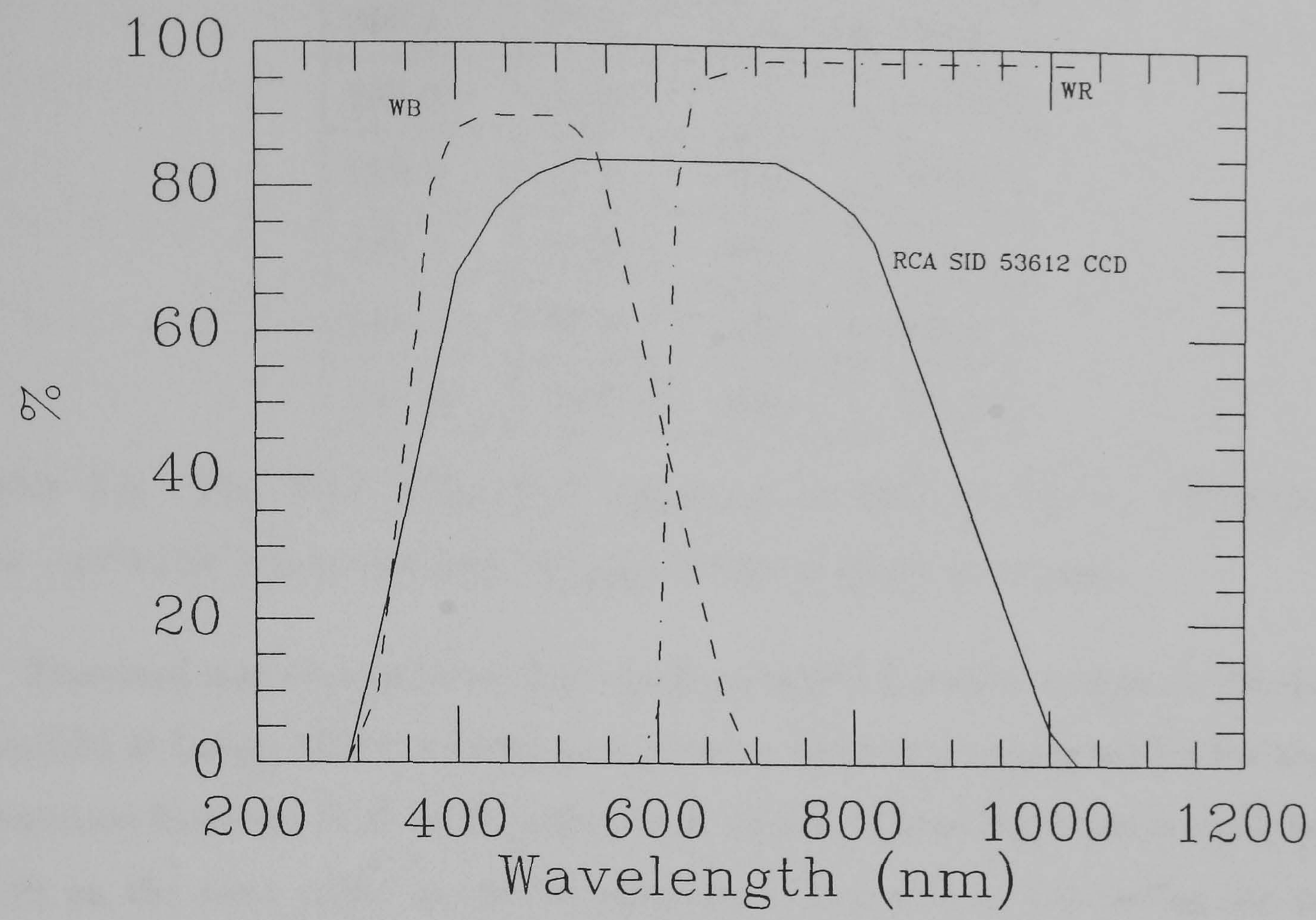

Figure 3.11: The transmission of the WB and WR filter system, and the response curve of the RCA SID 53612 CCD chip, expressed as a percentage, against wavelength. The filter measurements were made in the laboratory, whilst the CCD response curve is from the manufacturers specifications.

WR passband is defined by a 2 mm RG610 filter. The transmission of these filters, as measured in the laboratory, and the manufacturers figures for the response of the RCA SID 53612 chip, are shown in Figure 3.11.

3.4.2 Observations

The observations were made on the night of the $25^{th}/26^{th}$ of May 1985, and the relevant details of the exposures are shown in Table 3.6. The exposures consisted of four long, and two short, in both the WB and WR passbands, to the field O1 (see Figure 3.3). The seeing was exceptionally good, below 1.8 pixels FWHM, *ie.* 0.9″ FWHM, reaching $\sim$ 0.7″ during exposure 249–3. Taking into account the convolution of the actual seeing profile with the scale size of the pixels, the true FWHM seeing was approximately $\sqrt{0.7^2 - (\frac{0.5}{\sqrt{2}})^2} \approx 0.6''$. This means that although these are relatively short exposures, the limiting magnitude attained is very deep.

Run No.	Filter	Exposure	UT_{start}
249–1	WB	60s	08:21
249–2	WR	60s	08:26
249–3	WR	500s	08:28
249–4	WB	500s	08:37
249–5	WB	500s	08:47
249–6	WR	500s	08:55

Table 3.6: The AAT WB, WR exposures to field O1 ($\alpha = 13^h21^m36.8^s$, $\delta = -47°11'54''$) in ω Centauri. Exposure time is given in seconds.

Standard star observations were made to bright E-region standards (Menzies, Banfield & Laing, 1980) in order to determine the colour equations for the transformation from the WB, WR system to V and B. These observations were made both on the same night as the observations of O1, and earlier during the same observing run. That an adequate transform can be attained for metal-poor cluster stars has been shown by Penny and Dickens (1986), who observed a sequence of metal-poor standards, and showed the results to be consistent with the measurements of the relatively metal-rich E-region stars.

Long night-sky exposures were made to sparse fields to calibrate the fringe distribution in these passbands, and dome flat-fields were taken. Bias and dark exposures were also made. No preflash corrections were necessary at the signal levels involved.

3.4.3 Data Reduction

The CCD exposures were pre-processed as described in Chapter 2. The CCD bias frame was subtracted, its level being normalised to the horizontal overscan strip of the image frame. The exposure was then divided by an average flat field frame, which had been normalised to an mean level of unity. Defringing was accomplished by subtracting an average fringe frame, which had been suitably scaled by comparison with a small area of the image frame, in which night-sky-line fringes were evident. Lastly, the column-type defects on the chip's surface were interpolated over, as were the larger cosmic ray events. One problem caused by the excellent seeing was that it was difficult to reliably differentiate between

the smaller cosmic ray events, and faint stars. Therefore, only the larger cosmic ray "spikes" were thus processed, relying on the multiple exposures to reduce the effect of the smaller events as noise.

The Colour Transformations

The E-region standards were measured by digital aperture photometry. Extinction corrections derived from the AAT mean standard extinction figures (A.J.Penny, private communication) were applied to these measures. The relations used were,

$$WB = wb - k_{wb} \sec z$$

and,

$$WR = wr - k_{wr} \sec z.$$

Where wb and wr are the instrumental aperture magnitudes of the standard stars, and k_{wb} and k_{wr} are 0.260 and 0.110 respectively.

No correction was made for second order extinction effects—the mean difference in airmass between the standard star and cluster observations was of the order of 0.09, leading to an uncertainty of, at the most, $0\overset{m}{.}003$ in the extinction corrected data. The extinction corrected instrumental magnitudes and colours were then fitted to the standard values, using a cubic polynomial. The resulting transformations were,

$$V = WB - 0.234(WB - WR) + 0.076(WB - WR)^2 + 0.008(WB - WR)^3,$$

and

$$(B - V) = 1.047(WB - WR) - 0.041(WB - WR)^2 - 0.152(WB - WR)^3.$$

The residuals between these fitted equations and the observations are shown in Figure 3.12.

The range in $(B - V)$ colour of the observed E-region standards was $\sim 1\overset{m}{.}3$ The faintest cluster observations were significantly redder than this, hence, for such stars the colour transformations are ill-defined. This will not unduly affect the results derived in this thesis; only the very faintest stars, from which no quantitative colour-dependent measurements were made, are involved. Similarly, the metal-poor standards of Penny and Dickens (1986) do not extend in colour beyond $(B - V) \approx 0.8$, and thus there is an increased element of uncertainty in the

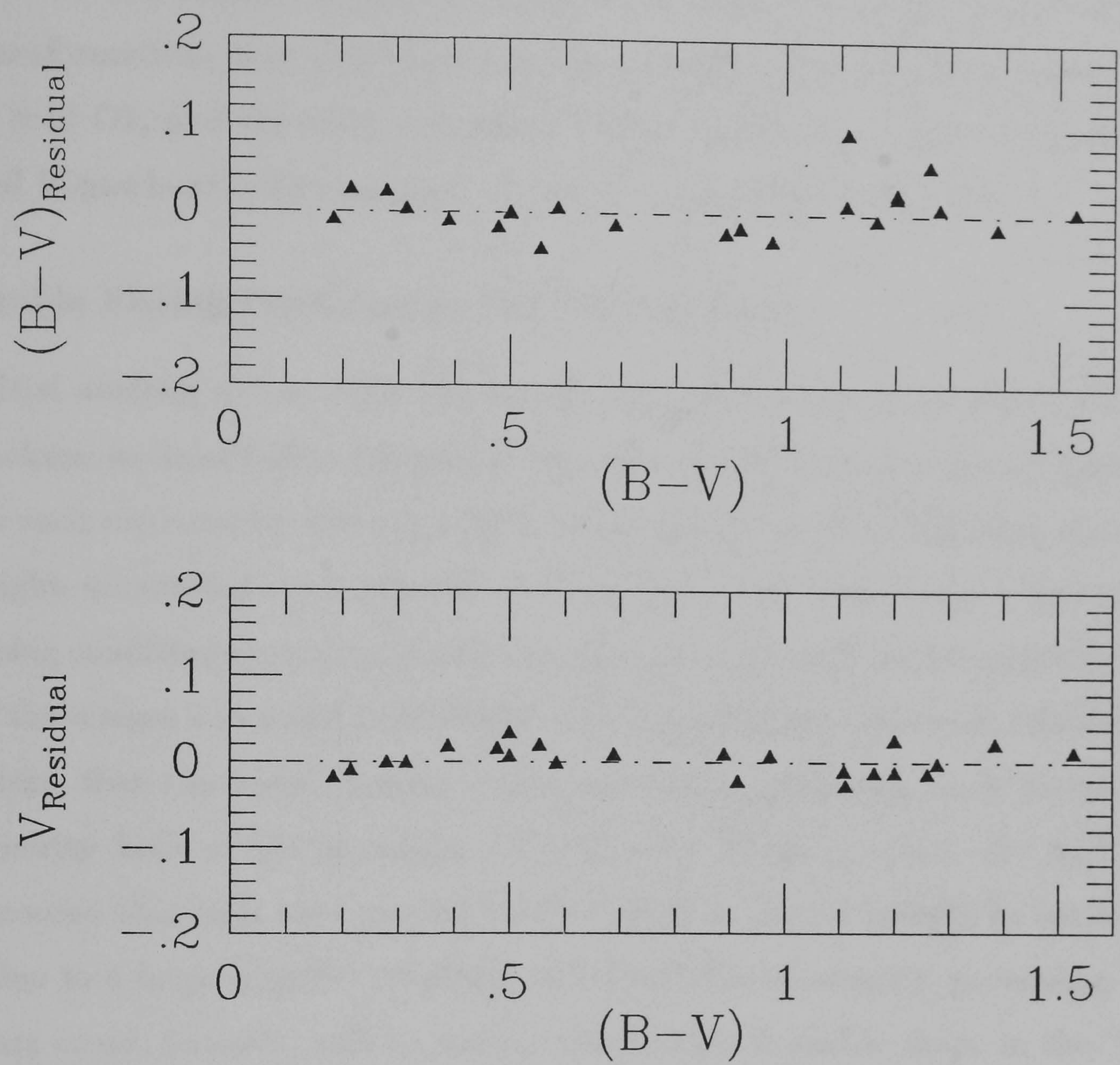

Figure 3.12: A plot showing the residuals to the derived WB, WR colour equations as determined from standard star observations. The residual is in both cases the difference between standard and wide band magnitude, plotted against the standard colour.

colour transformation beyond this value. Unfortunately, detailed comparisons of the faint observations of field O1 in the WB, WR and the Johnson B,V system were not possible. The uncertainty in the B,V observations is too large at the faint, red end of the MS. Again, however, this uncertainty does not unduly affect the quantitative analysis in the present work. The zeropoints of the colour transformations were determined by comparing the magnitudes of stars common to field O1, and the fields containing brighter stars measured in the Johnson B and V passbands. The accuracy of this process is discussed below.

Profile Fitting Photometry–the WB,WR Data

Initial analysis of the CCD frames was performed with the LORENTZ software package, as described in Chapter 2. The mean profile parameters were determined for each exposure by obtaining the average best-fit analytic PSF from about 8–12 bright, uncrowded stars, selected by visual inspection of the images. The excellent seeing conditions prevalent during the exposures ensured that the geometric extent of the images was small, minimising crowding problems. However, this same fact meant that the cores of many stars were either saturated, or in excess of the linearity limit of the particular CCD in use. Pixels in which the ADU count exceeded this limit were automatically flagged as invalid (simply by setting their value to a large negative number), and ignored in subsequent processing. These stars could, however, still be used to determine the profile shape in the "wings" of the distribution.

When satisfactory profile fits had been obtained, one of the images (No. 3, chosen as it appeared to have the faintest magnitude limits) was inspected and the positions of as many stars as could be seen on the frame were recorded, for later submission to the LORENTZ measuring program LORMAG. This was done with an interactive program, using a cursor to identify star positions upon a VAX architecture computer running STARLINK[1] software, and a Sigmex Advanced Raster Graphics System (ARGS) display. This process is extremely time-consuming, but at this stage of software development, there was no automatic algorithm for

[1]STARLINK is the United Kingdom astronomical community's network of data processing computers. At Leeds, the University Computing Service and the Physics Department Astrophysics Group jointly operate a computer of similar architecture, running the same software as *bona fide* STARLINK machines, for the purposes of astronomical data reduction.

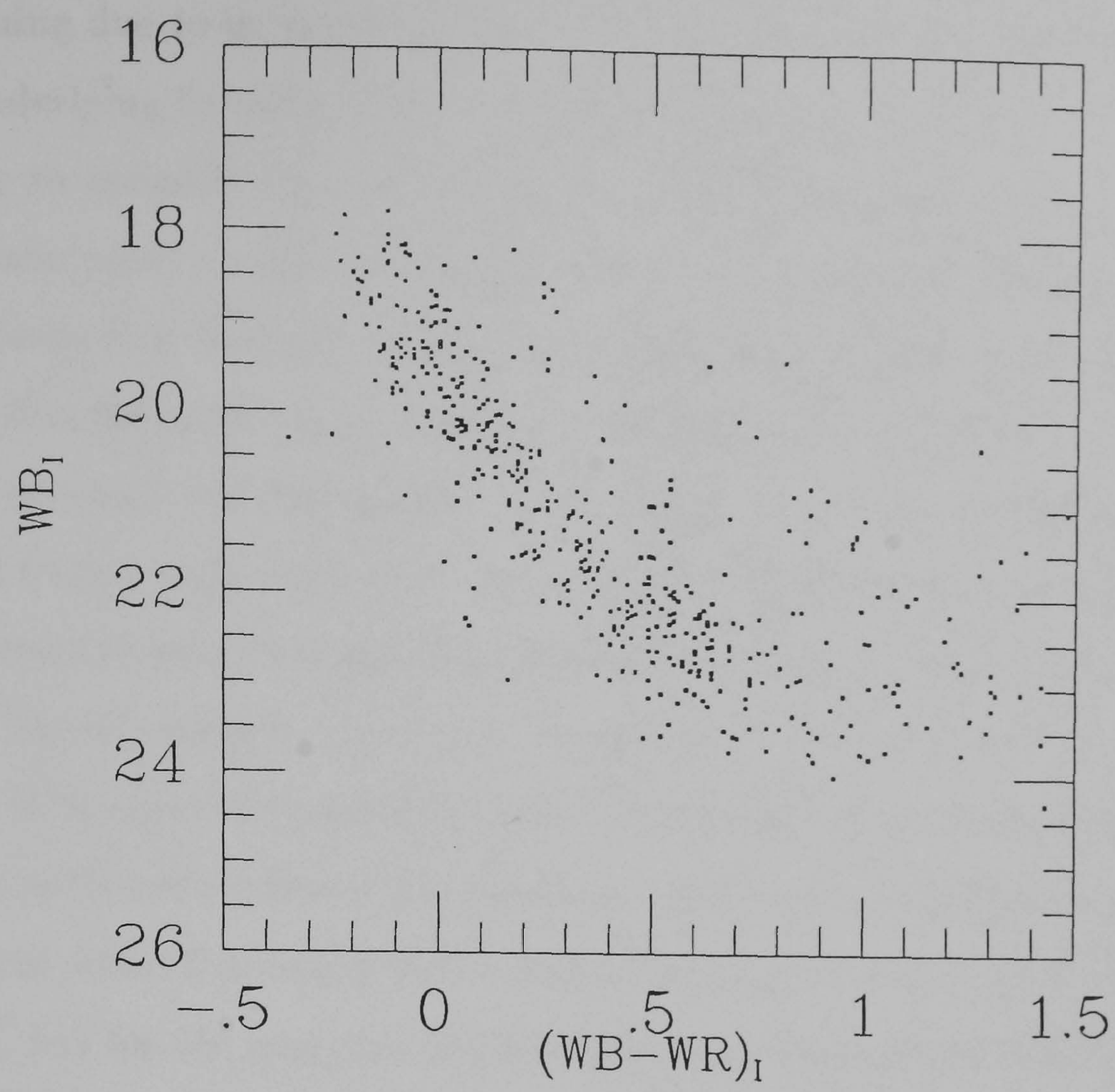

Figure 3.13: The WB,WR instrumental CMD of ω Centauri. Note the large spread in colour of the main sequence.

starfinding as discerning as the human eye. Some seven hundred and fifty likely stellar images were identified and, for each frame, submitted to the analysis of the LORMAG measuring program. The resulting magnitude estimates were treated as described in Chapter 2. Magnitude estimates of the same stars, on different frames, were averaged. The profile-fitting program returns a measure of the goodness of fit for each stellar measurement as a parameter, RMS. As its name implies RMS is the root mean square residual between the profile fit and the stellar image, and it can be used to make an assessment of the quality of fit for each star. Those stars with unusually large RMS residuals for their brightness were discarded, as were those stars which had unusually large differences in magnitude from frame to frame.

One feature of the resulting CMD was strikingly obvious, even upon examination of the plot of instrumental magnitudes and colours. There was a very wide spread in apparent colour index along the main sequence. This is shown in Figure 3.13. Figure 3.13 shows that even at the faint end of the main sequence,

the broadening due to increased photometric uncertainty is slight in comparison with the underlying breadth of the main sequence.

In order to estimate the uncertainties in the photometric measurements of the programme stars, artificial starfields, containing stars with approximately the same luminosity function and degree of crowding as the cluster stars, were made, and analyzed in the same manner as the actual CCD observations. These artificial starfields were made by adding fake stellar images to a "sky" background which was derived from a region of a WB exposure which had had all detectable stellar images subtracted from it during the LORMAG fitting process, as described in Chapter 2. The star images were computer generated, with profiles similar to those in the WB, WR exposures, and with added Poissonian noise. The background sky distribution as described above is not really a valid one, as it already contains the signal element from those stars in the real WB exposure which were too faint to be detected, but for the purposes of this experiment is adequate. The fake stellar images were placed at random positions on the "sky" image, which was some 100 pixels square. Five such frames were made and analyzed, containing over 800 artificial stellar images in total. The same analysis techniques as were used for the programme data were employed, and afterwards the output magnitudes from the fitting program were compared with the "known" magnitudes of the artificial stars. This process also allowed the "completeness rate" of the observations to be investigated, *i.e.* the percentage of recovered stars as a function of magnitude, an important parameter in the discussion of the cluster luminosity function (see Section 4.1.5 below). The estimates of internal photometric error, as derived from these simulations, are shown in Table 3.7. The internal photometric errors shown in Table 3.7 are clearly, for the bright part of the main sequence, much too small to cause the observed spread in colour.

At first it was suspected that there might be an astrophysical explanation of the unduly large width of the MS, namely that it was a consequence of large scale variations in stellar CNO abundances, which might cause a large spread in the main sequence colours as determined from these wide passband filters. The observed spread is too large to be associated with the differential line blanketing and temperature effects associated with any reasonable metallicity variation. That a spread in CN band strengths exists in evolved stars has been shown (see for example, Smith, 1987). The existence of correlations of CN band strength with

WB	σ_{WB}	$\sigma_{(WB-WR)}$
< 18	0.0021	0.0030
18–19	0.0032	0.0045
19–20	0.0048	0.0065
20–21	0.013	0.017
21–22	0.024	0.037
22–23	0.065	0.083
23–24	0.16	0.22
24–25	0.33	0.39

Table 3.7: The uncertainties in the WB,WR photometry as derived from analysis of simulated starfields (as discussed in the text).

heavy element abundance within ω Cen has also been demonstrated (Norris and Smith, 1983, Norris and Freeman, 1983), and suggests strongly that the observed variation is, at least in part, primeval in nature. Initial calculations, based upon colours generated from synthetic spectra, from appropriately composed stellar models, by R.J.Dickens, suggested that this was a possibility, but that variations in CN abundance much larger than those seen in the earlier studies of evolved stars would be required to produce such a large spread in colour.

In effecting the transformation from instrumental to standard magnitude, the reason for the apparent spread in colour of some $0\overset{m}{.}2$ became evident. When performing the matching of the profile-fitted magnitude scale to that derived from aperture photometry, as described above, an unduly large scatter in the differences between the two systems, of the order of $0\overset{m}{.}05$ rms, was observed. When these differences were examined as a function of position within the CCD frame, specifically against the CCD x-coordinate, it immediately became obvious that there was a systematic nature to these residuals. Figure 3.14 illustrates this for one particular CCD exposure (No. 5), showing a variation of some 10% in photometric zeropoint from one side of the frame to the other.

The most obvious source for such a systematic discrepancy with position within the CCD frame is a variation of stellar profile across the frame. The conventional wisdom has been (see, for example, Tody, 1980) that the stellar profile can be considered to be geometrically invariant across the CCD frame, and hence, photo-

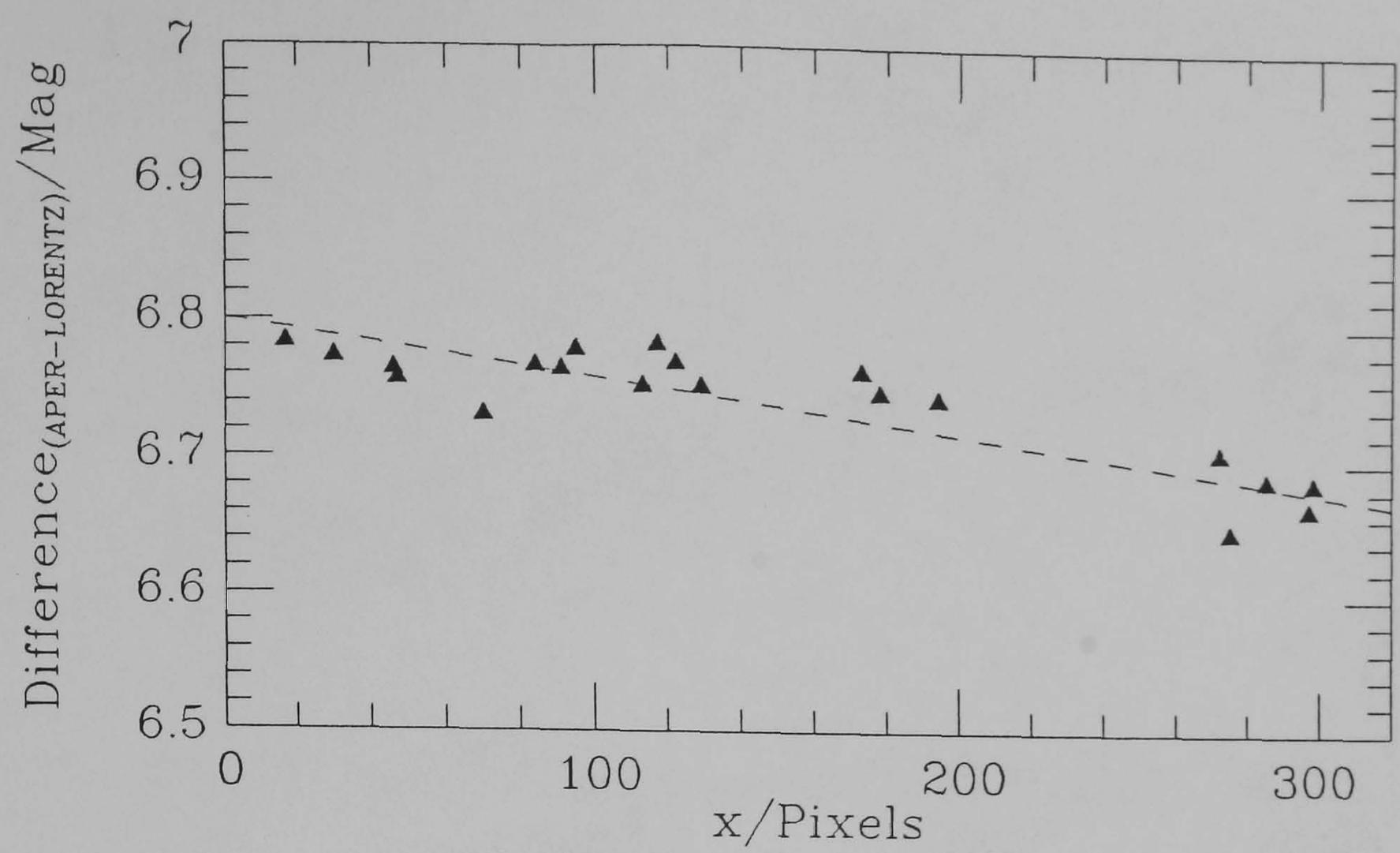

Figure 3.14: Difference between aperture and profile fitting photometry versus CCD x-coordinate for frame 249–5. A systematic variation with x-coordinate can be seen.

metric processing and analysis software has been designed to deal only with fixed profiles.

To test the hypothesis that a systematic variation of star profile was responsible for the variation of photometric zeropoint, another, larger sample of bright, isolated stars were fitted with Lorentzian/Gaussian profiles, using the LORENTZ program LORFIT. This enables the best-fit values for all nine of the Lorentzian profile parameters (see Section 2.7.2) to be obtained for each individual star. The usual procedure, and that which was followed previously, is to make an estimate of the analytic PSF for the CCD exposure, by taking a weighted average of these individual fits. In this case, however, these parameters were examined as a function of position in the frame. Figure 3.15 shows the variation of the profile r_x parameter with the frame x-coordinate for frame 249–5. A variation of some 20% in r_x across the frame is evident. It should be noted that there is also a variation of r_x with the frame y-coordinate, albeit of much smaller amplitude, and this serves to increase the scatter about the mean line, which is a best fit by eye to the data. The problem was found to affect all of the six CCD frames obtained through the WB,WR filters on that night, although to a varying degree, with the mean variation at approximately 15% across the frame. All of the characteristic parameters of the Lorentzian PSF seemed to be geometrically variant, but seemed

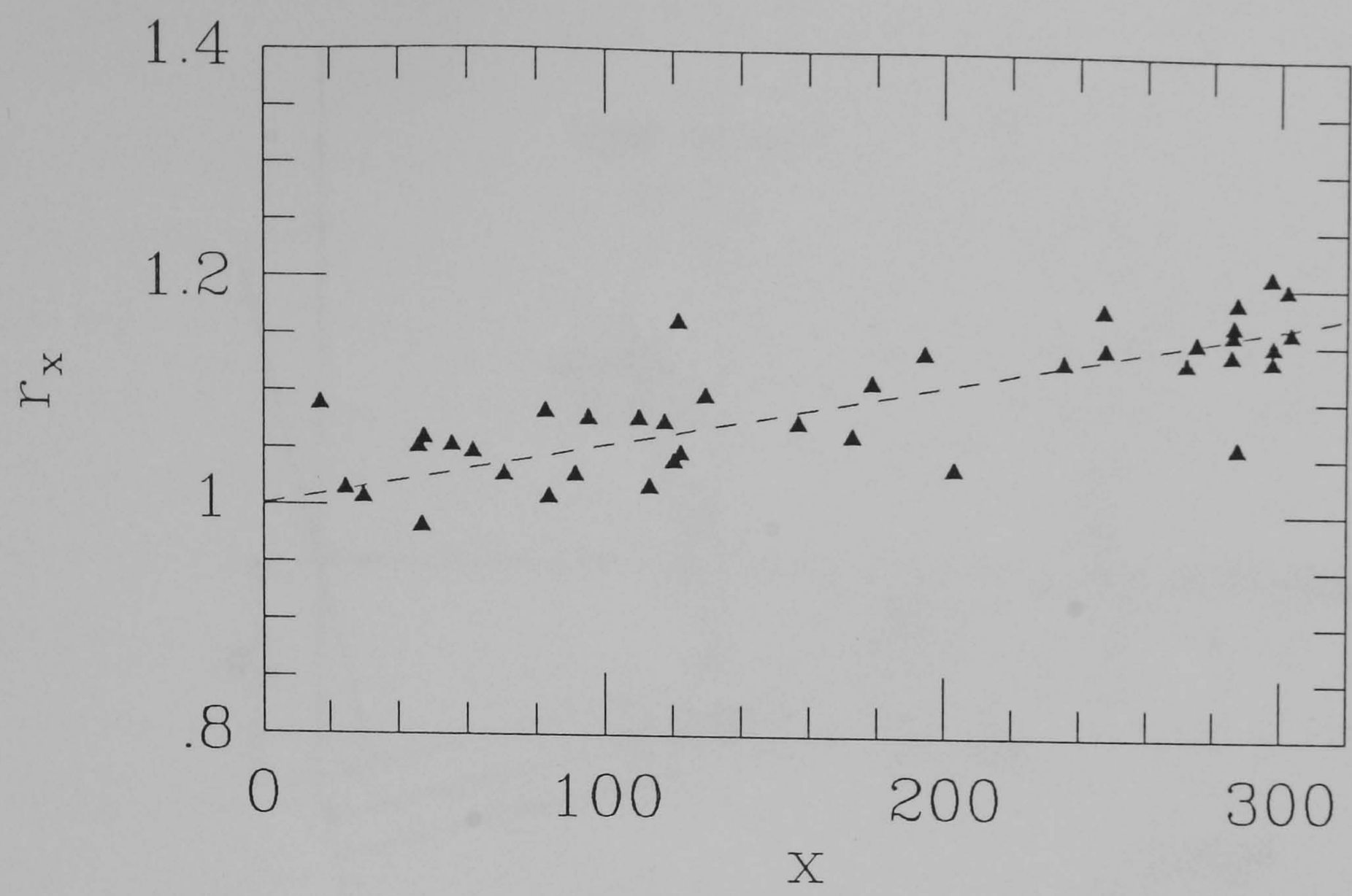

Figure 3.15: The variation of profile parameter r_x with CCD x-coordinate for frame No. 5. There is a variation of some 20% in r_x across the CCD frame which is apparently a linear first order function of x (and y). The line drawn through the points is a best fit by eye.

to be a simple function of x and, to a lesser extent, y-coordinate.

Such a variation in photometric zeropoint due to the changing nature of the PSF across the chip has been reported by Stetson (1987) for CCD data from the Kitt Peak No.1, 0.9 m telescope. Stetson gives further details of modifications to his DAOPHOT analysis code which allow the application of a linearly varying PSF across the CCD frame. A 10% change in effective photometric zeropoint is large enough to render "fixed-profile" photometry from such frames worthless as a precision tool for studying the main sequence of ω Cen.

The most obvious cause of such a profile variation would seem to be misalignment of the CCD chip in the focal plane of the telescope. Whether such a large change can be brought about in this way can be examined by simple geometrical optics. The 10% change in r_x across the chip is analogous to a change in characteristic radius of the actual profile by some 10%, or in this case $\sim$ 0.1 pixels, or 2.5μ. At the prime focus of the AAT, which is an $f/3.5$ beam, a 2.5μ change in the lateral focal position is equivalent to a change of $2.5 \times 3.5 \approx 9\mu$ in focal position, in the normal direction to this, *i.e.* in the in-beam direction. If the chip were mounted askew, such that its surface were not parallel to the image plane, then such a path difference in the in-beam direction might occur. To produce a

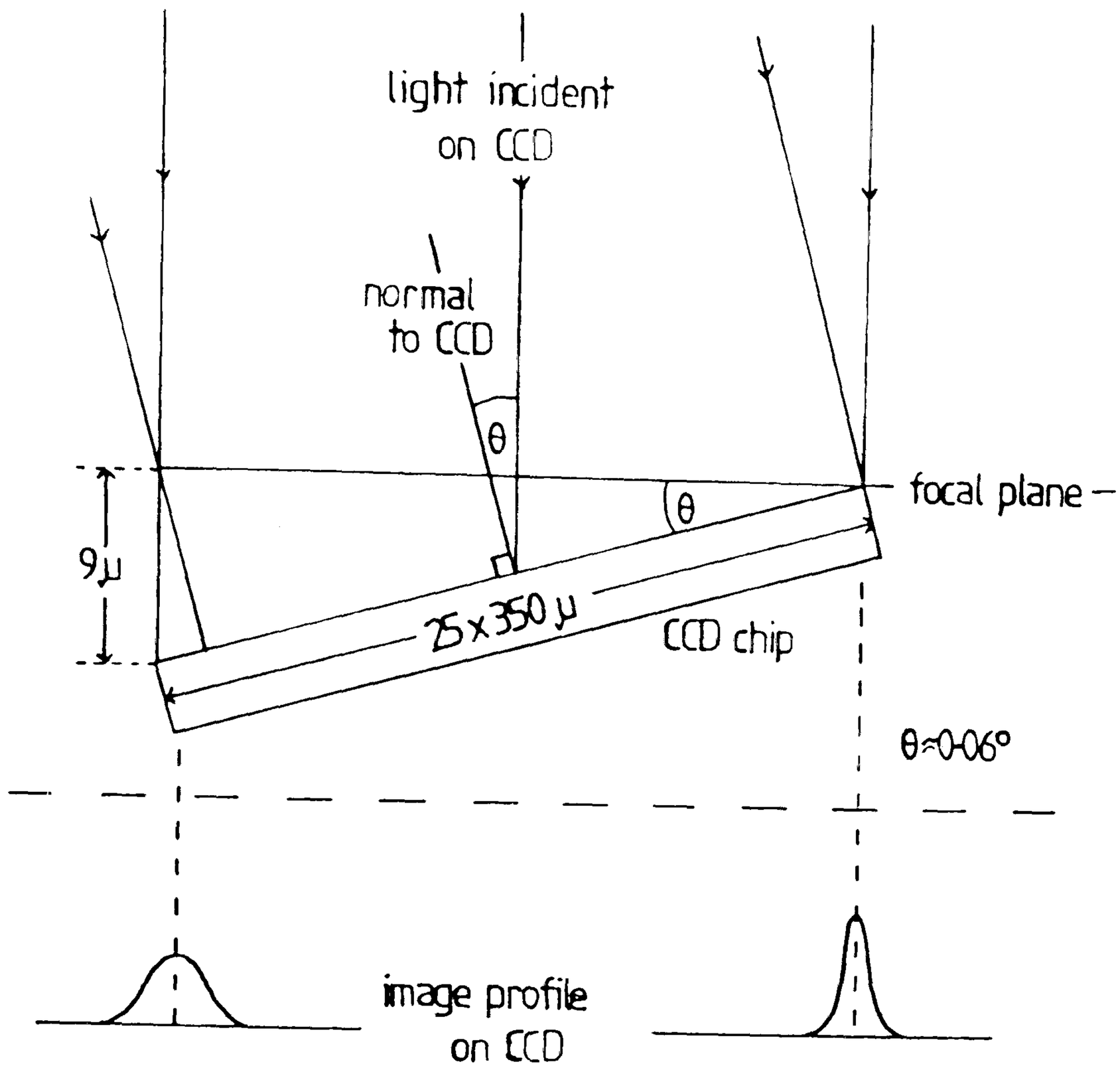

Figure 3.16: Schematic diagram showing the postulated misalignment of the AAT CCD chip. As explained in the text, a small difference between the normal drawn from the chip's surface, and the beam direction at the $f/3.5$ prime focus, can cause a relatively large change in PSF shape across the chip, and hence in the magnitude derived from profile-fitting.

difference of 9μ in beam path across the chip, *i.e.* from $x = 1$ to $x = 320$, would thus require the chip to be misaligned by some $(\frac{9}{25 \times 320} \times \frac{180}{\pi}) \approx 0.06°$. This is shown schematically in Figure 3.16. To mount such a device within these slight tolerances is a difficult task, requiring special precautions. The quoted accuracy of the CCD mounting in the AAT–RGO CCD camera is $\leq 10\mu$ (R.J.Dickens, private communication), thus it is entirely feasible that such an effect could be produced by a simple misalignment of the chip in its mounting.

Additionally, it can be seen from the above argument that the "depth of field" of such an optical arrangement is critically small. The method of focussing the CCD for these exposures, was to change the focus position, for each filter combination, until visual inspection of the star images showed the focussing to be

satisfactory. This position, as read from the encoders of the focussing system, was then used for subsequent observations through that filter. Because of the difficulty of judging when the image was "in focus", the chosen focus may be offset appreciably from the optimum focus position, exacerbating the profile problem, and presumably explaining the linear variation across the chip, where a more complex form of the profile variation might be expected near to the true focus.

It is probable that the variation in profile, and its effect upon the photometric zeropoints of the frames concerned, is only so drastically noticeable because of the extremely good seeing at the time. The change in image profile FWHM can be considered to be due to a convolution of some varying Gaussian-like function, representing the variation due to the departure of the chip surface from the focal plane, which to a first approximation should be true, with a constant PSF dependent upon the seeing and optical performance of the telescope. The FWHM size of the function, s, causing this change in profile, of the order of $0.05''$ for a FWHM of $0.7''$, is given by,

$$s \approx \sqrt{0.75^2 - 0.7^2} \approx 0.27''.$$

So in the seeing conditions normally prevalent, where the FWHM may be $1.5''$, say, the increase in profile FWHM across a frame might be approximated by,

$$\Delta s \approx \sqrt{1.5^2 + 0.27^2} - 1.5 \approx 0.02''.$$

In fractional terms, this is approximately one fifth of the size of the effect observed when the seeing is $0.7''$, which, were zeropoint error to also scale in this way, would represent a change of photometric zeropoint of some $0\overset{m}{.}02$ across the CCD frame. Obviously this is much harder to identify than in the case where extremely good seeing renders this effect relatively conspicuous.

The V and B exposures taken in March 1986 were thus examined to see if any evidence of varying profiles or photometric zeropoints was present. Both the stellar profiles, and differences between profile-fitted magnitudes and those derived via aperture photometry, showed similar variations, albeit reduced in amplitude, to those present in the WB, WR data. The estimated change in zeropoint for these data from one side of the frame to the other was of the order of $0\overset{m}{.}01$–$0\overset{m}{.}04$, and seemed to be rather more variable than in the case of the WB, WR data.

Although the linear nature of the variation of photometric zeropoint across the wide-band frames meant that in all probability a simple position-dependent cor-

rection could be applied to the magnitude of each star, as derived by profile-fitting, it was decided to re-analyze the data, taking into account the profile variation. Unfortunately the lengthy period required precluded the re-analysis of both the wide-band, and the conventional B, V observations, and hereafter the March 1986 B and V observations to region O1 will be dispensed with.

The design of the LORENTZ software package is such that it is not feasible to attempt the measurement of many stellar images, each with a different analytic PSF. Fortunately, by the time such an analysis became necessary, A.J.Penny had made radical improvements to his earlier profile fitting software, and pre-release versions of his STARMAN photometric package were available (see Penny, 1987).

STARMAN is a complete reduction package for the photometric analysis of linear intensity-scaled digital data, and its profile-fitting photometry routines are based upon the successful LORENTZ code. However, STARMAN represents a substantial improvement to LORENTZ in many respects. The chosen profile is once again a rotated elliptical Lorentzian, with the optional addition of a wider, low Gaussian to represent the wide "wings" of the profile. To cater for large optical, or guiding aberrations, the profile also incorporates an empirically derived "map" of small corrections to be applied to the analytic profile. This profile map is sampled on a grid which is dependent upon the radius of the Lorentzian profile applied. For small image radii, *i.e.* in good seeing, the map is sampled on a grid finer than the actual pixel grid, by interpolation between the pixel values. Thus the effects of undersampling in the data are accounted for in the empirical profile map, as well as in the analytic part of the profile.

STARMAN has been designed, in part, to cater for the special requirements of analysis of data from the Hubble Space Telescope (HST). The PSF at the focal plane of the HST photometric imaging detectors, namely the Wide Field/Planetary Camera (Westphal, 1982) and the Faint Object Camera (Macchetto, 1982) will be entirely dominated by the wavelength dependent optical performance of the telescope and detector combination (see, for example King, 1983). Stars of widely differing colours will therefore have significantly different image profiles when observed through broad band filters. Therefore, to cater for this, the STARMAN photometry package has the ability to fit each measured star with an individually specified PSF, and can deal with both position, and colour dependent point spread functions.

The procedure adopted was as follows. First a sample of some 40 or so relatively bright, isolated stars was chosen by eye from the CCD frame to be measured. In the particular case of the WB, WR data this was not difficult due to the very good seeing. The profile parameters of these stars were then derived using the STARMAN program PROFILE. The full form of the fitted profile is,

$$I(x,y) = H\left(\frac{1}{1+d_1^{P(1+d_2)}} + QHe^{-d_3^{QP}} + F(x,y)\right) + A + Bx + Cy \qquad (3.1)$$

Where,

$I(x,y)$ is the value of the star profile at position x, y

$d_1 = \sqrt{(\frac{x_1}{RX})^2 + (\frac{y_1}{RY})^2}$,

$d_2 = \sqrt{(\frac{x_1}{PRX})^2 + (\frac{y_1}{PRY})^2}$,

$x_1 = (x - x_0)\cos(THETA) + (y - y_0)\sin(THETA)$ and

$y_1 = -(x - x_0)\sin(THETA) + (y - y_0)\cos(THETA)$.

$d_3 = \sqrt{(\frac{x-x_0}{QR})^2 + (\frac{y-y_0}{QR})^2}$.

QH is small, of the order ≈ 0.01, and

QR is large when compared to PRX and PRY.

$F(x,y)$ is the empirically determined profile "map".

and A, B, and C are the coefficients of a sloping, planar background.

Examination of the variation of the parameters describing the PSF showed that a first order linear function of x and y gave an adequate fit to the data, and a computer program was written to fit such functions to the data, using the method of least-squares fitting. The profile parameters RX, RY, P, PRX, PRY, and THETA were all fitted independently, but neither the wide Gaussian image aureolae, nor empirical profile map corrections were deemed to be changing significantly over any of the 6 data frames, and were therefore not fitted. Below are shown the equations governing the fitted profile for one particular WB frame, number 5.

$$\begin{aligned}
RX &= 1.005 + 0.00054x \\
RY &= 0.823 + 0.00048x - 0.00011y \\
P &= 2.30 - 0.00002x + 0.00016y \\
PRX &= 4.61 - 0.00171x + 0.00065y \\
PRY &= 5.22 - 0.00273x + 0.00126y \\
THETA &= -66.50 + 0.0072 - 0.0118y
\end{aligned}$$

The stars which were formerly identified upon the CCD frames were now submitted to the STARMAN program MEASURE, to obtain the best-fit magnitude estimates using the chosen profile parameters. STARMAN returns a measure of the goodness of fit, RMS, for each measured star; this parameter was examined to check that there was no obvious correlation of quality of fit with position within the CCD frame. The fitted profiles were subtracted from the original data and the resulting image was similarly examined.

The instrumental CMD, derived from these measurements, is shown in Figure 3.17. This can be compared with Figure 3.13, which shows the instrumental CMD obtained from measurements with constant profiles for each frame. The main sequence now appears much better defined, and the spread in colour is greatly reduced. The quantitative nature of this improvement will be discussed below.

These data were now transformed using the relations derived from the observations of E-regions standards above. The V and $(B-V)$ zeropoint terms were derived from the overlap with the brighter SAAO observations. The transformed colour-magnitude data are shown in Table 3.8. These data were then co-added to the existing V, $(B-V)$ SAAO and AAT (short exposure) photometry, and the resulting CMD is shown in Figure 3.18.

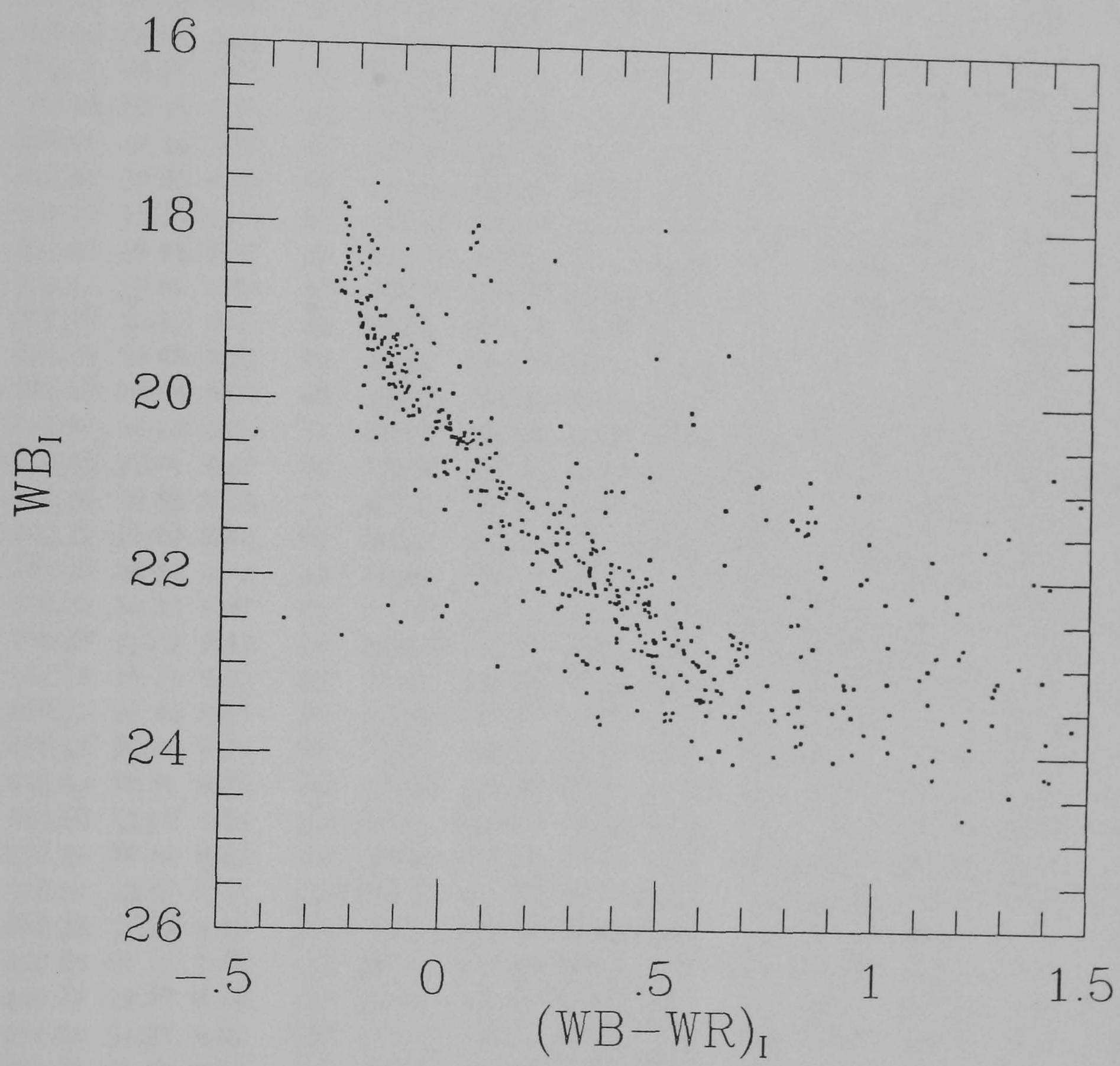

Figure 3.17: The instrumental CMD for the WB, WR exposures of field O1, as derived by fitting data with a geometrically variant PSF. This can be compared with Figure 3.13, which shows the instrumental CMD obtained by fitting the data with fixed PSFs.

N	X	Y	V	(B-V)	N	X	Y	V	(B-V)	N	X	Y	V	(B-V)
1	16.26	31.54	19.68	0.57	2	87.55	31.48	20.02	0.58	3	125.65	31.86	19.90	0.58
4	181.18	33.55	19.74	0.63	5	274.83	42.98	19.83	0.57	6	132.16	49.21	19.50	0.52
7	172.36	57.45	20.36	0.63	8	285.60	58.33	19.04	0.47	9	127.13	60.82	20.06	0.51
10	178.58	78.00	19.45	1.39	11	213.62	70.11	20.64	1.17	12	120.68	71.70	20.28	0.69
13	257.58	79.43	19.54	0.56	14	297.18	81.06	19.02	0.50	15	192.60	85.43	19.26	0.50
16	247.07	88.23	18.49	0.61	17	109.88	93.22	19.47	0.82	18	38.51	97.35	18.56	0.50
19	235.27	99.69	18.73	0.77	20	61.93	101.20	19.66	0.53	21	12.18	103.55	18.73	0.60
22	95.09	103.97	19.14	0.62	23	248.72	107.82	19.61	0.57	24	75.14	112.07	20.69	0.29
25	186.35	116.34	19.53	1.22	26	44.23	121.74	18.91	0.45	27	83.59	130.57	19.03	0.47
28	130.28	126.69	20.64	0.74	29	148.31	133.34	19.47	0.79	30	172.67	142.52	19.27	0.55
31	117.31	146.96	19.19	0.54	32	303.03	149.85	18.24	0.76	33	55.37	151.80	18.69	0.51
34	129.82	155.10	20.54	0.68	35	39.51	161.78	20.36	0.71	36	163.18	166.28	18.51	0.50
37	178.51	168.09	18.07	0.48	38	13.41	168.51	18.64	0.48	39	220.00	170.73	17.97	0.56
40	152.77	173.76	20.47	0.72	41	316.38	174.29	17.77	0.54	42	28.11	184.19	19.06	0.53
43	302.37	183.80	20.19	0.64	44	200.06	189.86	19.66	0.52	45	255.15	196.23	20.26	1.31
46	180.44	208.66	19.19	0.70	47	155.94	212.84	19.15	0.51	48	306.26	212.95	19.53	0.67
49	230.29	225.31	20.05	0.69	50	181.54	228.47	19.46	0.59	51	61.90	229.64	19.13	0.50
52	24.60	237.77	18.02	0.47	53	114.82	230.00	19.05	0.90	54	265.73	236.43	18.78	0.81
55	199.11	237.42	20.04	0.67	56	297.75	247.84	18.60	0.53	57	82.59	248.37	19.02	0.46
58	309.67	250.13	19.67	0.89	59	275.75	256.65	19.42	0.54	60	175.22	257.22	18.82	0.52
61	80.58	267.70	19.37	0.51	62	29.74	271.78	19.83	0.58	63	100.98	276.78	18.63	0.48
64	82.96	284.60	20.65	0.55	65	34.31	295.77	18.88	0.49	66	55.82	285.33	20.39	0.77
67	257.64	290.48	19.86	0.60	68	261.74	298.27	20.08	0.72	69	59.89	298.10	20.49	0.68
70	190.53	304.64	19.59	0.59	71	32.94	307.96	18.17	0.78	72	239.54	310.29	18.36	0.77
73	122.09	328.85	18.76	0.47	74	173.65	327.54	18.43	0.76	75	33.05	321.29	19.99	0.60
76	247.66	331.34	19.50	0.58	77	45.74	338.91	19.58	0.55	78	47.31	353.21	19.79	0.58
79	129.37	354.27	18.62	0.52	80	26.04	364.31	18.70	0.48	81	200.13	358.74	20.29	0.64
82	236.08	362.15	20.42	0.72	83	78.54	369.13	20.03	0.57	84	267.33	374.15	18.92	0.56
85	287.00	386.23	18.39	0.47	86	131.32	387.96	19.67	0.59	87	87.39	390.89	18.77	0.48
88	156.71	395.87	18.42	0.53	89	119.33	405.87	19.75	0.56	90	284.98	409.13	19.79	0.61
91	194.05	418.26	18.74	0.52	92	72.02	413.00	20.86	0.80	93	267.16	413.73	19.58	0.62
94	177.06	416.11	20.33	0.81	95	273.31	427.87	19.26	0.56	96	296.95	423.05	20.47	0.58
97	239.49	429.12	20.50	0.72	98	75.23	430.55	19.97	0.56	99	204.31	430.22	20.42	0.56
100	187.39	435.54	20.61	0.77	101	290.85	437.65	20.28	0.70	102	272.07	442.91	18.36	0.52
103	46.67	454.60	18.07	1.23	104	15.76	455.03	19.66	0.63	105	234.51	452.63	19.53	0.54
106	70.56	454.89	20.04	0.62	107	195.09	455.88	20.05	0.65	108	305.26	457.67	19.41	0.51
109	31.87	478.01	19.60	0.61	110	201.10	474.28	20.73	0.83	111	241.18	474.56	20.51	0.75
112	285.96	488.35	18.28	0.48	113	311.68	483.86	20.32	0.64	114	129.20	488.77	19.05	0.53
115	14.90	490.89	21.13	0.84	116	33.77	491.46	20.59	0.81	117	271.85	492.83	18.21	0.47
118	24.03	448.77	19.77	0.74	119	25.65	456.98	20.59	0.50	120	18.83	496.58	20.98	1.67
121	78.25	464.59	21.27	0.96	122	119.17	476.11	21.01	2.01	123	166.51	481.17	21.84	1.03
124	182.39	481.26	21.63	0.91	125	196.73	486.48	20.64	2.03	126	186.36	461.28	20.64	0.76
127	178.19	443.67	20.89	1.21	128	183.67	437.92	21.40	1.93	129	178.50	432.33	21.53	0.99

Table 3.8: The faint colour-magnitude data from the WB, WR observations. The positions are shown as CCD x and y-coordinates in field O1

N	X	Y	V	(B-V)	N	X	Y	V	(B-V)	N	X	Y	V	(B-V)
130	203.98	411.49	19.52	0.59	131	248.75	427.51	19.92	0.64	132	243.54	454.18	21.97	1.06
133	223.14	443.76	20.79	0.81	134	259.86	439.80	21.30	1.59	135	293.57	455.80	20.95	1.01
136	290.08	469.61	20.13	0.67	137	290.42	479.82	20.52	0.79	138	277.51	490.78	22.14	1.20
139	309.23	445.23	21.38	0.97	140	280.45	419.58	20.37	0.99	141	288.75	417.34	22.24	1.18
142	302.60	412.48	21.23	0.84	143	309.78	391.97	21.10	1.10	144	307.24	387.73	21.29	1.54
145	213.15	387.91	18.51	0.54	146	228.51	383.59	21.67	0.85	147	264.32	361.63	21.12	0.86
148	255.67	358.95	21.65	1.07	149	273.70	350.48	21.44	1.57	150	273.23	338.21	21.94	1.61
151	257.36	335.28	20.65	0.74	152	255.92	338.74	21.92	1.12	153	241.74	338.89	20.82	0.78
154	196.54	355.50	21.72	0.98	155	172.07	338.47	20.58	0.73	156	168.41	329.76	18.50	0.96
157	165.49	319.58	20.42	0.68	158	148.42	312.32	21.30	1.48	159	129.30	312.67	20.94	0.82
160	105.41	311.48	21.03	0.68	161	61.51	319.54	21.13	1.58	162	92.20	326.01	22.25	0.94
163	56.54	332.90	21.17	0.79	164	62.77	331.86	22.16	1.18	165	33.51	355.32	20.49	0.71
166	29.18	328.69	20.12	0.61	167	19.46	321.04	20.94	0.82	168	12.97	313.64	22.15	1.07
169	18.96	289.18	21.47	0.89	170	28.58	291.73	20.57	0.72	171	40.41	286.03	19.70	0.58
172	85.24	275.10	21.91	1.05	173	113.92	279.51	21.18	0.89	174	126.82	267.30	22.18	1.16
175	132.85	260.41	21.75	1.07	176	110.73	259.40	20.85	0.78	177	89.03	256.38	21.50	0.85
178	107.77	229.62	19.49	0.54	179	160.63	303.20	21.19	0.89	180	171.72	301.11	21.17	0.81
181	183.76	306.35	20.92	1.46	182	199.20	294.35	21.96	0.92	183	197.44	270.92	20.38	0.62
184	208.98	266.90	20.06	0.59	185	236.23	285.69	21.67	1.07	186	270.69	293.95	20.70	0.76
187	282.53	303.44	21.31	1.57	188	279.21	277.69	20.85	0.72	189	308.80	268.62	21.19	0.77
190	282.05	233.26	21.19	0.85	191	249.82	247.29	21.38	1.02	192	222.30	243.21	21.08	1.11
193	244.22	209.97	19.07	0.52	194	293.88	149.50	20.61	0.74	195	258.30	154.51	20.55	0.75
196	242.31	144.78	19.10	0.52	197	237.85	144.64	20.58	0.74	198	214.62	160.42	21.95	1.13
199	184.38	234.92	20.30	0.69	200	181.03	243.45	21.08	1.14	201	160.28	179.95	21.54	0.96
202	289.52	117.86	20.04	0.60	203	261.30	101.65	21.33	0.79	204	258.75	89.19	20.94	1.46
205	276.56	79.80	18.89	0.47	206	279.54	85.01	20.87	0.70	207	283.21	77.33	21.91	1.96
208	238.15	76.75	21.32	0.92	209	233.11	71.25	21.59	1.01	210	228.80	77.76	21.39	1.55
211	236.02	59.47	21.60	0.89	212	246.00	59.93	21.57	1.06	213	259.14	17.90	20.99	0.71
214	261.90	11.76	20.93	0.74	215	279.46	13.99	20.78	1.03	216	199.24	79.00	21.03	0.76
217	185.34	70.76	19.68	0.59	218	171.78	59.85	21.58	0.82	219	173.13	52.93	22.35	1.20
220	164.12	54.16	21.99	1.68	221	125.89	46.61	20.07	0.62	222	134.16	66.28	21.13	0.84
223	125.20	84.30	21.70	1.81	224	26.56	10.16	20.47	0.71	225	31.92	34.53	21.55	0.85
226	26.36	77.25	21.01	0.71	227	30.26	99.01	20.18	0.59	228	21.51	109.35	20.30	0.61
229	52.05	124.74	21.53	0.87	230	83.83	105.90	20.71	1.99	231	91.28	123.74	19.51	0.56
232	112.97	160.83	20.34	0.71	233	114.63	172.46	19.31	0.65	234	85.76	163.35	20.95	0.77
235	90.75	166.06	21.59	0.98	236	89.42	177.20	21.70	1.01	237	99.24	176.39	21.57	1.90
238	78.48	186.40	21.04	0.83	239	147.91	162.22	21.22	0.64	240	148.01	157.96	21.74	1.10
241	164.47	149.66	20.13	1.30	242	134.59	183.35	21.72	0.81	243	131.54	202.17	21.66	0.93
244	107.98	190.71	22.27	0.95	245	109.01	204.29	21.91	0.98	246	91.73	207.74	21.35	0.99
247	77.09	199.27	21.24	0.85	248	53.16	197.54	21.52	1.70	249	22.45	199.24	20.53	0.77
250	311.65	181.54	21.06	1.00	251	297.09	262.19	22.11	1.21	252	285.95	252.86	21.89	1.04
253	285.34	316.38	19.23	0.64	254	293.33	307.21	21.27	0.91	255	296.10	301.14	19.20	0.54
256	223.61	370.05	22.05	1.20	257	162.34	369.91	20.60	0.77	258	151.72	390.28	21.22	1.39

Table 3.8 continued.

N	X	Y	V	(B-V)	N	X	Y	V	(B-V)	N	X	Y	V	(B-V)
259	50.02	402.05	20.26	0.63	260	69.78	378.00	20.62	0.75	261	38.62	260.30	21.46	1.57
262	25.81	230.10	19.63	0.55	263	97.80	192.50	21.92	1.69	264	93.23	8.30	20.62	0.66
265	133.66	284.38	19.53	0.52	266	105.02	361.67	19.88	0.61	267	120.50	369.14	20.86	1.58
268	106.93	367.54	21.77	1.08	269	109.59	381.91	21.81	0.86	270	106.77	387.71	21.84	1.21
271	32.78	438.22	19.29	0.51	272	25.92	426.53	21.80	0.95	273	62.62	431.35	22.03	0.98
274	60.58	443.59	22.06	1.06	275	128.81	397.84	20.41	0.69	276	287.17	394.98	22.50	1.54
277	266.56	352.40	22.40	1.16	278	254.69	294.67	21.95	0.99	279	243.98	264.58	22.04	1.17
280	206.53	115.73	21.41	0.71	281	183.92	130.45	21.83	0.93	282	103.94	112.50	21.97	0.99
283	113.27	138.11	22.22	0.68	284	158.29	106.82	20.31	0.51	285	155.77	99.47	22.01	1.06
286	147.94	30.70	20.64	0.79	287	56.15	47.98	18.55	0.48	288	94.20	63.62	22.15	1.11
289	230.97	170.17	22.28	1.00	290	191.01	197.83	22.02	1.27	291	206.98	209.96	19.86	0.52
292	232.09	303.27	22.01	1.12	293	294.14	190.56	22.26	1.13	294	49.74	486.11	22.35	1.21
295	105.43	457.90	21.80	1.07	296	117.70	452.42	21.85	1.39	297	150.79	434.30	22.36	1.13
298	152.20	408.29	22.26	1.58	299	154.65	424.26	22.79	1.27	300	194.66	440.42	23.27	0.05
301	224.56	394.19	22.79	1.86	302	260.86	478.24	22.17	1.53	303	279.41	430.54	22.75	1.44
304	247.38	439.92	22.31	1.21	305	246.74	375.56	22.23	0.79	306	273.70	317.44	22.32	1.18
307	207.01	366.02	22.54	1.13	308	203.63	366.25	22.42	1.14	309	186.61	295.38	22.25	1.04
310	77.13	422.88	22.19	1.08	311	71.94	438.17	22.72	1.25	312	15.07	447.79	22.65	1.25
313	65.77	370.34	21.27	1.00	314	304.63	407.13	22.76	1.59	315	218.22	386.17	22.32	1.27
316	135.52	307.72	22.59	1.06	317	123.26	306.00	22.80	1.13	318	63.22	274.17	22.77	0.35
319	75.27	255.65	22.88	1.19	320	95.13	257.06	22.48	1.21	321	116.07	216.98	22.39	1.15
322	83.64	196.19	22.45	0.99	323	62.20	183.22	22.28	1.85	324	63.76	200.04	22.28	1.14
325	33.91	243.32	22.78	1.20	326	80.63	149.09	21.81	1.60	327	80.96	144.52	22.84	1.29
328	48.21	139.71	22.14	1.78	329	25.59	124.81	22.42	1.00	330	78.35	53.61	22.27	1.06
331	83.25	56.72	23.40	1.33	332	93.31	43.08	22.27	1.08	333	94.60	31.85	22.73	1.31
334	100.73	32.93	22.09	1.84	335	162.78	39.64	22.85	1.35	336	212.59	87.46	22.54	0.58
337	212.17	99.24	22.46	1.23	338	247.88	104.64	21.06	0.85	339	257.61	73.48	22.17	1.15
340	289.77	80.93	22.78	1.22	341	241.56	32.34	22.34	1.14	342	286.72	20.48	22.63	1.16
343	205.92	146.68	22.96	1.81	344	209.97	151.12	22.80	1.42	345	255.75	189.34	22.50	1.06
346	237.15	223.46	22.40	1.20	347	280.69	213.04	22.63	1.40	348	289.06	227.64	22.49	1.55
349	277.38	264.95	22.59	1.18	350	299.85	269.41	22.70	1.73	351	308.75	245.42	22.75	1.22
352	273.36	285.04	22.87	1.17	353	179.83	197.19	22.73	0.61	354	175.69	205.41	21.82	0.95
355	164.08	200.47	22.50	0.72	356	160.69	232.80	21.96	1.98	357	132.62	243.89	22.20	1.13
358	167.72	245.07	22.58	1.29	359	181.74	254.53	22.22	1.03	360	202.49	248.58	21.97	1.16
361	131.95	104.63	22.10	1.11	362	173.04	21.93	22.62	0.70	363	281.42	172.13	22.70	1.19
364	167.71	371.98	22.63	1.18	365	190.11	465.83	22.36	1.13	366	178.99	487.55	22.30	1.01
367	171.42	485.01	22.75	1.41	368	113.30	469.17	22.92	1.22	369	115.96	465.27	22.39	0.90
370	53.45	393.84	22.88	1.44	371	137.78	89.32	22.80	1.82	372	125.09	282.50	22.57	1.33
373	169.55	260.57	22.92	1.23	374	10.58	474.54	22.63	1.14	375	32.80	467.64	24.04	1.63
376	52.91	473.84	24.66	1.87	377	58.40	471.51	24.03	1.79	378	46.45	444.55	23.87	1.32
379	64.23	425.63	23.11	1.22	380	68.65	423.19	23.28	1.37	381	104.84	428.54	23.41	1.36
382	132.85	439.48	23.47	1.63	383	123.02	463.60	23.52	1.66	384	157.26	476.47	22.92	1.41
385	157.89	481.04	23.21	1.91	386	172.04	462.38	23.40	1.65	387	223.54	492.83	22.43	1.21

Table 3.8 continued.

N	X	Y	V	(B-V)	N	X	Y	V	(B-V)	N	X	Y	V	(B-V)
388	213.30	477.53	23.20	1.65	389	216.28	494.13	23.20	1.49	390	261.00	465.83	23.72	1.73
391	288.21	456.56	22.75	1.13	392	306.38	494.08	22.54	1.28	393	254.47	493.59	22.73	1.28
394	259.70	504.73	22.34	1.12	395	267.22	420.46	23.83	1.88	396	279.37	398.69	23.47	1.50
397	284.41	374.49	23.23	1.55	398	246.92	358.12	23.38	2.09	399	268.10	341.82	23.50	1.87
400	231.59	405.22	22.73	1.43	401	242.88	423.11	23.00	1.32	402	168.75	420.63	23.15	0.84
403	165.34	387.27	23.24	1.55	404	170.66	389.98	23.02	1.33	405	165.24	393.43	23.43	1.34
406	135.54	354.73	22.89	1.95	407	127.88	324.02	23.13	1.91	408	136.05	329.04	22.33	1.20
409	225.05	339.67	23.61	2.06	410	254.03	325.78	23.15	1.65	411	249.42	298.67	23.33	1.26
412	24.69	332.38	23.59	1.51	413	41.87	325.27	24.11	2.07	414	26.09	327.09	23.08	1.13
415	46.36	298.29	23.84	1.56	416	71.55	281.65	23.64	1.55	417	74.79	268.72	24.25	2.03
418	63.30	260.48	23.59	2.01	419	104.48	289.21	24.15	1.98	420	61.07	323.88	24.16	2.05
421	55.14	352.69	22.71	1.86	422	68.36	345.08	23.07	1.34	423	87.95	359.65	23.45	1.43
424	85.02	380.02	23.07	1.06	425	88.28	347.32	22.92	1.21	426	191.61	343.10	23.10	1.14
427	263.70	266.19	23.33	1.81	428	251.52	252.27	23.57	1.35	429	268.89	210.12	23.74	1.98
430	298.48	175.78	23.41	1.34	431	260.45	158.67	24.56	2.09	432	300.40	119.29	24.12	1.41
433	285.06	112.88	23.74	1.09	434	279.33	104.86	22.95	0.93	435	267.46	113.90	23.27	1.35
436	282.21	45.39	22.94	0.93	437	294.74	41.76	23.71	1.69	438	233.62	37.11	23.57	1.41
439	219.05	56.26	23.06	1.06	440	165.49	45.98	23.57	1.39	441	220.49	102.69	23.06	1.40
442	202.70	121.50	23.29	1.17	443	219.13	131.56	24.40	2.09	444	249.77	120.00	23.50	1.53
445	171.54	132.85	22.98	1.42	446	136.03	106.50	22.84	1.56	447	160.40	108.98	23.06	1.41
448	162.08	171.53	22.77	1.23	449	202.63	193.47	22.97	1.03	450	226.98	211.25	22.97	1.32
451	168.59	290.02	23.46	1.74	452	148.67	255.45	23.53	1.91	453	164.40	243.74	23.39	1.06
454	167.98	204.19	23.54	1.83	455	191.35	177.79	23.15	1.01	456	270.50	199.87	23.66	1.25
457	310.66	154.65	23.94	1.67	458	258.08	47.30	23.66	1.09	459	21.52	80.10	23.04	1.98
460	31.55	89.20	23.19	1.30	461	9.87	81.03	23.12	1.73	462	41.20	134.32	23.40	1.34
463	64.26	148.99	23.07	1.92	464	41.17	165.06	22.95	2.09	465	24.15	166.32	22.56	1.13
466	89.26	191.22	23.30	1.16	467	67.98	180.01	23.15	1.37	468	70.87	174.14	23.64	1.26
469	115.90	193.72	23.39	1.33	470	169.23	153.27	23.96	1.82	471	115.27	27.26	23.03	1.63
472	106.20	45.93	23.05	1.22	473	110.03	83.03	23.07	1.34	474	114.50	221.59	23.03	1.05
475	68.98	235.15	23.18	1.67	476	37.63	216.25	23.59	2.08	477	26.38	254.60	23.15	1.25
478	18.58	271.23	23.06	1.79	479	12.30	277.83	22.88	1.29	480	71.26	303.88	22.90	1.37
481	160.43	256.69	23.57	1.25	482	151.42	265.31	23.87	1.55	483	193.01	266.11	24.06	1.34
484	202.91	258.72	23.97	1.38	485	207.44	257.97	24.00	1.50	486	302.53	226.00	23.41	1.55
487	309.55	421.27	22.20	1.10	488	195.53	448.15	23.31	1.38	489	151.55	443.94	23.28	1.37
490	123.78	222.29	23.64	1.56	491	286.07	474.02	24.18	1.98	492	189.42	498.21	23.28	2.05
493	170.37	495.57	23.13	1.29	494	159.45	494.01	21.33	1.10	495	54.03	500.58	22.22	1.73
496	41.60	492.86	22.66	1.41	497	69.49	481.26	23.56	1.27	498	66.56	492.29	23.90	1.74
499	59.81	489.24	23.56	1.18	500	156.61	137.98	24.37	1.93	501	164.17	134.60	24.19	1.82
502	71.76	129.87	23.82	1.43	503	22.69	103.31	23.10	1.09	504	11.63	36.69	22.91	0.47
505	10.53	47.74	23.28	1.44										

Table 3.8 continued.

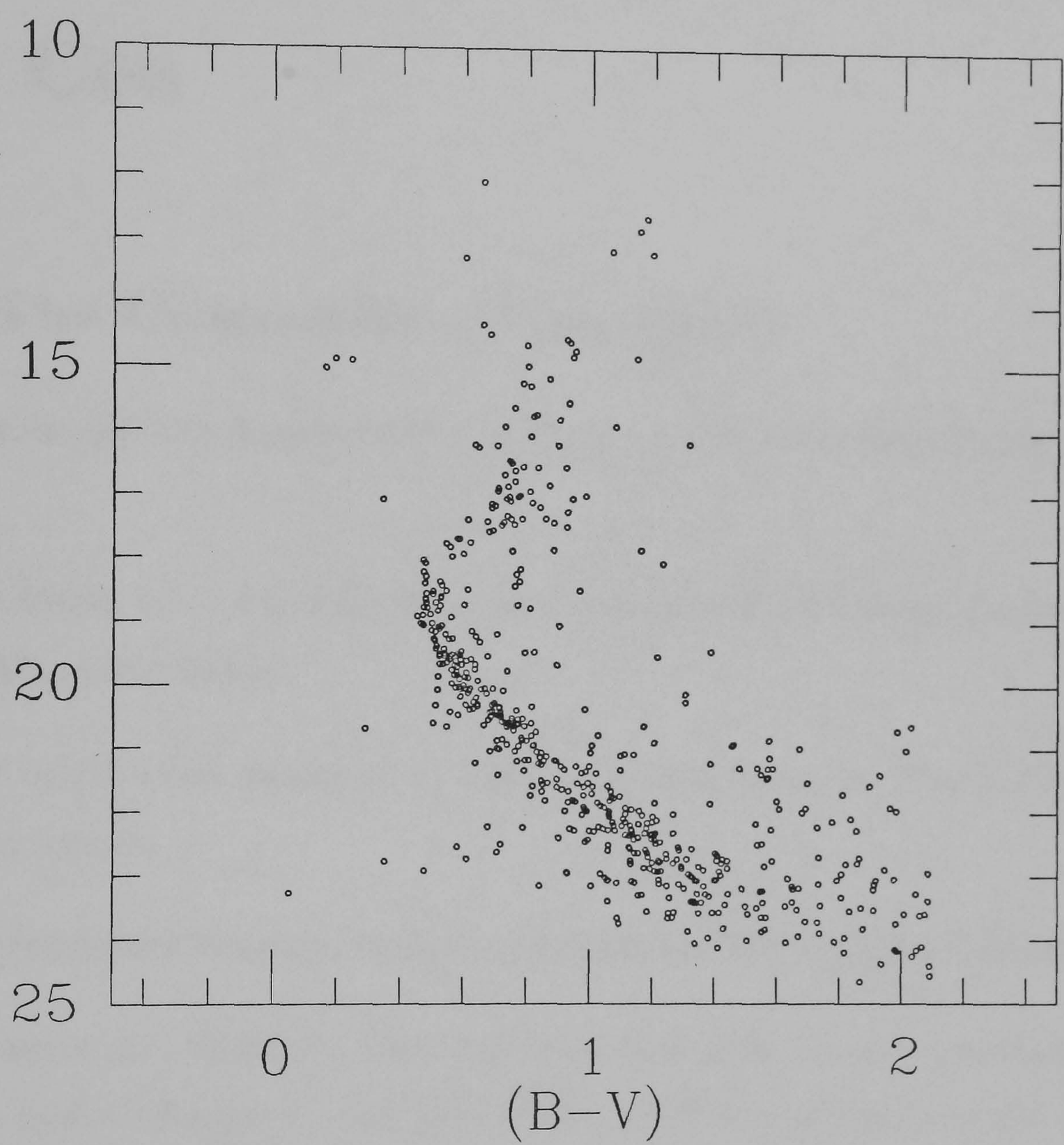

Figure 3.18: The composite colour-magnitude diagram of ω Centauri. This diagram contains the brighter SAAO and AAT stars, measured in regions F5–F9 and O2–O4, and the faint AAT stars in region O1, observed through the WB, WR filters.

Chapter 4

Results of the CCD Observations of ω Cen

4.1 The Composite ω Cen CMD

The colour-magnitude diagram shown in Figure 3.18 includes three distinct groups of stars.

- The bright ($V < 18$) stars measured in regions F5–F8, from the June 1985 SAAO observations.
- The bright stars measured in regions O2–O4, from the March 1986 AAT observations.
- The faint stars measured in region O1, from the May 1985 AAT observations.

The diagram is not, therefore, truly representative of the cluster luminosity function, the number of stars in each part of the CMD depending upon the number of frames taken, their exposure times, the aperture of the telescope with which the observations were made, and the seeing during the exposure. The "gap" at $V = 18$, $(B - V) = 0.6$ is unfortunate, but is due to a paucity of measurable stars in this magnitude range. Stars of this luminosity in the SAAO fields, and the bright AAT V, $(B - V)$ exposures have photometric errors too large to warrant inclusion in the final diagram, and the stars within this magnitude range in the deep AAT WB, WR exposures are too saturated. The deep AAT V and B exposures of region O1, taken in March 1986, will probably provide the solution.

However, as noted above, these data also suffer from the variable profile problem, and unfortunately lack of time precluded their re-analysis using the methods applied to the wide band data.

4.1.1 The Uncertainties in the CMD

Discussion of the uncertainties in the colour-magnitude data shown in Figure 3.18 and tabulated in Tables 3.5 and 3.8 can be separated into two distinct sections; the overall zeropoint errors in the calibration of the data, and the internal photometric scatter in the magnitude estimates. In the following sections the uncertainties quoted are standard deviations, unless stated otherwise.

The Overall Zeropoint Error

Ultimately, the calibration of the entire data-set rests upon the observations of E-region standards, made during the June 1985 SAAO observations. The photometric zeropoints derived from the E-region standards were transferred to the programme stars by digital aperture photometry as described in Chapter 2. Due to the crowded nature of these fields, the aperture photometry of bright stars is probably the principal source of photometric uncertainty in the transfer process. Precautions taken to minimise the problems caused by the congestion in these CCD images include using only relatively bright, isolated stars, measuring with as small an aperture as possible and choosing only those stars whose profile-fitting photometry suggested were likely to be unaffected by faint companions. Nevertheless, it proved impossible to choose an adequate number of such stars to effect a reliable transform, even in the least crowded SAAO field. Thus some aperture measurements were made upon stars subsequent to removing one or more fainter companions, by subtracting their fitted profiles. To estimate the uncertainty involved in the digital aperture photometry, the magnitude estimates were compared with those from profile-fitting—which should be of superior internal photometric accuracy for these bright stars (see, for example, Table 3.7). The scatter in the difference between measurements obtained via the two different methods therefore gives a reliable estimate of the uncertainty associated with the aperture photometry.

Another factor which would contribute to the overall uncertainty in the transfer

would be any error in the extinction figures, and overall zeropoint term, derived from the standard star observations. The likely extent of such an effect can be gauged by examination of the RMS deviation of the individual E-region stars from the mean transform equations.

These two factors suggest a total uncertainty (standard deviation) in the transfer process of the order of $\sim 0\overset{m}{.}01$ in V, and $0\overset{m}{.}013$ in $(B-V)$. This analysis, of course, cannot take into account the possibility of any systematic error present in the measurements, which might have been introduced by the charge transfer efficiency problem described above. The likely manifestation of this problem, as a slightly increased uncertainty in the DAP measurements of the E-region standard stars, has also been discussed above; no further gross systematic effects are envisaged, and the transformation equations agree well with those previously determined for this telescope and detector (See, for example, Chapter 5 herein).

The photometric zeropoints determined by the standard star observations were subsequently transferred between the overlapping CCD fields, to the more crowded regions. The uncertainty in each transfer between frames was estimated from the scatter in the frame to frame differences for individual stars, and was found to be $0\overset{m}{.}006$ on average. For the bright SAAO stars there were never more than three such transfers, and normally only one or two, and thus an estimate of the additional uncertainty introduced by this process of $\sqrt{3} \times 0\overset{m}{.}006 \approx 0\overset{m}{.}01$ is perhaps a little pessimistic, but has been adopted nonetheless. For the brighter AAT observations, those made through the conventional B and V filters, there were generally a similar number of transfers made, and thus a similar uncertainty has been used.

Adding these derived uncertainties in quadrature leads to an estimate of the total zeropoint uncertainty in the bright (*i.e.* $V < 18.0$) observations of $\Delta V = 0\overset{m}{.}014$ and $\Delta(B-V) = 0\overset{m}{.}017$.

For the main sequence data, there is an additional stage involved, that of transferring the zeropoint terms from the bright SAAO observations to the faint WB, WR observations. Unfortunately there was a marked paucity of measurable stars with good signal to noise ratios which were not too saturated to measure. This was due in part to the form of the cluster luminosity function in the appropriate magnitude range—there simply are not many stars in the range $16 < V < 18$ within the area of one CCD frame, at this distance from the cluster core. The

principal problem however was that the excellent seeing of the wide band observations rendered any star brighter than $V = 18$ hopelessly saturated. Thus, in order to make the zeropoint transfers, some of the faintest stars measured in the SAAO observations were used, with a resulting degradation in the zeropoint accuracy. The uncertainties introduced by this transfer were evaluated from the scatter in the frame to frame differences between individual stars as $\sim 0\overset{m}{.}014$ in V, and $0\overset{m}{.}021$ in $(B-V)$.

Furthermore the main sequence data may be systematically affected by the uncertainty in the wide-band colour equations, which are by no means as well defined as the SAAO colour equations. Examination of the RMS deviation of the standard star observations from the mean transformation equations, as shown in Figure 3.12, reveals that the likely extent of any error is less than $0\overset{m}{.}03$ in the magnitude range $18 < V < 22$, and consequently an additional uncertainty of $0\overset{m}{.}012$ in V and $(B-V)$ has been adopted as appropriate. As discussed above, the transformation is poorly determined redward of $(B-V) \approx 1.2$ (*i.e.* fainter than $V \approx 22.5$), but it is likely that the observational scatter (see Section 4.1.1 below) is dominant at such faint luminosities.

The cumulative uncertainty in the main sequence zeropoints, as derived from these estimates of the individual contributions, is thus $\sigma_V \approx 0\overset{m}{.}024$ and $\sigma_{(B-V)} \approx 0\overset{m}{.}031$. These estimates, whilst perhaps marginally pessimistic, are significant enough to be somewhat disconcerting in their implications for some part of the quantitative analysis presented hereafter. The principal conclusions made from these observations are not affected though, and depend more upon the internal observational scatter in the measurements.

The Internal Photometric Uncertainty

For the most part, this discussion will be limited to the main sequence data, derived from the WB and WR AAT observations. It is only on the main sequence proper that there is a statistically large enough sample of stars to address the question of intrinsic spread in colour due to differential blanketing, and that the problems of field star contamination become tractable.

Examination of the frame to frame scatter between repeated measurements of individual stars in the SAAO and AAT bright star observations suggest that the

standard deviation is never greater than $0^m.02$ in V and $0^m.025$ in $(B-V)$, and these figures only apply for the faintest measurements ($17 < V < 18$). In general the uncertainties in these data, as judged in this way, are of the order of $0^m.01$ in both V and $(B-V)$. There is, however, an additional source of scatter in the bright AAT data—that of the error in profile-fitted magnitude due to the geometrically invariant fitting profile. The AAT observations made through the conventional B and V filter set exhibited this problem and hence, as discussed above, the main sequence observations from the March 1986 run were not included in the composite CMD of ω Cen. The difference between aperture and profile-fitting photometry, when examined as a function of position within the CCD frame, indicated an extreme deviation from the mean zeropoint relation of some $0^m.02$ in both colour and magnitude for this data-set. Thus a reasonable estimate of the uncertainty caused by the profile mismatch, taking into account that the deviation is linearly, rather than normally, distributed, is ~ 0.014. Such indeterminacy is acceptable in the brighter parts of the CMD, and will only affect the AAT observations. As noted above, it proved impractical to re-analyze these data using geometrically variant profile-fitting, and the uncertainty in the March 1986 AAT main sequence data was considered too great to justify inclusion in further quantitative analysis.

The internal measuring error of the profile-fitting photometry can be estimated by constructing "artificial" CCD frames with similar stellar content to the actual programme observations and then submitting these images to the same analysis as the cluster stars, as described in Section 3.4.3. Such a process yielded the data in Table 3.7, which is in terms of standard deviation in instrumental magnitude units. At this stage of the analysis the starfield simulation software was not versatile enough to permit the construction of frames with variations of stellar profile like those seen in the wide-band data. Therefore a direct and realistic assessment of the uncertainty in the magnitude estimates derived by profile-fitting with a geometrically variant PSF was not possible using this method.

However, as the parameters governing the variation of profile were independently appraised for each of the six wide-band exposures to O1, it was possible to use the scatter in the frame to frame differences between individual stars to estimate the uncertainty. The derived standard deviation in V and $(B-V)$ is shown in Table 4.1, together with that derived from the simulated starfields. It can be seen from inspection of this table that the actual internal scatter is gener-

ally larger than would be expected from the simulations with model data, which does not incorporate geometric variation in the fitted PSF. This discrepancy is presumably caused by the imperfect matching of the modelled profile variation with the actual distribution, and is probably due to the inadequacy of the simple linear fit employed and the fact that no variation of the wide Gaussian halo, or empirical profile map was included in the fitted PSF.

The expected uncertainties as derived from the simulated data seemed to increase faster than those determined from the actual data at faint magnitude levels. If this effect is real it is likely that it is due to the nature of the "sky" background to which the artificial stellar images were added. As noted, above the background distribution was derived from a region of one of the wide band exposures which had been cleaned of all fitted stellar images. However it will still contain those stars not measured in the photometry, whose presence will appear as noise, and will also be degraded by the process of removing those stars detected and measured by the profile-fitting photometry. Removal of bright stars leaves a "noisy patch" in the sky background due to the Poissonian fluctuations in the stellar flux. Similarly where, for reasons of excessive crowding, residual CCD defects or fits to objects with non-stellar profiles (for example stars which are blended with significant cosmic ray event spikes or extended galaxies), the photometry, and hence the image subtraction, is poor and again spurious noise is introduced into the background. The overall effect of the increased noise is to degrade the signal to noise level for the faintest stars measured, and the magnitude uncertainties are correspondingly larger. The overall agreement, however, is good and corroborates the validity of employing the frame to frame differences for individual stars as an estimator of the internal photometric error as a function of magnitude.

4.1.2 The Distance of ω Centauri

In order to determine the distance modulus of ω Cen, a fit to an empirically derived main sequence locus was used. To define this stellar sequence, a subset of 6 of the Carney (1979) subdwarfs was used. This sequence was employed in Chapter 1 to determine a self-consistent distance scale for 10 recently studied globular clusters. The latest available subdwarf parallaxes (R.J.Dickens, private communication) were used to derive the absolute magnitudes of the subdwarfs,

V Range	Observed $\sigma_{(B-V)}$	Expected $\sigma_{(B-V)}$
18–19	0.009	0.0041
19–20	0.014	0.0060
20–21	0.023	0.015
21–22	0.057	0.034
22–23	0.085	0.076
23–24	0.179	0.200
24–25	0.240	0.340

Table 4.1: The observed and calculated internal observational error along the ω Cen main sequence. The calculated uncertainties do not take into account the residual effects of the geometrically variant stellar profile.

and the uncertainties in these figures. These were then adjusted in colour to compensate for the difference in metallicity between the individual subdwarfs and the cluster, as described in Chapter 1. The adopted mean metallicity was [Fe/H] = −1.5 (see the discussion in Chapter 3).

The subdwarfs have been further reddened by $0\overset{m}{.}11$, to compensate for the cluster reddening. There is much support in the literature for this value of $E(B-V)$. In a recent study of cluster RR Lyrae stars, using the accurate and well calibrated Walraven photometric system (Lub, 1977), de Bruijn & Lub (1987) determined the reddening to be $0\overset{m}{.}11 \pm 0.01$. Butler *et al.* (1978), derived $0\overset{m}{.}10 \pm 0.01$ from their study of the cluster RR Lyrae stars. Burstein & McDonald (1975) also determined $E(B-V)$ to be $0\overset{m}{.}11$, as did Newell *et al.* (1969).

A slightly higher value, $0\overset{m}{.}14 \pm 0.04$, has been derived by Cannon (1974), from an empirical calibration based upon the two-colour relation for BHB stars in NGC 6752. This value has subsequently been used by Bell *et al.* (1981) and by Hesser *et al.* (1985). Bearing in mind the relative uncertainties in the quoted values, and the accuracies of the techniques employed, the value of $0\overset{m}{.}11 \pm 0.01$ was adopted in this thesis.

The subdwarf sequence was then shifted vertically until the best fit was obtained. The fit was made by eye, because the small number of subdwarf stars involved, and the relative size of uncertainties in the various parameters involved

(see below for discussion), rendered a more rigorous fitting technique unwarranted. The best fit is shown in Figure 4.1, and indicates a distance modulus of $(m - M)_V = 14.29$. There are several sources of error contributing to the final uncertainty in this value.

- The uncertainty (and the range) in cluster metallicity, in the subdwarf metallicities, and in the correction applied to the subdwarf colours to make the comparison.
- The uncertainty in the adopted reddening.
- The uncertainty in the adopted V and $(B - V)$ zeropoints.
- The fitting uncertainty between the mean loci of the main and subdwarf sequences.

Adopting a MS slope of approximately 5 in this region of the CMD, in order to convert $\Delta(B - V)$ to ΔV, gives a total uncertainty of ± 0.18 in distance modulus. Rodgers & Harding (1983) infer a similar distance modulus, $(m - M)_V = 14.3$, from their photometry of subgiant and turnoff stars. However this must be considered fortuitous as the method which they adopt involves comparing the blue envelope of their cluster observations with the locus of the Sandage & Katem (1983) M92 colour-magnitude diagram—which has subsequently been shown by the CCD photometry of Heasley & Christian (1986) to lie systematically off of the true main sequence. Adopting a correction based upon the difference between the Sandage & Katem M92 distance modulus and that found by Heasley & Christian (1986) would suggest that the Rodgers & Harding estimate should be increased to $(m - M)_V = 14.50$. The Sandage & Katem (1983) distance modulus was calibrated by assuming the horizontal branch level in M92 to be $0^m.6$. If one adopts the horizontal branch luminosity which is derived for M92 in the study of recent, accurate colour-magnitude photometry in Chapter 1, namely $M_V^{RR} = 0^m.4$, then the distance modulus derived from the work of Rodgers & Harding is once again lowered to 14.30. Harris & Racine (1979), in their review of cluster properties, give the distance modulus of ω Cen as 13.92—a value based upon their adoption of a universal value of $M_V^{RR} = 0^m.60$.

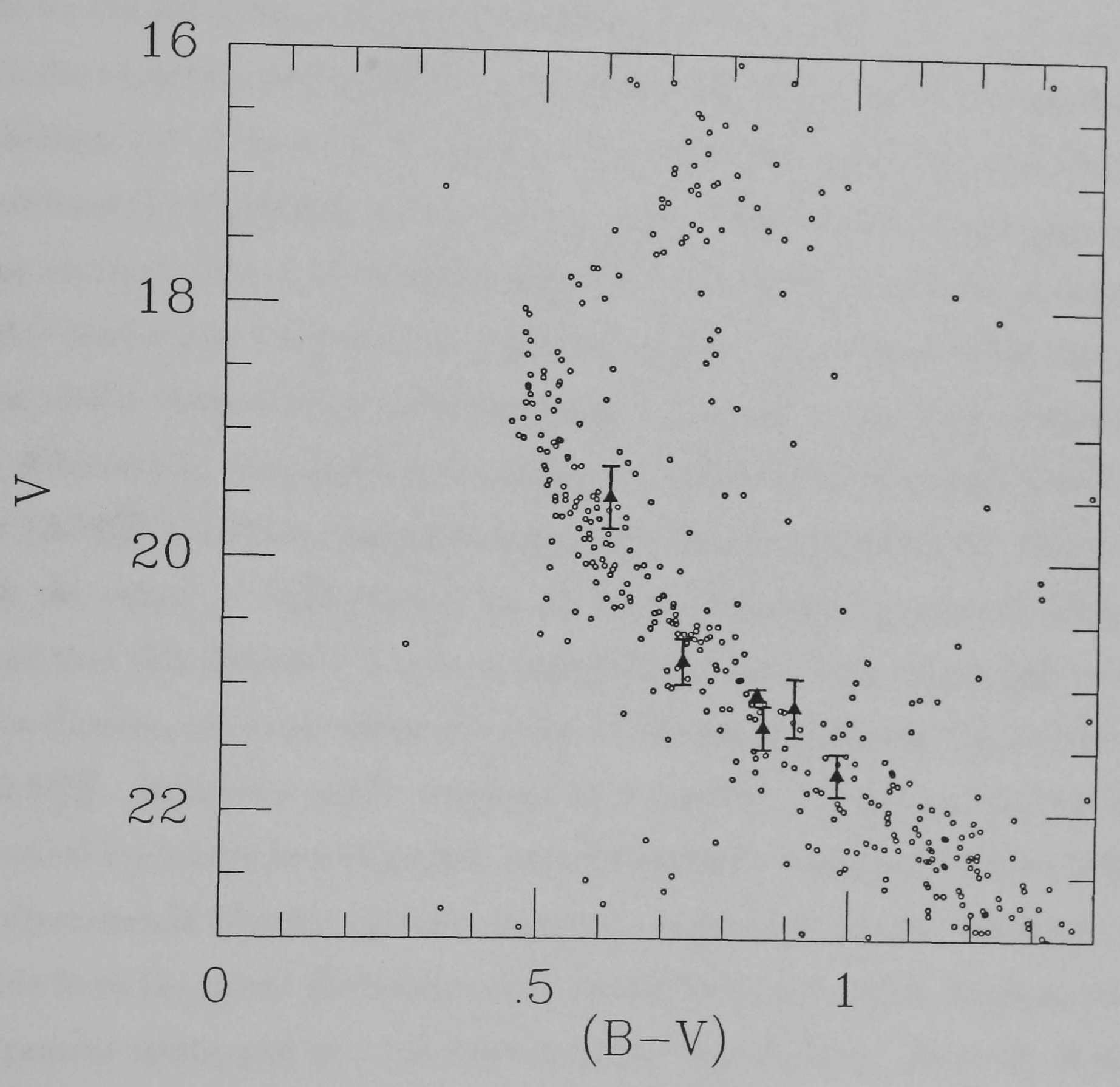

Figure 4.1: Determination of the distance modulus of ω Cen by subdwarf sequence fitting. The best fit by eye gives a value of $(m - M)_V = 14.29$.

The Luminosity of the Cluster RR Lyrae Stars

Following the procedures outlined in Chapter 1, the estimate of the cluster distance modulus obtained from the subdwarf fits above can now be used to determine the absolute magnitude of the horizontal branch at the RR Lyrae instability strip.

Butler, Dickens & Epps (1978) have studied a large sample of RR Lyrae variables within ω Cen, and the mean apparent magnitude of their sample is $\langle V \rangle = 14.54$, with a mean metallicity of [Fe/H] $= -1.43 \pm 0.43$. Combining this value with the distance modulus derived above leads to a mean absolute magnitude for the RR Lyrae stars in ω Centauri of $M_V^{RR} = 0\overset{m}{.}25$. This can be compared with the expected value of $M_V^{RR} \approx 0\overset{m}{.}5$, derived from the empirical relation found in Section 1.5. Cannon & Kontizas (1974) and Cannon & Stewart (1981) have considered the possibility that ω Cen possesses a brighter horizontal branch than other clusters. One possible explanation for this is an enhanced helium abundance in this cluster (see Chapter 1 for a discussion of the dependence of HB luminosity upon stellar composition). This argument was based upon the observation that the difference in magnitude between the turnoff and the horizontal branch in ω Cen ($\Delta M_{TO}^{RR} \approx 3.75$) is somewhat larger than that in other clusters. Comparison with the values of M_{TO}^{RR} derived for 10 Galactic globular clusters in Chapter 1 shows that this difference is indeed slightly larger than those values inferred from other clusters, although within the range of the uncertainties in the derived value of ΔM_{TO}^{RR}. Relatively small variations in a number of input parameters to the canonical horizontal branch models (see, for example, Sweigart & Gross, 1976 and the discussion in Chapter 1) could account for a variation of a few tenths of a magnitude from the norm. Such hypotheses cannot be tested within the framework of the present study, and so a full discussion has been deferred. However, if ΔM_{TO}^{RR} is significantly larger in ω Cen than other globular clusters it might provide some new insight into the reasons for its peculiarity.

Butler *et al.* (1978) have divided a subset of 55 of the *ab*-type variables in their study into metal-rich and metal-poor groups, of mean metallicity $\langle$[Fe/H]$\rangle = -0.72 \pm 0.06$ and $\langle$[Fe/H]$\rangle = -1.60 \pm 0.07$ respectively. The mean magnitudes of these two groups are $\langle V \rangle = 14.62 \pm 0.07$ and $\langle V \rangle = 14.53 \pm 0.02$, with the metal-poor group being the brighter. These values lead to RR Lyrae absolute magnitudes of $0\overset{m}{.}33$ and $0\overset{m}{.}24$ respectively for the metal-rich and metal-poor groups. Whilst

these values once again lie above the mean line defined by the ten clusters in Figure 1.6, there is excellent qualitative agreement between the slope of the mean line and that defined by these two metallicity groups. Thus the RR Lyrae stars in ω Cen agree well with the mean metallicity–luminosity relationship defined by the ten clusters surveyed in Chapter 1.

4.1.3 The Intrinsic Width of the Main Sequence

Before the question of whether there is an intrinsic spread in colour upon the main sequence can be addressed, it is necessary to estimate the relative numbers of field stars on, and around, the main sequence. Unfortunately, the distribution of field stars cannot be determined from the observations described within this thesis, and no other observational studies are available which address the problem of field star contamination in the relevant magnitude range, for this particular cluster.

Ratnatunga and Bahcall (1985) have applied the Galaxy models of Bahcall and Soneira (1980,1984) to fields in the direction of some 76 Galactic globular clusters with $|b| < 10°$ in order to estimate the stellar contribution from the Galactic disk and spheroid in these regions. In their table 1a, Ratnatunga & Bahcall tabulate the predicted numbers of Galactic field stars within two-magnitude wide strips in the range $13 < V < 29$ and in the three colour regions $(B - V) < 0.8$, $0.8 < (B-V) < 1.3$ and $1.3 < (B-V)$. This study also presents predicted field star counts within ± 0.25 in $(B-V)$ of the clusters' principal sequences. It was decided to use the results of this study, suitably scaled to the area of the CCD frame, to provide an estimate of the relative distribution of Galactic field stars with colour and magnitude within the deep field O1, and hence those stars contaminating the main sequence observations. In order to determine the absolute values for the numbers of such stars, comparisons were made with previous observations to brighter regions of the colour-magnitude diagram.

Hesser *et al.* (1985) have presented a spectroscopic study of a nearly complete subset of the subgiant ($16 < V < 17.8$) stars measured photometrically by Cannon & Stewart (1981), allowing them to determine the line-of-sight velocity of these stars, and hence their association with the cluster (ω Cen has a high radial velocity, $v_r = 228$km s^{-1} according to Webbink, 1981). Of the 57 stars measured by Cannon

& Stewart within this magnitude range, some 26 are non-members (assuming from the observations of stars placed in a similar position in the colour-magnitude array that of the 10 stars lying upon the blue envelope of Cannon & Stewart's photometry, which have not been measured spectroscopically, 6 are members and 4 non-members).

Although the Cannon & Stewart (1981) colour-magnitude diagram, based upon photographic iris-photometry, does not contain a complete sample of stars within the measured region due to stellar crowding, the selection of stars is not biased with respect to position in the colour-magnitude diagram and so the fraction of field stars derived from the Hesser *et al.* (1985) study can be used to derive the number of field stars in the magnitude range $16 < V < 17.8$ in the present study. The luminosity function of the region O1 is calculated in Section 4.1.5, and has been used to determine the total number of stars, within the magnitude range covered by the observations of Hesser *et al.* (1985), in region O1. The total number of stars in the range $16 < V < 17.8$ in region O1 is 21, and assuming from the work of Hesser *et al.* that a fraction $\frac{26}{57}$ or ~ 0.46 of these are non-members, then the estimated number of Galactic field stars within this magnitude range in region O1 is 10. The likely error in this estimate will be of the order of 20%, assuming that the number distribution of stars within this magnitude range is Poissonian.

The predicted star counts of Ratnatunga & Bahcall (1985) estimate the total number of field stars in this magnitude range to be 18, exceeding the number calculated above by a factor of 1.8. Therefore, the adopted procedure was to scale the Ratnatunga & Bahcall figures by a factor of 0.56 (after normalising to an area of 11.305 arcmin^2, equal to the field area of the CCD) to obtain the estimated field star distribution within field O1.

The photometry presented in Table 3.8 does not represent a complete sample of the stars within region O1 at any magnitude level between the bright and faint limits. The stars measured by PSF-fitting photometry were chosen rather arbitrarily—particularly with respect to avoiding those stars which were excessively crowded, or in the proximity of CCD defects and the edges of the frame. Furthermore, only those stars with small internal fitting errors (judged from the STARMAN parameter RMS), small frame to frame differences in photometry, and strictly non-saturated cores were utilized in constructing the final colour-

m_V	N
17–18	3
18–19	3
19–20	4
20–21	5
21–22	6
22–23	9
23–24	17

Table 4.2: The predicted number of field stars per magnitude within $\pm 0^m.25$ in $(B-V)$ of the ω Cen principal sequence in the final CMD. Column 1 contains the relevant magnitude range, and column 2 the number of field stars as predicted by an empirical modification of the Ratnatunga & Bahcall (1985) Galactic field star distribution.

magnitude diagram. The total number of stars appearing in Table 3.8 and Figure 3.18 is approximately one third of the total number of stars detected in the determination of the cluster luminosity function (see Section 4.1.5 below). The predicted field star counts were thus further scaled by the ratio of the number of stars within the relevant magnitude range in the photometry of Table 3.8 to the number in that range as deduced from the cluster luminosity function. In the case of the faintest magnitudes, where a significant proportion of the stars remain undetected, and hence not measured, incompleteness was corrected for using the completeness factors calculated from starfield simulations (see Sections 3.4.3 and 4.1.5). The predicted numbers of field stars within ± 0.25 in $(B-V)$ of the cluster's principal sequences, in the range $17 < V < 24$, are shown in Table 4.2.

In order to test the validity of the above empirical modifications to the predicted field star counts, the number of stars in three rectangular regions of the colour-magnitude diagram of region O1, removed from the main sequence, were compared with the predicted values. The regions chosen for the comparison are shown in Figure 4.2 and Table 4.3 shows the predicted and actual star counts in the three regions. The general agreement between the predicted and observed field star counts is very good, and it is noted that the factor of two discrepancy between the observations and the calculated distribution in region 3 would disappear were the distinct grouping of 8 stars at $V = 21.3$, $(B-V) = 1.55$ removed.

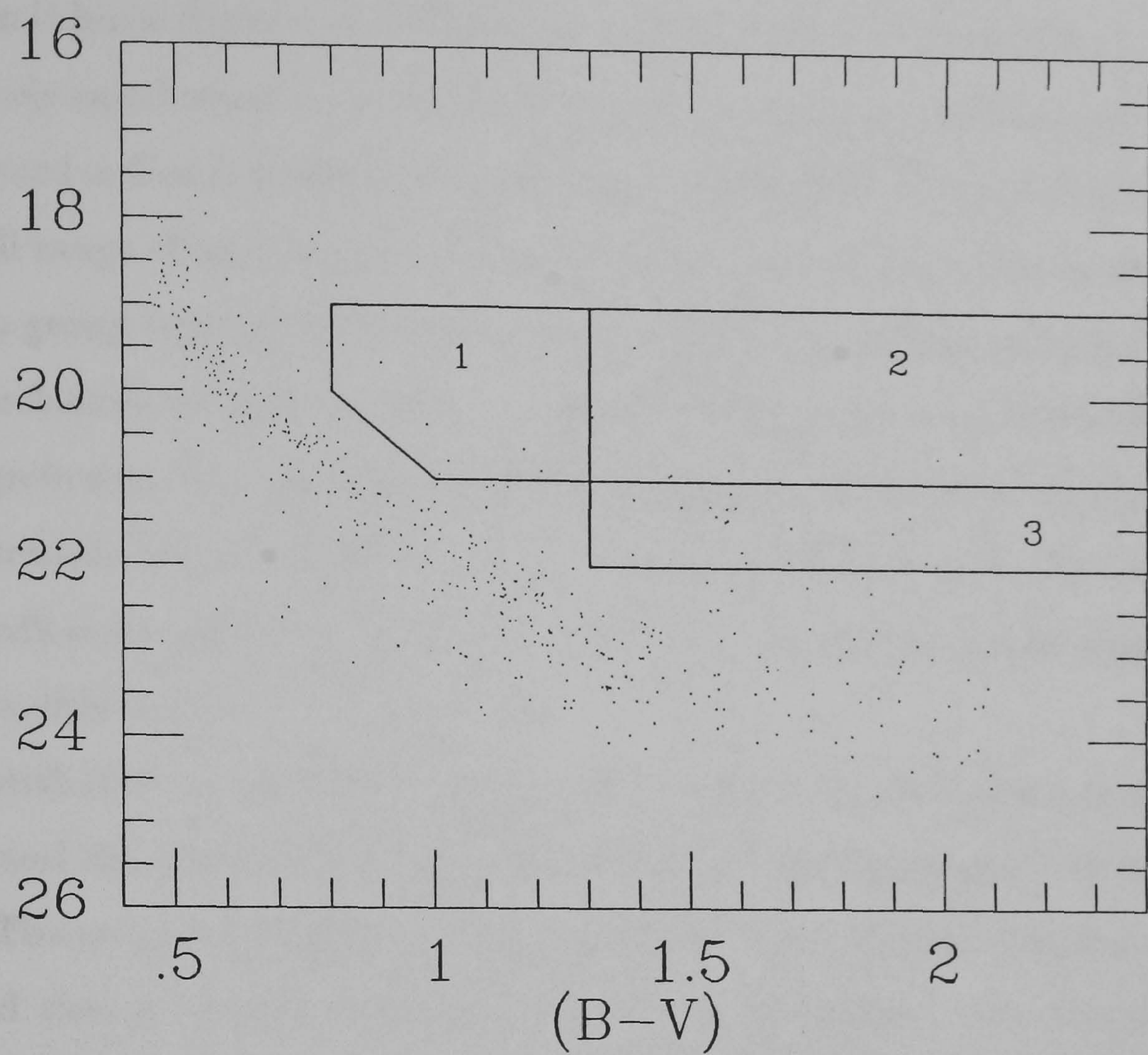

Figure 4.2: Field star counts in three regions of the ω Cen main sequence colour-magnitude diagram. These field star counts within these regions were made to provide a consistency check upon the field star distribution derived for the region O1.

Region	N_p	N_o
1	8	9
2	6	8
3	11	20

Table 4.3: Comparison of the predicted and observed field star numbers in the colour-magnitude photometry of field O1. Column 1 shows the region in Figure 4.2 in which the counts were made, columns 2 and 3 give the predicted and observed field star counts respectively.

Why such a group, if it is not simply a statistical fluctuation, should be present, is not obvious. If this grouping represents some association of main sequence stellar objects then it has a distance modulus of $(m-M)_V \approx 11.5$, and consists of stars of approximately equal mass. Even if this is a small group, or open cluster in the line of sight toward ω Cen it is difficult to see why it would be composed of stars with such a small range of luminosities. No known class of non-stellar objects would be expected to group together with such a small dispersion in colour and magnitude, and the conclusion can only be that this apparent clustering is a statistical effect, and not significant. The agreement between the predicted and observed field star counts is, considering the small numbers involved and the uncertainties inherent in such predictions, entirely adequate for the purposes of the quantitative work presented in this thesis.

The distribution in colour of the stars along the main sequence can now be examined, and the effects of field star contamination reliably gauged and compensated for. The mean locus of the main sequence (shown in Figure 4.3) was drawn by eye, and then a smooth curve was fitted by cubic splines. The fitted curve followed closely the shape of the VandenBerg & Bell (1985) isochrone with the following parameters; Age = 16 Gyr, $Y = 0.24$ and [Fe/H] = -1.77 (the matching of VandenBerg & Bell (1985) isochrones to the data will be further discussed in Section 4.1.4 below). The spline function was then used to interpolate the mean locus to the magnitude of each observation, and in each case the colour residual between the main sequence locus and the observation was determined. Figure 4.4 shows histograms of these colour residuals in one magnitude bins in the range $18 < V < 24$. The solid curves are Gaussian distributions fitted by repeatedly calculating a mean and standard deviation of the data-set and rejecting those stars which lie more than 2.5 times the standard deviation from the mean, until further iterations caused no more stars to be rejected. This is essentially an arbitrary limit chosen so that field stars and bad photometric measures would not unduly affect the fits to the main sequence data; in a Gaussian distribution some 97% of the data points should lie in the range $\pm 2.5 \times \sigma$, where σ is the standard deviation of the distribution. Each histogram shows the number of stars to which the fit was made, the mean, and the standard distribution of the normal function. In each case the dispersion of each fitted Gaussian is significantly larger than would be expected from the estimated internal errors alone (see Table 4.1

above). Comparisons of the variance of the fitted Gaussian distribution and that of the expected error distribution, in the magnitude range $18 < V < 21$, show that the two distributions are different at over the 99% confidence level. At fainter magnitudes, the distribution of colour residuals becomes increasingly dominated by the internal photometric uncertainty. The field star estimates derived above, and shown in Table 4.2, demonstrate that the numbers of field stars within $\pm 0\overset{m}{.}25$ of the mean main sequence locus are negligible for the brighter regions, and do not significantly affect the distributions in Figure 4.4 above $V = 22$. It can be seen that the fits are, in some cases, distinctly non-Gaussian. Chi-squared tests show that the deviations from normality are of moderate significance—with values of χ^2 indicating probabilities in the range 5–15% that these distributions are drawn from populations described by the fitted Gaussians. The histogram of the range $18 < V < 19$ contains few stars, partly because the cluster luminosity function dictates there are simply not many such stars within the frame, and partly because such stars were often saturated and, therefore, were rejected from the measuring process. Table 4.4 shows the "true" dispersion of this spread in colour, derived by assuming that the observed width is produced by the addition, in quadrature, of the intrinsic dispersion and the expected internal scatter. The unweighted average intrinsic dispersion of the main sequence in the range $18 < V < 23$, derived from the figures shown in Table 4.4, is $0\overset{m}{.}056 \pm 0.016$.

The Abundance Distribution on the Main Sequence

Whilst it is difficult to infer accurately the true distribution in metallicity of stars upon the main sequence from these data, it is possible to postulate the likely distribution of metallicity amongst main sequence stars and, using this information, model the expected distribution in colour for comparison with the present observations.

Although the mechanisms for differential enrichment of cluster stars at the same luminosity are still unclear, it is difficult to envisage a scenario in which the range of abundance is a function of stellar mass, and thus position in the CM diagram. Assuming then that there were no sharp differentiation by mass in the amount and nature of chemical enrichment in the protocluster, the range and distribution of metallicity should be approximately constant between the main

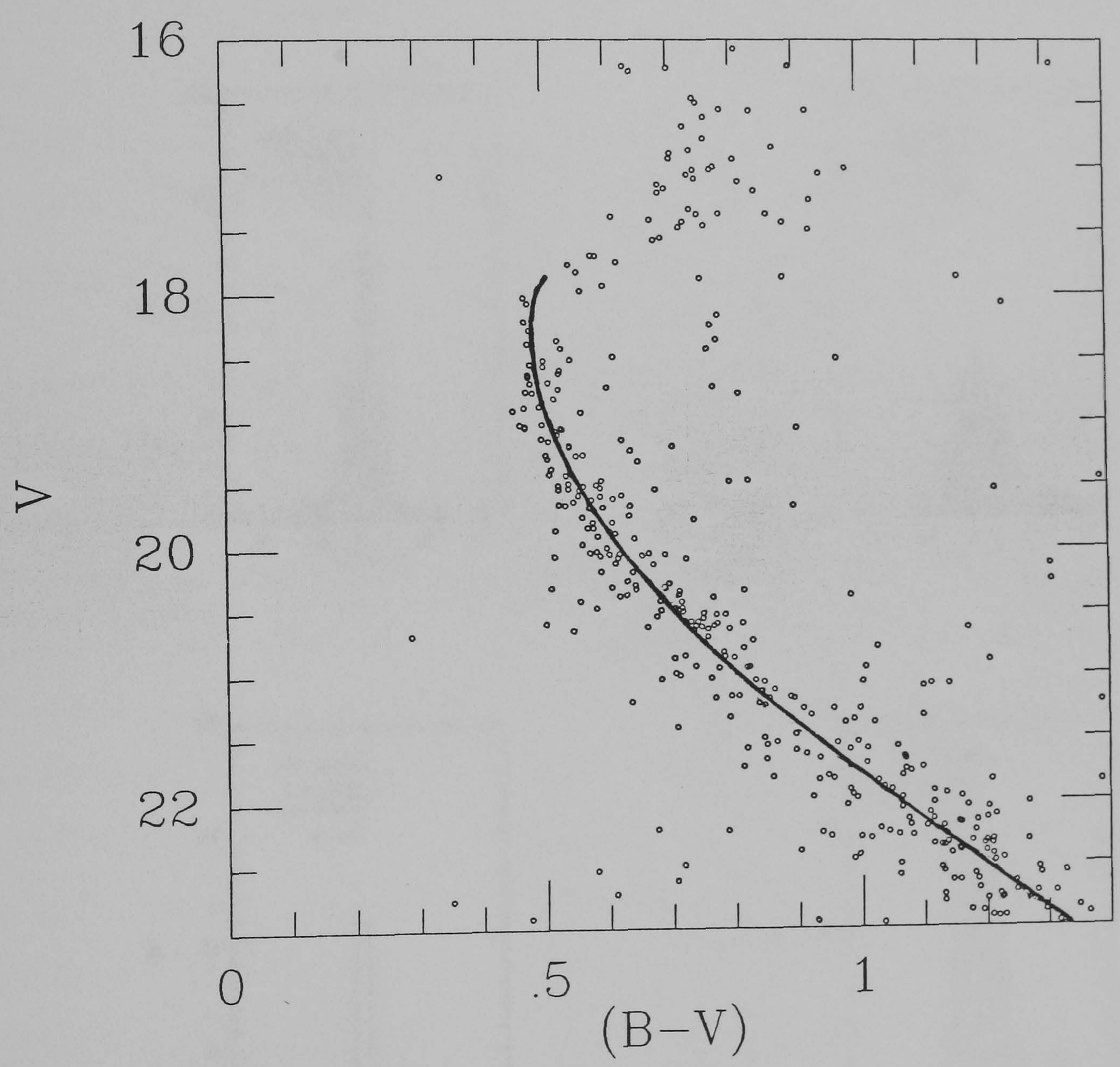

Figure 4.3: The mean locus of the ω Cen main sequence. The fit was made by eye.

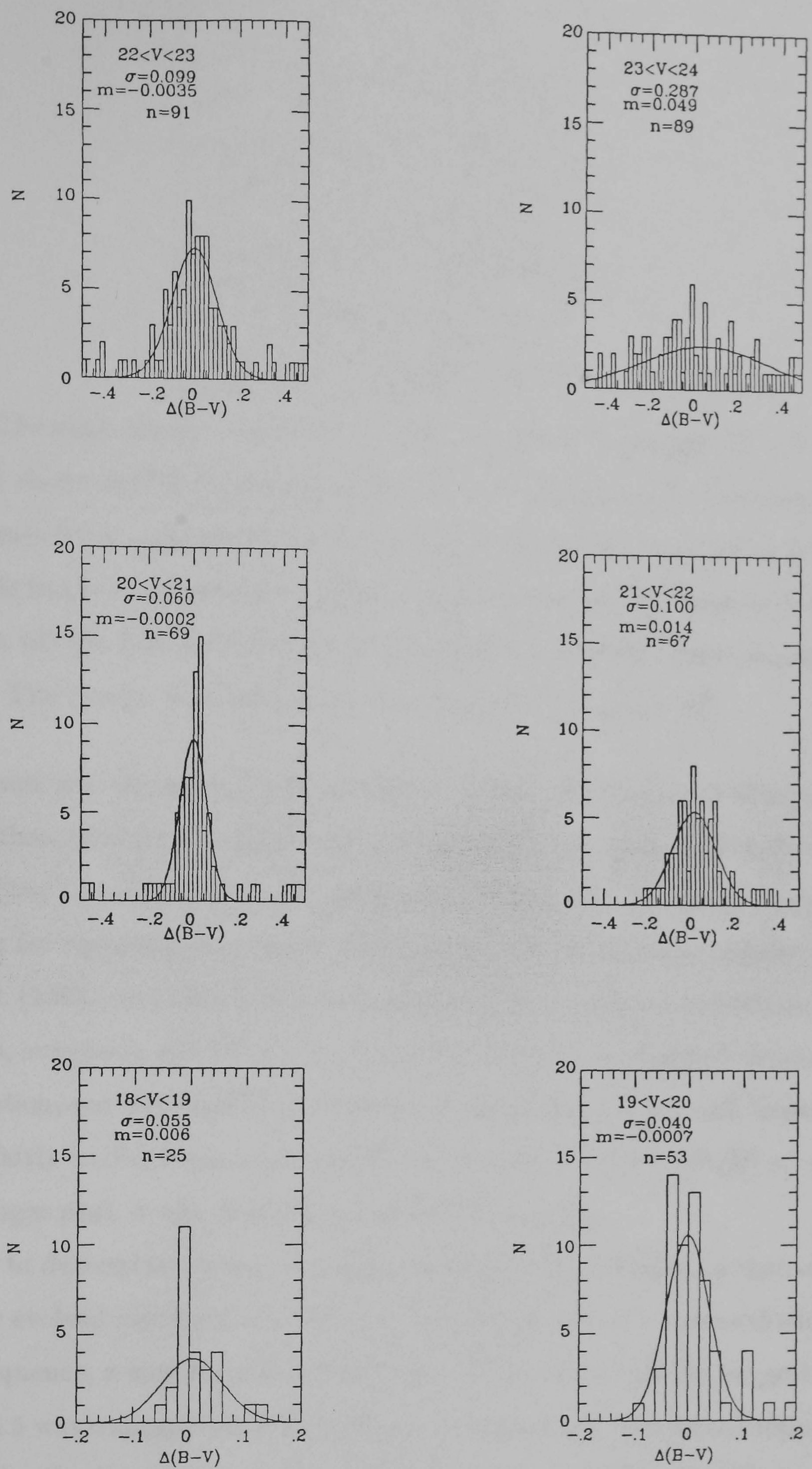

Figure 4.4: Colour residuals from the main sequence mean locus. The data have been divided into one-magnitude bins in V. The curves are fitted normal distributions, as described in the text.

V	σ_p	σ_o	σ_i
18–19	0.009	0.055	0.054
19–20	0.014	0.040	0.037
20–21	0.023	0.060	0.055
21–22	0.057	0.100	0.082
22–23	0.085	0.099	0.051
23–24	0.179	0.287	0.224

Table 4.4: The main sequence intrinsic width in the magnitude range $18 < V < 24$. Column (2) shows the internal photometric error derived from the frame to frame scatter in magnitude, column (3) the dispersion of a Gaussian distribution fitted to the residuals from the main sequence mean locus in the relevant magnitude range, and column (4) the inferred intrinsic width (dispersion) of the main sequence in this range. The results were calculated according to $\sigma_i = \sqrt{\sigma_o^2 - \sigma_p^2}$.

sequence stars and the more highly-advanced cluster members. As discussed in Chapter 3, there have been a number of spectroscopic abundance studies of evolved stars in ω Cen, and the results of these can be used to infer the likely abundance distribution for main sequence stars. Figure 4.5 is a reproduction of figure 15 of Hesser *et al.* (1985), and shows their compilation of the results of metallicity studies of giants, subgiants and RR Lyraes in ω Cen. There is no marked skewness to the distribution, nor any significant evidence of bimodality, the overall impression being of a fairly uniform spread in metallicity between $-2.25 <$ [Fe/H] < -0.75, with a stronger peak in the distribution at [Fe/H] ~ -1.5.

In order to determine whether a similar metallicity distribution to that seen in more highly evolved members of ω Cen was consistent with the observed width of the main sequence, a simple model of the distribution in metallicity suggested by the Figure 4.5 was constructed. This is shown in Figure 4.6. The model represents a uniform distribution of stars in the metallicity range $-2.25 <$ [Fe/H] < -0.75, plus a Gaussian peak centred at [Fe/H] $= -1.5$, with a dispersion of 0.4. The relative numbers in the two components of the distribution are equal. Spline interpolation between the isochrones of VandenBerg & Bell (1985) was used to make the transformation from [Fe/H] to colour residual. The transformation was defined such that [Fe/H] was -1.50 when $\Delta(B-V)$ was $0\overset{m}{.}0$. The resulting distri-

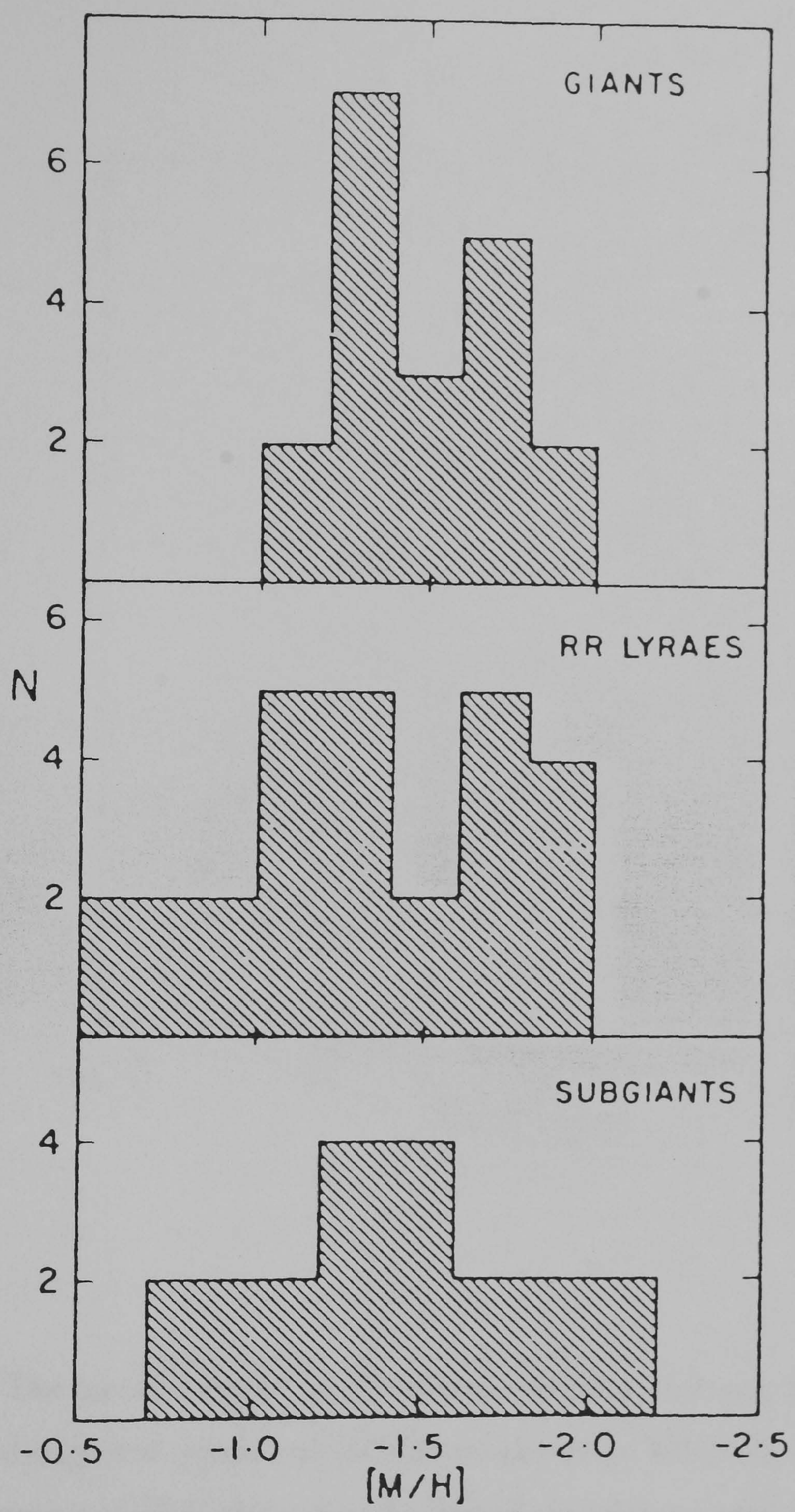

Figure 4.5: The metallicity distribution of evolved stars in ω Cen (from Hesser *et al.* 1985).

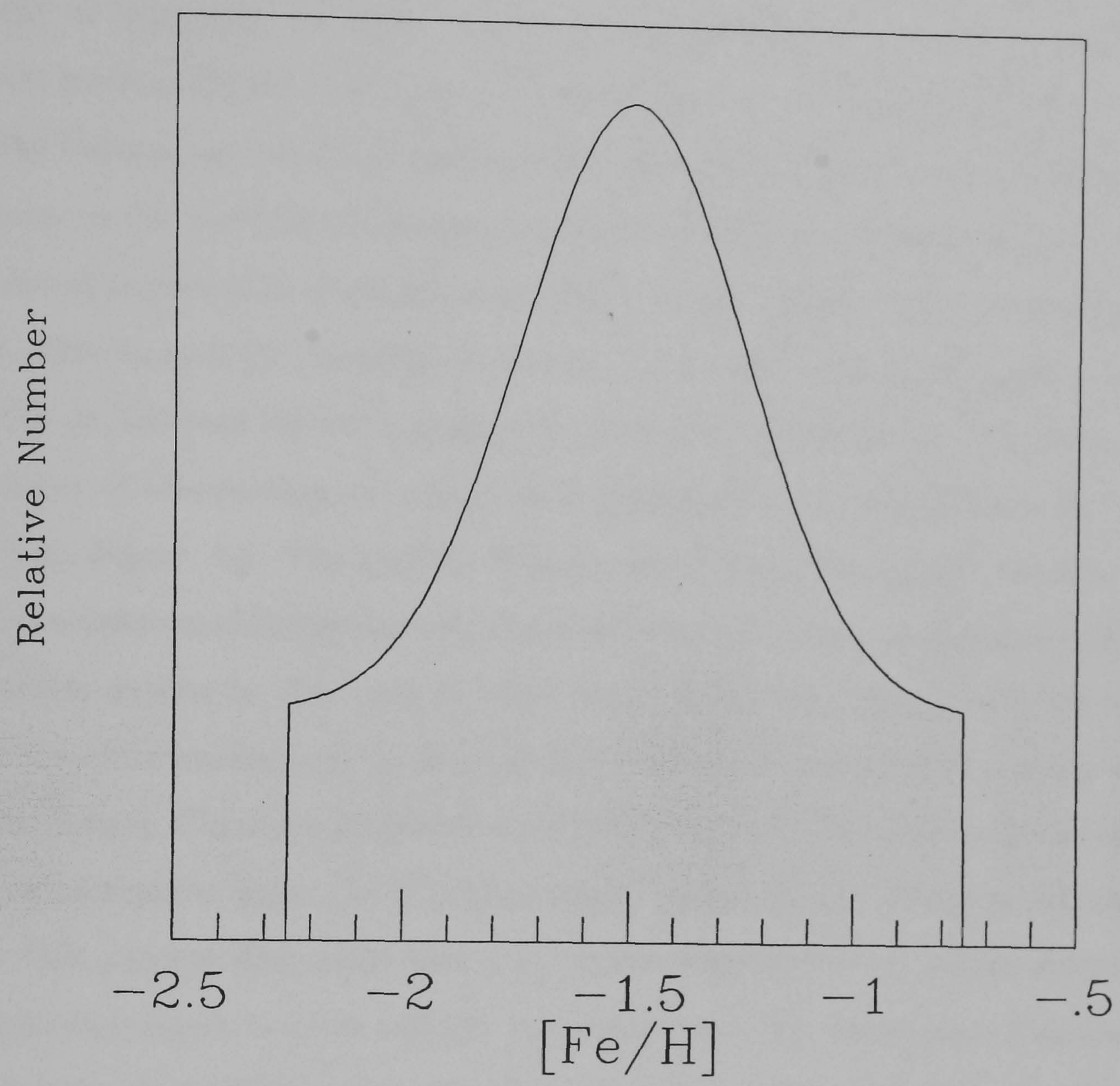

Figure 4.6: The model metallicity distribution used in effecting the comparison of observed and expected colour residuals about the mean MS locus. The distribution is a simple representation of the distribution of abundance suggested by Figure 4.5.

bution in colour was then compared with the colour residuals of Figure 4.4 above. In order to make the comparison with the histograms for each magnitude range, the model colour distribution was first convolved with the expected internal error function for that magnitude range (see Table 4.1 above), and secondly, scaled in height to represent the same number of observations suggested by the fitted Gaussian peak in Figure 4.4. Figure 4.7 shows the resulting distributions overlaid upon the histograms of colour-residual from the main sequence mean locus. The solid lines on the individual histograms represent the expected distribution if the data were distributed in abundance according to the simple model shown in Figure 4.6. The form of the distribution is modified by the internal photometric error σ_p, which is different for each magnitude range, as shown in the diagrams; n is the number of observations to which the distribution is normalized and has been taken from Figure 4.4. The quality of fit obtained from this simple model is very good, especially considering the only input parameters are a postulated metallicity distribution similar to that seen in other stars within the cluster, and the internal photometric uncertainty as derived from repeated measurements made upon individual stars. Chi-squared goodness of fit tests show these curves to be a considerable improvement upon the Gaussian distributions shown in Figure 4.4 above. Whilst this process illustrates that the stellar distribution in colour about the main sequence mean locus is entirely consistent with the abundance distribution inferred from observations of cluster stars at more advanced evolutionary stages, the present observations allow for considerable latitude in the actual shape of the main sequence metallicity distribution. For instance, it is only when comparatively extreme model metallicity distributions are employed, such as a continuous uniform distribution in the range $-2.5 < [\mathrm{Fe/H}] < -0.5$ or a Gaussian of mean $[\mathrm{Fe/H}] = -1.4$ with dispersion of 0.2 dex, that the quality of fit achieved becomes significantly poorer. Unfortunately this means that potentially important information about the physical processes which have given rise to the observed metallicity spread, such as the presence of significant skewness or bimodality in the abundance distribution, would remain undetected in the present observations. Figure 4.8, in Section 4.1.4 below, shows VandenBerg & Bell isochrones in the abundance range $-2.27 < [\mathrm{Fe/H}] < -0.79$ overlaid upon the present data. These isochrones appear to fit well the observed colour-magnitude data along the main sequence, but at the turnoff and subgiant region the fit seems to be poorer, in

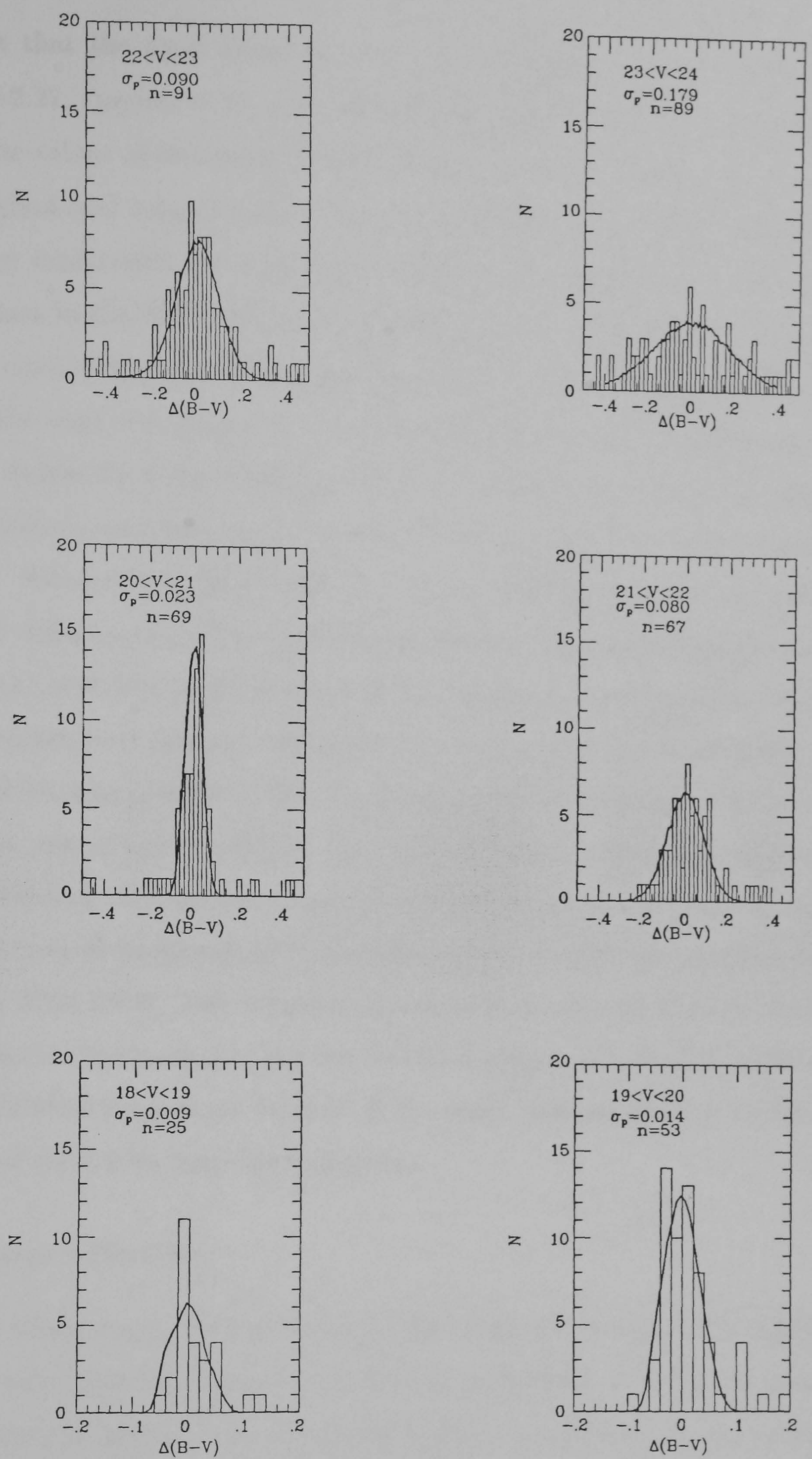

Figure 4.7: Overlays of the expected colour-residual distribution derived from the adopted model metallicity distribution. Solid lines represent the predicted colour distribution, σ_p the internal photometric scatter, and n the number of observations.

the respect that the most metal-poor isochrone, representing an abundance of [Fe/H] = −2.27, appears to lie substantially blueward of the observed cluster sequence. The colour of the cluster CMD sequence is more sensitive to metallicity in the subgiant and turnoff regions than at any stage in its main sequence evolution. One explanation for this would obviously be that the metallicity range found in stars in the MS luminosity regime is smaller than that implied by the range in composition observed amongst more highly evolved stars. Along the main sequence, the expected spread in colour becomes progressively smaller, and the apparently better fit of the [Fe/H] = −2.27 isochrone to the blue extreme of the colour-magnitude data may simply be due to the increasing size of the photometric scatter. Alternatively there may be some discrepancy between the subgiant branch and main sequence due to the relatively large zeropoint uncertainty (see Section 4.1.1) of $0\overset{m}{.}031$ in the transfer of the magnitude scale from the brighter stars to the faint main sequence data, and the main sequence may lie significantly blueward of its true position. The corollary of this assumption would be that this study is now in agreement with the results of the overwhelming majority of recently-published CCD colour-magnitude diagrams of globular clusters, namely that the theoretical isochrones of VandenBerg & Bell (1985) are too blue, by approximately $0\overset{m}{.}02$–$0\overset{m}{.}06$. This is further discussed in Section 4.1.4 below. It seems likely that some combination of the two factors is responsible, but it is difficult to make quantitative judgements because of the small number of stars available in this region of the colour-magnitude diagram.

Main Sequence Binaries

The present observations show no strong evidence for the presence of a significant number of main sequence binary stars. Such a component would be expected to form a sequence parallel to, and, in the case of equal-mass companions, some $0\overset{m}{.}75$ brighter than, the cluster main sequence. Evidence for such a sub-population has been seen in the sparse remote cluster E3 by Ortolani *et al.* (1986), but currently no convincing identifications have been made in the more centrally-concentrated, massive clusters which have so far been studied with CCD techniques. McClure *et al.* (1987a) found a slight excess of stars redward of their main sequence CMD of M68, which they attributed to possible poor photometry, or alternatively to

the presence of a small number of main sequence binaries. The histograms shown in Figures 4.4, and 4.7 do suggest there may be a slight excess in the number of stars in the magnitude range $18 < V < 22$ lying to the red of the main sequence at $\Delta(B-V) \approx 0\overset{m}{.}05$–$0\overset{m}{.}15$, however, the small numbers mean that it is not statistically significant. The field star density is expected to increase to the right of the MS in this magnitude regime, and thus field star contamination may be one explanation. Additionally, an effect inherent in the magnitudes derived from profile-fitting photometry may produce such an effect. A slight excess in the number of positive colour residuals has been observed in the analysis of simulated starfield images, which was carried out to help calibrate the results of Sections 4.1.5 and 3.4.3, and was shown to be due to the fitting of a single PSF to two or more significantly overlapping stars. Of course, a binary system is just a rather special subset of the above case, but the analysis of simulated starfields has shown that, despite the rigorous checks incorporated in STARMAN, this effect can produce a small, but detectable, percentage of poor measurements when physically unassociated stars which are coincident upon the CCD image are submitted to analysis by profile-fitting methods.

4.1.4 The Age of ω Centauri

The use of CCD detectors, large telescopes, and sophisticated software for profile-fitting photometry, combined with parallel advances in the modelling of stellar evolutionary tracks, has resulted in the achievement of new levels of accuracy and precision in the dating of globular clusters (see, for example, Hesser *et al.* 1987, Penny & Dickens 1986 and Fahlman *et al.* 1985). Whilst the present observations represent a substantial improvement, both in terms of the magnitude limits attained and the precision achieved, upon previously published colour-magnitude photometry of ω Cen, the unusual nature of the cluster makes accurate dating difficult. The range in colour in the upper main sequence, turnoff and subgiant branch of the ω Cen colour-magnitude diagram (as seen in Figure 3.18) is sufficient to introduce large uncertainties in the process of dating the cluster by isochrone fitting. In addition to the problems created by the width of the principal cluster sequences in the CMD, the small numbers of stars around the turnoff, which have been measured in this study, make accurate placing of the isochrones

difficult. Formal methods of determining the parameters of an isochrone which best describes an observed cluster CMD are difficult to apply and, as shown by Flannery & Johnson (1982) and Heasley & Christian (1986), produce results with inherently large uncertainties. This is hardly surprising considering the relative insensitivity of the isochrones to age and composition differences, and the large number of input parameters, some of which may be rather poorly determined.

The strategy adopted in this study has therefore been to simply overlay isochrones upon the CMD and obtain the best solution (or solutions) by eye, attempting to constrain as many of the input parameters as possible. The distance modulus derived from fitting subdwarfs to the main sequence, $(m - M)_V = 14.29$, was adopted, and the reddening was again taken to be $E(B-V) = 0.11$. The VandenBerg & Bell (1985) isochrones were linearly interpolated between the published models with helium mass fractions $Y = 0.2$ and $Y = 0.3$ to provide a grid of isochrones with $Y = 0.24$—this being the currently preferred value for the helium abundance in globular clusters (see Chapter 1). Figure 4.8 shows the overlay of 16 Gyr isochrones, with abundances in the range $-2.27 <$ [Fe/H] < -0.79. This represents the best fit to the colour-magnitude data within the age range 14–18 Gyr, but the uncertainties in this estimate are large, a conservative assessment of the likely error being ± 3 Gyr. This is the probable maximum error, determined by examining the goodness of fit of a range of isochrones. An illustration of the latitude present in this age determination is given in Figure 4.9, which shows overlays of isochrones of 14, 16 and 18 Gyr and the abundance value [Fe/H] $= -1.27$, with the above distance modulus, reddening and helium mass-fraction.

It is interesting to note that, contrary to the majority of recently published cluster colour-magnitude diagrams (see for example Heasley & Christian, 1986 and Fahlman *et al.* 1985), isochrones fitted with the preferred parameters of $(m - M)_V = 14.29$ and $E(B - V) = 0.11$ do not seem to lie significantly blueward of the actual colour-magnitude data. Various reasons have been proposed for the discrepancies between the published data and the theoretical models including the use of incorrect opacities in the atmosphere modelling or inappropriate values of α, the convective mixing length constant. No truly satisfactory solution to the problem exists and it seems highly likely that the VandenBerg & Bell (1985) isochrones are indeed some $0\overset{m}{.}02$–$0\overset{m}{.}06$ too blue. This being the case, it may be that the adopted photometric zeropoints are inaccurate and the data in

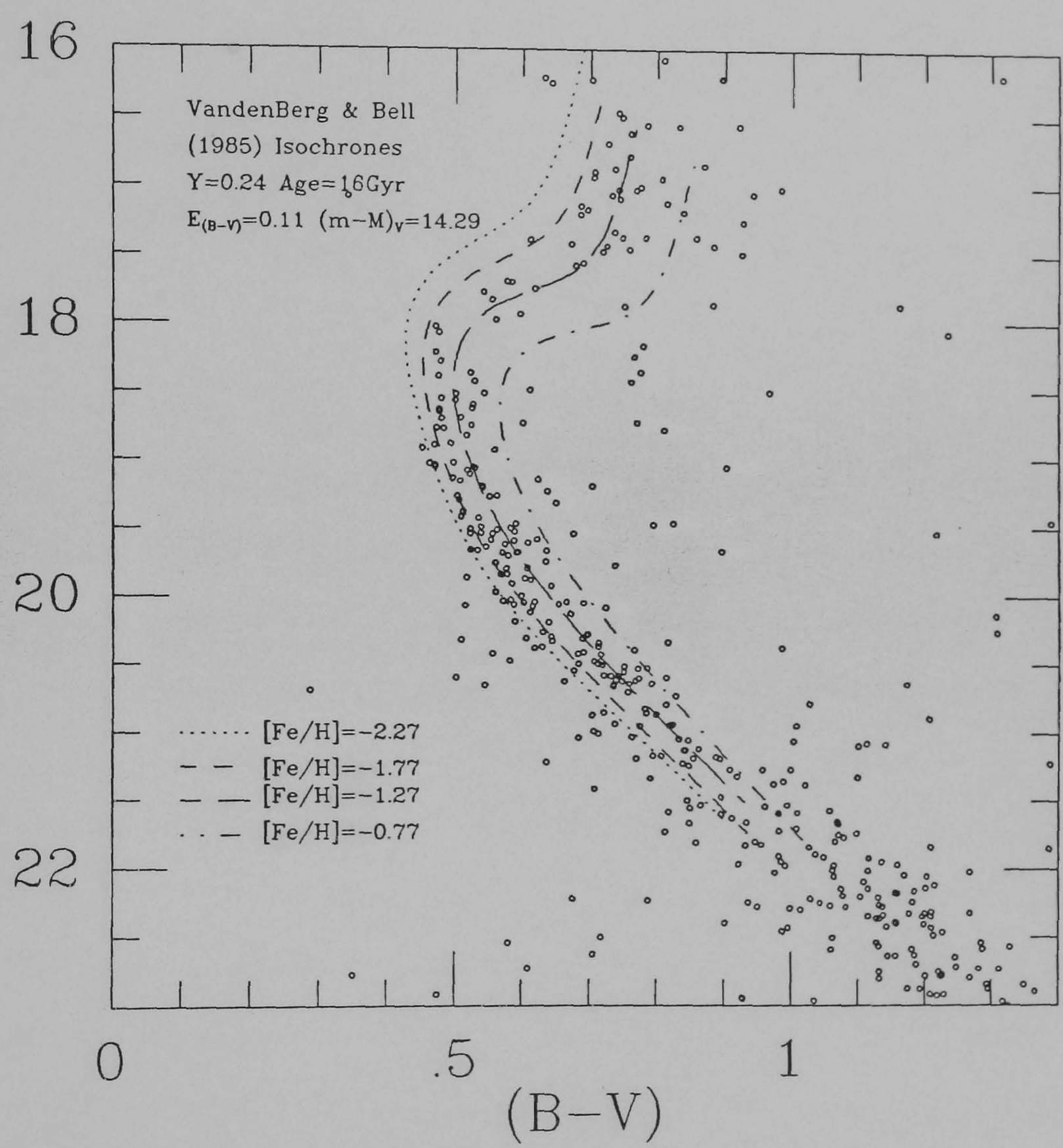

Figure 4.8: 16 Gyr VandenBerg & Bell (1985) isochrones overlaid upon the ω Cen CMD.

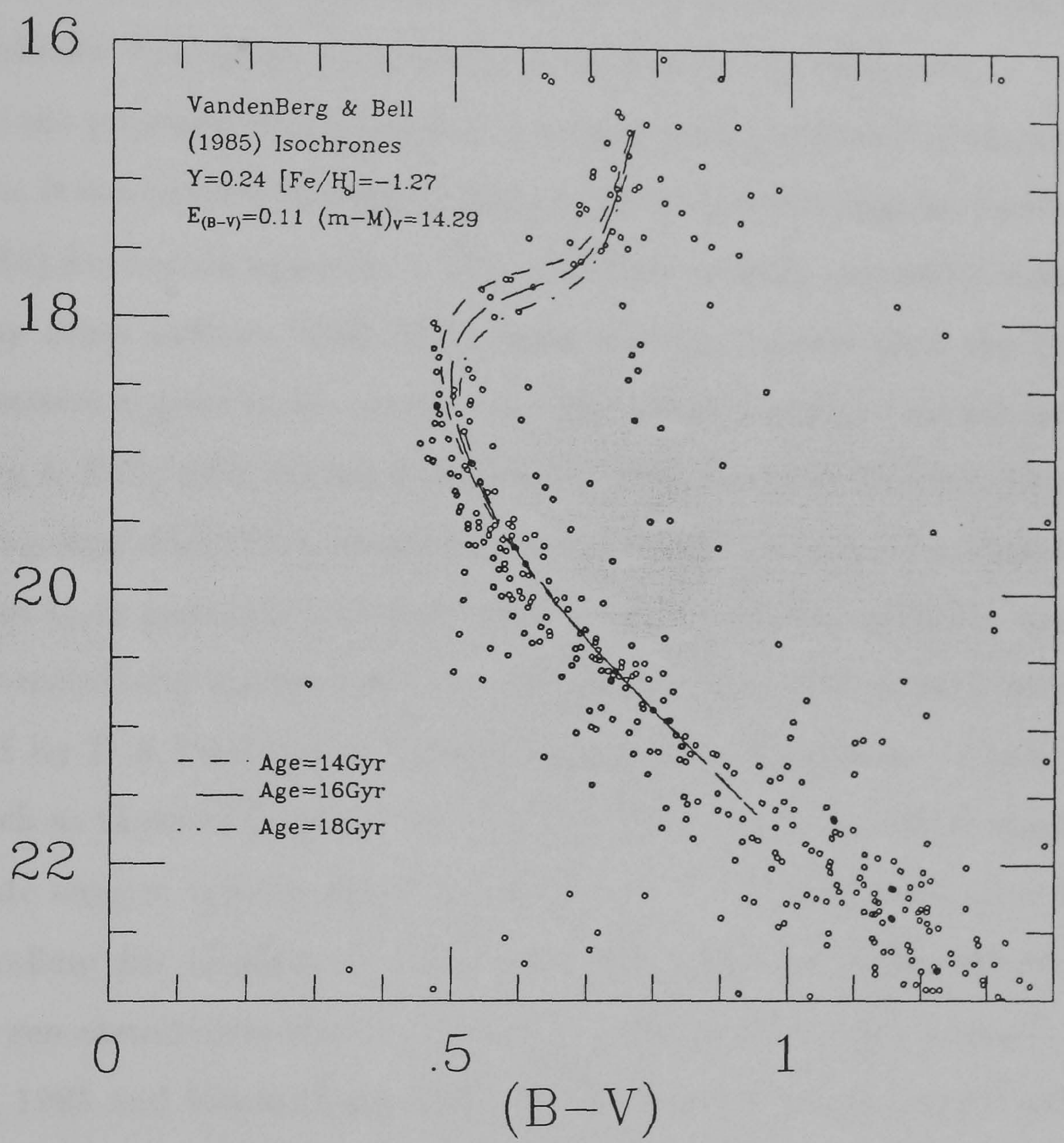

Figure 4.9: 14, 16, and 18 Gyr VandenBerg & Bell (1985) isochrones of [Fe/H] = −1.27 overlaid upon the ω Cen CMD.

this present study are actually too blue by approximately $0^m.04$. Such a zeropoint shift is entirely feasible within the large estimated zeropoint uncertainty (see Section 4.1.1 above). This is perhaps corroborated by the fact that comparison with isochrones show a slight inconsistency between the positions of the subgiant branch and the main sequence. Further evidence that there is a significant zeropoint error in the main sequence photometry is that a shift redward of the data of the order of $0^m.04$ would reduce the distance modulus derived by subdwarf sequence fitting to $(m - M)_V \approx 14.10$, and hence the magnitudes derived for the cluster RR Lyraes in Section 4.1.2 would agree more closely with the globular cluster RR Lyrae metallicity–luminosity relationship as determined in Chapter 1.

Despite the presence of this possible systematic misplacement of the main sequence data, it can be seen that the results obtained by overlaying the VandenBerg & Bell (1985) isochrones upon the ω Cen CMD are entirely consistent with those obtained by other authors using these same models, namely that the Galactic globular clusters appear to be coeval with ages around 16 Gyr (see for example, VandenBerg & Bell, 1985, Richer & Fahlman, 1984, Penny & Dickens, 1986).

Following suggestions that isochrones incorporating non-solar abundance ratios (see Chapter 1), in particular positive enhancements of [O/Fe], are more appropriate for low-metallicity cluster stars, several studies have used revised isochrones constructed by D.A.VandenBerg incorporating these refinements. These recent studies (such as those of Hesser *et al.* 1987 and McClure *et al.* 1987a) show that, for moderate oxygen enhancements $0.3 < [O/Fe] < 0.7$, isochrones of ~ 14 Gyr provide excellent fits to observed CMD data. The most noticeable effects of enhanced oxygen abundances are seen in the turnoff region (see, for example, Rood & Crocker, 1985 and VandenBerg, 1985, 1987), and as a broad generalization, it can be said that one effect of such oxygen enhancement is to decrease the age derived by isochrone fitting by approximately 2 Gyr. Thus, assuming that such oxygen enhancements are appropriate for ω Cen, the age estimate should perhaps be modified to 14 ± 3 Gyr, where, once again, the quoted uncertainties represent the probable maximum and minimum ages for which an adequate fit could be achieved. It is, however, difficult to see how the age of the cluster could be significantly less than 11 Gyr, unless there are serious errors or omissions in the theoretical models.

To maintain consistency with the survey of recent CCD colour-magnitude pho-

tometry made in Section 1.5, estimates of the age of ω Cen have also been made by comparing the turnoff luminosity with the models of VandenBerg & Bell (1985), and by the $\Delta M_{TO}^{RR}(bol)$ method which is discussed in Section 1.5. The turnoff luminosity is difficult to estimate because of the small number of stars in this region and the breadth of the main sequence, however the overlaid isochrones in Figure 4.8 suggest that the turnoff is at $V \approx 18.3 \pm 0.2$. This leads to values of $t_{\Delta} = 18.5 \pm 4$ Gyr and $t_{TO} = 16.5 \pm 3$ Gyr where the notation is the same as in Section 1.5.

One intriguing possibility which is raised by the results of Section 1.5 is that there is a metallicity-dependent age spread within the globular clusters. This is by no means a new suggestion (see, for example, Carney, 1980), however, recent studies (see Section 1.4) seem to be in broad agreement and suggest the globular clusters are coeval and approximately 14–16 Gyr old. Because of the breadth of the main sequence, and the subtle effects of a variation in age correlated with metallicity, it is impossible to rule out a difference in age of up to 3 Gyr between the metal-rich and metal-poor component of the cluster, on the strength of the present data. Were such a process to have occurred within ω Cen it, seems likely that it must have been continuous over a relatively long period of time, there being no evidence for multiple, discrete epochs of star formation.

4.1.5 The Cluster Luminosity Function

In the light of the discovery by McClure *et al.* (1986) that the slope of the initial mass function (IMF) of a globular cluster appears to be correlated with its metallicity, there has been greatly increased interest in the difficult task of constructing faint globular cluster luminosity functions. The colour-magnitude data shown in Figure 3.18 is in no sense complete; the measured stars were chosen (rather arbitrarily) by eye, avoiding excessive overcrowding or defective areas of the CCD chip. Furthermore, poor measurements (*i.e.* those showing excessive frame-to-frame differences or identified by the photometry program as being likely bad measures) were stringently weeded from the final CMD. In order to construct a more complete and reliable luminosity function, two of the faint AAT exposures (numbers 4 and 5) were reanalyzed using the robust and efficient star-finding program FIND, a new addition to the STARMAN photometric suite developed by

A.J.Penny. Stellar images discovered by the program were measured and removed by subtracting their fitted analytic/empirical PSFs, allowing any missed by the FIND program to be identified by eye and added to a second run through the measuring program. The number of stars missed by FIND was invariably only a tiny fraction of the total number, and this procedure was both considerably quicker and more efficient than the previous method of searching by eye. Stars were accepted for measurement if they appeared upon each frame, their RMS fitting parameter was within specified (generous) limits, and the frame to frame difference between the two measures fell below a magnitude-dependent threshold. The limits chosen were considerably higher than for the photometry which was used to construct Figure 3.18, ranging from $0\overset{m}{.}1$ for the brightest stars in the frame, to over $1\overset{m}{.}00$ for the very faintest stars. In addition to this, stars with saturated cores were included in the final results, however only the parts of the stellar image which did not exceed the linearity limit of the chip were used for the fit. The data were transformed from the wide band system to the Johnson system using the same extinction values and colour transformations as before, and then the data were transformed from the apparent to absolute magnitude scale by the subtraction of the derived distance modulus. Two further corrections were necessary to derive the cluster luminosity function. A correction was made for the photometric completeness of the data, and the field star contribution to the luminosity function subtracted. The former correction was derived by analysis of the artificial starfields discussed in Sections 3.4.3 and 4.1.1. Comparison of the characteristics of the stars placed randomly in the artificial starfields with the results of their analysis (using exactly the same techniques applied to the programme observations) allows the "completeness factor" *i.e.* the fraction of stars in the image recovered by the FIND and MEASURE procedure, to be calculated for each magnitude range. Figure 4.10 shows the fraction of recovered stars as a function of magnitude, derived from the analysis of artificial starfields. No correction for incompleteness was applied for stars brighter than $M_V = 6$, the completeness factor being greater than 0.98 above this limit. The field star contribution in each half-magnitude bin was determined from the same empirical modification of the Ratnatunga & Bahcall (1985) model Galactic star counts employed in Section 4.1.4 above. No correction was applied for stars brighter than $M_V = 2.5$. The small numbers of stars in the magnitude bins brighter than this limit render

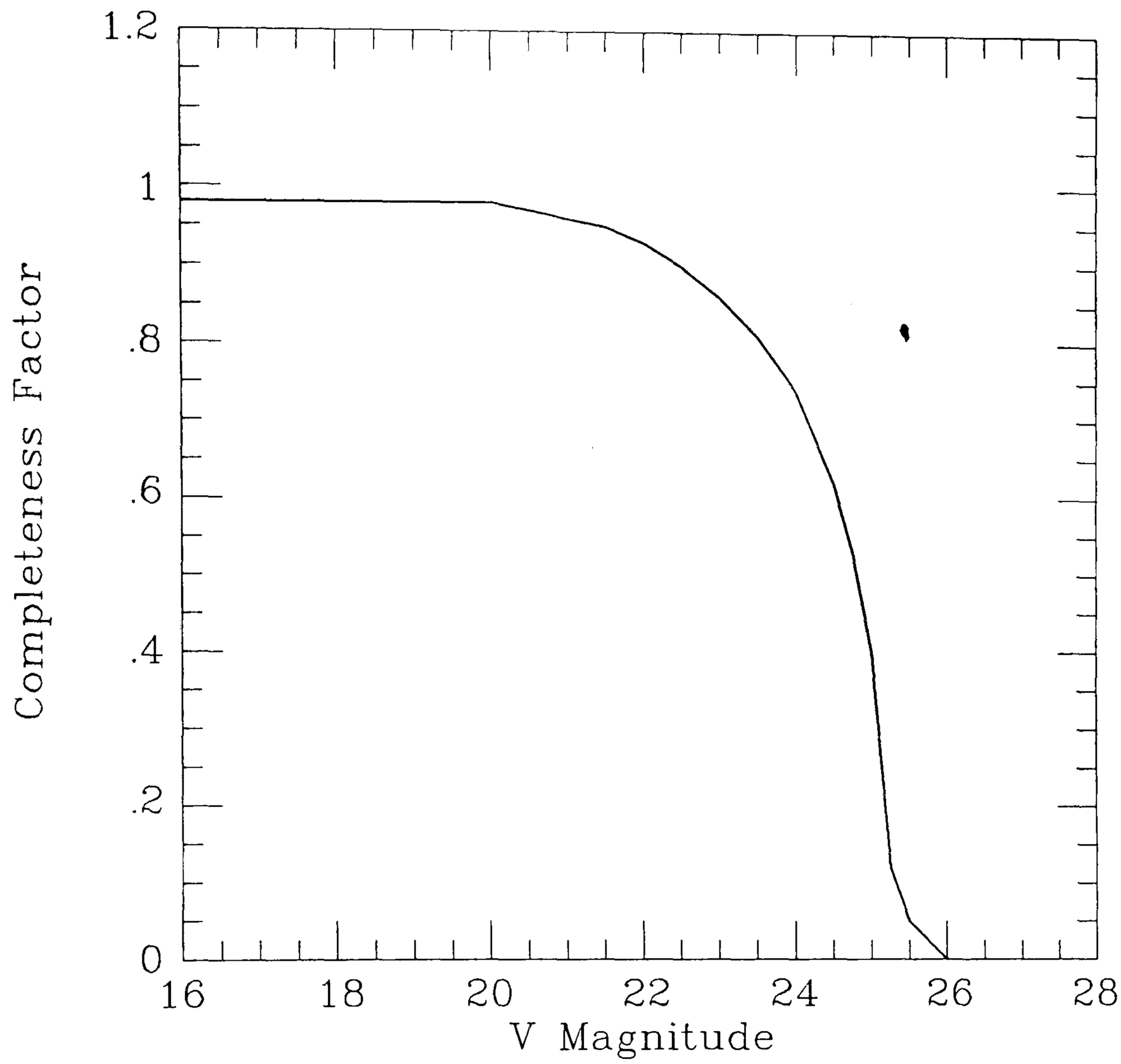

Figure 4.10: The fraction of recovered stars as a function of magnitude. Artificial starfields were used to determine the fraction of stars detected and measured, by the STARMAN photometry programs, as a function of magnitude.

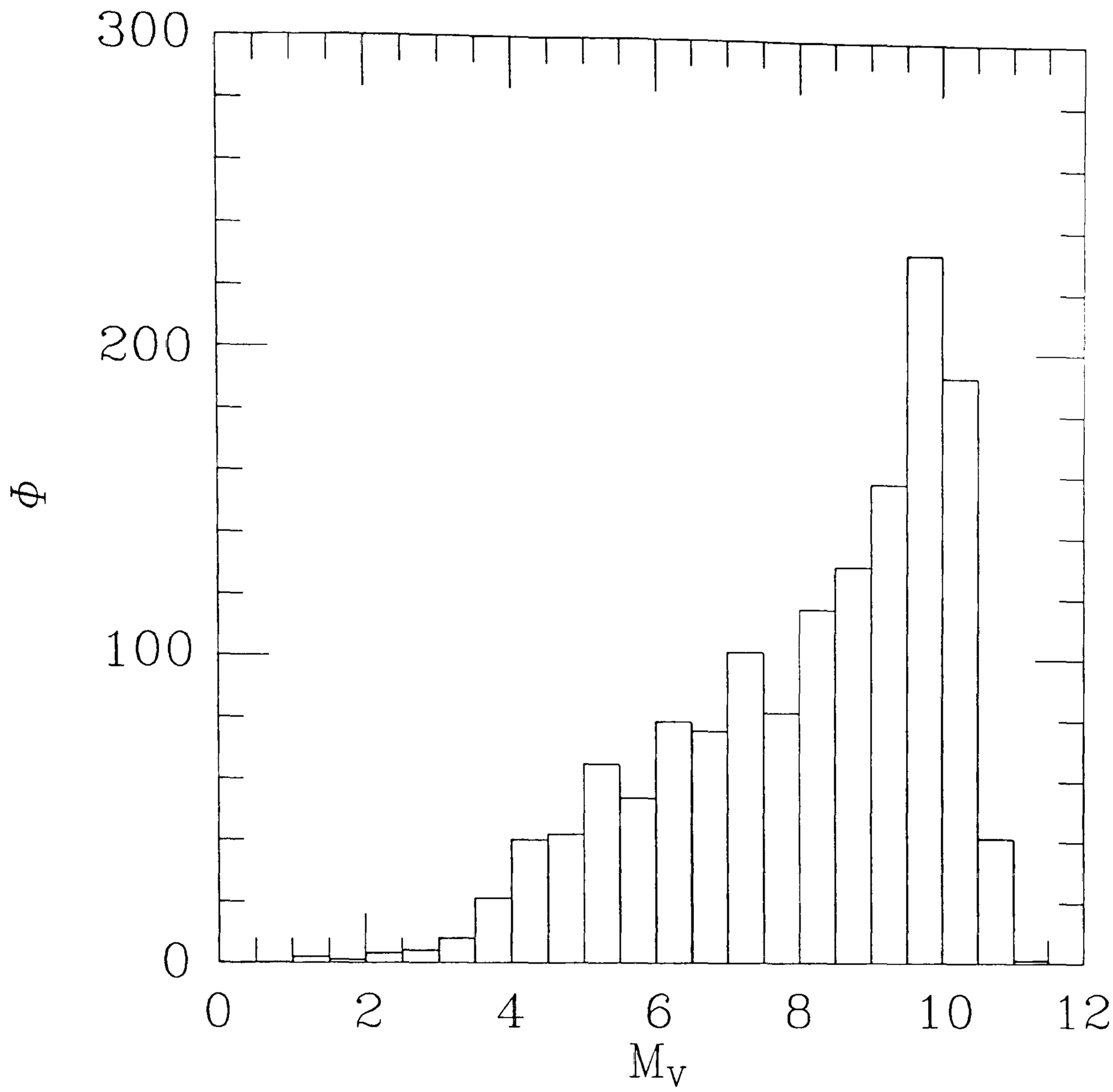

Figure 4.11: The ω Cen main sequence luminosity function before correction for incompleteness and field star contamination. The diagram shows the number of stars in half-magnitude bins in the magnitude range $-1 < M_V < 11.5$.

this approach unreliable and unwarranted.

The luminosity function, prior to the application of these corrections, is shown in Figure 4.11, whilst Figure 4.12 shows the luminosity function incorporating these corrections. The work of McClure *et al.* (1986) has shown there to be a correlation between x, the power-law index of the present-day mass function and cluster metallicity[1]. The most metal-poor clusters ([Fe/H] ≈ -2.3) require a value of $x \approx 2.5$ to obtain a good fit to model luminosity functions constructed from the evolutionary tracks of VandenBerg & Bell (1985), whereas a value of $x \approx -0.5$ is appropriate for the most metal-rich clusters. The derived luminosity function for

[1]The canonical models of the initial mass function of globular cluster stars are based upon a mass spectrum of the form $\phi(m)dm = Km^{-(1+x)}dm$, where $\phi(m)$ is the number of stars formed in the mass range m to $m + dm$. Further explanation of the terms used in this section is given in Chapter 1.

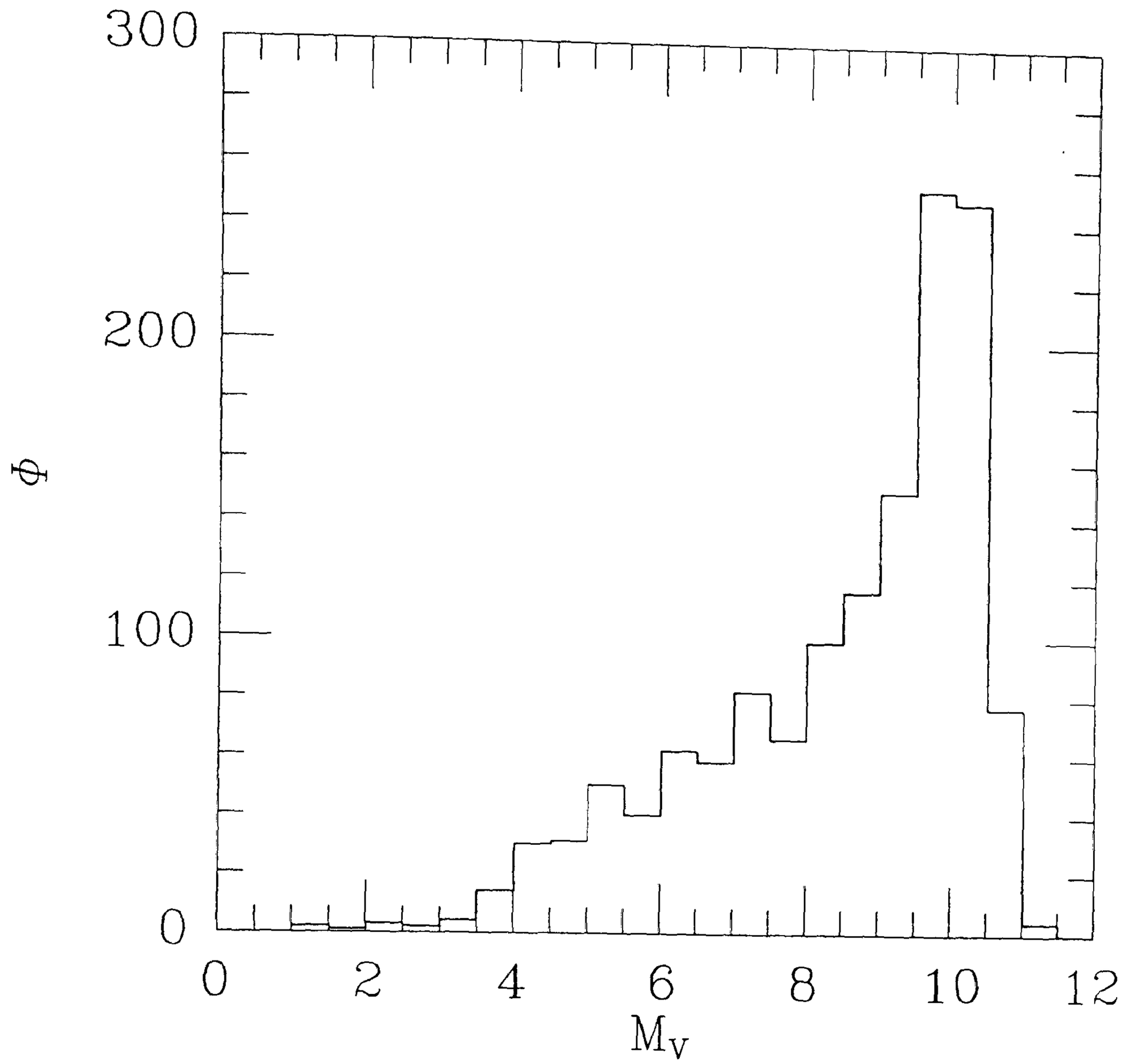

Figure 4.12: The ω Cen luminosity function after correction for incompleteness and field star contamination. The diagram shows the corrected number of stars in half-magnitude bins in the magnitude range $-1 < M_V < 11.5$.

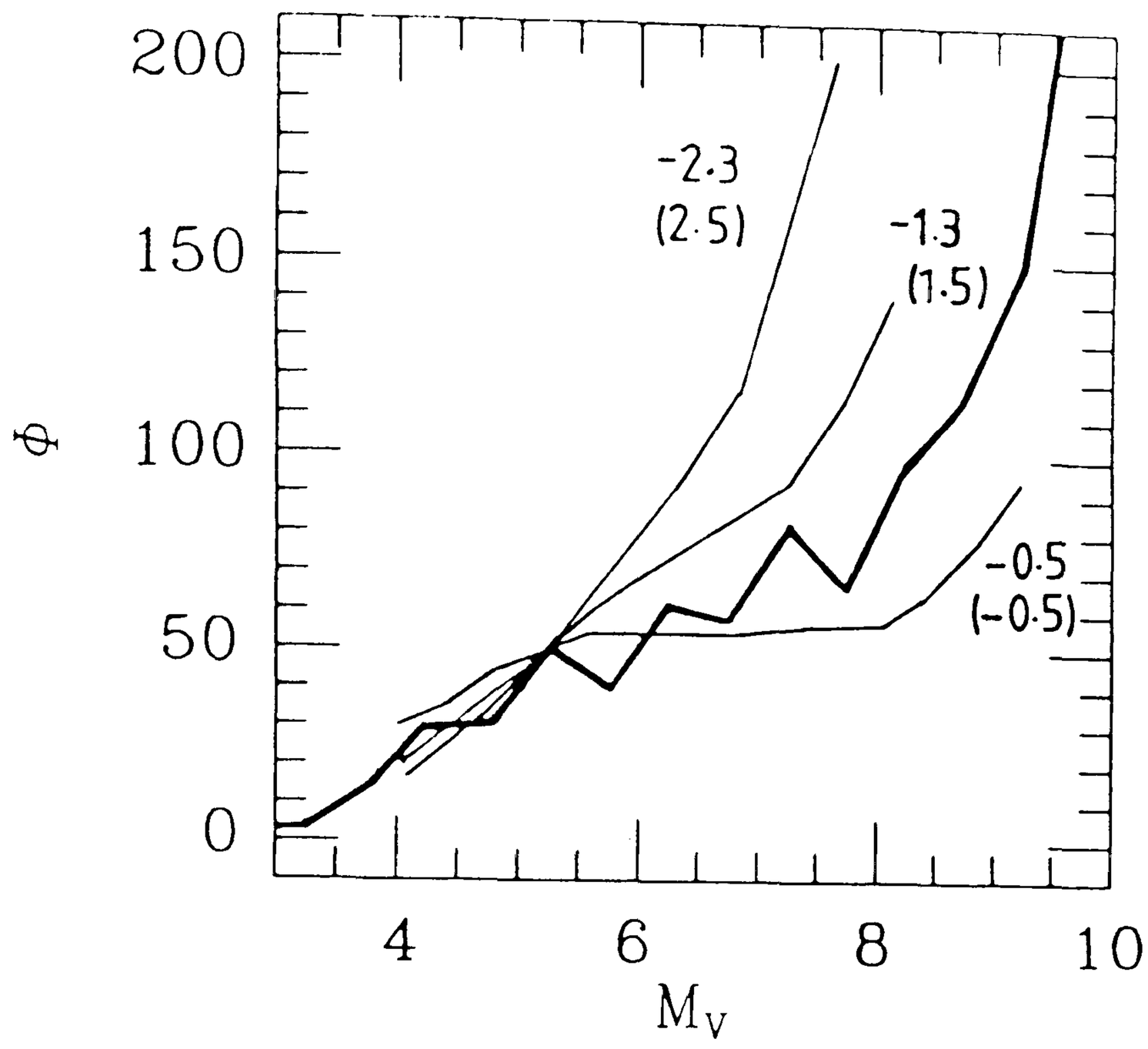

Figure 4.13: Comparison of the observed luminosity function of ω Cen with model luminosity functions. The model luminosity functions (light curves) are taken from McClure *et al.* (1986). The relevant metallicity and fitted mass function power-law index are shown next to each curve, with the latter in parentheses.

ω Cen has been superimposed upon figure 3 of McClure *et al.* (1986); this is shown in Figure 4.13, where, following McClure *et al.*, the observed luminosity function has been normalised to 50 stars in the absolute magnitude range $5.0 < M_V < 5.5$. The light solid curves in Figure 4.13 are the "best fit" model luminosity functions for the three metallicity values shown, the value of x adopted for each curve is shown in parentheses. The observed luminosity function appears to lie significantly below the relation predicted by the study of McClure *et al.* (1986) for a cluster of intermediate metallicity; even when the data is "smoothed" to alleviate the effect of statistical fluctuations, the luminosity function lies marginally below that expected for a cluster of Omega's metallicity. Applying the models of VandenBerg & Bell (1985) to obtain masses of cluster stars at the observed luminosities suggests that the power-law index of the ω Cen present-day luminosity function, x, is 0.8 ± 0.4. Unfortunately the published models of VandenBerg & Bell do not extend fainter than $M_V \approx 7.5$ and therefore data from the observed luminosity function,

in the range $7.5 < M_V < 9.5$ could not be used to determine the power-law index of the mass function in this way.

Smith & McClure (1987) have examined the possibility that it is the initial mass function of the cluster which determines the metallicity by its regulation of the number of massive stars capable of enriching the protocluster via supernovae and stellar winds. The value derived above is inconsistent with the prediction of Smith & McClure (1987) that ω Cen should exhibit a power-law index similar to the most metal-poor clusters, $x \approx 2.2$. This prediction was based upon the estimate made by Smith (1986) of the amount of metals required to produce the observed abundance spread in ω Cen, and upon the authors' assumptions about the influence of the initial mass function on the amount of metals released into the protocluster environment by short-lived, massive stars. Comparison with figure 4 of Smith & McClure (1987) shows that, for intermediate and high-metallicity clusters, their model consistently predicts higher values of x than are actually observed (this is simply an alternative way of saying that, in this metallicity regime, for an observed value of x, their model predicts a significantly higher cluster metallicity than is observed). Thus it is perhaps not surprising that the observed luminosity function of ω Cen suggests a value of x somewhat lower than the prediction of Smith & McClure (1987). Smith & McClure advance two alternative hypotheses to explain this discrepancy; a modification of the mass spectrum at high masses such that fewer high mass stars are formed from the protocluster cloud, or substantial loss of mass from the cluster in the violent conditions accompanying the formation and rapid evolution of large numbers of high-mass stars. As noted by Smith & McClure (1987), it is by no means clear that it is the initial mass function which determines the cluster metallicity, it could equally well be the case that the mass spectrum of the cluster stars is influenced by the metallicity of the protocluster cloud.

4.1.6 The Search for Cluster White Dwarfs

The faintest blue object in the cluster colour-magnitude diagram (see Figure 3.18 above) is located at $V = 23.27$, $(B - V) = 0.05$. Available information suggests that the likelihood of there being any quasars within the observed field down to $V \approx 25$ is small (Braccesi *et al.* 1980);similarly there should be very few field white

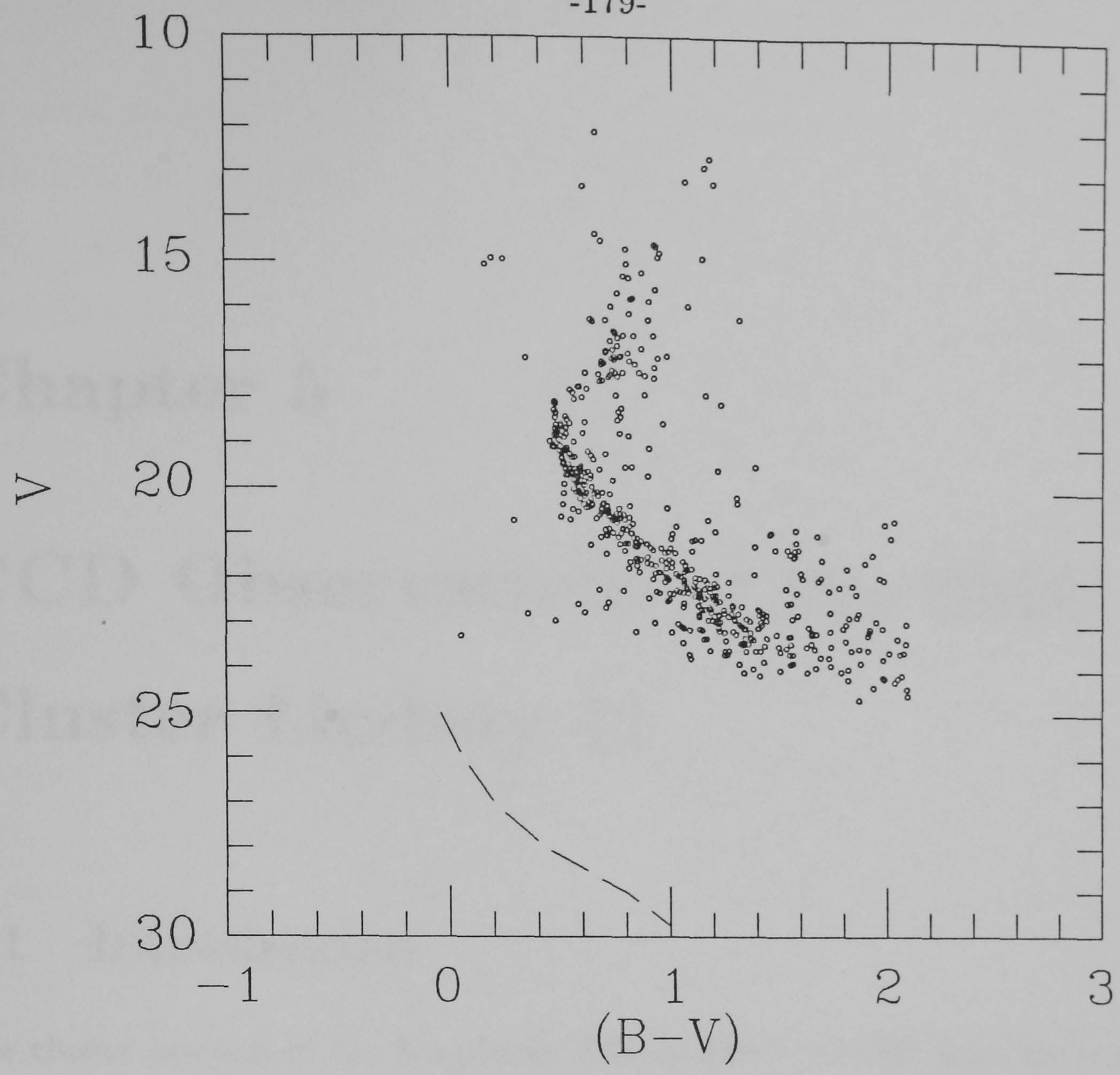

Figure 4.14: The colour-magnitude diagram of ω Cen showing the predicted location of the cluster white dwarf sequence. The broken line is the white dwarf sequence of Greenstein (1976) shifted to the distance modulus of ω Cen.

dwarfs (Gilmore, 1981). Figure 4.14 shows the observed cluster CMD, with the white dwarf sequence of Greenstein (1976) shifted to the same distance modulus as the cluster. Whilst it appears unlikely that the object seen at $V = 23.27$, $(B - V) = 0.05$ is a main sequence star which has been scattered to its observed position by observational error, it can be seen from Figure 4.14 that even the very brightest white dwarf stars ($M_V < 10$) are close to, if not beyond, the detection limits of the current data. Furthermore, the predictions of Bahcall (1985) suggest that the number of white dwarf stars of this luminosity should be significantly less than one within the field studied. Close scrutiny of this object on the CCD frames shows no indication that the object is non-stellar, nor that it is subject to any optical or electronic defect of the CCD camera. Thus, whilst it does not seem likely that the object is a cluster white dwarf, its true nature remains unknown.

Chapter 5

CCD Observations of the SMC Cluster Lindsay 11

5.1 Introduction

The cluster systems of the Magellanic Clouds differ radically from those of the Galaxy. Within the Galaxy, old and young clusters are readily differentiated by their appearance, and Galactic globular clusters appear to be coeval, or at least to have ages lying within a relatively small range. However, there exist, in the Magellanic Clouds, globular clusters which possess a large range in age and yet are morphologically similar to the globular clusters within the Galaxy. Photometric and spectroscopic studies of the integrated light from Magellanic Cloud clusters (see, for example, van den Bergh, 1981, Harris & Racine, 1979 and Searle, Wilkinson & Bagnuolo, 1980) have shown that there exists a large range in cluster age, and, furthermore, that cluster age is correlated with chemical composition. Magellanic Cloud globular cluster ages appear to range from a few million years to ages comparable with those of the Galactic halo globular clusters (Chiosi *et al.* 1986).

The great range in age of the clusters of the Magellanic Clouds therefore presents a unique opportunity in the study of stellar evolution. Not only can observations of these clusters provide insight into the history of the Magellanic Clouds, but may also contribute significantly to the understanding of the formation and evolution of cluster systems within galaxies. Their faintness, and relatively high concentration, combined with contamination by Magellanic Cloud

field stars, makes these objects difficult to observe with conventional ground-based telescopes. Recent observations of Magellanic Cloud clusters (see, for example, Rich *et al.* 1984, Da Costa & Mould, 1986 and Mould *et al.* 1986) with 4 metre class telescopes and CCDs have reached below the main sequence turnoff, providing much information about the nature of these objects. However, the most detailed photometric studies of the properties of these clusters must await the advent of space observatories. Prior to the tragic loss of the NASA Space Shuttle *Challenger*, a consortium lead by Dr. R.D.Cannon of the Anglo-Australian Observatory, and including members of the Physics Department of the University of Leeds, secured observing time on the Hubble Space Telescope to undertake observations of Magellanic Cloud clusters. The prime candidate of this study was to have been the Small Magellanic Cloud (SMC) cluster Lindsay 11 (L11). As part of the preparations for the observing programme, ground-based observations of this cluster were undertaken by the Author.

Lindsay 11 (Lindsay, 1958) is situated in the western region of the Small Magellanic Cloud ($\alpha = 00^h26^m13^s$, $\delta = -73°01'20''$, 1950). The cluster is also known as Kron 7, from the classification scheme of Kron (1956) who declined to describe the cluster as globular because of its apparent diffuseness as seen on the photographic plates available at the time. Lindsay 11 lies near to a much larger and more concentrated globular cluster, Kron 3 (Kron, 1956), and it has been suggested that L11 and Kron 3 share their origins in the same gas cloud (Grindlay, 1978). Lindsay 11 is classified as an old (age greater than 1 Gyr) red cluster in the two-colour survey of van den Bergh (1981). Infra-red photometry of cluster giant-branch stars by Mould & Aaronson (1982) suggests the cluster's age to be less than or equal to 6 Gyr. The core and tidal diameters of Lindsay 11 are 10.3″ and 516″ respectively (Kontizas, 1984). Previous photographic colour-magnitude photometry, calibrated by electronographic sequences, by Kontizas (1980) revealed a condensed grouping of stars at $V \approx 19.5$ in the range $0.5 < (B - V) < 1.0$; crowding and local background variations made photographic photometry near the core of L11 impossible and this study must suffer critically from the effects of field star contamination.

Run No.	Filter	Exposure Time (s)
266	R	100
268	V	100
269	B	120
270	V	300
271	B	400
272	R	300
302	V	900
303	B	1200
304	R	700
402	B	1200
403	R	600
404	V	1700

Table 5.1: The SAAO B, V and R observations of L11.

5.2 Observations

The present observations of Lindsay 11 were made using the UCL CCD camera (Walker *et al.* 1984) on the 1.0 m telescope of the South African Astronomical Observatory at Sutherland, Cape Province, South Africa on the nights of $26^{th}/27^{th}$ and $27^{th}/28^{th}$ of October 1984. Figure 5.1 shows the region observed. The cluster core (in the north of the CCD image) is comfortably encompassed within the 2×3 arcminute field of view of the CCD camera. Exposures were made in the Johnson B, V and Cousins R photometric passbands; the details are shown in Table 5.1. In order to determine the nightly extinction coefficients, observations were made of E-region standard stars (Menzies *et al.* 1980) during the observing run. The standard star observations were interspersed with the programme exposures, in a manner similar to conventional photoelectric photometry. Flat-field exposures were made to the twilight sky at the beginning and end of each night's observations, and master fringe frames were obtained from observatory staff. As described in Chapter 3, the SAAO-UCL CCD camera suffers from charge transfer inefficiency at low signal levels, and hence calibrating frames of the preflash signal were made. In all cases, the preflashing procedure produced a charge level in the CCD chip within the limits specified by the operating manual; it must be noted

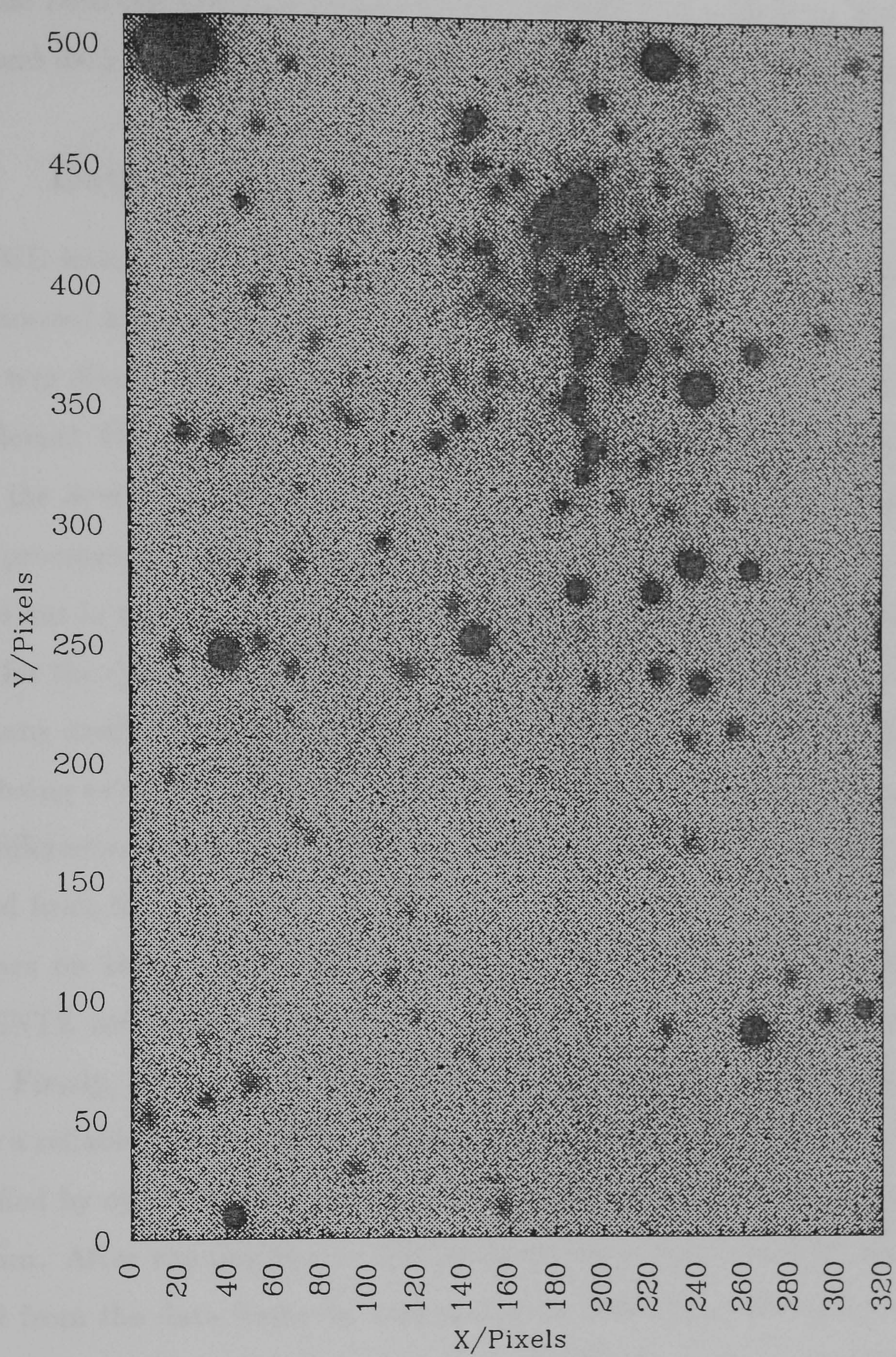

Figure 5.1: The region of the SMC cluster L11 observed during the present study. North is to the top, east to the right.

that there was no evidence of the defect seen on short ($\sim$ 1–5s) exposures during the June 1985 observations of the cluster ω Centauri (see Chapter 3). Bias exposures and dark frames were also made to enable calibration of the observations.

5.2.1 Data Reduction

The CCD frames were processed as described in Chapter 2. Firstly, the bias level was removed from the CCD image and the preflash signal subtracted. Each CCD frame was divided by the normalized, average flat-field exposure appropriate for the relevant filter combination, and pixels which had accumulated charge levels above the device's non-linearity threshold were flagged and ignored in all subsequent processing. Aperture photometry of the E-region standard observations was carried out in order to derive the nightly extinction corrections and the zeropoint terms for the colour transformations. The coefficients of the colour transformation equations used were the standard values provided by the SAAO staff, the equations being extremely accurate and stable (A.R.Walker, private communication). The differences between the standard magnitudes and colour indices, and those derived from the observations, are shown in Figure 5.2.

Stars on the frames were measured using the profile-fitting routines of the LORENTZ software package developed by A.J.Penny, and described in Chapter 2. Firstly, 4–10 bright, isolated stars were chosen in each frame and used to derive a reliable estimate of the stellar profile in that CCD image. Then stars were identified by eye from the frames, and entered into the profile-fitting photometry program. After running the profile-fitting program, the measured stars were removed from the data frame by subtracting their fitted profiles from the original data frames. Any stars which had been missed during the first run of the photometry program, and revealed by the removal of the fitted stars, were now entered and the photometry program run again. This was repeated for the available data frames. Stars were matched from frame to frame by position, and the average calculated for each star in each colour. The results were then corrected for atmospheric extinction and transformed to the standard magnitude scale using the relations derived from the E-region star observations. The positions, magnitudes and colours of the measured stars are shown in Table 5.2.

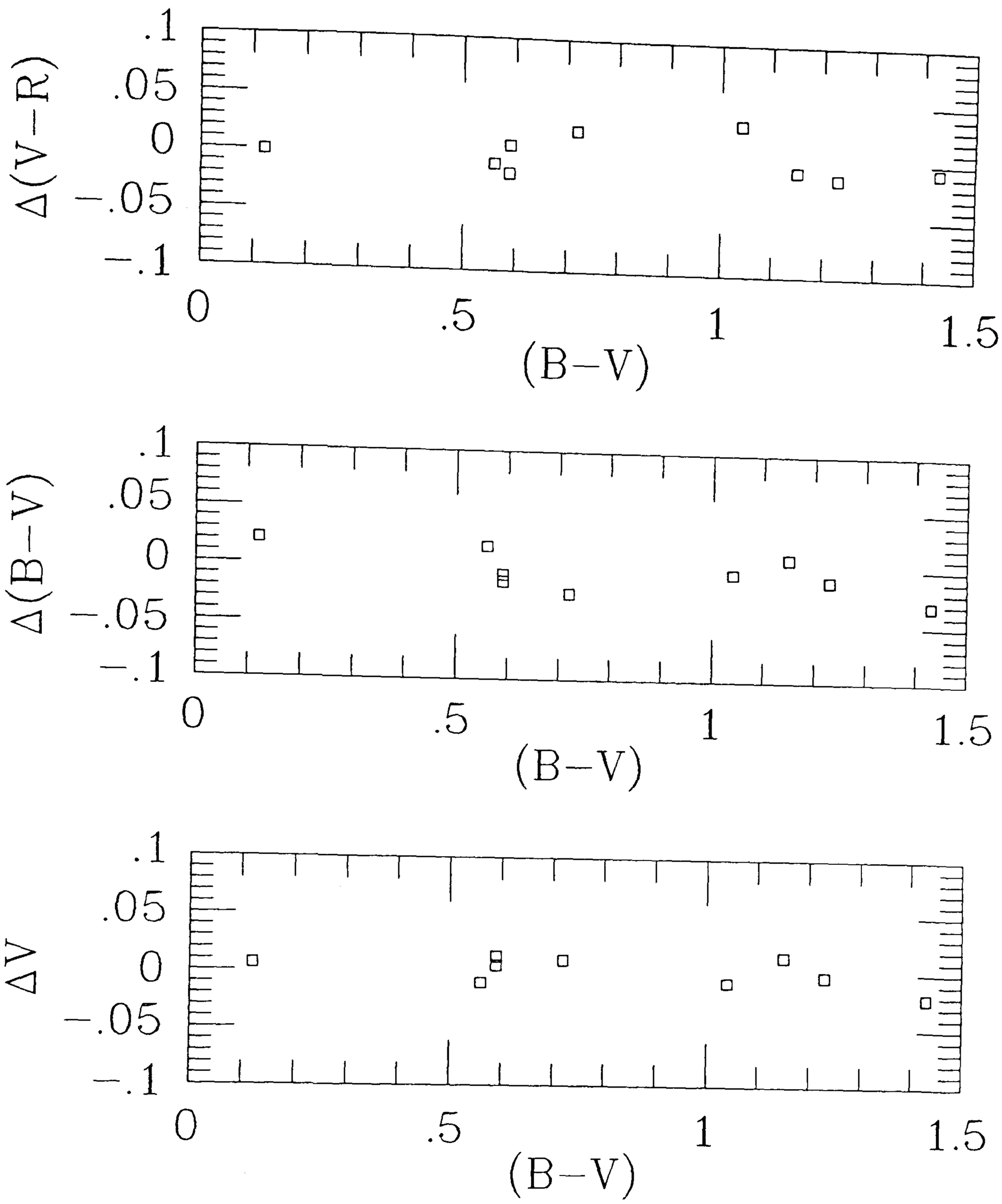

Figure 5.2: Differences between the E-region standard magnitudes and colour indices and those derived from the observations plotted against the standard $(B-V)$ colour index.

N	X	Y	V	(B-V)	R	(V-R)
1	193.53	484.88	18.87	0.68	18.22	0.64
2	204.41	472.04	19.57	0.74	18.99	0.57
3	244.93	443.03	19.02	0.84	18.26	0.76
4	243.52	427.50	17.38	2.70	15.55	1.83
5	233.96	429.96	18.45	0.72	17.78	0.66
6	218.87	426.45	19.46	0.74	18.82	0.63
7	209.24	424.45	19.57	1.19	19.31	0.26
8	196.85	458.39	19.73	1.06	19.14	0.58
9	246.80	395.74	19.61	0.77	19.04	0.57
10	225.98	414.51	18.70	0.85	18.05	0.65
11	262.46	378.33	18.56	0.95	17.79	0.76
12	292.23	387.84	19.62	1.24	18.84	0.78
13	238.26	363.40	16.98	1.08	16.14	0.83
14	211.96	381.17	18.58	0.76	17.89	0.69
15	204.71	372.96	18.53	0.53	17.96	0.56
16	196.45	426.76	19.58	0.90	18.67	0.90
17	188.56	444.90	17.35	1.21	16.48	0.86
18	179.74	431.26	16.84	1.53	15.81	1.03
19	177.62	437.35	17.22	1.23	16.29	0.93
20	170.56	408.53	19.61	0.65	18.88	0.73
21	164.90	385.74	19.48	0.46	18.87	0.61
22	145.10	401.46	19.47	0.48	19.04	0.43
23	150.98	412.41	19.52	0.57	18.90	0.61
24	146.53	421.37	18.77	0.93	18.07	0.69
25	145.96	455.39	19.35	0.60	18.66	0.68
26	135.45	455.34	19.41	0.65	18.85	0.56
27	142.76	474.47	18.08	0.94	17.31	0.76
28	112.18	378.26	20.45	0.91	19.74	0.70
29	122.96	373.87	20.41	0.36	19.76	0.64
30	134.87	368.51	19.87	0.68	19.15	0.71
31	151.27	367.89	19.48	0.80	18.84	0.64
32	149.28	353.01	19.42	0.80	18.76	0.65
33	128.05	357.59	19.60	0.79	19.02	0.58
34	136.63	348.61	19.06	0.67	18.43	0.62
35	126.77	340.20	18.82	1.11	18.11	0.70
36	188.42	352.81	18.14	1.04	17.30	0.84
37	193.85	337.98	18.12	0.91	17.39	0.73
38	189.54	326.76	18.86	0.94	18.18	0.68
39	216.20	332.17	19.44	0.67	18.88	0.56
40	180.54	314.34	19.27	1.01	18.65	0.62
41	52.56	471.42	19.47	0.70	19.00	0.47
42	84.69	446.14	19.64	0.49	19.00	0.64

Table 5.2: Details of measured stars in Lindsay 11. The positions are in pixel x and y coordinates in Figure 5.1.

N	X	Y	V	(B-V)	R	(V-R)
43	45.89	439.75	19.09	0.42	18.49	0.59
44	35.24	340.73	18.87	0.94	18.12	0.74
45	69.42	344.31	19.86	0.66	19.37	0.49
46	91.06	366.15	20.19	0.97	19.73	0.45
47	235.55	289.58	17.46	0.86	16.77	0.68
48	218.82	277.79	18.41	0.92	17.70	0.71
49	186.53	278.10	18.19	1.00	17.47	0.71
50	102.35	300.24	19.15	1.03	18.54	0.61
51	68.67	321.51	20.19	0.69	19.56	0.62
52	66.45	291.27	19.65	0.58	19.07	0.58
53	36.66	251.00	17.33	1.03	16.53	0.80
54	52.36	256.04	19.52	0.78	18.80	0.71
55	65.30	244.36	19.48	0.90	18.78	0.69
56	133.81	271.71	19.26	0.86	18.55	0.71
57	142.84	257.04	17.12	0.38	16.64	0.47
58	114.62	244.22	19.20	0.84	18.51	0.69
59	221.63	243.48	18.96	0.99	18.25	0.71
60	239.19	238.43	18.35	0.93	17.61	0.74
61	252.23	221.77	19.12	0.68	18.46	0.65
62	235.59	171.18	19.62	0.62	19.05	0.56
63	275.68	116.13	19.59	0.74	18.98	0.61
64	296.48	93.57	19.45	1.01	18.84	0.61
65	223.30	94.69	19.40	0.78	18.81	0.58
66	115.19	142.18	20.30	0.45	19.65	0.65
67	168.94	202.28	20.30	1.19	19.97	0.33
68	58.37	160.03	20.60	0.57	20.18	0.42
69	47.17	69.47	19.47	0.63	18.86	0.60
70	29.04	62.52	19.47	0.92	18.83	0.64
71	89.29	35.93	19.47	0.93	18.96	0.51
72	56.58	85.48	20.87	0.19	20.49	0.38
73	56.44	364.90	20.65	0.56	19.78	0.86
74	225.46	496.73	-	-	15.95	0.97
75	242.74	475.96	-	-	18.76	0.72
76	223.81	449.30	-	-	19.18	0.69
77	218.60	409.18	-	-	18.78	0.61
78	230.09	382.31	-	-	18.95	0.59
79	202.20	394.37	-	-	17.58	0.74
80	188.97	385.19	-	-	18.23	0.69
81	189.11	377.56	-	-	18.57	0.59
82	214.46	421.46	-	-	19.94	0.35
83	202.35	404.63	-	-	19.40	0.27
84	186.24	429.85	-	-	18.53	0.91

Table 5.2 continued.

N	X	Y	V	(B-V)	R	(V-R)
85	170.79	422.15	-	-	18.79	0.59
86	190.13	405.08	-	-	19.07	0.74
87	177.68	408.29	-	-	18.90	0.90
88	173.83	398.88	-	-	18.48	0.68
89	162.00	392.07	-	-	19.17	0.48
90	151.90	398.79	-	-	19.15	0.62
91	131.76	424.59	-	-	19.04	0.57
92	161.56	452.57	-	-	18.37	0.71
93	153.28	445.95	-	-	18.63	0.57
94	139.75	468.91	-	-	18.93	0.64
95	109.92	439.70	-	-	18.64	0.81
96	189.95	350.01	-	-	19.31	0.33
97	203.97	316.82	-	-	19.18	0.72
98	226.42	312.74	-	-	18.81	0.70
99	69.56	492.99	-	-	18.98	0.49
100	86.99	416.13	-	-	18.97	0.63
101	52.01	402.71	-	-	19.01	0.62
102	75.60	383.33	-	-	18.97	0.59
103	23.98	340.83	-	-	18.21	1.21
104	86.29	354.52	-	-	19.00	0.55
105	91.13	350.04	-	-	19.13	0.82
106	250.73	315.36	-	-	19.12	0.53
107	261.06	288.30	-	-	17.76	0.71
108	54.90	284.13	-	-	18.96	0.64
109	18.96	249.03	-	-	18.76	0.68
110	194.54	239.97	-	-	18.88	0.58
111	235.12	215.91	-	-	18.89	0.59
112	262.51	92.63	-	-	16.78	0.86
113	138.51	85.04	-	-	20.08	0.36
114	117.67	98.64	-	-	19.84	0.73
115	107.52	115.18	-	-	19.28	0.56
116	72.64	174.79	-	-	19.71	0.66
117	63.77	226.83	-	-	19.77	0.66
118	29.40	89.83	-	-	19.72	0.53
119	66.95	180.15	-	-	20.08	0.54
120	168.38	339.14	-	-	20.16	0.04
121	179.14	412.78	19.53	0.22	-	-

Table 5.2 continued.

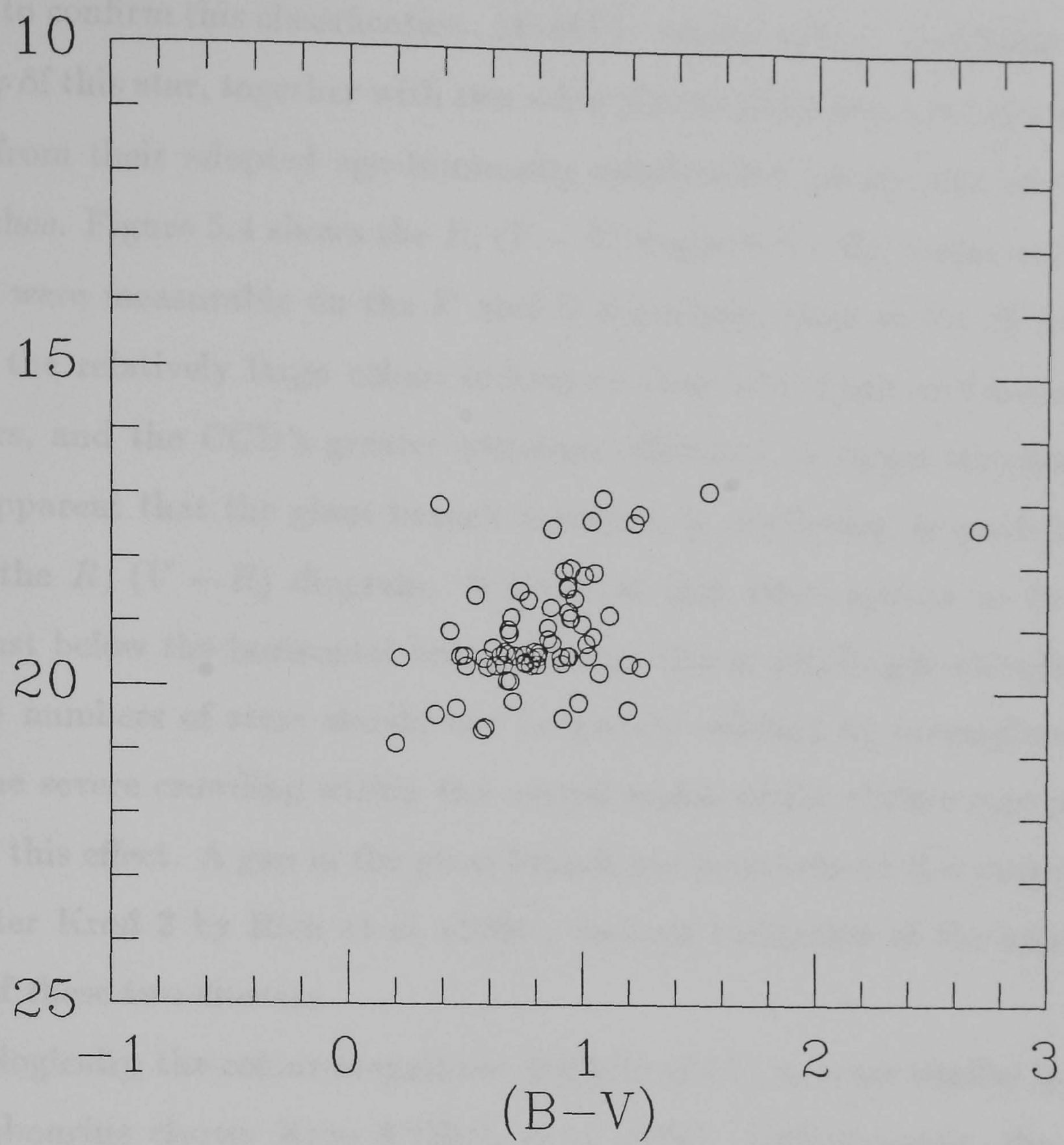

Figure 5.3: The Lindsay 11 V, $(B-V)$ colour-magnitude diagram, as derived from the present observations.

5.3 The CMD of Lindsay 11

The V, $(B-V)$ colour-magnitude diagram is shown in Figure 5.3. The principal feature is a strong clump of horizontal branch stars at $V \approx 19.5$ ranging in $(B-V)$ from 0.6 to 0.9, and a sequence of upper giant-branch stars. The uncertainties in the V and $(B-V)$ measurements are of the order of $0\overset{m}{.}03$ and $0\overset{m}{.}04$ respectively, and the detection limit is at $V \approx 21$; therefore the horizontal branch clump is a real effect, and not simply due to the effects of poor photometry near the faint limits of the observations. Star number 4 in Table 5.2 has an extremely high colour index, $(B-V) = 2.70$, and is thus probably a cluster carbon star (a highly evolved AGB star in which large amounts of carbon, synthesized within the star's core, have been mixed to the surface–see, for example, Mould & Aaronson, 1979). This star, situated some 10″ to the southeast of the cluster core, has been similarly noted by Mould & Aaronson (1982), but no spectroscopic studies have

been made to confirm this classification. Mould & Aaronson have used their JHK photometry of this star, together with two other cluster AGB stars, to infer an age $t < 6$ Gyr from their adopted age–luminosity relationship for the tips of cluster giant branches. Figure 5.4 shows the R, $(V-R)$ diagram for the measured stars. More stars were measurable on the V and R exposures, than on the B frames, because of the relatively large colour indices of these cool giant and horizontal branch stars, and the CCD's greater quantum efficiency at longer wavelengths. It is also apparent that the giant branch sequence, in particular, is much better defined in the R, $(V-R)$ diagram. It is noted that there appear to be very few stars just below the horizontal branch clump; this is still bright enough that the relative numbers of stars should not be greatly affected by incompleteness, although the severe crowding within the central region of the cluster may partly account for this effect. A gap in the giant branch has been seen at this magnitude in the cluster Kron 3 by Rich *et al.* (1984), another indication of the apparent similarity of these two clusters.

Morphologically, the colour-magnitude diagram of L11 appears similar to that of its neighbouring cluster Kron 3 (Rich *et al.* 1984). Unfortunately, the faint limit of the photometry is such that only a relatively rudimentary analysis can be carried out upon the data. Assuming a horizontal branch luminosity $M_V^{HB} = 0\overset{m}{.}6$ leads to a distance modulus $(m-M)_V = 19.0$, which suggests the true distance modulus to be $(m-M)_0 = 18.85$, if the reddening in the line of sight to the SMC is $E(B-V) = 0.05$ (Rich *et al.* 1984). Brück & Hawkins (1982), and Rich *et al.* (1984) have shown that the background SMC population in this region is similar in the colour-magnitude diagram to the cluster stars in the present study; Figure 5.5 shows the R, $(V-R)$ colour-magnitude diagram for all those stars within 40″ ($\sim$ 8 core radii) of the cluster centre. The radial distribution of stars within the CCD frame suggests that a reasonable estimate of the ratio of cluster to field stars within this area is at least 10:1. Thus it can be seen that the giant branch and horizontal branch clump are real features of the cluster CMD. Digital aperture photometry of the cluster with an 80″ aperture shows that the integrated magnitude and colour index of the cluster are $V_i = 13.96$ and $(B-V)_i = 0.93$. The integrated magnitude is in good agreement with that derived by Grindlay (1978) using photoelectric photometry through a 51″ aperture, $V_i = 14.04$, although Grindlay's integrated colour index, $(B-V)_i = 0.73$ is somewhat smaller than

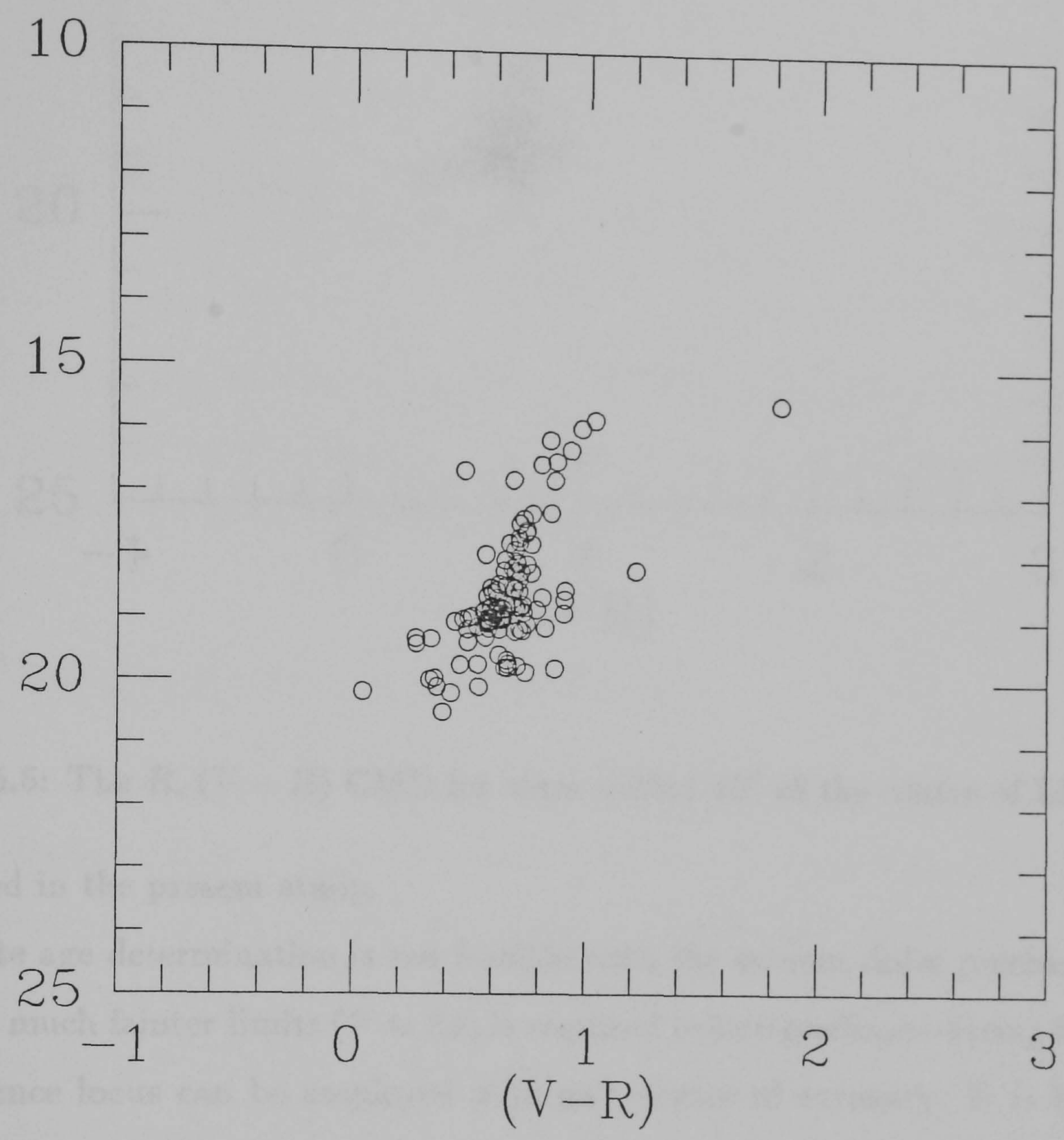

Figure 5.4: The Lindsay 11 R, $(V - R)$ colour-magnitude diagram, as derived from the present study.

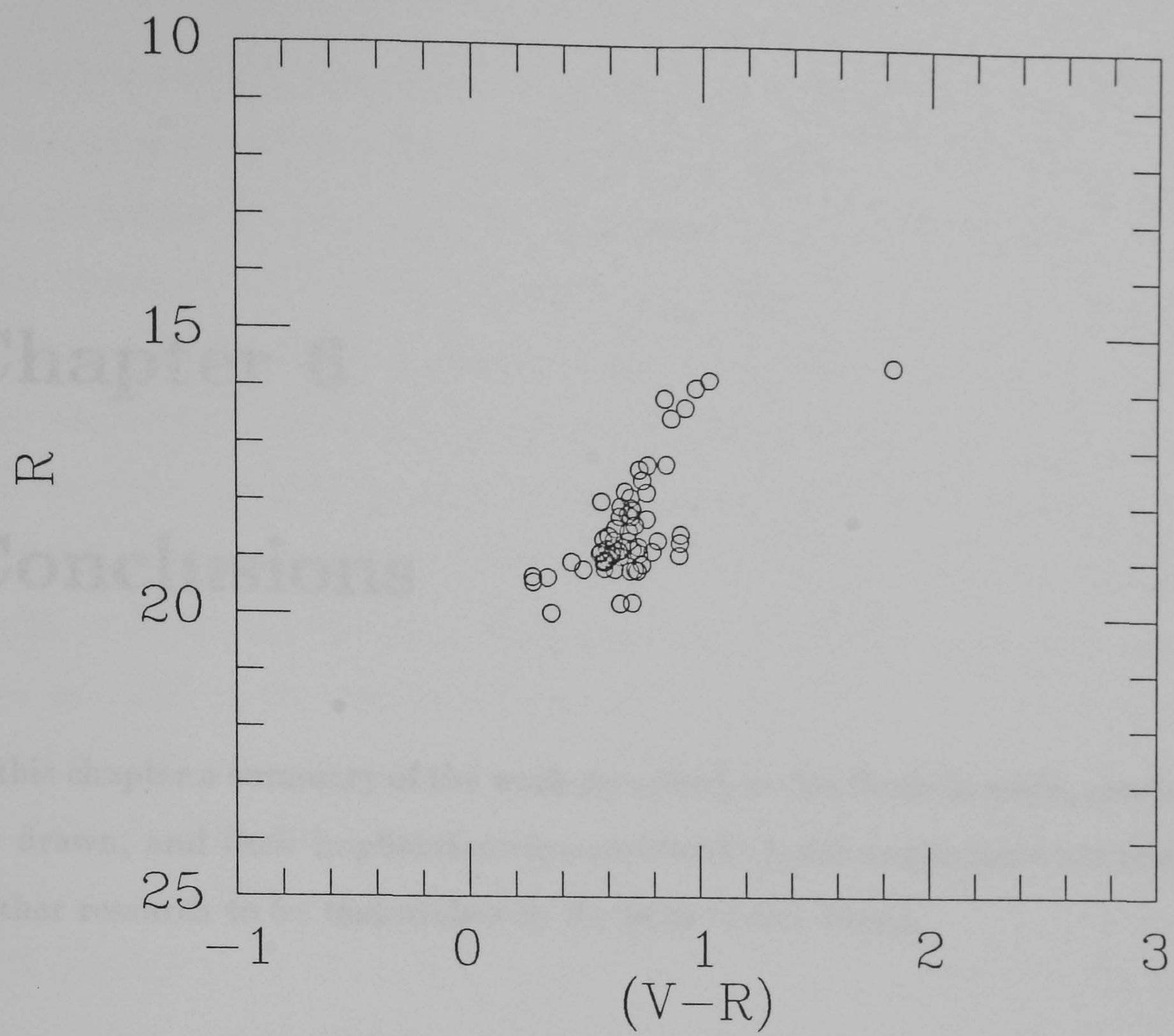

Figure 5.5: The R, $(V-R)$ CMD for stars within 40″ of the centre of L11.

that derived in the present study.

Accurate age determination is not feasible with the current data; precise photometry to much fainter limits ($V \approx 23$) is required before isochrone-fitting to the main sequence locus can be employed with any degree of accuracy. It is hoped that this problem will be resolved by observations made with the Hubble Space Telescope (HST). Preliminary studies by J.Buttress and A.J.Penny (private communication), using the present data as a basis for simulating HST images of SMC clusters, predict that exposures to the central region of Lindsay 11 will allow high-precision photometry of several thousand stars, to some four magnitudes below the main sequence turnoff.

Chapter 6

Conclusions

In this chapter a summary of the work presented in this thesis is made, conclusions are drawn, and their implications are reviewed. Some suggestions are made for further research to be undertaken in the light of this thesis.

6.1 Observations of ω Centauri

CCD photometry of fields in ω Centauri has enabled the construction of a colour-magnitude diagram in the V, $(B-V)$ plane which incorporates stars as bright as $V \approx 13$, and delineates the cluster main sequence to some five magnitudes below the main sequence turnoff, which is situated at $V = 18.3(\pm 0.2)$ and $(B-V) \approx 0.50$.

The mean locus of the cluster main sequence has been fitted to an empirical main sequence of nearby subdwarf stars; the resulting distance modulus is $(m - M)_V = 14.29 \pm 0.18$. From the adopted cluster reddening $E(B-V) = 0.11$, and the relationship $A_V = 3E(B-V)$, the true distance modulus of ω Cen is $(m-M)_0 = 13.96$, corresponding to a distance of 6.2 kpc. This new determination of apparent cluster distance modulus has been combined with the extensive photometry of RR Lyrae stars in ω Cen presented by Butler *et al.* (1978), to estimate the mean absolute magnitude of the cluster RR Lyraes. Taking the sample of Butler *et al.* as a whole, leads to the result, $M_V^{RR} = 0\overset{m}{.}25$, for a mean metallicity [Fe/H] $= -1.43$. This is approximately $0\overset{m}{.}2$ brighter than the value expected from the results of the survey of recent CCD colour-magnitude diagrams conducted in Chapter 1. This is not significantly larger than the standard deviation of the distance modulus (the major source of uncertainty in the derivation of M_V^{RR}) and it is therefore

probably not significant; however, it should be borne in mind that relatively small variations of a number of the fundamental parameters of horizontal branch stars, such as helium abundance and rotation, can cause changes in luminosity of this order (Sweigart *et al.* 1987). It would be informative, therefore, to obtain a more precise calibration of the photometric zeropoint of the present data, in order to fully resolve the question of the ω Cen horizontal branch magnitude. Dividing the stars into metal-poor and metal-rich groups, according to the suggestion of Butler *et al.* (1978), leads to $M_V^{RR} = 0\overset{m}{.}33$ and $M_V^{RR} = 0\overset{m}{.}24$ for metallicities of [Fe/H] = −0.72 and [Fe/H] = −1.60 respectively. This is in excellent agreement with the slope of the luminosity–metallicity relationship determined for cluster horizontal branches in Chapter 1.

Field star contamination in the ω Cen colour-magnitude diagram has been estimated by empirically modifying the Galactic field star models of Ratnatunga & Bahcall (1985). The published models were scaled according to the ratio of field to cluster stars on the subgiant branch, in the region studied. This figure was derived from the spectroscopic work of Hesser *et al.* (1985). The accuracy of this model field star distribution was checked by performing star-counts in regions of the colour-magnitude diagram well removed from the cluster's evolutionary sequences, and comparing the results with the predicted numbers. The field star predictions were shown to be consistent with the observed numbers of stars in these regions. These field star models were then used to estimate the number of field stars in close proximity to the cluster main sequence.

The internal photometric dispersion in the stellar magnitude estimates was calculated from the frame to frame differences in measurements of individual stars. The dispersion in colour from the mean locus of the cluster main sequence, in the range $18 < V < 23$, was found to significantly exceed that which would be expected were observational scatter the sole cause.

It is assumed that this spread in colour is due to variations in effective temperature from star to star, caused by the effects of changing chemical composition upon opacity, as well as upon the degree of line-blanketing and back-warming. This is the first clear evidence that the chemical inhomogeneity exhibited by more highly evolved stars in ω Cen is present at luminosities fainter than the turnoff region, upon the main sequence proper. This implies that the compositional differences observed in the member stars of ω Centauri have their common origins

in the early history of the cluster. The deviation in colour from the MS ridge line is not well described by a Gaussian fit. However, subtracting the contribution of the, approximately, normally-distributed internal photometric scatter, leads to an estimate of the intrinsic dispersion in colour of $\sim 0\overset{m}{.}05 \pm 0\overset{m}{.}01$. The shape of the colour distribution about the main sequence ridge line provides little information about the exact nature of the underlying distribution in metallicity, although thus far the treatment of this aspect has been somewhat rudimentary. The distribution in colour has, however, been shown to be entirely consistent with the metallicity distribution suggested by published spectroscopic studies of subgiant, giant and horizontal branch stars within the cluster; namely an extreme range in metallicity of approximately $-2.25 < [\mathrm{Fe/H}] < -0.75$, with a distinct peak in the distribution at $[\mathrm{Fe/H}] \approx -1.5$. Alternative morphologies cannot be ruled out, however, and further work is required to determine the true nature of the underlying metallicity distribution. The Author is continuing to work upon the technique of fitting geometrically variant profiles to CCD data, and it is hoped that subsequent re-analysis of the faint exposures to region O1 will obtain satisfactory fits to many more stars than the 500 or so used in the current colour-magnitude diagram. The luminosity function presented in Chapter 4 was derived using more powerful and sophisticated techniques for starfinding and profile determination than the earlier colour-magnitude data; unfortunately these reductions were incomplete at the time of writing, and an improved colour-magnitude diagram could not be presented in this study. The increased numbers of measured stars will advance many aspects of the study of the ω Cen CMD, but will, in particular, improve the definition of the main sequence colour distribution. Furthermore, the application of more sophisticated statistical techniques to the data may allow definitive quantitative results, upon the nature of the main sequence metallicity distribution, to be achieved.

Comparisons of the fit of the main sequence and subgiant branch to the isochrones of VandenBerg & Bell (1985) suggest that, for the region of the subgiant branch, the metal-poor extreme of the metallicity distribution is located at $[\mathrm{Fe/H}] \approx -1.7$, whereas the published results from brighter stars suggest the metal-poor extreme of the metallicity distribution is located at $[\mathrm{Fe/H}] \approx -2.2$. Alternatively, there may be a systematic zeropoint error in the transfer from the subgiant branch to main sequence part of the diagram. This is suggested by

the difficulty in fitting an isochrone to the blue envelopes of both the subgiant branch, and the main sequence. A redward shift of the main sequence data by $\sim 0^m.04$ would enable consistent isochrone fits to be made to both the main sequence, and subgiant regions. The uncertainty in the transfer of zeropoints to the faint main sequence data is calculated to be $0^m.031$, and, therefore, it is not unreasonable that such a systematic error should exist. There is a large body of evidence in the literature which suggests that the isochrones of VandenBerg & Bell (1985) are too blue, by approximately $0^m.02$–$0^m.06$ (see, for example, Fahlman *et al.* 1985, Penny & Dickens, 1986, McClure *et al.* 1987a, Hesser *et al.* 1987). Thus, were the transfer of photometric zeropoint to the main sequence in error, as suggested above, not only would consistency with other recent colour-magnitude studies be preserved, but the adopted distance modulus would be reduced somewhat, to $(m - M)_V \approx 14.10$. A further implication of this is that the average absolute magnitude of the cluster RR Lyrae stars in ω Cen would be modified to $M_V^{RR} \approx 0^m.45$, a value in better agreement with the relationship between RR Lyrae absolute magnitude and cluster metallicity, as derived in Chapter 1.

The large spread in colour upon the main sequence and subgiant branch, and the small number of measured stars in the turnoff region, preclude age determination of the highest accuracy, from isochrone fits. Overlaying the isochrones of VandenBerg & Bell (1985) upon the data, shows that an age estimate of 16 ± 3 Gyr is entirely consistent with the observed colour-magnitude diagram. The uncertainty quoted is not a standard deviation, but rather an estimate of the probable maximum deviation in age from the "best fit" value determined from the VandenBerg & Bell (1985) isochrones. This derived value of the cluster age is in close agreement with the results of other authors, who have compared their colour-magnitude data with these isochrones (see, for example, Penny & Dickens, 1986, Richer & Fahlman, 1984, 1986, 1987 and Bolte, 1987). As has been discussed in Chapter 1, there is growing evidence to support the hypothesis that elemental abundances in low-metallicity cluster stars are not scaled in solar ratios, and in particular that oxygen is somewhat overabundant. It is noted that the qualitative effect of these predicted increases in oxygen abundances is to force the absolute magnitude of the cluster main sequence turnoff to fainter luminosities. It is estimated that the incorporation of O enhancements, appropriate to the metallicity of ω Cen, would lead to a lowering of the age derived by isochrone fitting by approximately 2 Gyr.

The present study does not preclude a (possibly metallicity dependent) age spread within ω Centauri of up to ~ 3 Gyr.

The cluster luminosity function has been constructed in the range $1 < M_V < 11$. The effects of photometric incompleteness have been compensated for, using corrections derived from measurements of artificial star fields. The model field star distribution, described above, has been used to correct the observed luminosity function for contamination by Galactic background stars. Comparison with the models constructed by McClure *et al.* (1986), suggests that the mass-function power-law index, x, is of the order of 0.5–1.0. This is slightly below the value, $x \approx 1.5$ predicted by the empirical relationship of McClure *et al.* (1986) for a cluster of [Fe/H] ≈ -1.5. The present result, however, disagrees with the calculations of Smith & McClure (1987), who predict a substantially higher index, $x \approx 2.5$, for ω Cen.

Although the work presented in this thesis advances substantially our knowledge of the observable characteristics of ω Cen, a number of questions remain unresolved. The uncertainty in the zeropoints of the main sequence data is unsatisfactorily large, and is a major contributing factor in the uncertainties associated with a number of the derived fundamental parameters, such as the distance and age of the cluster. Further CCD photometry, to $V \approx 19.5$, in the observed fields, would help resolve the problems of transforming the wide-band data to the standard system. A relatively modest telescope (~ 1.0 m) would be required for this task, but many repeated observations would be desirable, with extensive standard star observations, interspersed with the programme exposures, to accurately determine the colour transformations and extinction corrections. Similarly, more extensive observations, at smaller radii from the cluster core, would help to better delineate the subgiant, giant, and horizontal branches of the cluster. The improved computational techniques for crowded field photometry make it possible to obtain reliable magnitude measurements, of bright stars, in close proximity to the cluster core. Preliminary experiments with artificial star fields indicate that it should be possible to work in regions where there are several hundred stars brighter than $V \approx 16.5$, within a single CCD frame. This would allow observations to be made as close as 6–8 arcmin from the centre of ω Cen. The Author is already in possession of a number of short CCD exposures made with the SAAO 1 m telescope, which will hopefully both strengthen the photometric transforma-

tions of the main sequence data presented in this study, and help further delineate the brighter regions of the CMD.

A major contribution to the experimental uncertainties in the photometric measures of the main sequence stars in this study has been the geometric variation of the stellar profile within the measured CCD frames. Although this has been minimised by the application of new software techniques for dealing with stars with differing profiles, there is still scope for repeating the observations with a detector which does not suffer from the problem of variable PSFs. This would allow the shape of the colour deviation from the main sequence ridge line to be better defined, and hence would allow the form of the metallicity distribution to be determined with greater precision. In addition, new spectroscopic techniques, such as fibre-optic spectroscopy, allow direct determination of metal abundances within faint cluster stars, as well as providing information on cluster membership. Studies involving such methods would be of great assistance in determining the nature of the heavy element distribution.

Although the empirically modified star-count models used in the present study were shown to give adequate field star estimates, it would be desirable to obtain faint CCD exposures to regions at the same galactic latitude as the present observations, but well outside of the the cluster tidal radius, in order that a more accurate estimate of the field star contamination can be made.

McClure *et al.* (1986) have shown that there appears to be a correlation between the metallicity of a cluster and the form of its initial mass function (as determined from its faint luminosity function). It would be interesting to compare the luminosity function of stars on the red and blue sides of the main sequence ridge line, in an attempt to ascertain whether there is any significant difference between the luminosity functions of metal-poor and metal-rich stars in ω Centauri. Resolution of this question could conceivably provide some insight into the mechanisms which have contrived to produce the observed correlation of cluster metallicity and mass-function power-law index in Galactic globular clusters. Shortage of time prevented such a comparison being undertaken in this study, but it would be a relatively straightforward task to obtain the required information from the faint main sequence data. The main sequence colour-magnitude diagram shows no evidence of a cluster white dwarf sequence, although one object has been observed which has $M_V \approx 8.9$ and $(B-V)_0 \approx -0.05$. This object is at least one

magnitude brighter than the high-luminosity limit of the white dwarf sequence of Penny & Dickens (1986), and predictions suggest (Bahcall, 1985) that there should be significantly less than one such star within the field studied. Therefore, it seems premature to identify this as a white dwarf candidate.

6.2 Some Implications of Recent CCD Colour-Magnitude Studies

In Chapter 1, a survey of 10 recent CCD colour-magnitude diagrams of globular clusters was made. The available colour-magnitude diagrams were used to determine the cluster distances, by fitting a sequence of nearby subdwarf stars the cluster main sequence loci. This is not a new technique, but this study is the most complete application of this technique to accurate CCD colour-magnitude diagrams, with a consistent subdwarf sequence. Lutz-Kelker (1973) corrections have been applied to the subdwarf parallaxes. From the derived cluster distance moduli, and published photometry of the cluster horizontal branch stars, the quantity M_V^{RR}, the absolute magnitude of the cluster horizontal branch in the region of the RR Lyrae instability strip, has been calculated. The absolute magnitude of the turnoff from the main sequence, M_V^{TO}, has likewise been obtained for each of the published colour-magnitude diagrams. The results show a correlation of M_V^{RR} with cluster metallicity according to $M_V^{RR} = 0.681(\pm 0.083) + 0.126(\pm 0.053)[\mathrm{Fe/H}]$. This result is qualitatively similar to that predicted by Sandage (1982) from his determination of the Oosterhoff period-shift–metallicity relationship for RR Lyrae stars in globular clusters, however, the slope is significantly different from that determined by Sandage. A more recent determination of the "Sandage effect" (period-shift versus metallicity relationship) in Galactic globular clusters by Noble & Dickens (1987) was combined with the above result to derive the relationship $\Delta M_V^{RR} = -1.6(\pm 0.07)\Delta \log P$. Sandage (1982) derived a different relationship, $\Delta M_V^{RR} = 3\Delta \log P$; the differing sign is due to a different convention for the measurement of the period-shift. The luminosity versus abundance relationship derived here is consistent with the predictions of canonical horizontal branch models. There is, however, still no single satisfactory solution to the problem posed by the period-shift–metallicity relation; namely that to reproduce the observations,

a correlation of the mass to light ratio for RR Lyrae stars with metallicity is logically required. The present study implies a difference in RR Lyrae mass of up to $\sim 0.1 M_{\odot}$ over the range of globular cluster abundances.

Ages have been derived for the sample of clusters studied by two methods; the isochrones of VandenBerg & Bell (1985) have been used to determine the age from the absolute magnitude of the cluster turnoff; the quantity $\Delta M_V^{RR}(bol)$ (the bolometric absolute magnitude difference between the main sequence turnoff and the horizontal branch at the colour of the RR Lyrae instability strip) has been used to provide an additional estimate. The average ages determined by these two methods are 15.1($\pm$1.9) Gyr and 15.0($\pm$1.8) Gyr respectively, showing the essential agreement between the different models used in the age determination. The ages determined from these published colour-magnitude studies suggest there may be a correlation of cluster age with metallicity, with the most metal-rich clusters being some 2–3 Gyr younger than the most metal-poor. This result is critically dependent upon the derived distances for the two metal-rich clusters in the sample, 47 Tuc and M4. In the case of M4 (Richer & Fahlman, 1984) the turnoff is not well delineated, and hence the derived age estimates have an uncertainty which is large in comparison with those of the other clusters in the sample. The 47 Tuc (Hesser *et al.* 1987) colour-magnitude diagram is extremely well delineated, and hence the uncertainty in determining the location of the main sequence turnoff should be relatively small. However, the turnoff luminosity is a function of the cluster abundance, as well as age, and uncertainties in the cluster abundance scale at the metal-rich end may explain the apparent age-metallicity relationship. For example, adopting the preferred value of Hesser *et al.* (1987) for the iron content of 47 Tuc, [Fe/H] = -0.8, would increase the derived ages from the turnoff magnitude and the ΔM_V^{RR} methods by approximately 1.5 Gyr, and the age discrepancy would largely disappear. Further high-precision photometric studies of high-metallicity clusters, which clearly delineate the main sequence to faint magnitude limits, are required to resolve the question of whether there is any significant metallicity-dependent age spread in the galactic globular cluster system. Furthermore, such observations would serve to clarify the nature of the globular cluster metallicity scale at the high abundance end.

Although the present study includes the latest available subdwarf parallaxes, the uncertainties in the absolute magnitudes of these stars are still large, and

future studies will benefit greatly from the improved parallaxes anticipated from space-borne observatories. Allied to the uncertainty in the location of the fiducial main sequence, defined by the subdwarfs, is the question of whether Lutz-Kelker (1973) corrections should be applied to the subdwarf parallaxes. Their omission from the present study would result in a significant ($\sim 0\overset{m}{.}1$) decrease in the derived distance moduli, and hence in the calculated RR Lyrae luminosities. The derived ages would also be increased by approximately 1 Gyr. There is confusion in the current literature, with some authors choosing to apply the full corrections as recommended by Lutz & Kelker (1973), whilst others apply smaller corrections, and a third group choose to omit them entirely. No convincing argument s to suggest that the corrections are inappropriate, have been forthcoming, and thus they have been applied in this present study. Work is necessary to clarify the situation, and determine the necessity, and magnitude of these statistical corrections. Until this question is resolved, it will remain a significant source of uncertainty in distance moduli derived from subdwarf fitting.

6.3 Observations of Lindsay 11

A preliminary colour-magnitude study of this small SMC globular has successfully delineated the red horizontal branch and giant branch tip. The luminosity of the horizontal branch implies a distance modulus $(m - M)_O = 18.85$. The SMC field star population is similar in nature to that of the cluster, and field star contamination, a severe problem in earlier photometric studies of this cluster, has been alleviated by the ability of profile-fitting photometry to measure stars in the densely-crowded central regions. The integrated magnitude and colour of the cluster (determined by digital aperture photometry through an 80″ aperture) are $V_i = 13.96$, and $(B - V)_i = 0.93$. An extremely red star (which has previously been noted as a photometric carbon star, by Mould & Aaronson, 1982) has been identified. The data do not reach faint enough limits to permit an age estimate to be made from isochrone fitting. Further observations, using a far more powerful telescope, such as the 4ḿetre AAT, would be necessary to locate the main sequence turnoff.

6.4 CCD Photometry

The CCD frames from which the faint ω Cen main sequence data are derived were found to exhibit significant geometric variation in stellar profile, resulting in a change of apparent photometric zeropoint of $\sim$ 10% within a single CCD frame, thus rendering conventional profile-fitting photometry with a fixed PSF impractical. The improved profile-fitting algorithms of A.J.Penny's STARMAN photometry package, which has the ability to fit each star with a different PSF, was used to overcome this problem. Software for determining the nature of the profile variations, and inputting the individual position-dependent profiles to the STARMAN programs was written by the Author. With these improvements, the positional variation in photometric zeropoint within a single CCD frame was reduced to $\sim$ 1%. Further refinements, such as utilizing non-linear fits when determining the form of profile variation, will improve the precision attainable with such techniques.

References

Aaronson,M., Mould,J., Huchra,J., Sullivan,W.T., Schommer,R.A. & Bothun,G.D., 1980. *Astrophys. J.*, **239**, 12

Allen,C.W., 1973. *Astrophysical Quantities*, (Athlone Press).

Anthony-Twarog,B.J., 1987. *Astron. J.*, **93**, 1454

Arp,H.C., 1955. *Astron. J.*, **60**, 317

Baade,W., 1944. *Astrophys. J.*, **100**, 137

Bahcall,J., 1985. In *Dynamics of Star Clusters*, IAU Symposium No. 113, eds. J.Goodman and P.Hut, (Dordrecht:Reidel)

Bahcall, J.N. & Soneira, R.M., 1980. *Astrophys. J. Suppl.*, **44**, 73

Bahcall, J.N. & Soneira, R.M., 1984. *Astrophys. J. Suppl.*, **55**, 67

Bell,R.A., 1987. in *Globular Clusters in Galaxies*, IAU Symposium No.126. eds. J.E.Grindlay and A.G.Davis Philip, (Dordrecht:Reidel), in press.

Bell,R.A. & Gustafsson, B., 1982. *Astrophys. J.*, **255**, 122

Bell,R.A. & Gustafsson,B., 1983. *Mon. Not. R. astr. Soc*, **204**, 249

Bell,R.A., Harris,G.L.H., Hesser,J.E. & Cannon,R.D., *Astrophys. J.*. 1985, **249**, 637

Belserene,E.P., 1959. *Astrophys. J.*, **64**, 58

Bessell,M.S., 1976. *Pub. A.S.P.*, **88**, 557

Bessell,M.S. & Norris,J., 1976. *Astrophys. J.*, **208**, 369

Bolte,M.J., 1987. *Astrophys. J.*, **315**, 469

Bond,H.E., 1975. *Astrophys. J.*, **202**, L47

Braccesi,A., Zitelli,V., Bonoli,F. & Formiggini,L., 1980. *Astron. Astrophys.*, **85**, 50

Brück,M.T. & Hawkins,M.R.S., 1982. *Mon. Not. R. astr. Soc*, **198**, 935

de Bruijn,J.W. & Lub,J., 1987. in *Stellar Pulsation*, eds. A.N.Cox, W.M.Sparks and S.G.Starrfield, (Springer-Verlag).

Buonanno,R., Corsi,C.E., Ferraro,I. & Fusi Pecci,F., 1987. *Astron. Astrophys. Suppl. Ser.*, **67**, 327

Burstein,D. & McDonald,L.H., 1975. *Astron. J.*, **80**, 17

Butler,D., Dickens,R.J. & Epps,E., 1978. 225, **148**,

Buzzoni,A., Fusi Pecci,F., Buonanno,R. & Corsi,C.E., 1983. *Astron. Astrophys.*, **128**, 94

Caldwell,S.P., 1983. *Ph.D. Thesis*, University of Sussex.

Cannon,R.D., 1974. *Mon. Not. R. astr. Soc*, **167**, 551

Cannon,R.D., 1981. *Mon. Not. R. astr. Soc*, **195**, 1

Cannon,R.D., 1983. in *Observational Tests of the Stellar Evolutionary Theory*, IAU Symposium No. 105. eds. A.Maeder and A.Renzini, (Dordrecht:Reidel).

Cannon,R.D. & Kontizas,M., 1974. *Mon. Not. R. astr. Soc*, **167**, 51p

Cannon,R.D. & Stewart,N.J., 1981. *Mon. Not. R. astr. Soc*, **195**, 15

Cannon,R.D. & Stobie,R.S., 1973. *Mon. Not. R. astr. Soc*, **162**, 207

Caputo,F., Castellani,V. & di Gregorio,R., 1983. *Astron. Astrophys.*, **123**, 141

Carney,B.W., 1979. *Astrophys. J.*, **233**, 211

Carney,B.W., 1980. *Astrophys. J. Suppl.*, **42**, 481

Carney, B.W., 1981. in *Astrophysical Parameters for Globular Clusters*, IAU Colloquium No. 68, eds. A.G.Davis Philip and D.S. Hayes, (Schenectady:L.Davis Press), p. 477.

Castellani,V., 1980. in *Globular Clusters*, eds. D.A.Hanes and B.Madore, (Cambridge:CUP).

Castellani,C., Giannone,P. & Renzini,A., 1970. *Astrophys. Space Sci.*, **9**, 418

Ciardullo,R.B. & Demarque,P., 1979. *Dudley Obs. Rept.*, **14**, 317

Chiosi,C., Bertelli,G., Bressan,A. & Nasi,E., 1986. *Astron. Astrophys.*, **165**, 84

Christy,R.F., 1966. *Astrophys. J.*, **144**, 108

Clegg,R.E.S., Lambert,D.L. & Tomkin,J., 1981. *Astrophys. J.*, **250**, 262

Cohen,J.G., 1980. *Astrophys. J.*, **241**, 981

Cohen,J.G., 1983. *Astrophys. J.*, **270**, 654

Cohen,J.G. & Gordon,G.A., 1987. *Astrophys. J.*, **318**, 215

Cox,A.N., Hodson,S.W. & Clancy,S.P., 1983. *Astrophys. J.*, **266**, 94

Da Costa,G.S., Norris,J. & Villumsen,J.V., 1986. *Astrophys. J.*, **308**, 743

Da Costa,G.S. & Villumsen,J.V., 1981. in *Astrophysical Parameters for Globular Clusters*, IAU Colloquium No. 68, eds. A.G. Davis Philip and D.Hayes, (Schenectady:L.Davis Press).

Davis Philip, A.G., 1979. ed., *Problems of Calibration of Multicolour Photometric Systems*, Dudley Observatory Reports No. 14, (New York:Dudley Observatory).

Demarque,P., 1980. in *Star Clusters*, IAU Symposium No. 85, ed. J.E.Hesser, (Dordrecht:Reidel)

Deupree,R.G., 1986. *Astrophys. J.*, **303**, 649

Deupree,R.G. & Cole,P.W., 1983. *Astrophys. J.*, **269**, 676

Dickens,R.J., 1972a. *Mon. Not. R. astr. Soc*, **157**, 281

Dickens,R.J., 1972b. *Mon. Not. R. astr. Soc*, **159**, 7p

Dickens,R.J. & Bell,R.A., 1976. *Astrophys. J.*, **207**, 506

Dickens,R.J. & Woolley,R.v.d.R., 1967. *R. Obs. Bull.* **128**

Driscoll,W.G. & Vaughan,W., eds., 1978. *Handbook of Optics*, (New York:McGraw-Hill).

Eccles,M.J., Sim,M.E. & Tritton,K.P., 1983. *Low Light Level Detectors in Astronomy*, (Cambridge:CUP).

Eggen,O.J., Lynden Bell,D. & Sandage,A.R., 1962. *Astrophys. J.*, **136**, 748

Eggleton,P.P. & Faulkner,J., 1981. in *Physical Processes in Red Giants*, eds. I.Iben and A.Renzini, (Dordrecht:Reidel).

Fahlman,G.G., Richer,H.B. & VandenBerg,D.A., 1985. *Astrophys. J. Suppl.*, **58**, 225

Faulkner,J., 1966. *Astrophys. J.*, **144**, 978

Faulkner,J. & Iben,I., 1966. *Astrophys. J.*, **144**, 995

Flannery,B.P. & Johnson,B.C., 1982. *Astrophys. J.*, **263**, 166

Franz,O.G., 1973. *J. R. Astr. Soc. Canada*, **67**, 81

Freeman,K.C. & Norris,J., 1981. *Ann. Rev. Astron. Astrophys.*, **19**, 319

Freeman,K.C. & Rodgers,A.W., 1975. *Astrophys. J.*, **201**, L71

Frogel,J.A., Cohen,J.G. & Persson,S.E., 1983. *Astrophys. J.*, **275**, 773

Gautschy,A., 1986. *On the Baade-Wesselink Method*, preprint series no. 23, Astronomical Institute, University of Basel.

Geisler, D., 1986. *Astrophys. J.*, **304**, L41

Geyer,E.H., 1967. *Zeitschrift für Astrophysik*, **66**, 16

Golay, M., 1974. *Introduction to Astronomical Photometry*, (Dordrecht:Reidel).

Gilmore,G., 1981. *Mon. Not. R. astr. Soc*, **195**, 183

Greenstein,J.L., 1976. *Astron. J.*, **81**, 323

Grindlay,J.E., 1978. *Astrophys. J.*, **224**, L107

Harding,G.A., 1962. *Observatory*, **82**, 205

Harding,G.A., 1965. *R. Obs. Bull.* , **99**, E65

Harding,G.A., Harbour,R.S. & Tritton,K.P., 1971. *R. Obs. Bull.* **172**

Harris,W.E., 1976. *Astron. J.*, **81**, 1095

Harris,W.E. & Racine,R., 1979. *Ann. Rev. Astron. Astrophys.*, **17**, 241

Harris,W.E., Pim Fitzgerald,M. & Cameron Reed,B., 1981. *Pub. A.S.P.*, **93**, 507

Hartwick,F.D.A., 1970. *Astrophys. J.*, **161**, 845

Haselgrove,C.B. & Hoyle,F., 1958. *Mon. Not. R. astr. Soc*, **118**, 519

Heasley,J.N. & Christian,C.A., 1986. *Astrophys. J.*, **307**, 738

Helfer,H.L., Wallerstein,G. & Greenstein,J.L, 1959. *Astrophys. J.*, **129**, 700

Hesser,J.E., 1987. in *Globular Clusters in Galaxies*, IAU Symposium No.126. eds. J.E.Grindlay and A.G.Davis Philip, (Dordrecht:Reidel), in press.

Hesser,J.E., Hartwick,F.D.A. & McClure,R.D., 1977. *Astrophys. J. Suppl.*, **33**, 471

Hesser,J.E., Bell,R.A., Cannon,R.D. & Harris,G.L.H., 1985. *Astrophys. J.*, **295**, 437

Hesser,J.E., Harris,W.E., VandenBerg,D.A., Allwright,J.W.B., Shott,P. & Stetson, P., 1987. *Pub. A.S.P.*, in press

Hodge,P.W., 1981. *Ann. Rev. Astron. Astrophys.*, **19**, 357

Hoyle,F. & Schwarzschild,M., 1955. *Astrophys. J. Suppl.*, **2**, 1

Iben,I., 1967. *Ann. Rev. Astron. Astrophys.*, **5**, 571

Iben,I., 1968. *Nature*, **220**, 143

Iben,I., 1974. *Ann. Rev. Astron. Astrophys.*, **12**, 215

Iben,I. & Renzini,A., 1983. *Ann. Rev. Astron. Astrophys.*, **21**, 271

Iben,I. & Renzini,A., 1984. *Phys. Rep.*, **105**, 329

Iben,I. & Rood,R.T., 1970. *Astrophys. J.*, **161**, 587

Jameson,R.F., 1986. *Vistas in Astronomy*, **29**, 17

Johnson,H.L., 1953. *Astrophys. J.*, **117**, 313

Johnson,H.L., 1963. in *Basic Astronomical Data*, ed. K.A.A.Strand, (Chicago:University of Chicago Press), p. 204.

Jorden,P.R., Thorne,D.J., & van Breda,I.G., 1982. in *Instrumentation in Astronomy, IV Proc. SPIE Conf.*, Tucson, Arizona.

King,C.R., Da Costa,G.S. & Demarque,P., 1985. *Astrophys. J.*, **299**, 674

King,I.R., 1966. *Astron. J.*, **71**, 64

King,I.R., 1983. *Pub. A.S.P.*, **95**, 163

Kontizas,M., 1980. *Astron. Astrophys.*, **131**, 58

Kontizas,M., 1984. *Astron. Astrophys. Suppl. Ser.*, **40**, 151

Kraft,R.P., 1979. *Ann. Rev. Astron. Astrophys.*, **17**, 309

Kraft,R.P., Suntzeff,N.B., Langer,G.E., Carbon,D.F., Trefzger,C.F., Friel,E. & Stone,R.R.S., 1982. *Pub. A.S.P.*, **94**, 55

Kron,G.E., 1956. *Pub. A.S.P.*, **68**, 125

Kunth,D. & Sargent,W.L.W., 1983. *Astrophys. J.*, **273**, 81

Leep,E.M. & Wallerstein,G., 1981. *Mon. Not. R. astr. Soc*, **196**, 543

Leep,E.M., Wallerstein,G. & Oke,J.B., 1986. *Astron. J.*, **91**, 1117

Lindsay,E.M., 1958. *Mon. Not. R. astr. Soc*, **118**, 172

Lloyd Evans,T., 1977a. *Mon. Not. R. astr. Soc*, **178**, 345

Lloyd Evans,T., 1977b. *Mon. Not. R. astr. Soc*, **181**, 591

Lub,J., 1977. *Ph.D. Thesis*, University of Leiden

Lub,J, 1987. in *Stellar Pulsation*, eds. A.N.Cox, W.M.Sparks and S.G.Starrfield,(Springer-Verlag).

Lutz,T.E. & Kelker,D.H., 1973. *Pub. A.S.P.*, **185**, 573

Macchetto, F., 1982. in *The Space Telescope Observatory*, IAU General Assembly No. 18, ed. Donald N.B.Hall, NASA CP-2244, 40

Mackay,C.D., 1986. *Ann. Rev. Astron. Astrophys.*, **24**, 255

Magain,P., 1985. *Astron. Astrophys.*, **146**, 95

Mallia,E.A., 1976. *Astron. Astrophys.*, **48**, 129

Manduca,A. & Bell,R.A., 1978. *Astrophys. J.*, **225**, 908

McClure,R.D., Hesser,J.E., Stetson,P.B. & Stryker,L.L., 1985. *Pub. A.S.P.*, **97**, 665

McClure,R.D. & Norris,J., 1977. *Astrophys. J.*, **217**, L101

McClure,R.D., VandenBerg,D.A., Smith,G.H., Fahlman,G.G., Richer,H.B., Hesser,J.E., Harris,W.E., Stetson,P.B. & Bell,R.A, 1986. *Astrophys. J.*, **307**, 149

McClure,R.D., VandenBerg,D.A., Bell,R.A., Hesser,J.E. & Stetson,P.B., 1987a. *Astron. J.*, **93**, 1144

McClure,R.D., Stetson,P.B., Hesser,J.E., Smith,G.H., Harris,W.E. & VandenBerg,D.A., 1987b. in *Globular Clusters in Galaxies*, IAU Symposium No.126. eds. J.E.Grindlay and A.G.Davis Philip, (Dordrecht:Reidel), in press.

McMullan,D. & Morgan,B.L.(eds.), 1978. *Proceedings of the Seventh Symposium on Photoelectronic Image Devices*, Imperial College, London.

Menzies,J.W., Banfield,R.M., & Laing,J.D., 1980. *SAAO Circulars*, **1**, 49

Mihalas,D., 1966. *Astrophys. J. Suppl.*, **13**, 1

Mironov,A.V., 1972. Soviet Astron.–A.J., **16**, 105

Mould,J.R., 1982. *Ann. Rev. Astron. Astrophys.*, **20**, 91

Mould,J.R. & Aaronson,M., 1979. *Astrophys. J.*, **232**, 421

Mould,J.R. & Aaronson,M., 1982. *Astrophys. J.*, **263**, 629

Noble,R.G. & Dickens,R.J., 1987. in *New Ideas in Astronomy*, Proceedings of IAU Colloquium, Venice, May 1986, (Cambridge:CUP), in press.

Newell,E.B., Rodgers,A.W. & Searle,L., 1969. *Astrophys. J.*, **158**, 699

Norris,J. & Bessell,M.S., 1975. *Astrophys. J.*, **201**, L75

Norris,J. & Bessell,M.S., 1977. *Astrophys. J.*, **211**, L91

Norris,J., & Freeman,K.C., 1983. *Astrophys. J.*, **266**, 130

Norris,J., & Smith,G.H., 1983. *Astrophys. J.*, **272**, 635

Oosterhoff,P.Th., 1939. *Observatory*, **62**, 104

Oosterhoff,P.Th., 1944. *Bull. astron. Inst. Netherlands*, **10**, 55

Ortolani, S., Rosino, L. & Sandage, A., 1986. *Astron. J.*, **90**, 473

Penny,A.J., 1976. *Ph.D. Thesis*, The University of Sussex.

Penny,A.J., 1979. *Mon. Not. R. astr. Soc*, **187**, 829

Penny,A.J., 1987. *The STARMAN User Manual*, Space Telescope Science Institute.

Penny,A.J. & Dickens,R.J., 1986. *Mon. Not. R. astr. Soc*, **220**, 845

Peterson,C.J., 1976. *Astron. J.*, **81**, 617

Peterson,C.J., 1986. *Pub. A.S.P.*, **98**, 1258

Peterson,C.J. & King,I.R., 1975. *Astron. J.*, **80**, 427

Persson,S.E., Frogel,J.A., Cohen,J.G., Aaronson,M. & Matthews,K., 1980. *Astrophys. J.*, **235**, 452

Pilachowski,C.A., 1984. *Astrophys. J.*, **281**, 614

Pilachowski,C.A., Canterna,R. & Wallerstein,G., 1980. *Astrophys. J.*, **235**, L21

Pilachowski,C.A., Sneden,C. & Wallerstein,G., 1983. *Astrophys. J. Suppl.*, **52**, 241

Poveda,A. & Allen,C., 1975. *Astrophys. J.*, **197**, 155

Pryor,C., Smith,G.H. & McClure,R.D., 1986. *Astron. J.*, **92**, 1358

Ratcliff,S.J., 1987. *Astrophys. J.*, **318**, 196

Ratnatunga,K.U. & Bahcall,J.N., 1985. *Astrophys. J. Suppl.*, **59**, 63

Renzini,A., 1977. in *Advanced Stages of Stellar Evolution*, eds. P.Bouvier and A.Maeder, (Sauverny:Geneva Observatory).

Renzini,A., 1983. *Mem. Soc. Astr. Italiana*, **54**, 335

Rich,R.M., Da Costa,G.S. & Mould,J.R., 1984. *Astrophys. J.*, **286**, 517

Richer,H.B. & Fahlman,G.G., 1984. *Astrophys. J.*, **277**, 227

Richer,H.B. & Fahlman,G.G., 1986. *Astrophys. J.*, **304**, 273

Richer,H.B. & Fahlman,G.G., 1987. *Astrophys. J.*, **316**, 189

Rodgers,A.W., Freeman,K.C., Harding,P. & Smith,G.A., 1979. *Astrophys. J.*, **232**, 169

Rodgers,A.W. & Harding,P., 1983. *Pub. A.S.P.*, **95**, 979

Rodgers,A.W., Newell,E.B., Stapinski,T., Harding,P. & Norris,J., 1980. *Pub. A.S.P.*, **92**, 288

Rood,R.T., 1973. *Astrophys. J.*, **184**, 815

Rood,R.T., 1983. in *Observational Tests of the Stellar Evolutionary Theory*, IAU Symposium No. 105, eds. A.Maeder and A.Renzini, (Dordrecht:Reidel).

Rood,R.T. & Crocker,D.A, 1985. in *Production and Distribution of C,N,O Elements*, ESO conference and workshop proceedings No. 21, eds. I.J.Danziger, F.Matteucci and K.Kjär.

Rowan-Robinson, M., 1985. *The Cosmological Distance Ladder*, (New York:Freeman).

Salpeter,E.E., 1955. *Astrophys. J.*, **121**, 161

Sandage,A.R., 1957. *Astrophys. J.*, **126**, 326

Sandage,A.R., 1969. *Astrophys. J.*, **157**, 515

Sandage,A.R., 1970. *Astrophys. J.*, **162**, 841

Sandage,A.R., 1973. *Astrophys. J.*, **183**, 711

Sandage,A.R., 1981. *Astrophys. J.*, **248**, 161–SII

Sandage,A.R., 1982. *Astrophys. J.*, **252**, 553–SIII

Sandage,A.R., 1986. *Ann. Rev. Astron. Astrophys.*, **24**, 421

Sandage,A.R., Katem,B. & Sandage,M., 1981. *Astrophys. J. Suppl.*, **46**, 41–SI

Sandage,A.R. & Smith,L.L., 1966. *Astrophys. J.*, **144**, 886

Sandage,A.R. & Tammann,G.A., 1976. *Astrophys. J.*, **210**, 7

Sandage,A.R. & Wallerstein,G., 1960. *Astrophys. J.*, **131**, 598

Sandage,A.R. & Wildey,R., 1967. *Astrophys. J.*, **150**, 469

Savage,B.D. & Mathis,J.S., 1979. *Ann. Rev. Astron. Astrophys.*, **17**, 73

Searle,L.S., Wilkinson,A. & Bagnuolo,W.G., 1980. *Astrophys. J.*, **239**, 803

Searle,L.S. & Zinn, R., 1978. *Astrophys. J.*, **225**, 357

Seitzer,P.O., 1983. *Ph.D. Thesis*, University of Virginia.

Simoda,M., 1972. *Pub. Astr. Soc. Japan*, **24**, 13

Simoda,M. & Iben,I., 1968. *Astrophys. J.*, **152**, 509

Smith,G.H., 1986. *Astrophys. J.*, **306**, 565

Smith,G.H., 1987. *Pub. A.S.P.*, **99**, 67

Smith,G.H. & Norris,J., 1982. *Astrophys. J.*, **254**, 149

Smith,G.H. & McClure,R.D., 1987. *Astrophys. J.*, **316**, 206

Smith,H.A., 1984a. *Pub. A.S.P.*, **96**, 505

Smith,H.A., 1984b. *Astrophys. J.*, **281**, 148

Sneden,C., Lambert,D.L. & Whitaker,R.W., 1979. *Astrophys. J.*, **234**, 964

Stetson,P.B., 1987. *Pub. A.S.P.*, **99**, 191

Strömgren, B., 1966. *Ann. Rev. Astron. Astrophys.*, **4**, 433

Strugnell,P., Reid,N. & Murray,C.A., 1986. *Mon. Not. R. astr. Soc*, **220**, 413

Sturch,C.R., 1978. *Pub. A.S.P.*, **90**, 264

Suntzeff,N.B., 1981. *Astrophys. J. Suppl.*, **47**, 1

Sweigart,A.V. & Gross,P.G., 1976. *Astrophys. J. Suppl.*, **36**, 367

Sweigart,A.V. & Gross,P.G., 1978. *Astrophys. J. Suppl.*, **38**, 405

Sweigart,A.V. & Mengel,J.G., 1979. *Astrophys. J.*, **229**, 624

Sweigart,A.V., Renzini,A. & Tornambé,A., 1987. *Astrophys. J.*, **312**, 762

Tayler,R.J., 1970. *The Stars: their structure and evolution*, (Wykeham:London)

Tody,D., 1980. *Applications of Digital Image Processing in Astronomy, SPIE*, **264**, 171

Trumpler,R.J. & Weaver,H.F., 1953. *Statistical Astronomy*, (Berkeley:University of California Press).

van Albada,T.S. & Baker,N.H., 1971. *Astrophys. J.*, **169**, 311

van den Bergh,S., 1981. *Astron. Astrophys. Suppl. Ser.*, **46**, 79

van Herk,G., 1965. *Bull. astron. Inst. Netherlands*, **18**, 71

VandenBerg,D.A., 1983. *Astrophys. J. Suppl.*, **51**, 29

VandenBerg,D.A., 1985. in *Production and Distribution of C,N,O Elements*. ESO conference and workshop proceedings No. 21, eds. I.J.Danziger, F.Matteucci and K.Kjär.

VandenBerg,D.A. & Bell,R.A., 1985. *Astrophys. J. Suppl.*, **58**, 561

Wagoner,R.V., 1973. *Astrophys. J.*, **179**, 343

Walker,A.R., 1984. *Mon. Not. R. astr. Soc*, **209**, 83

Walker,D.D., Walker,A.R., Carter,D.B. & Mack,P., 1983. *Observers Manual for the SAAO–UCL CCD Camera System*, SAAO.

Walker,D.D., Walker,A.R., Sanford,P.E., Mack,P., Lyons,A., Fordham,J., Bone,D. & Boksenberg,A., 1984. In *Proceedings of the Eighth Symposium on Photoelectronic Imaging Devices*, ed. B.L.Morgan, (London:Academic Press).

Webbink,R.F., 1981. *Astrophys. J. Suppl.*, **45**, 259

Webbink,R.F., 1985. in *Dynamics of Star Clusters*, IAU Symposium No. 113, eds. J.Goodman and P.Hut (D.Reidel:Dordrecht), p.541.

Weiss,A., 1983. *Astron. Astrophys.*, **127**, 411

Westphal, J.A., 1982. in *The Space Telescope Observatory*, IAU General Assembly No. 18, ed. Donald N.B.Hall, NASA Special Publication CP-2244, 28.

Woolley,R.v.d.R., *et al*, 1966. *R. Obs. Ann.*, **2**

Yang,J., Turner,M.S., Steigman,G., Schramm,D.N. & Olive,K.A., 1984. *Astrophys. J.*, **281**, 493

Young,A.T., 1974. *Methods Exp. Phys.*, **12A**, 123

Zinn,R., 1980. *Astrophys. J. Suppl.*, **42**, 19

Zinn,R. & West,M.J., 1984. *Astrophys. J. Suppl.*, **55**, 45